COMPLEXES CONTAINING A DIRECT, UNSUPPORTED LANTHANIDE-TRANSITION METAL BOND

A Dissertation

by

COREY P. BURNS

Submitted to the Office of Graduate and Professional Studies of
Texas A&M University
in partial fulfillment of the requirements for the degree of

DOCTOR OF PHILOSOPHY

Chair of Committee,	Michael Nippe
Committee Members,	Lei Fang
	Jaime Grunlan
	Hong-Cai Zhou
Head of Department,	Simon North

August 2019

Major Subject: Chemistry

ABSTRACT

The synthesis and characterization of molecules containing a direct, unsupported lanthanide transition metal bond is an ambitious task. Adding to this challenge, it is difficult to design a system in which both the lanthanide and transition metal can be interchanged to assess the nature of this interaction. As metal-metal bonding has provided significant insights into chemical bonding, catalysis, and electronic structure, it is important to pursue this rarely reported interaction. Additionally, lanthanide-transition metal heterometallics have drawn recent interest in the field of single-molecule magnetism (SMMs).

Initially, dinuclear lanthanide complexes containing bridging chloride (Cl^-) or triflate ($OCF_3SO_2^-$) ligands were isolated as synthons for future reactions. These complexes were successfully prepared by reacting a dysprosium salt with the previously reported 2,6-bis(methylenecyclopentadienyl)pyridine disodium salt Na_2PyCp_2 ($PyCp_2$ = 2,6-$(CH_2C_5H_3)_2C_5H_3N]^{2-}$) to yield $[(PyCp_2)Dy(\mu\text{-}OTf)]_2$ and $[(PyCp_2)Dy(\mu\text{-}Cl)]_2$. Of note, this was the first structurally characterized organometallic dysprosium triflate complex. These complexes exhibited properties of an SMM as evidenced by static and dynamic magnetic measurements. Despite the identity of the bridging ligand differing in the compounds, both exhibited a similar energy barrier (U) to reorient spin.

As dysprosium garners substantial attention in the field of SMMs, complexes containing a Dy-TM were first targeted. The reaction between $[(PyCp_2)Dy(\mu\text{-}OTf)]_2$ and anionic transition metal fragments KFp or KRp (Fp = $[CpFe(CO)_2]^-$, Rp = $[CpRu(CO)_2]$),

afforded the complexes $PyCp_2Dy$-$FeCp(CO)_2$ and $PyCp_2Dy$-$RuCp(CO)_2$. Infrared and Mössbauer spectroscopic studies suggested this interaction to be strong TM→Dy bonding interactions which is further supported by computational analysis. Magnetization dynamics performed in this study determined both compounds exhibited field induced slow magnetic relaxation with similar barriers despite different relaxation times. A later study compared the spectroscopic and magnetic properties of (thf)$PyCp_2Ce$-$FeCp(CO)_2$ to that of $PyCp_2Dy$-$FeCp(CO)_2$ and concluded that the identity of the lanthanide has an influence on the magnetic properties of these heterobimetallic systems. Spectroscopic and computational analysis demonstrated weaker TM→Ln interactions in the (thf)$PyCp_2Ce$-$FeCp(CO)_2$ as compared to $PyCp_2Dy$-$FeCp(CO)_2$. Preliminary findings on other Ln-TM bonded complexes isolated with this ligand system will be shared.

DEDICATION

To my family, Phillip, Ryan, Nolan, Peyton, and Margie, the most important people in my life. A special dedication to Lisa Burns, who God has taken elsewhere.

ACKNOWLEDGEMENTS

First and foremost, thank you to my thesis advisor, Dr. Michael Nippe. It is fair to say that Michael took a risk taking on a student with little synthetic experience in his first year as an Assistant Professor. I cannot thank Michael enough for personally teaching me how to think and work like an inorganic chemist. Michael, as I imagine you most thoroughly enjoyed guessing who I was for Halloween for five years, I can assure you a photo each future Halloween despite being aware you will have no idea who I am.

I would also like to acknowledge my committee members, Dr. Lei Fang, Dr. Jaime Grunlan, and Dr. Hong-Cai Zhou. I appreciated the insights you provided regarding my work, particularly during the preliminary exam. Additionally, thank you to the support staff, especially Dr. Nattamai Bhuvanesh, Dr. Joseph Reibenspies, and Dr. Gregory Wylie for training on X-Ray diffraction and NMR, respectively. A special acknowledgement to Bhuv, for finalizing the structures presented in this dissertation.

Thank you to Larry Vernier (B.S. 2018) and Zach Grant (B. S. 2019) for working with me during their undergraduate careers here at A&M. It is refreshing to get students who were enthusiastic about research and motivated me to continue to improve as a scientist during rough patches in lab.

As my project involved a variety of collaborations, I want to acknowledge all that assisted with the project outside of the Nippe Lab. Thanks to Bryan Foley and Dr. Alex Kosanovich (Ph.D. 2019) of the Ozerov Lab for infrared spectroscopy measurements, Dr. Joshua Wofford (Ph.D. 2018) of the Lindahl Lab for Mössbauer measurements, and Dr.

Stefan Minasian for X-ray absorption measurements. A special acknowledgement to Dr. Michael Hall and Xin Yang who provided all the computational analysis on the Ln-TM heterobimetallics. I enjoyed our conversations and your insights into these unique systems.

I would like to make a special mention to all my teaching mentors, Dr. Daniel Collins, Dr. Edward Lee, Dr. Tamara Powers, Dr. Ra’sheedah Richardson, and Dr. Amber Schaefer. I think it is obvious for those who know me teaching is what I have found most rewarding during my graduate career and know I aspire to be an instructor after graduation. These professors taught me the most important qualities an instructor could have, determination, dedication, discipline, and enthusiasm for the material. I would like to specifically thank Tamara. You have been my favorite mentor at A&M (do not tell Michael, or Dave for that matter).

Past and present Nippe Group Members: I could not ask for better people to work with. Firstly, a special shout out to Dr. Courtney Dickie (Ph.D. 2018) and Siyoung Sung, the two that along with myself have the distinction of being Michael’s first students. The first year was certainly grueling, and I would not have survived without you two. Courtney, I noticed in your thesis you acknowledged my affection for feminist punk, so I feel I should mention that great road trip to Houston to see Sleater-Kinney. I could not have asked for a better role model in the group despite it being difficult at times to understand your Canadian accent. Siyoung, I have no idea how you tolerated me for five years, but thank you. You were certainly the best person to vent frustrations to in lab and our coffee and Northgate trips were always a pleasure. Thank you to the other past members of the group, Dr. Davinder Kumar my synthetic mentor, Dr. Apoorva Upadhyay my movie buddy, Soomin Park, and Dr. Marcos “Carlos” Gil-Sepulcre for positive contributions to the group. Finally, I cannot put into words my appreciation and gratitude for Branford Wilkins. Branford, I have kidnapped you multiple times to attend atrocious music concerts, beat you senselessly in Mario Kart (notice I am not mentioning Smash Bros.), and subjected you to some awful movies. How are we still friends? I value our friendship and hopefully I can make it back to your defense someday #CorfordWilkurns.

Many thanks to my undergraduate research advisor, Dr. Gary Small and graduate student mentor, Dr. Sanjeewa Karunathilaka for my first exposure to research. They helped me find my passion and were supportive when it came to selecting a graduate school. Additionally, thanks to Dr. Elizabeth Stone and Dr. David Wiemer, two of my letter writers I continued to keep in touch with.

Thank you to the graduate school office at A&M, particularly Dr. Joanna Goodey-Pellois, Sandy Horton, and Valerie McLaughlin for keeping me sane during tough points in my graduate career. Your advice was greatly appreciated.

An acknowledgment is necessary for the bands that made up my playlists and shows I attended during my time in Texas. This includes, but is not exclusive to Jenny Lewis, Joyce Manor, Tiny Moving Parts, Motion City Soundtrack, Dead Kennedys, Tacocat, Kathleen Hanna, PUP, Sleater-Kinney, AJJ, Chastity Belt, Modern Baseball, Bad Religion, Social Distortion, and Less than Jake. Y’all are awesome despite what my group tells me.

A thank you is in order to all the friends I have made during my time in Bryan-College Station. I enjoyed my time being part of the R-NH_2 team and Buckyballers despite mostly being unsuccessful at kickball, soccer, and softball. Dr. Michael Eller and Tom Malinski, game nights were a great break from the stress and those times will be missed as we move on in the near future. To my RPG buddies, Greg Day (who tolerates WAY too much as a DM), Elizabeth Joseph, Zac Perry, Francisco Birk, Eli Little, Parker Schofield, Kevin Glennon, and Eric Braham, thank for making my first experience in D&D a memorable one. A special acknowledgement to Chris Watson, his much better half Dr. Alexandra Trott-Watson (Ph.D. 2018), and Brad Scurria. You were there when I needed you most during the lowest and most frustrating points of my graduate career. I can never repay the encouragement and support I received from you three.

As mentioned in my dedication, the most important people in my life are my family. Ryan and Margie, you have been excellent hosts the times I have visited Georgia and I cannot wait to visit the house and Tubby Nightmare Sausage after graduation. Nolan, it was a pleasure the year you were nearby in Houston to watch baseball and break things. Feel free to tell people your brother received a Ph.D. in dumb. Peyton, you will always be my best friend and it has been amazing watching you grow up. Thank you also to Mart Grinton, the fifth Burns Boy. Dad, aka Philly Cheese aka El Bistec de Philly con Queso, you have offered nothing but support since I was born. You have been the greatest teacher of all to me, and if I am half as good a teacher to my students as you were to me, they should be fine.

A final acknowledgement to my mother, Lisa Burns, who passed away August 2018. You were the most special person in the world and it is a shame you could not see me get my doctorate. You live on in the lessons and qualities you have passed down to your children, and I will never forget your kindness. You constantly made me aspire to be the best I could be, and hopefully my future students will acknowledge and appreciate that.

CONTRIBUTORS AND FUNDING SOURCES

Contributors

This work was supervised by a dissertation committee consisting of Professor Michael Nippe, Professor Lei Fang, and Professor Hongcai Zhou of the Department of Chemistry and Professor Jaime Grunlan of the Department of Mechanical Engineering.

Computational Data and Analysis in **Chapters 3** and **4** was provided by Xin Yang and Dr. Michael Hall. All ^{57}Fe Mössbauer data in the thesis was provided by Dr. Joshua Wofford of Dr. Lindahl's Group. All IR spectroscopic data was provided by Dr. Alex Kosanovich and Bryan Foley of Dr. Ozerov's group. All crystal reports were provided by Dr. Nattamai Bhuvanesh. Cyclic voltammetry measurements made in **Chapter 4** were conducted by Siyoung Sung. All other work conducted for the thesis was completed by the student independently.

Funding Sources

This work was also made possible in part through generous start-up funds provided by the Department of Chemistry at Texas A&M University, the Welch Foundation (A-1880), and the National Science Foundation (CHE-1753014). Computational data was made possible from the National Science Foundation Grant No. CHE-1664866. Mössbauer spectra were made possible by NIH Grant No. GM084266.

TABLE OF CONTENTS

Page

LIST OF FIGURES

LIST OF TABLES

Page

1. INTRODUCTION TO METAL-METAL BONDED COMPOUNDS

1.1 Introduction to Metal-Metal Bonding

Ever since Cotton's report of metal-metal multiple bonding in $[Re_2Cl_8]^{2-}$ anion in 1964, a significant portion of research has been dedicated to studying the bonding between metals.[1-2] As the field evolved, studies were not only confined to homobimetallic complexes, as compounds containing heterobimetallic metal-metal bonds were successfully isolated.[3] These heterobimetallics have garnered significant interest given the variety of compounds that can be prepared utilizing different metal combinations. These types of complexes have encroached the fields of catalysis[4-5] in addition to being vital in the understanding of structure and bonding.[1,6]

While there were a variety of metal-metal bonded complexes reported during the field's infancy, metal-metal quadruply bonded compounds were most prevelant.[1] Most interesting, there is speculation the first metal-metal quadruply bonded compound was initially synthesized in 1844.[7] As X-ray crystallography had yet to be developed until 1912, it was difficult, if not impossible, to observe the short distances between the two metal centers. The limits of metal-metal multiple bonding continue to be explored, with reports to expand the bond order to five and six.[8] As synthetic strategies developed and evolved, the field of metal-metal bonding has even expanded to heterometallics and metal-metal bonding between f-block elements and transition metals. These aspects will be discussed in further detail later in the introduction, as will the current state of metal-metal bonding. An emphasis will be placed on the electronic structure of these systems, as this is what gives rise to their unique properties.

1.1.1 Metal-Metal Multiple Bonding in Transition Metal Complexes

As previously mentioned, most compounds containing metal-metal bonds studied were homobimetallic metal-metal quadruply bonded systems. In particular, group six and group seven transition metals (Re, Cr, Mo, W), were most common. The first complex reported containing a metal-metal quadruple bond was octochlorodirhenate ($[Re_2Cl_8]^{2-}$).[2] The bonding between the two metals can be rationalized with molecular orbital theory and the d-orbitals of the metals (**Figure 1.1**).

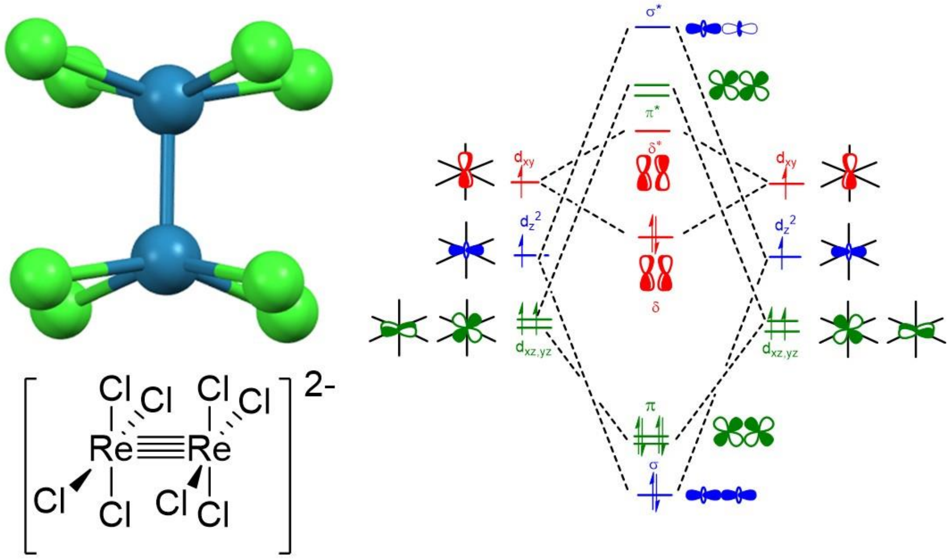

Figure 1.1: Qualitative molecular orbital diagram of $[Re_2Cl_8]^{2-}$. Adapted from Falvello et al. (2014).[9]

Most notably in the diagram is the delta (δ) bond between the two d_{xy} orbitals of the rhenium centers. It was hypothesized that the chloride ligands in $[Re_2Cl_8]^{2-}$ were eclipsed as opposed to the sterically favored staggered confirmation to allow for the greatest overlap between the two d_{xy} orbitals. Strongest support for presence of this bond was most reported in the photoelectron spectrum of octochlorodirhenate (**Figure 1.2**).[10]

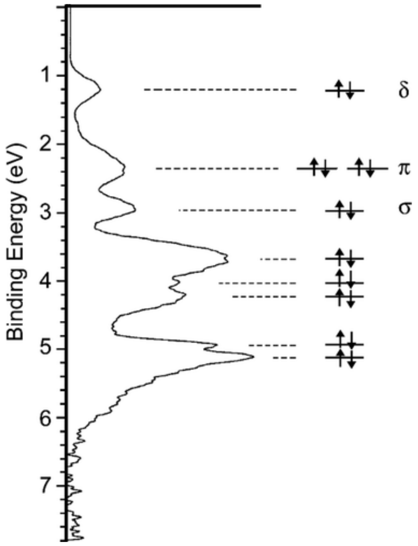

Figure 1.2: Photoelectron spectrum of $[Re_2Cl_8]^{2-}$. Adapted from Wang et al. (2000).[10]

This bond contains two nodes and its strength is dependent on rotation about the metal-metal bond. Consequently, this weak interaction compared to a σ or π bond imparts unique properties to these complexes.

Evidence for δ bond strength depending on the twist angles about the metal-metal bond was demonstrated with molybdenum compounds containing halide and chelating phosphine ligands. The addition of steric bulk around the phosphine ligands allowed for systematic study of isostructural compounds with increasing torsional strain. In general, the Mo-Mo distance increased as the twist angle between the two metal centers increased from 0° to 45°.[11]

Destabilizing the δ bond has also led to some metal-metal quadruply bonded complexes acting as strong reducing agents. Specifically a series of $W_2(hpp)_4$ (hpp = 1,3,4,6,7,8-hexahydro-2*H*-pyrimido[1,2-*a*]pyrimidine complexes were reported to reduce TCNQ (TCNQ = tetracyanoquinodimethane), fullerenes, and halogenated hydrocarbons.[12-13] These complexes reportedly had lower ionization energies (3.76 eV) to that of elemental, gaseous cesium (3.89 eV). Computational analysis (DFT calculations) suggested the sp^2 hybridized core of the guandinate ligands strongly destabilizes the electrons in the δ orbital. The electronic structure of these complexes has led to interest in other applications, specifically light emitting diodes[14], metal-organic frameworks[15], and anticancer treatment.[16]

1.1.2 Metal-Metal Bonding in Transition Metal Heterobimetallic Complexes

The field naturally gravitated to the synthetic challenge of preparing complexes with different metal-metal bond combinations. The earliest reports of these systems were $MoW(OAc)_4$ with later work studying first-row transition metal heterobimetallics in the gas phase in the 1980s.[17-18] A significant challenge in preparing these systems is the different electronic structure of each metal. This results in poor orbital overlap due to energy differences in atomic orbitals and occasional non-bonding interactions (**Figure 1.3**).[19]

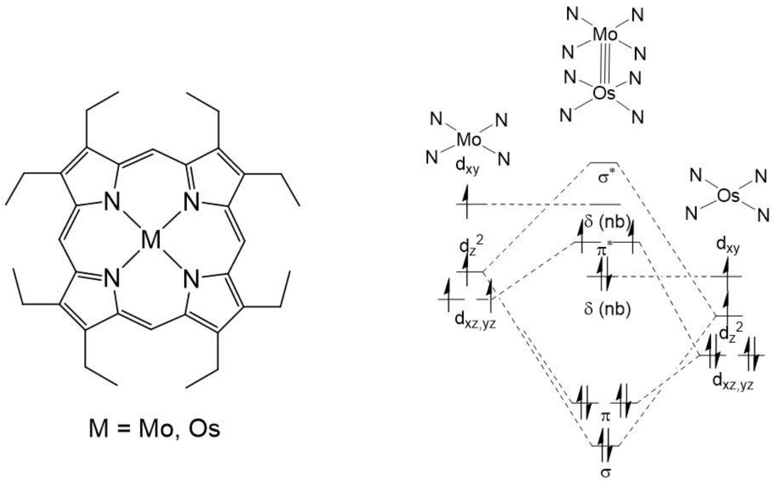

Figure 1.3: Qualitative molecular orbital diagram of metal-metal multiply bonded heterobimetallic system supported by porphyrin ligands. Differences in energy of the metals is author's rationale for complex's paramagnetism. Figure adapted from Collman et al. (1994).[19]

Recently, the groups of Lu and Thomas have successfully isolated heterometallic metal-metal multiply bonded systems utilizing three-fold symmetric ligand systems.[3.20] Most notably, both systems have stabilized heterobimetallic metal-metal bonded complexes of first row transition metals. This is a significant accomplishment given weaker metal-metal bonds between first row transition metals and poor spatial overlap 3d transition metals.[21-22]

While there have been strides both computationally and experimentally to evaluate the nature of heterometallic metal-metal bonding, the field is still in its early stages. What has been determined is the electronic structure is dependent on the ligand system and electron count of each metal (**Figure 1.4**). More specifically, the bond order between the metals tends to decrease as the difference in atomic number between the metals increases.[20] What is hypothesized is the orbital energies become more disparate, ultimately preventing δ and π overlap between the metals.

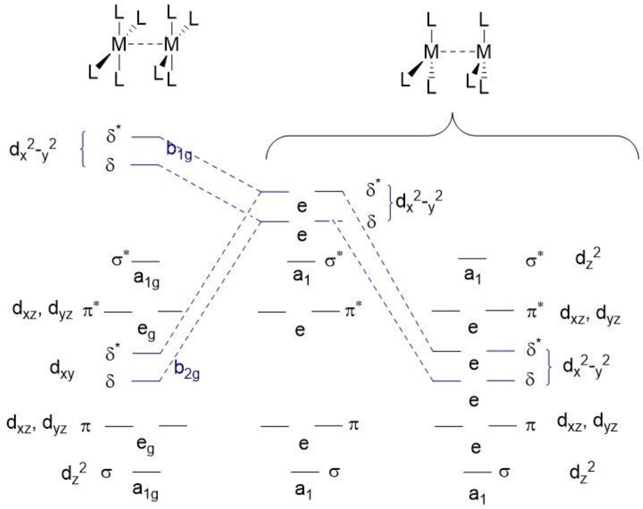

Figure 1.4: Qualitative molecular orbital diagram of four-fold and three-fold symmetric homobimetallic complexes. The relative energy of the δ/δ* is variable as a function of metal and ligand identity. Adapted from Krogman & Thomas (2014).[20]

The polarity of the metal-metal bond has been exploited towards reactivity that is not possible in monometallic systems. Of particular note, a complex containing a Cu-Fe bond behaved as a catalyst in the photochemical borylation of benzene.[5] The authors proposed a mechanism in which both the copper and iron center underwent a single electron oxidation to facilitate catalysis. This mechanism contrasts single noble metal site mechanisms of two electron processes occurring at the metal or previous attempts to achieve catalysis at a single iron center.[23] Other reports in literature describe small molecule activation (such as CO_2), dinitrogen binding, and dinitrogen silylation by heterometallic metal-metal bonded systems.[24-25] It is proposed the polarized metal-metal bond acts as a source of two electrons to achieve the desired reactivity.

1.1.3 Metal-Metal Bonding between f-block and Transition Metals

The final class of metal-metal bonds in molecules to be studied is a bond between a transition metal and an f-block element (actinides and lanthanides). While there have been numerous reports of metal-metal bonds between f-block elements and main group metals, examples of discrete molecules with lanthanide-transition metal (Ln-TM) or actinide-transition metal (An-TM) are scarce in literature (**Figure 1.5**).[6] The primary reason for this can be attributed the synthetic challenges associated with isolating compounds with a direct, unsupported Ln-TM or Ac-TM bond.

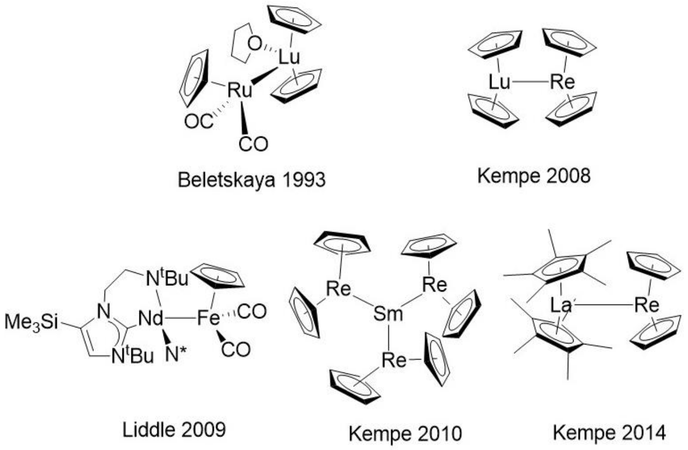

Beletskaya 1993

Kempe 2008

Liddle 2009

Kempe 2010

Kempe 2014

Figure 1.5: Selected examples of complexes containing an unsupported Ln-TM bond.

Looking specifically at Ln-TM bonds, there have been two approaches to prepare the target molecules (**Figure 1.6**)**.** The earliest report of such a complex was by Beletskaya and co-workers,[26] utilizing a halide bearing lanthanide synthon and an anionic transition metal fragment such as Rp^- ($Rp = [CpRu(CO)_2]^-$) or Fp^- ($Fp = [CpFe(CO)_2]^-$. This salt elimination method has been employed in other work to generate more compounds containing Ln-TM bonds.[27] In contrast, Kempe and co-workers have synthesized similar complexes via an alkane elimination between an acidic transition metal hydride and Ln-alkyl species.[28]

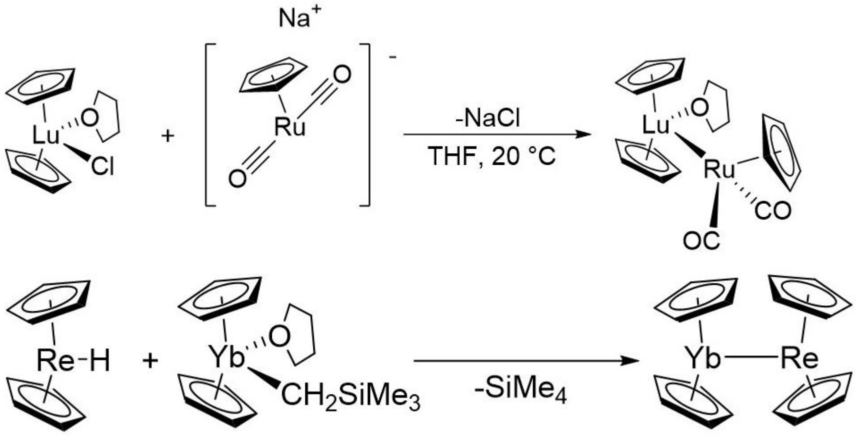

Figure 1.6: Two common synthetic approaches to synthetize Ln-TM bonds, salt elimination (top) and alkane elimination (bottom).

Although roughly a dozen of these compounds have been reported, studies have been mostly limited to computational methods and no system has been reported to systematically substitute the lanthanide or transition metal.[29] Designing this system would be valuable to assess the nature of Ln-TM bonding and provide a physical description of the bond.

While Ln-M or Ac-M complexes have been isolated and sufficiently stable to structurally characterize, experimental information has been mostly reserved to reactivity studies. Examples have included CO_2 insertion, alcoholysis, and ketone insertion.[30-31]

Notably, there have not been any studies on the magnetization dynamics of Ln-TM bonded molecules. As some of the strongest bulk magnets are lanthanide transition metal heterometallics, it would be valuable to study if this behavior translates to the molecular level.[32] The electronic structure of lanthanide ions that make them appealing candidates for single-molecule magnets (SMMs) and how to assess SMM behavior will be discussed in later sections.

1.2 Single-Molecule Magnetism

Single-molecule magnets are an interesting class of compounds drawing attention to the fields of high capacity data storage, qubits in quantum computing, and molecular spintronics.[33-35] Defined as single molecules that exhibit properties associated with bulk materials, three main criteria are evaluated to determine if a molecule behaves as an SMM. The molecule must possess a bistable magnetic ground state and magnetic anisotropy (1), have an energy barrier associated with reorienting their molecular spin, U (2), and exhibit magnetic hysteresis below a certain blocking temperature, T_B (3). Magnetic properties of molecules are influenced by a variety of factors, including identity of the paramagnetic center, ligand field effects, and ligand symmetry around the metal center.[36]

The first single molecule magnet reported was $Mn_{12}O_{12}(OAc)_{16}(H_2O)_4$, colloquially known as Mn_{12}.[37] This was the first molecule to exhibit magnetic hysteresis and the origin of the term single-molecule magnet when it was published in 1993. Approximately 25 years later, a trivalent, metallocenium lanthanide complex $[(Cp^{iPr5})Dy(Cp^*)]^+$ (Cp^{iPr5} = penta-iso-propylcyclopentadienyl, Cp^* = pentamethylcyclopentadienyl) exhibited magnetic hysteresis up to 80 K.[38] This marked a significant achievement in the field of SMMs, as this was the first report of a molecule exhibiting SMM behavior at temperatures above the boiling point of liquid nitrogen (77 K). While the field is still in its infancy, substantial progress has been made in molecular magnetism over the years and the theory of molecular magnets continues to develop in order to rationally design systems towards ideal magnetic behavior.

1.2.1 Characterizing SMMs

Assessing magnetic behavior is best achieved by using a Superconducting Quantum Interference Device (SQUID) magnetometer. Utilizing liquid helium, a commercial SQUID can reach temperatures as low as 1.8 K and fields up to 7 T (70000 Oe) can be applied during measurements. A SQUID contains two superconducting coils which are separated by insulating layers to form Josephson junctions.[39] A SQUID magnetometer is incredibly sensitive with the ability to detect magnetic fields as small as 10^{-15} T on milligram amounts of material.[40]

Static magnetic properties are determined using direct current (dc) fields. Assuming magnetization (M) depends linearly on field (H), $\boldsymbol{M} = \boldsymbol{\chi_V H}$, where χ_V is the volume susceptibility and dimensionless value. The magnetic susceptibility is dependent on a paramagnetic (χ_{para}) and diamagnetic ($\chi_{diamagnetic}$) component. The diamagnetic component, a result of paired electrons in a molecule, is a negative value and small in magnitude compared to the paramagnetic component. According to **Equation 1.1**, $\chi_{paramagnetic}$ can be derived from the experimentally χ value by applying a diamagnetic correction.[41]

$$\boldsymbol{\chi = \chi_{diamagnetic} + \chi_{paramagnetic}} \text{ (Equation 1.1)}$$

The temperature susceptibility product, or χT, is utilized to determine deviations from paramagnetic behavior. According to the Curie Law (**Equation 1.2**), χT should be constant for non-interacting spins and independent of temperature.[42]

$$\boldsymbol{\chi = \frac{M}{H} = \frac{Ng^2\mu_B^2 J(J+1)}{2k_B T} = \frac{C}{T}} \text{ (Equation 1.2)}$$

This operates under the assumption H is small and temperature is not too low as to satisfy the relationship $\boldsymbol{g\mu_B H \ll k_B T}$. The variable g is known as the Landé factor, a value normally of 2 for transition metals and can be calculated based on **Equation 1.3** for lanthanides.

$$\boldsymbol{g_J = 1 + \frac{S(S+1)-L(L+1)+J(J+1)}{2J(J+1)}} \text{ Equation 1.3}$$

Based on the temperature dependence of χ_T, magnetic exchange interactions and Curie behavior can be determined in a system. If a molecule obeys the Curie Law, a plot of χ_T *vs*. T will result in a straight line parallel to the x-axis. In general, trivalent lanthanide complexes obey the Curie Law at room temperature, but deviate from the Curie law as temperature decreases. If the $\chi_M T$ value decreases, it is attributed to either a thermal depopulation of Stark sublevels or antiferromagnetic interactions.[3] An increase in $\chi_M T$ suggests the possibility of ferromagnetic interactions.

Another static magnetic measurement that can be performed is to determine the effective magnetic moment, μ_{eff}. Calculated from the experimentally measured susceptibility, it is expressed in Bohr magnetons (μ_B) and the field dependence of μ_{eff} can assess magnetic saturation (**Equation 1.4**).

$$\boldsymbol{\mu_{eff}^2 = \frac{3k_BT_\chi}{N\mu_B^2} = g^2(J(J+1))} \text{ Equation 1.4}$$

Magnetization dynamic measurements are useful in estimating a barrier height (U_{eff}) and predicting the likelihood a molecule will exhibit magnetic hysteresis. These measurements are ideally performed in the absence of a dc field and the application of a small alternating current (ac) field of about 2 Oe. By varying the frequency of the oscillating field (ω), magnetization relaxation times (τ) can be investigated. The total ac susceptibility can be calculated according the **Equation 1.5**, where χ_T is the isothermal susceptibility and χ_S is the adiabatic susceptibility.[42] At low frequencies of the oscillating field ($\omega\tau << 1$), the spin system is in thermal equilibrium with the lattice and the measured susceptibility is equal to a static one. On the contrary, the spin system is uncoupled in the lattice if $\omega\tau >> 1$ at higher frequencies.[42] The total ac susceptibility is equal to the sum of the real (or in-phase) component (χ') and imaginary (out-of-phase) components (**Equation 1.6, 7**). This observation holds if the isothermal and adiabatic susceptibility are real.

$$\boldsymbol{\chi_\omega = \chi_s + \frac{\chi_T - \chi_s}{1+i\omega\tau}} \text{ Equation 1.5}$$

$$\boldsymbol{\chi' = \frac{\chi_T - \chi_s}{1+\omega^2\tau^2} + \chi_s} \text{ Equation 1.6}$$

$$\boldsymbol{\chi'' = \frac{(\chi_T - \chi_S)\omega\tau}{1+\omega^2\tau^2}} \text{ Equation 1.7}$$

It should be noted that τ is not typically a single value. A parameter (α) is incorporated into **Equation 1.5** to account for this. The closer α is to 0, the closer the relaxation time is a result of a single relaxation process.[42]

The in-phase and out-of-phase components of the ac susceptibility can be plotted to generate a Cole-Cole plot (χ'' *vs.* χ'). From Cole-Cole plots, relaxation times can be extracted. The Cole-Cole plots of each temperature can be fit utilizing a least squares regression to the generalized Debye Equation (**Equations 1.8, 9**).[43] The extracted relaxation times are used in an Arrhenius plot (*ln* (τ) *vs.* 1/T) to estimate a barrier height for thermal relaxation.

$$\chi'_{\omega} = \chi_S + (\chi_T - \chi_S)\frac{1+(\omega\tau)^{1-\alpha}\sin(\frac{\pi\alpha}{2})}{1+2(\omega\tau)^{1-\alpha}\sin\left(\frac{\pi\alpha}{2}\right)+(\omega\tau)^{2-2\alpha}} \text{ Equation 1.8}$$

$$\chi''_{w} = (\chi_T - \chi_S) + \frac{(\omega\tau)^{1-\alpha}\cos(\frac{\pi\alpha}{2})}{1+2(\omega\tau)^{1-\alpha}\sin\left(\frac{\pi\alpha}{2}\right)+(\omega\tau)^{2-2\alpha}} \text{ Equation 1.9}$$

There are two common ways to calculate a barrier. The first method is to fit the linear portion of an Arrhenius plot (**Equation 1.10**). This assumes that magnetic relaxation occurs solely via the Orbach mechanism. In an alternative method, multiple magnetic relaxation pathways are considered to estimate U (**Equation 1.11**).[44] This equation includes terms for relaxation mechanisms such as quantum tunneling of magnetization (QTM), Raman, and direct (assuming a dc field was applied) processes.

$$\tau^{-1} = \tau_0^{-1}e^{\frac{-U_{eff}}{k_BT}} \text{ Equation 1.10}$$

$$\tau^{-1} = AH^4T + \tau_{QTM}^{-1} + CT^{n_2} + \tau_0^{-1}e^{\frac{-U}{k_BT}} \text{ Equation 1.11}$$

Specifically looking at quantum tunneling, it is a through barrier relaxation pathway.[45] This phenomena is observed when sublevels on either side of the energy well are degenerate and mixed, allowing the relaxation process of a magnet to circumvent the associated energy cost of overcoming the thermal barrier.[45] In the worst case scenario, quantum tunneling hinders an SMM to the point that the effective barrier to reorient spin is essentially zero. As a result of quantum tunneling observed in most SMMs, the barrier (U) reported is an effective barrier (U_{eff}).

Two common methods to overcome observed tunneling in an SMM are diamagnetic dilutions and applying a dc field during ac susceptibility measurements.[46] The purpose of applying a dc field is to reduce mixing of magnetic sublevels (**Figure 1.7**).

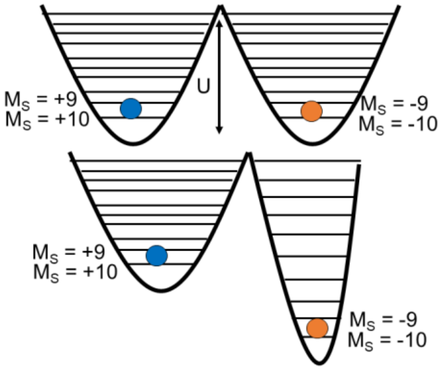

Figure 1.7: Depiction of energy well diagram of Mn_{12} before (top) and after (bottom) applying an external dc field. Figure adapted from Glaser.[46]

Although this effectively reduces tunneling, it does not completely shut down the tunneling relaxation pathway and merely reduces the rate of tunneling.[47] It should also be noted that in cases when a material can exhibit slow relaxation in the presence of an external dc field, the material itself is not a magnet as it will not show this relaxation under zero applied field nor magnetic hysteresis. In the other method to suppress tunneling, samples can be doped with a diamagnetic material. Cocrystallization of isostructural Y^{3+} is commonly used.[45,47] Diamagnetic dilutions result in reduction of dipole-dipole interactions between the lanthanide ions within a crystal lattice which is one cause of fast tunneling at lower temperatures.[45,47]

A barrier can still be determined for a material that exhibits slow magnetic relaxation under an applied dc field. Initially, an optimal field to run a temperature dependent study is evaluated. This experiment involves applying various dc fields at a constant temperature. Generally, relaxation times (τ) increase with increasing field as contributions from quantum tunneling decreases. However, further application of higher fields introduces the possibility of direct relaxation processes and a subsequent decrease in τ. Cole-Cole plots can be generated from these field dependent studies to extract the relaxation times. A plot of τ *vs.* H can be fit to **Equation 1.12**, where A is a direct relaxation parameter, B_1 and B_2 are quantum tunneling parameters, and D accounts for field independent Orbach and Raman contributions to τ.[48] After an optimal field is determined, a variable temperature study of the ac susceptibility can be performed to estimate a barrier using **Equation 1.11**. Normally, values obtained for parameters A, B_1, and B_2 are fixed with other parameters refined as to avoid over parameterization.

$$\tau^{-1} = AH^{n_1}T + \frac{B_1}{1+B_2H^2} + D \quad \text{Equation 1.12}$$

Although not directly correlated, a high value calculated for U (or U_{eff}) generally is a good indicator for magnetic blocking. To probe a molecule for magnetic hysteresis, a certain scan rate is utilized to cycle through fields in a positive and negative direction. When a field is applied, the system is magnetized up to a certain saturation point. The field is lifted and a degree of that field is retained if there is magnetic memory. In order to return to zero magnetization, a field of specific magnitude in an opposite direction is applied. This field is known as the coercive field. The highest temperature in which hysteresis is still observed is known as the blocking temperature, T_B. Due to efficient quantum tunneling of magnetization under zero field, waist restricted hysteresis is typically observed in SMMs (**Figure 1.8**).

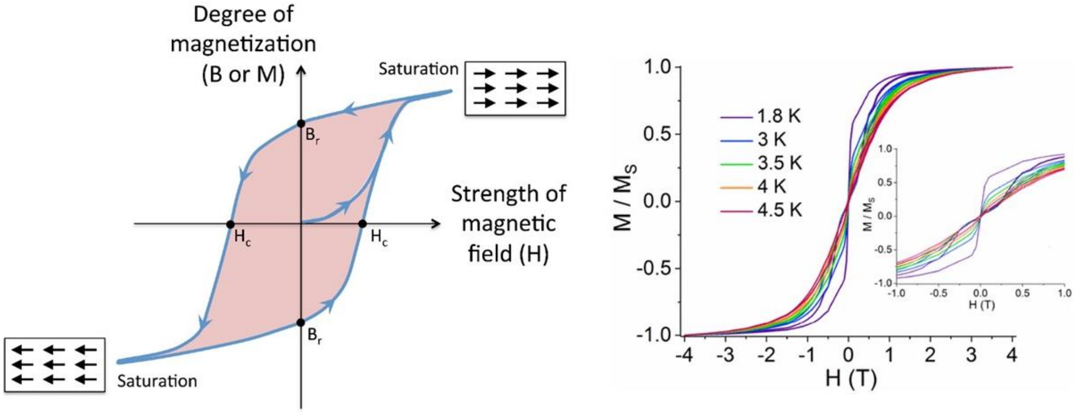

Figure 1.8: Generic hysteresis loop for bulk magnetic material[49] (left) and waist restricted hysteresis loop for molecule[50] (right). The waist restricted loop is a consequence of quantum tunneling. Adapted from Latendresse et al. (2017).

1.2.2 Evaluating SMMs

The two primary parameters to evaluate the performance of SMMs are the barrier height (U) and blocking temperature (T_B). The energy barrier represents the transition between the two levels of the ±m_S ground states for transition metal based SMMs and ±m_J states for lanthanide based SMMs (**Figure 1.9**).

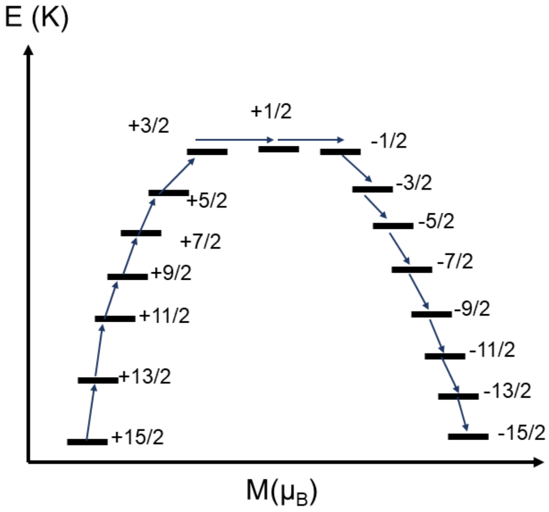

Figure 1.9: Barrier for reversal of magnetization for Dy^{3+} complex. Adapted from Ungur & Chibotaru (2011).[51]

The barrier height is influenced by the magnetic anisotropy and changes in the ligand field. Maximizing the energy separation of the magnetic ground state and first excited state is ideal to observe high barriers.

One of the difficulties in comparing T_B between molecules are the different definitions and methods in reporting a blocking temperature. The most common method is the highest temperature at which an opening in the hysteresis loop is observed. However, this definition of T_B is scan rate dependent and sweeping the field at greater rates can result in higher temperatures in which hysteresis is observed. Another definition involves zero-field cooled dc experiments in which a sample is cooled prior to the application of a field. The temperature at which the ZFC measurement deviates from a field cooled experiment indicates magnetic blocking and is considered an alternative definition of blocking temperature. The final definition is the temperature at which a relaxation time of 100 s is observed. This is an advantageous definition because it makes it easy to compare blocking temperatures between compounds. In the rest of the thesis, the first definition described of blocking temperature will be used.

1.2.3 Transition Metal based SMMs

The term single-molecule magnet originated in 1993 when describing the magnetic behavior of Mn_{12}.[37] This compound had a reported barrier of 42 cm^{-1} and opening of the hysteresis loops were detected at temperatures below 4 K. The structure of Mn_{12} was described as an external ring of 8 Mn^{3+} ions (S = 2) and 4 internal Mn^{4+} ions corresponding to an S = 10 ground state. The large uniaxial anisotropy was ascribed to a Jahn-Teller distortion that favors tetragonally elongated geometry.

Considering the equation accepted for the barrier, $U_{eff} = |D|S^2$ (integer spin) and $U_{eff} = |D|(S^2 - 0.25)$ (non-integer spin) where Ising-type anisotropy is expressed by the axial zero-field splitting parameter, D, and S is the total spin of the molecule, initial efforts focused on increasing S of molecules to achieve high barriers.[52-53] Focus transitioned later to large Ising-type anisotropy once an S= 83/2 $\{Mn_{19}\}$ cluster synthesized was determined to have a barrier of 2.8 cm^{-1} (4 K) and practically zero D value.[54] Theoretical work conducted by Neese and Pantazis proposed D varied nearly inversely with S.[55] Following this theory, focus shifted towards increasing anisotropy. This marked the transition to the development of single-ion magnets of d and f-block elements.

Since the report of Mn_{12}, significant strides have been made in transition metal based SMMs. One notable example was a two-coordinate Co(II) imido complex, $[(sIPr)Co^{II}NDmp]$ (sIPr = 1,3-bis(2,6-disopropylphenyl)-4,5-dihydro-imidizole-2-ylidene, Dmp = 2,6-dimesitylphenyl). Additionally, a two-coordinate Fe(I) complex $[Fe(C(SiMe_3)_3)_2]^-$ reported exhibited a barrier of 226 cm^{-1} and magnetic blocking below 4 K.[56-57] Despite the progress that has been made in the field of transition metal-based SMMs, the best performing magnets in literature are typically lanthanide-based single-ion magnets (SIMs).

1.2.4 Electronic Structure of Lanthanide Ions

One of the most desired qualities in an SMM is magnetic anisotropy. As trivalent lanthanide ions possess large inherent anisotropy, they are attractive candidates to implement in SMMs. Additionally, most lanthanide ions have large unquenched angular momentum.[58] Consequently, spin-orbit coupling splits the $^{2S+1}L_J$ ground state into different m_J states with the ligand field acting as a small perturbation on the lanthanide.[44] To obtain the most desirable magnetization dynamics in SMMs, the ground state should be the largest magnitude $\pm m_J$ state with a large energy separation from the excited m_J states.[58]

Of all the lanthanides, dysprosium(III) based SMMs are the most commonly reported lanthanide based SMMs. There are two factors contributing to the ubiquity of Dy^{3+} SMMs: the high degree of magnetic anisotropy in Dy(III) ions (1) and Dy^{3+} is a Kramers ion (odd number of unpaired f electrons) (2). As dysprosium is a Kramers ion, the ground state will always be bistable (one criteria for an SMM). While lanthanide ions such as Tb^{3+} have a high degree of anisotropy, it is not a Kramers ion. Therefore, the ground state might not be stable, and highly axial symmetry is necessary to observe a bistable ground state.

A prudent choice of ligand is also necessary in regards to designing an ideal SMM. Depending on the identity of the lanthanide, the electron density around the ion can be considered either an oblate or prolate shape.[47]

A large energy separation between ground and excited m_J states for oblate ions (such as dysprosium) are expected if ligands place negative charge at the axial sites, whereas for prolate ions (such as erbium), an equatorial field of negative charges would be preferred[47] Considering this trend, it is ideal to have rigid ligand designs that coordinate to axial sites in the case of dysprosium. A common moiety utilized in SMM design considering this factor is cyclopentadienyl (Cp) and its various derivatives.[59-60]

1.2.5 Lanthanide based SMMs

The first lanthanide-based SIM (single-ion magnet) was reported in 2003 by Ishikawa and coworkers. The trivalent double decker terbium pthalocyanate complexes exhibited slow magnetic relaxation in a yttrium diluted sample. The reported barrier of the complex $[Bu_4N][Tb_{0.02}Y_{0.98}Pc_2]$ was 230 cm^{-1}.[61] The diluted dysprosium analogue was also prepared, but the Tb complex performed better in terms of barrier (U_{eff} = 28 cm^{-1}). It was proposed that the strong axial field provided by the pthalocyanate ligands promoted the ground state of the greatest magnitude ($m_J = \pm6$ for Tb) and large separation between the ground state and first excited state ($m_J = \pm5$). Upon a one-electron oxidation of the ligand system, the undiluted, neutral compound $TbPc_2$ was determined to have a U_{eff} of 410 cm^{-1}.[62] The increase in barrier was attributed to delocalization of the unpaired electron density of the ligand interacting more strongly with the highly anisotropic Tb^{3+} center. Given that this was the earliest example of a lanthanide SIM and the variability of the Pc ligand, this remains one of the most studied systems in the field of SMMs.[52] The field's current understanding of SMM behavior can mostly be credited the pthalocyanate system.

A ligand geometry that has provided promising results to lanthanide-based SMMs is pentagonal bipyramidal (D_{5h} symmetry around the metal ion). More specifically, a pentagonal bipyramidal geometry with strong axial ligands and weak equatorial ligands has led to Dy-based SMMs with impressive barriers. For example, the complex $[Dy(Cy_3PO)_2(H_2O)_5]Br_3 \cdot (2Cy_3PO) \cdot 2H_2O \cdot 2EtOH$ by Chen and coworkers exhibited a U_{eff} = 377 cm^{-1} and a blocking temperature of 20 K (200 Oe/s scan rate).[63] Quantum tunneling of magnetization was reduced due to transverse anisotropy being quenched by the weak equatorial ligand field. Another example of a high barrier magnet with D_{5h} symmetry reported by Ding and coworkers $[Dy(O^tBu)_2(py)_5][BPh_4]$ contains anionic axial ligands and weak pyridine equatorial ligands.[64] This complex demonstrated magnetic blocking according to ZFC/FC experiments at temperatures below 14 K. Despite mitigation of quantum tunneling due to the weak equatorial ligands in these examples, it is not completely quenched as evidenced by QTM observed in the hysteresis loops.

An important development in minimizing transverse anisotropy in oblate lanthanide ions (such as Dy^{3+} and Tb^{3+}) was reported by Chilton in 2015.[65] *Ab initio* calculations suggested ideal symmetry of C_∞ or D_∞ (only axial ligands) would result in record breaking barriers and blocking temperatures. Calculations on the theoretical $[Dy(N(SiMe_3)_2)_2]^+$ estimated the barrier to be 1800 cm^{-1} with magnetic hysteresis above liquid nitrogen temperatures (>77 K). Calculations that further supported this ideal symmetry demonstrated a significant decrease in U_{eff} as the N-Dy-N angle deviated from 180° and equatorial solvent molecules were introduced in the system.

Support for this hypothesis was reported a few years later. The first instance was reported independently by Goodwin et al. and Guo et al. in 2017.[66-67] The complex was the dysprosocenium compound $[Dy(Cp^{ttt}{}_2)][B(C_6F_5)_4]$ ($Cp^{ttt} = C_5H_2{}^tBu_3$-1,2,4) and nearly axial symmetry as demonstrated by the Cp^{ttt}-Dy-Cp^{ttt} angle of 147.59(7)°. Hysteresis studies for this complex reported blocking temperatures of 60 K (39 Oe/s scan rate). This blocking temperature was further corroborated with ZFC/FC experiments and magnetic relaxation studies.[66-67] The axial symmetry was improved in the heteroleptic complex $[(Cp^{iPr5})Dy(Cp^*)](BH_4)$.[38] The conclusion was supported by both the shorter average Cp-Dy distances and wider Cp-Dy-Cp angle of $[(Cp^{iPr5})Dy(Cp^*)]^+$ (2.296[1] and2.284[1] Å and 152.845[2]°) as compared to $[Dy(Cp^{ttt}{}_2)]^+$ (2.32380[8] and 2.30923[8] Å, ∠Cp-Dy-Cp 147.59[7]°]. This stronger axial field translated to a record-breaking barrier, U_{eff} = 1541 cm^{-1} and blocking temperature, T_B = 80 K.

1.3 Lanthanide Transition Metal Heterometallic Survey

Heterometallic lanthanide transition metal complexes are currently an emerging field. While extended structures and polymers incorporating f-block and transition metals have been reported in the early part of this century, discrete molecules containing lanthanides and transition metals are uncommon.[68] Even more rare are examples of discrete complexes containing direct, unsupported, lanthanide-transition metal bonds. Initial studies of these heterometallics have been in the fields of catalysis, magnetism, and luminescence.

1.3.1 Single-Molecule Magnetism

While there have been no previous studies on the magnetization dynamics of Ln-TM bonded molecules, mixed 3d/4f molecules have been recently reported. In most established examples, the lanthanide ion in these systems is either Tb(III) or Dy(III) with a variety of 3d metals coupled through single-atom or conjugated multi-atom bridges.[47] A notable mixed metal system is $Mn_{21}Dy$ cluster, $[Mn^{IV}_3Mn^{III}_{18}DyO_{20}(OH)_2(Bu^tCO_2)_{20}(HCO_2)_4(NO_3)_3(H_2O)_7]$, which exhibited a barrier of 51 cm^{-1} and T_B of 3 K (sweep rate of 700 Oe/s).[69] There is current debate over the high spin state or increased anisotropy is more important to magnetic properties in these systems.[70-71]

Efforts have also been made to design 3d/4f air stable SMMs. As decomposition upon exposure to air is one of the drawbacks of the current record holders for SMMs, there have been efforts towards preparing molecules with SMM properties that are air stable. A recent example was a series of isostructural mononuclear complexes with the formula $[Co(Tp)_2]_{1.3}[Ln(NO_3)_2(dbm)_2](NO_3)_{0.3}$ (Ln = Tb, Dy, Er, Y; Tp = tris(pyrazolyl) borate; dbm = 1,3-propanedionate).[72] The dysprosium analogue exhibited a barrier of 67 cm^{-1} under 200 Oe applied dc field.

A final interesting example involves redox switchable SMMs. The complex $K(thf)_5[Ln(fc(NSi(t\text{-}Bu)Me_2)_2)_2$ (Ln = Dy^{3+}, Er^{3+}) which contains a single lanthanide center and two redox active ferrocene based ligands exhibited different dynamic magnetic properties based on the oxidation state of the ferrocene.[73] The dysprosium analogue demonstrated slow magnetic relaxation as evidenced by a signal in χ'' under no applied dc field with U_{eff} = 27 cm^{-1} and no signal in χ'' upon a single oxidation of a Fc moiety using I_2. Further experimental analysis, such as UV-vis and ^{57}Fe Mössbauer spectroscopy, suggested this single oxidation occurred locally at one of the iron centers in ferrocene. Molecules with external stimuli controlling their magnetic properties can be potentially implemented into molecular switches.

1.3.2 Catalysis

With the uncommon occurrence of Ln-TM bonded molecules, there is one example in which a type of system has been utilized in catalysis. A series of Lu-Ni heterobimetallics, $NiLu(^iPr_2PCH_2\text{-}NPh)_3$, $NiLu(thf)(^iPr_2PCH_2\text{-}NPh)_3$, and $NiLu\{(^iPr_2PCH_2NAr)_3tacn\}$ (tacn = 1,4,7-tris(2-aminophenyl)1,4,7-triazacyclononane), were recently reported.[4] Two of these complexes contain a Lu-Ni bond and were studied for their ability to catalytically hydrogenate a series of olefins. It was discovered $NiLu(^iPr_2PCH_2\text{-}NPh)_3$ hydrogenated styrene to ethylbenzene in over 90% conversion with 2.5 mol% catalyst loading and 4 atm H_2 according to NMR studies performed in d_8-toluene. It should be noted the Ni-Lu heterobimetallic complex was a better catalyst when compared to monometallic Ni complexes and the Lu metalloligand precursor. It was proposed that the Lu center drew electron density away from the Ni center, allowing for a more stable Ni(η^2-H_2) adduct formation during the catalytic cycle.

1.3.3 Luminescence

Some lanthanides are attractive candidates for optical applications given their sharp f-f transitions and high quantum yields.[74] Implementing transition metals ions into a system sensitizes the luminescence of a Ln(III) system and improves their overall optical properties. A common moiety encountered in literature are Zn^{II}/Ln^{III} heterometallic complexes containing Salen-type or Salamo-type ligands.[74] These types of systems of been studied towards implementing in optical, luminescent, and sensing applications.

1.4 Outlook

Metal-metal bonding has provided further understanding of chemical bonding and allowed for interesting applications in fields such as magnetism and catalysis. With an initial focus on metal-metal multiply bonded homobimetallic transition metal systems, the field has evolved to include heterometallic bonds and *n*d-4f bonding. As there has yet to be a ligand system designed to allow for a systematic study of Ln-TM bonded compounds, we have developed a powerful synthetic method to perform a systematic study into the nature of Ln-TM bonding.

Given the strength of bulk magnetic magnets containing Ln-TM interactions, an interesting avenue yet to be studied are the magnetization dynamics of Ln-TM bonded molecules. Our work has provided the foundation for magnetic properties of discrete molecules and how the lanthanide influences magnetization dynamics in this system. To further characterize a Ln-TM bond, new spectroscopic and computational techniques continue to be explored. Given the relative infancy of the field of Ln-TM bonding, applications are ripe with possibility as demonstrated through other work in catalysis and luminescence.

2. A COMPARATIVE STUDY OF MAGNETIZATION DYNAMICS IN DINUCLEAR DYSPROSIUM COMPLEXES FEATURING BRIDGING CHLORIDE OR TRIFLUOROMETHANESULFONATE LIGANDS*

2.1 Introduction

Molecules possessing intrinsic magnetic anisotropy potentially display magnetic hysteresis and slow magnetic relaxation. Development of such single-molecule magnets (SMMs) allow the manufacture of high capacity data storage devices[33] or spin qubit devices.[34] While the earliest SMM work reported transition metal based molecules, most notably $[Mn_{12}O_{12}(OAc)_{16}(H_2O)_4]$,[37] the field gravitated towards lanthanide compounds given the large magnetic anisotropy of trivalent lanthanide ions.[75] Organometallic lanthanide complexes, particularly complexes containing the cyclopentadienide (Cp^-) ligand, continued to be studied given their impressive magnetic properties. More specifically, dinuclear complexes with bridging ligands are of interest given the variability of the system. Modifications to the lanthanide ion[76], bridging ligand[77] (both closed shell and radicals), and Cp ring[60] allow for systematic studies to assess how each factor contributes to magnetic behavior.

---

*The results of this chapter were published in *Chem. Commun.* 2017, *53*, 8419-8422. Reproduced by permission of The Royal Society of Chemistry Copyright, 2017 Royal Society of Chemistry.

The previously reported 2,6-Bis(methylenecyclopentadienyl)pyridine disodium salt ($PyCp_2Na_2$) was of interest to me for two reasons. Firstly, attempts to isolate the μ_2-Cl bridged product by reacting $DyCl_3$ and NaCp together resulted as a mixture of $[Cp_2Dy(\mu\text{-}Cl)]_2$ along with a polymeric species $[Cp_2Dy(\mu\text{-}Cl)]_n$.[78] It was predicted the pyridine linking the two Cp rings would afford structural rigidity to prevent formation of a polymer. Additionally, being able to incorporate triflates as the bridging ligand appealed to me in regards to reactivity. Being a better leaving group as compared to halides, it was hypothesized substitution chemistry would be more facile in the triflate system.

In this study, organometallic dinuclear Dy^{3+} complexes featuring bridging $^-OSO_2CF_3$ ($[(Py(Cp_2Dy\text{-}(\mu\text{-}O_2SOCF_3)]_2$) (**2-1**) or Cl^- ($[(Py(Cp_2Dy\text{-}(\mu\text{-}Cl)]_2$) (**2-2**) were structurally characterized. A mononuclear complex, $(PyCp_2)Dy(OSO_2CF_3)(thf)$ (**2-3**) was also prepared. All three complexes' magnetic properties were studied. All three exhibited slow magnetic relaxation while **2-1** and **2-2** displayed similar effective energy barrier to magnetization (U_{eff}). Computational studies performed support the similarities in magnetization dynamics observed in **2-1** and **2-2**.

2.2 Materials & Methods

2.2.1 General Considerations

Synthesis of 2,6-bis(methylenecyclopentadienyl)pyridine disodium salt, $[(PyCp_2)Dy(\mu\text{-}OTf)]_2$ (**2-1**), $[(PyCp_2)Dy(thf)(OTf)]$ (**2-3**), and $[(PyCp_2)Dy(\mu\text{-}Cl)]_2$ (**2-2**) were carried out under strictly anaerobic and anhydrous conditions using an Ar filled glovebox (Vigor) and solvents dried and flushed with Ar using an SPS system (JC Meyer

Solvent System). All glassware used in the glovebox was oven dried and cycled into the glovebox overnight. 2,6-bis(hydroxymethyl)pyridine and thionyl chloride were used to synthesize 2,6-bis(chloromethyl)pyridine and were purchased from Acros Organics and EMD Millipore, respectively. Anhydrous $DyCl_3$, NaCp (0.1 mol in THF), and anhydrous $Dy(OTf)_3$ were purchased from STREM. Elemental analyses were carried out by ALS Group USA. All syntheses were based on previously reported procedures.[79-80] Samples used for magnetic characterization were either single crystalline material or microcrystalline powders prepared by dissolving materials in minimal amounts of CH_2Cl_2 or THF followed by the addition of hexanes and placing in a freezer (-30 °C) overnight. Magnetic samples of **2-1**, **2-2**, and **2-3** were prepared with an eicosane matrix in a high purity NMR tube which was flame sealed under vacuum. The eicosane (Acros Organics) was melted in a hot water bath (45 °C) and was dispersed homogeneously throughout the sample. Magnetic characterization of **2-1**, **2-2**, and **2-3** as well as magnetically dilute analogues of **2-1** and **2-2** were obtained using a Quantum Design MPMS 3 SQUID magnetometer. Direct current (dc) measurements were acquired under an applied 1000 Oe field at a temperature range of 2-300 K. Variable temperature ac measurements for all compounds were taken under zero applied dc field at temperature ranges of 15-1.8 K with 2 Oe switching fields. ^1H NMR spectra were collected on Mercury 300 MHz spectrometer.

2.2.2 Synthesis

Synthesis of 2,6-bis(chloromethyl)pyridine (**2-4**)**.** (similar to previous method[79-80])

2,6- bis(hydroxymethyl)pyridine (10 g, 71.8 mmol) was weighed out in a 100 mL Schlenk flask and thionyl chloride (50 ml) was added dropwise while stirring at 0 °C. The solution was heated to 60 °C and stirred for 3 h. The reaction was cooled and added dropwise to 1 L of stirring ice water. The solution was neutralized with aqueous ammonia (25 %, EMD Milipore), and the white precipitate collected was washed extensively with water followed by vacuum drying. The solid was recrystallized from absolute ethanol/water (2:1 v:v) and the white needles were vacuum dried overnight prior to use in further reactions (11.9 g, 94%). ^{1}H NMR (300 MHz, $CDCl_3$) δ 7.77 ppm (1H, t, J = 6 Hz, py-H4), 7.45 ppm (2H, dd, J = 6 Hz, py-H3,H5), 4.66 ppm (4H, s, methylene).

Synthesis of 2,6-bis(methylenecyclopentadienyl)pyridine disodium salt ((PyCp$_2$)Na$_2$) (2-5). (similar to previous method[79-80]) To a stirring solution of NaCp (0.1 mol) in 100 mL THF, a solution of 2,6- bis(chloromethyl)pyridine (4.4010 g, 0.025 mmol) in 150 mL THF was slowly added over time using an addition funnel. This solution was stirred overnight and the reaction was filtered to remove the white precipitate and washed with THF (3 X 25 mL). The orange filtrate was evaporated down to approximately 80 mL and hexanes (150 mL) was slowly added to the solution and set aside overnight. The white crystals were collected by filtration, washed with hexanes (3 X 50 mL), and dried under vacuum to yield 3.1000 g (44 %). ^{1}H NMR (300 MHz, THF-d_8) δ 7.42 ppm (1H, t, J = 6 Hz, py-H4), 6.92 ppm (2H, d, J = 9 Hz, pyH3,H5), 5.55 ppm (4 H, t, J = 3 Hz, Cp protons), 5.36 ppm (4 H, t, J = 3 Hz, Cp protons), 3.95 ppm (4 H, s, methylene).

Synthesis of [(PyCp$_2$)Dy(μ-OTf)]$_2$ (2-1). To a solution of Dy(OTf)$_3$ (1.2194 g, 2.00 mmol) in 30 mL of THF, a solution of (PyCp$_2$)Na$_2$ (0.5460 g, 2.00 mmol) in 60 mL of THF was added dropwise and kept in a cold well at -30 °C. The reaction was occasionally stirred manually over 2 h and warmed to room temperature. After 2 d of stirring, the THF was removed and replaced with CH_2Cl_2 (30 mL) and left to stir overnight. The reaction was filtered and hexanes (50 mL) was slowly added to the filtrate and left overnight. Pale yellow crystals (0.125 g) were collected and the remaining mother liquor was collected and solvent removed. This was redissolved in CH_2Cl_2, layered with hexanes, and placed in a freezer (-30 °C) overnight to collect more crystals. The total yield was 0.3589 g (33 %). Anal. Calcd. for $C_{36}H_{30}Dy_2F_6N_2O_6S_2$ (**2-1**): C, 39.68; H, 2.77; N, 2.57. Found: C, 39.84; H, 2.73; N, 2.54.

Synthesis of [(PyCp$_2$)Dy(thf)(OTf)] (2-3). Approximately 50 mg of **2-1** was dissolved in 2 mL of THF and layered with 5 mL of hexanes and placed in a freezer (-30 °C) overnight. The resulting colorless plates were collected for further characterization. Anal. Calcd. for Anal. Calcd. for $C_{20}H_{19}DyF_3NO_{3.5}S$ (**2-3**(0.5 thf)): C, 41.35; H, 3.30; N, 2.41. Found: C, 40.91; H, 3.10; N, 2.46.

Synthesis of [(PyCp$_2$)Dy(μ-Cl)]$_2$ (2-2). The preparation followed the previously reported method for the isolation of **2-2**.[80] To a suspension of $DyCl_3$ (0.5095 g, 1.895 mmol) in 50 mL of THF, a solution of (PyCp$_2$)Na$_2$ (0.5293 g, 1.895 mmol) in 60 mL of THF was added dropwise and kept in a cold well at -30 °C. The reaction was occasionally stirred manually for 2 h and warmed to room temperature. After 2 d of stirring, the reaction was filtered through Celite and the THF was removed and replaced with CH_2Cl_2 (30 ml) and stirred overnight. The reaction was filtered through Celite and hexanes (50 mL) was slowly added to the filtrate and left overnight. The white microcrystalline material was collected and dried, 0.3334 g (40 %). Dissolving crystalline material of **2-2** in thf and crystallization via slow diffusion of hexanes into the solution resulted in the formation of plate crystals of **2-2**(thf).

Synthesis of magnetically dilute 2-1 [(PyCp$_2$)Ln(μ-OTf)]$_2$ (Dy : Y = 1 : 11.9). A magnetically dilute sample of **2-1** was prepared by dissolving 60.7 mg (63.3 μmol) of [(PyCp$_2$)Y(μ-OTf)]$_2$ and 5.8 mg (5.3 μmol) of **2-1** in a minimal amount of CH_2Cl_2. The solution of **2-1** was added to the solution of [(PyCp$_2$)Y(μ-OTf)]$_2$, layered with hexanes, and left in a freezer at -30 °C overnight to form crystals suitable to conduct magnetic measurements. Unit cell parameters determined for single crystals of the dilute sample matched those of **2-1**.

Synthesis of magnetically dilute 2-2 [(PyCp$_2$)Ln(μ-Cl)]$_2$ (Dy : Y = 1 : 12). A magnetically dilute sample of **2-2** was prepared by dissolving 35.9 mg (49.1 μmol) of [(PyCp$_2$)Y(μ-Cl)]$_2$ and 3.6 mg (4.1 μmol) of **2-2** in a minimal amount of CH_2Cl_2. The solution of **2-2** was added to the solution of [(PyCp$_2$)Y(μ-Cl)]$_2$, layered with hexanes, and left in a freezer at -30 °C overnight to form crystals suitable to conduct magnetic measurements. Unit cell parameters determined for single crystals of the dilute sample matched those of **2-2**.

2.2.3 X-Ray Crystallography

Data Collection. A Leica MZ 75 microscope was used to identify a suitable colorless crystal (for **2-1**: plate with dimensions (max, intermediate, and min) 0.185 x 0.14 x 0.138 mm^3 ; for **2-3**: plate with dimensions 0.216 x 0.141 x 0.137 mm^3 ; for **2-2**: needle with dimensions 0.142 x 0.023 x 0.022 mm^3 ; for **2-2**(thf): plate with dimensions 0.112 x 0.039 x 0.009 mm^3) with very well defined faces from a representative sample of crystals of the same habit. The crystal mounted on a nylon loop was then placed in a cold nitrogen stream (Oxford) maintained at 110 K (100 K for **2-2**(thf)). A BRUKER APEX 2 Duo X-ray (three-circle) diffractometer was employed for crystal screening, unit cell determination, and data collection for **2-1**, **2-2**, and **2-3** (for **2-2**(thf) BRUKER Venture X-ray (kappa geometry) diffractometer). The goniometer was controlled using the APEX2 software suite, v2008-6.0.[81] The sample was optically centered with the aid of a video camera such that no translations were observed as the crystal was rotated through all positions. The detector was set at 6.0 cm from the crystal sample (APEX2, 512x512 pixel). The X-ray radiation employed was generated from a Mo sealed X-ray tube (K_α = 0.70173Å) for **2-1**, **2-2**, and **2-3** and a Cu-Iμs X-ray tube (K_α = 1.5418Å with a potential of 50 kV and a current of 1.0mA) for **2-2**(thf). 45 data frames were taken at widths of 1.0°. For **2-1** and **2-3**, these reflections were used in the auto-indexing procedure to determine the unit cell. A suitable cell was found and refined by nonlinear least squares and Bravais lattice procedures. The unit cell was verified by examination of the h k l overlays on several frames of data. No super-cell or erroneous reflections were observed. For **2-2**, the unit cell was determined using Cell_Now,[82] which showed twinning. A suitable cell was found and refined by nonlinear least squares and Bravais lattice procedures. After careful examination of the unit cell, an extended data collection procedure (21 sets for **2-1**; 23 sets for **2-3**; 25 sets for **2-2**; 15 sets for **2-2**(thf)) was initiated using omega and phi scans. Data Reduction, Structure Solution, and Refinement. Integrated intensity information for each reflection was obtained by reduction of the data frames with the program APEX2[81,83] (including both the twin domains for **2-2**). The integration method employed a three-dimensional profiling algorithm and all data were corrected[82] for Lorentz and polarization factors, as well as for crystal decay effects. Finally, the data was merged and scaled to produce a suitable data set. The absorption correction program SADABS[84] was employed to correct the data for **2-1** and **2-3** for absorption effects (for **2-2**: TWINABS[85] was employed to correct the data for absorption effects as well as to generate TWIN4.hkl containing only the major component, and TWIN5.hkl with reflections from both the twin domains; while the former was used for structure solution the latter was used for the final least squares refinement).

Additional details for 2-1. Systematic reflection conditions and statistical tests of the data suggested the space group P-1. A solution was obtained readily using XT/XS in APEX2.[81,83] Hydrogen atoms were placed in idealized positions and were set riding on the respective parent atoms. All non-hydrogen atoms were refined with anisotropic thermal parameters. Absence of additional symmetry and voids were confirmed using PLATON (ADDSYM).[86] CHECKCIF suggested pseudo-merohedral twinning and was included in the refinement. The structure was refined (weighted least squares refinement on F^2) to convergence.[83,87] Olex2 was employed for the final data presentation and structure plots.[87]

Additional details for 2-3. Systematic reflection conditions and statistical tests of the data suggested the space group P-1. A solution was obtained readily using XT/XS in APEX2.[81,83] Hydrogen atoms were placed in idealized positions and were set riding on the respective parent atoms. All non-hydrogen atoms were refined with anisotropic thermal parameters. Absence of additional symmetry and voids were confirmed using PLATON (ADDSYM).[86] The structure was refined (weighted least squares refinement on F^2) to convergence.[83,87] Olex2 was employed for the final data presentation and structure plots.[87]

Additional details for 2-2. Systematic reflection conditions and statistical tests of the data suggested the space group $P2_1/n$. A solution was obtained readily (Z=2; Z'=0.5) using XT/XS in APEX2.[81,83] Dichloromethane was found partially solvated. Hydrogen atoms were placed in idealized positions and were set riding on the respective parent atoms. All non-hydrogen atoms were refined with anisotropic thermal parameters. Occupancy of the solvent dichloromethane were refined to 0.882. Absence of additional symmetry and voids were confirmed using PLATON (ADDSYM).[86] The structure was refined (weighted least squares refinement on F^2) to convergence.[83,87]

Additional details for 2-2(thf). Systematic reflection conditions and statistical tests of the data suggested the space group Pnnm. A solution was obtained readily (Z=2; Z'=0.25) using XT/XS in APEX2.[82-83] A molecule of THF was found solvated and partially occupied. Hydrogen atoms were placed in idealized positions and were set riding on the respective parent atoms. All non-hydrogen atoms were refined with anisotropic thermal parameters. Elongated thermal ellipsoid on C2S suggested disorder and was successfully modeled between two positions. Considering symmetry and disorder, initial occupancy refinement suggested 1/4th occupancy for C2S and was fixed to that value for the final least squares refinement. Absence of additional symmetry or void were confirmed using PLATON (ADDSYM).[86] The structure was refined (weighted least squares refinement on F^2) to convergence.[83,87]

2.2.4 Computational Details

Ab initio calculations were performed on compounds **2-1**, **2-2**, and **2-3** utilizing the MOLCAS 8.0 suite of computational chemistry programs.[88] All atom positions for each compound were provided to the GATEWAY module from solved and refined single crystal structures. Douglas−Kroll Hamiltonian[89] was considered to account for the relativistic effects. 1-electron velocity integrals and 1-electron atomic mean field integrals were computed with the SEWARD module, along with the 2-electron integrals which were Cholesky-decomposed. All the atomic basis sets used were of the ANO-RCC type[90] with the following contractions: hydrogen (2s), carbon, nitrogen, oxygen, and sulfur (3s2p1d), fluorine (3s2p), chlorine (5s4p2d1f), lutetium (7s6p4d2f) (used as a diamagnetic place-holder for one dysprosium atom in the dimers), and dysprosium (8s7p5d3f2g1h). The integrals computed were further used to develop starting orbitals for the compounds, by way of the GUESSORB module. A Complete Active Space Self-Consistent Field (CASSCF)[91] calculation was implemented with an active space of the seven f-orbitals of dysprosium Dy(III) containing nine electrons, using the RASSCF module. The twenty-one sextet roots of dysprosium Dy(III) were found through the configuration interaction procedure enacted by this module and then the resulting twenty-one states were mixed by the RASSI module. The RASSI module was then used to determine the interactions between the twenty-one roots, while taking into account spin-orbit coupling.[92] The output from RASSI was subsequently used by the SINGLE_ANISO module[93] to compute the magnetic properties (g-tensors and single-ion energy barrier) based on the eight low-lying Kramers doublet (KDs). for the compounds featured in this paper. To model the exchange and dipolar coupling present in the chloride (**2-2**) and triflate (**2-1**) dimer compounds, the POLY_ANISO program[94-96] was utilized by producing fits to the DC magnetic susceptibility data for the two compounds ($zJ = -0.01\ \text{cm}^{-1}$ for **2-1** and **2-2**). The magnetic couplings of compounds **2-1** and **2-2** are extracted using the following Hamiltonian.

$$\hat{\mathrm{H}}_{\boldsymbol{coupling}} = -(\boldsymbol{J_i S_i S_{i+1}})$$

Here, $\boldsymbol{J_i} = \boldsymbol{J_i^{dipolar}} + \boldsymbol{J_i^{exch}}$ (i.e. J_i are the total magnetic interaction in combination of calculated J_i^{dipolar} and fitted J_i^{exch} parameters; this describes the interaction between the intramolecular metal centers.)

2.3 Results & Discussion

2.3.1 Synthesis & Structure of Dy Compounds

Compound **2-1** can be prepared via the reaction of anhydrous $Dy(OSO_2CF_3)_3$ with the disodium salt $PyCp_2Na_2$ (**Figure 2.1**) and subsequent work up (see **2.2.2**).[79-80]

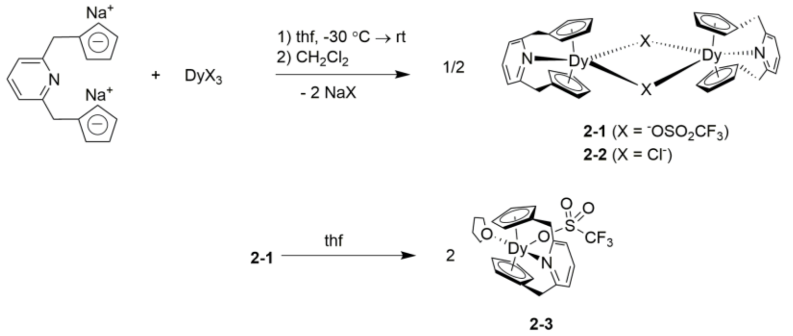

Figure 2.1: Synthetic overview of compounds **2-1**, **2-2**, and **2-3**.

Single crystals of **2-1** can be obtained by crystallization from CH_2Cl_2/hexane solvent mixtures. Dissolution of **2-1** in thf and crystallization from thf/hexane solvent mixtures results in crystalline material of monomeric **2-3**. A dinuclear chloride-bridged complex **2-2** is obtained by the reaction of $DyCl_3$ with $PyCp_2Na_2$ in thf and subsequent extraction into CH_2Cl_2 and recrystallization. It is important to note that the analogous reaction of two equivalents of NaCp with $DyCl_3$ was previously reported to yield the desired dinuclear μ_2-Cl bridged product only as a mixture with a polymeric species after sublimation.[78] Clearly, the intramolecular pyridine moiety blocks the formation of a polymeric side product and allows for a more facile access to the desired dinuclear complexes. In contrast to **2-1**, **2-2** does not dissociate in thf and crystalline material of **2-2**(thf) was obtained. Thus, the triflate anions in **2-1** are more labile leaving groups than the chloride ions in **2-2**.

The molecular structures of neutral compounds **2-1**, **2-2** and **2-3** were investigated by means of single crystal X-ray diffraction studies (**Figure 2.2**, **Tables A.1, A.2**). The Dy^{3+} ions in all three structures have a ligand bond number of nine, with bonds to two Cp and one pyridine moiety and two additional ligands.

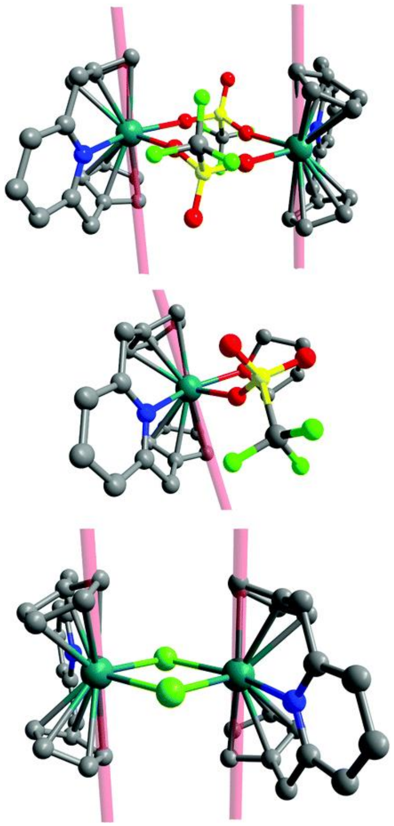

Figure 2.2: Molecular structures of **2-1**, **2-3**, and **2-2**, respectively. Teal = Dy, yellow = S, red = oxygen, blue = N, light green = F, green = Cl, and grey = C. Hydrogen atoms and co-crystallized solvent molecules have been omitted for clarity. The pink transparent lines indicate g_{zz} directions of the magnetic ground states.

In complexes **2-1**, **2-2**, and **2-3**, the average Dy–C distances (2.63[1] Å, 2.64[1] Å, and 2.628[2] Å, respectively), and the Dy–N distances (2.554[9] Å, 2.581[9] Å, and 2.538[2] Å, respectively) are fairly comparable for the two triflate complexes **2-1** and **2-3** and are only slightly longer in the chloride bridged dimer **2-2**. The Dy–Cl distances in **2-2** (2.683[3] Å and 2.785[3] Å) are much longer than the Dy–O distances in **2-1** (2.338[9] Å and 2.346[8] Å) and **2-3** (Dy–O$_{\text{thf}}$ = 2.456[1] Å and Dy–O$_{\text{OTf}}$ = 2.335[1] Å).

For dinuclear complexes **2-1** and **2-2**, the relative orientation of the pyridine moieties on each Dy^{3+} ion to each other could result in *cis* or *trans* geometries. As has been noted previously for closely related lanthanide $[PyCp_2]^{2-}$ complexes, the solid structure of **2-1** and **2-2** solely displays the *trans* isomer even though *cis* and *trans* isomers can readily interconvert as suggested by variable temperature NMR solution studies.[79]

The two bridging chloride ligands in **2-2** allow for an intramolecular Dy···Dy distance of 4.252(1) Å whereas the larger bridging triflate ligands in **2-1** result in larger Dy···Dy distances of 6.068(1) Å. The very tight crystal packing in crystals of **2-3** (**Figure A.1**) results in close intermolecular Dy···Dy distances of 6.541(1) Å. This close intermolecular proximity likely results in intermolecular interactions leading to weak intermolecular magnetic coupling as well as enhanced quantum tunneling of the magnetization (**2.3.2**) for

2.3.2 Magnetic Properties of Dy Complexes

The static magnetic properties of complexes **2-1**, **2-2** and **2-3** were investigated by means of variable temperature direct current (dc) magnetometry using an applied field of 1000 Oe (**Fig 2.3**). The room temperature $\chi_M T$ values of 27.90, 26.99, and 13.52 emu K mol^{-1} obtained for **2-1**, **2-2** and **2-3** respectively, are in good agreement with the expected values of 28.34 emu K mol^{-1} and 14.17 emu K mol^{-1} for di- and mononuclear Dy^{3+} complexes ($^6H_{15/2}$, S = 5/2, L = 5, and g = 4/3).

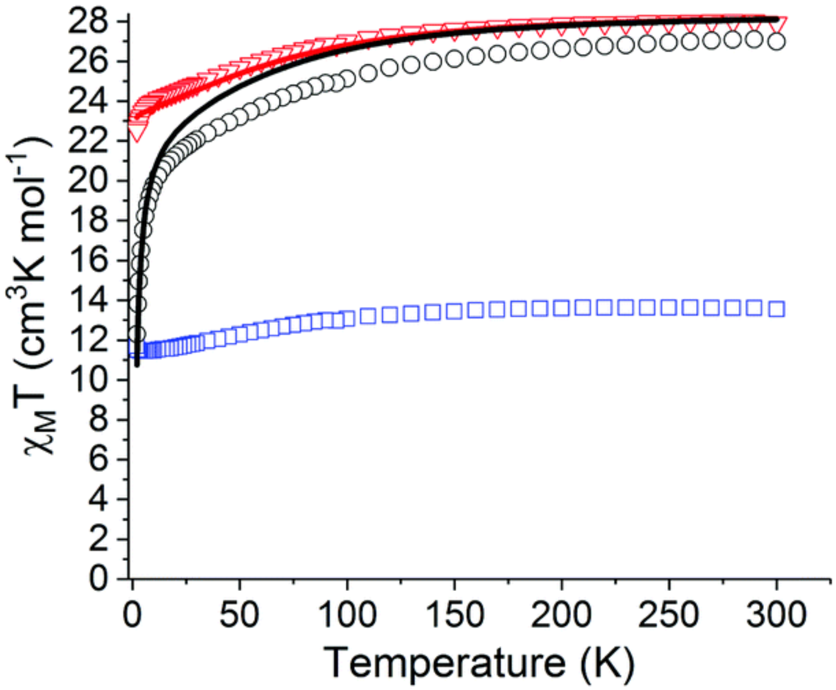

Figure 2.3: Temperature dependence of $\chi_M T$ for **2-1** (red triangles), **2-2** (black circles), and **2-3** (blue squares) (1000 Oe; 2–300 K). The solid lines are fits of the data.

All complexes display decreases in their respective χ_MT values upon lowering the temperature with a more significant decrease at low temperatures for **2-1** and **2-2**. Such a decrease in χ_MT values is typically observed and ascribed to the thermal depopulation of the Stark sublevels of Dy^{3+} and/or possible magnetic interactions between Dy^{3+} centers (see **2.3.3.**).[13] Surprisingly, complex **2-3** features a slight increase of χ_MT at very low temperatures (2 K) which may be indicative of intermolecular ferromagnetic coupling, but this aspect was not further investigated.

Variable temperature *magnetization vs. field* measurements were carried out for **2-1** (**Figure A.2**), **2-2** (**Figure A.4**), and **2-3** (**Figure A.6**). For all three complexes, magnetic saturation is approximately reached at 7 T. The magnetization values are significantly smaller than the expected free ion values (10 μ_B per Dy^{3+} ion). This observation is indicative of breaking the degeneracy of the $^6H_{15/2}$ ground states by crystal/ligand field effects. Additionally, the *M vs. H/T* curves for complexes **2-1** (**Figure A.3**), **2-2** (**Figure A.5**), and **2-3** (**Figure A.7**) are non-superimposable as a result of the magnetically anisotropic Dy^{3+} ion(s).

The magnetization dynamics of compounds **2-1**, **2-2** and **2-3** were probed by alternating current (ac) magnetometry. All three complexes display signals in the out-of-phase component (χ_M'') of the ac magnetic susceptibility in the absence of an externally applied dc field. The maximum of χ_M'' of complex **2-1** (**Fig. 2.4**; see **Figure A.8** for χ_M') remain temperature independent at temperatures between 1.8 and 6 K. At temperatures above 6 K, the maxima of χ_M'' become temperature dependent and move to higher frequencies. The latter observation indicates the dominant quantum tunneling of the magnetization (QTM) at low temperatures (< 6 K) and a transition to a thermally activated process at higher temperatures. This transitional behavior of the magnetization dynamics is also qualitatively observed for complexes **2-2** and **2-3**. For the mononuclear complex **2-3**, the signals in χ_M'' are observed at 0 Oe dc field, albeit at higher frequencies (**Figure A.10**, **Figure A.11**). Above 9 K, the χ_M'' maxima shift to frequencies beyond the 1 kHz instrument limit which prevents the extraction of an effective energy barrier to magnetization reversal (U_{eff}). Application of dc fields resulted in significant shifts of the χ_M'' maxima to lower frequencies (as compared to zero field measurements) which were clearly temperature dependent above 2.5 K. However, for all fields studied, we obtained ill-defined shoulders in the ac data which are indicative of the presence of multiple, overlapping relaxation pathways (**Figures A.12**, **A.13**) The variable temperature ac susceptibility of **2-2** (**Figure 2.4** and **Figure A.9**) is well defined in the absence of dc fields. The maxima of χ_M'' remain temperature independent up to a temperature of 4 K (QTM) and become temperature dependent at higher temperatures.

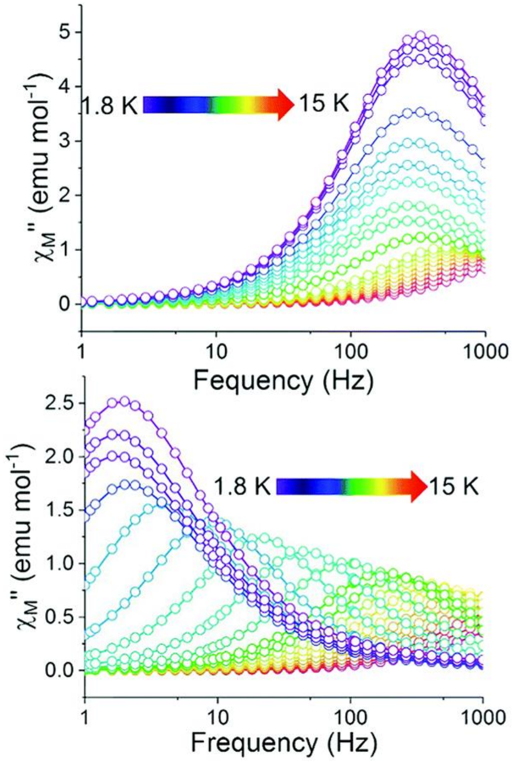

Figure 2.4: Frequency dependence of the out-of-phase component (χ_M'') of the ac susceptibility of **2-1** (top) and **2-2** (bottom) at an applied dc field of 0 Oe in the temperature range of 1.8–15 K (2 Oe switching field).

Cole–Cole plots (χ_M'' *vs.* χ_M') corresponding to the above discussed ac magnetization data for complexes **2-1** and **2-2** are shown in (**Figure A.14**, **Figure A.15**), respectively. Quantitative relaxation times were extracted by fitting the data for each temperature using the generalized Debye model (solid lines in **Figure A.14** and **Figure A.15**) and used to construct the Arrhenius plots (*ln t vs. 1/T*) as shown in **Figure 2.5**. The barrier height U_{eff} was determined by fitting the linear temperature dependent part of the Arrhenius plots (the predominant Orbach relaxation mechanism). Interestingly, we obtained identical U_{eff} values for complexes **2-1** and **2-2** of 70 K (49 cm^{-1}) and pre-exponential factors τ_0 of 4.8 x 10^{-7} s and 7.2 x 10^{-7} s, respectively. The non-linear dependence of τ at low temperatures of the Arrhenius plot is indicative of the presence of other relaxation pathways such as Raman and quantum tunneling processes.[44]

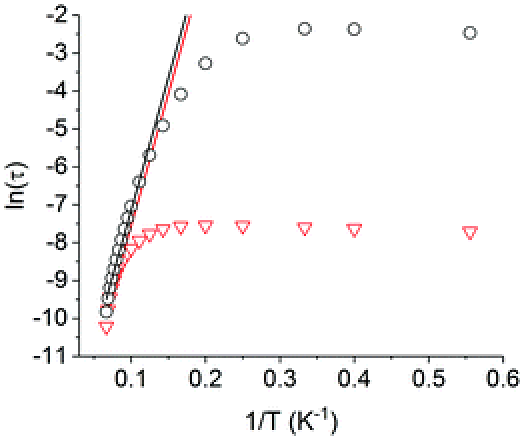

Figure 2.5: Arrhenius plots of magnetization relaxation time data for **2-1** (red triangles) and **2-2** (black circles) in no applied dc field. The lines correspond to fits to the Arrhenius equation yielding $U_{eff} = 70$ K (49 cm^{-1}) and 70 K (49 cm^{-1}), and $\tau_0 = 4.8 \times 10^{-7}$ s and 7.2×10^{-7} s for **2-1** and **2-2**, respectively.

The similarity in the magnetization dynamics of **2-1** and **2-2** is also confirmed by ac measurements performed for magnetically dilute (Dy : Y = 1:~12) analogues which display almost identical temperature dependences of χ_M' (**Figure A.16**, **Figure A.18**) and χ_M'' (**Figure A.17**, **Figure A.19**).

2.3.3 Computational Analysis of Dy Complexes

These surprising findings were further investigated by means of *ab initio* calculations of the CASSCF/RASSI/SINGLE_ ANISO type, using the MOLCAS 8.0 program.[88] Both Dy sites of dinuclear complexes **2-1** and **2-2** were calculated separately by replacing one Dy^{3+} ion with a diamagnetic Lu^{3+} ion and displayed very similar properties (**Table A.3**). The ground state Kramers doublets (KDs) of the Dy^{3+} ions in all three complexes are predominantly $m_J = \pm 15/2$ in character with small contributions from $m_J = \pm 11/2$ (**Figure 2.6**) with corresponding g_z values of 19.3, 19.1, and 18.8 for **2-1**, **2-2**, and **2-3**, respectively. The first excited state KDs of dinuclear complexes **2-1** and **2-2** are mostly $m_J = \pm 11/2$ in character whereas for mononuclear **2-3** a highly mixed doublet was calculated with contributions from ±5/2, ±3/2, and ±1/2 and others.

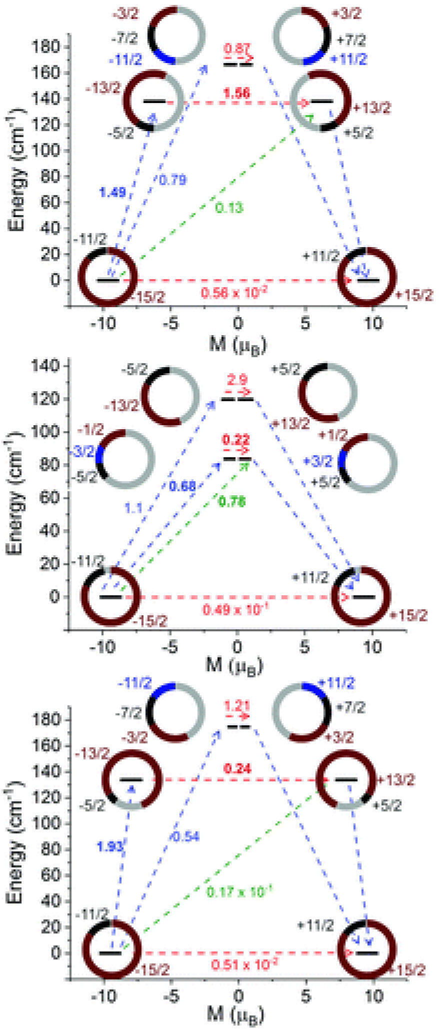

Figure 2.6: Magnetization blocking barrier for single Dy sites in **2-1** (top), **2-3** (center), and **2-3** (bottom) computed *ab initio*. The black lines indicate KDs as a function of computed magnetic moments; green/blue and red arrows indicate pathways through Orbach/Raman relaxation and QTM/TA-QTM. The numbers on each arrow are the mean absolute values for the corresponding matrix element of the transition magnetic moment. The donut diagrams indicate the nature of the contributing m_J states to KDs (light grey = combined contributions of several other m_J states).

The energies of the first excited state KDs for **2-1** and **2-2** are very similar (138 cm^{-1} and 134 cm^{-1}) and significantly higher than those of compound **2-3** (84 cm^{-1}). Based on the calculated probabilities for tunneling, Raman, and Orbach processes (arrows in **Figure 2.6**), we propose that the magnetic relaxation for all three complexes occurs via a thermally assisted quantum tunneling of the magnetization (TA-QTM) process involving the first excited state. The calculated values of **2-1** and **2-2** are in very good agreement with the identical U_{eff} values determined experimentally and suggest that the magnetization dynamics in **2-1** and **2-2** are dominated by the single ion magnetic anisotropy. This point is further supported by the small magnetic coupling constants (J_{exch} = +0.018 cm^{-1} and 0.138 cm^{-1} ; $J_{dipolar}$ = +0.032 cm^{-1} and 0.0892 cm^{-1}) which were calculated within the Lines model using the POLY-ANISO routine (fits in **Figure 2.2** and **Tables A.4**, **A.5**).[16] Interestingly, substitution of $^{-}OSO_2CF_3$ by Cl^{-} (in going from **2-1** to **2-2**) results in a change from ferro- to antiferro-magnetic coupling (J_{total} = 0.05 cm^{-1} and 0.05 cm^{-1}) but the small magnitude is expected to significantly affect the magnetization dynamics only at much lower temperatures than the experimentally employed ones.

2.4 Conclusion & Outlook

A series of di- and mononuclear Dy^{3+} complexes were synthesized, structurally characterized, and probed for SMM behavior. While all three complexes exhibited slow magnetic relaxation under no applied dc field, a barrier was calculated only for complexes **2-1** and **2-2**. Despite the identity of the bridging differing in these complexes, identical U_{eff} values (49 cm^{-1}) were calculated for both. Experimental observations were further supported by computational data and suggested magnetic relaxation dynamics involves TA-QTM *via* the first excited state of the single Dy^{3+} sites. The organometallic triflate complexes prepared will be further investigated in terms of substitution chemistry at the triflate. The hypothesis that substitution chemistry will be more facile at the triflate site is supported in future chapters **3**, **4**, and **5** of this work.

3 STRUCTURE AND MAGNETIZATION DYNAMICS OF DY−FE AND DY−RU BONDED COMPLEXES*

3.1 Introduction

Given the synthetic challenges associated with synthesizing a direct, unsupported bond between a lanthanide (Ln) and transition metal (TM) in a discrete complex, little is understood about the interaction.[68] The earliest report of such a complex was by Beletskaya and co-workers in 1993.[26] This approach utilized a salt elimination with a halide bearing lanthanide synthon and anionic transition metal fragment Rp^- ($[RuCp(CO)_2]^-$) to furnish a Lu-Ru bond. A similar synthetic route was later used to prepare a Nd-Fe complex with a Nd synthon and Fp^- ($[FeCp(CO)_2]^-$) anion.[27] Another synthetic approach known as an alkane elimination developed by Kempe and co-workers involves a Ln-alkyl and acidic TM-hydride species. This synthetic route afforded a variety of Ln-Re bonded species (**Figure 3.1**).[28]

---

*The results in this chapter were published in *Angew. Chem. Int. Ed.* **2018**, *57*, 8144-8148, Copyright, 2018 Wiley-VCH Verlag GmbH & Co. KGaA, Weinheim.

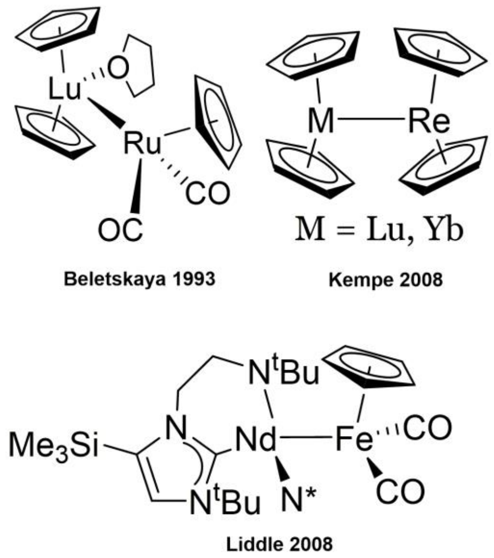

Figure 3.1: Examples of discrete molecules possessing direct, unsupported, Ln-TM bonds.

While these methods proved valuable to isolate Ln-TM compounds, no synthetic procedure currently allows for substitution of either Ln or TM to prepare an isostructural set of compounds. This would allow for a systematic study to determine how the identity of the lanthanide or transition metal influences the bonding. Identifying a system that is viable towards metal substitution would allow for a thorough physical description of a Ln-TM bond. This endeavor is ultimately valuable, as it could potentially provide insight into the degree of covalency in metal-ligand bonding in f-block elements.[97-99]

In addition to this fundamental question, I am interested in studying the static and dynamic properties of Ln-TM bonded complexes. To the best of my knowledge, no magnetization dynamics have been reported for Ln-TM complexes. Lanthanides such as Dy^{3+} and Tb^{3+} are of particular interest, given the high degree of single ion anisotropy of these trivalent ions.[75]

In this chapter, two complexes containing a Dy-TM bond, (PyCp$_2$Dy-FeCp(CO$_2$) (**3-1**) ([PyCp$_2$]$^{2-}$ = [2,6-(CH$_2$C$_5$H$_3$)$_2$C$_5$H$_3$N]$^{2-}$) and (PyCp$_2$Dy-RuCp(CO)$_2$) (**3-2**), are discussed. In addition to structural characterization of these compounds, spectroscopic, magnetic, and computational analysis were performed to provide insights into the nature of the bonding. Magnetization dynamic studies determined both complexes exhibit field-induced slow magnetic relaxation and similar barriers to magnetization reversal despite relaxation times differing between the two complexes. Spectroscopic analysis suggested strong TM→Dy σ donation which was further supported by computational data.

3.2 Materials & Methods

3.2.1 General Considerations

Synthesis of 2,6-bis(methylenecyclopentadienyl)pyridine disodium salt, [(PyCp$_2$)Dy(μ-OTf)]$_2$ (**2-1**), [(PyCp$_2$)Dy(OTf)(thf)] (**2-3**), KFp, and KRp were carried out under strict anaerobic and anhydrous conditions using an Ar filled glovebox (Vigor) utilizing previous procedures[79-80,100] and solvents dried and flushed with Ar using an SPS system (JC Meyer Solvent System). All glassware used was oven dried and cycled into the glovebox overnight. 2,6-bis(hydroxymethyl)pyridine and thionyl chloride to synthesize 2,6-bis(chloromethyl)pyridine were purchased from Acros Organics and EMD Millipore respectively. Anhydrous, Dy(OTf)$_3$, bis(cyclopentadienyliron dicarbonyl), and NaCp (0.1 mol in THF) were purchased from STREM. The complex bis(cyclopentadienylruthenium dicarbonyl) dimer was purchased from Sigma Aldrich. Samples used for magnetic characterization was crystalline material prepared by dissolving materials in minimal amounts of THF and placing in a freezer (-30 °C) overnight. Magnetic samples of **3-1** and **3-2** were prepared with an eicosane matrix in a high purity NMR tube which was flame sealed under vacuum. The eicosane (Acros Organics) was melted in a hot water bath (42 °C) and was dispersed homogeneously throughout the sample. Magnetic characterization of **3-1** and **3-2** were obtained using a Quantum Design MPMS 3 SQUID magnetometer. Direct current (dc) measurements were acquired under an applied 1000 Oe field at a temperature range of 2-300 K. Alternating current (ac) measurements for **3-1** and **3-2** were taken under various dc fields at temperature ranges of 10-2 K. Elemental analysis was carried out by Midwest Microlab. All IR spectra were obtained in the solid state in an argon filled glove box (Vigor) equipped with an Agilent CARY 630 FT-IR spectrometer (32 background scans, 32 scans @ 650-4000 cm^{-1}, Apodization: Happ-Genzel). Mössbauer spectra were collected on a model MS4 WRC low-field, variable temperature spectrometer (See Co., Edina, MN). Zero magnetic field spectra were obtained by removing the 500 G magnets from the exterior of the instrument. Temperatures were varied using a temperature controller on the heating coil on the sample holder. The instrument was calibrated using an α-Fe foil at room temperature. Obtained spectra were fitted using WMOSS software (See Co.).

3.2.2 Synthesis

Synthesis of PyCp$_2$Dy-FeCp(CO)$_2$ (3-1). A solution of KFp (34.4 mg, 159 μmol) in THF (2 mL) and a solution of [(PyCp$_2$)Dy(μ-OTf)]$_2$ (98 mg, 159 μmol) in THF (2 mL) were placed in a freezer for 1 hour at -30 °C. The solution of KFp was added dropwise to the solution of [(PyCp$_2$)Dy(μ-OTf)]$_2$ and placed in the freezer at -30 °C. Yellow crystals suitable for X-Ray diffraction formed overnight and the solution was decanted off and crystals were dried for magnetic measurements in an 87.9% (80.0 mg) yield. IR (solid, cm^{-1}, %T) 1910(ν_{CO}, 68), 1840 (ν_{CO}, 66), 1586 (81) 1567 (81), 1418 (78), 1414 (76), 1165 (80), 1008 (74), 859 (71), 776 (55).Anal. Calcd. $C_{24}H_{20}NO_2DyFe$ C, 50.33; H, 3.52; N, 2.41. Found: C, 50.37; H, 3.60; N, 2.45.

Synthesis of $PyCp_2Dy$-$RuCp(CO)_2$ (3-2). The heterobimetallic complex was synthesized similarly to **3-1**. A solution of KRp (24.0 mg, 91.8 μmol) in THF (2 mL) and a solution of $[(PyCp_2)Dy(\mu\text{-}OTf)]_2$ (50.0 mg, 45.9 μmol) in THF (2 mL) were placed in a freezer for 1 hour at -30 °C. The solution of KRp was added dropwise to the solution of $[(PyCp_2)Dy(\mu\text{-}OTf)]_2$ and placed in the freezer. Colorless crystals suitable for X-Ray diffraction formed overnight and the solution was decanted off and crystals were dried for magnetic measurements in a 38.4% (21.8 mg) yield. ν_{CO} (solid, cm-1): IR (solid, cm-1, %T) 1930 (ν_{CO}, 77), 1851 (ν_{CO}, 75), 1590 (85) 1566 (86), 1415 (81), 1415 (81), 1165 (85), 1008 (81), 843 (76), 772 (68). Anal. Calcd. $C_{24}H_{20}NO_2DyRu$ C, 46.64; H, 3.26; N, 2.27. Found: C, 47.04; H, 3.40; N, 2.25.

3.2.3 X-Ray Crystallography

Data Collection. A Leica MZ 75 microscope was used to identify a suitable crystal with dimensions (max, intermediate, and min) 0.138 x 0.12 x 0.069 mm^3 (for **3-1**; yellow block) or 0.226 x 0.142 x 0.08 mm^3 (for **3-2**; colorless block) from a representative sample of crystals of the same habit. For diffraction the crystal was centered focusing at the top portion. The crystal mounted on a nylon loop was then placed in a cold nitrogen stream (Oxford) maintained at 110 K. A BRUKER APEX 2 Duo X-ray (three-circle) diffractometer was employed for crystal screening, unit cell determination, and data collection. The goniometer was controlled using the APEX2 software suite, v2008-6.0.15.[81] The sample was optically centered with the aid of a video camera such that no translations were observed as the crystal was rotated through all positions. The detector was set at 6.0 cm from the crystal sample (APEX2, 512x512 pixel). The X-ray radiation employed was generated from a Mo sealed X-ray tube (K_α= 0.70173Å with a potential of 40 kV and a current of 40 mA). 45 data frames were taken at widths of 1.0°. These reflections were used in the auto-indexing procedure to determine the unit cell. A suitable cell was found and refined by nonlinear least squares and Bravais lattice procedures. The unit cell was verified by examination of the h k l overlays on several frames of data. No super-cell or erroneous reflections were observed.

For 3-1. After careful examination of the unit cell, an extended data collection procedure (4 sets) was initiated using omega scans.

For 3-2. After careful examination of the unit cell, an extended data collection procedure (5 sets) was initiated using omega scans. Data Reduction, Structure Solution, and Refinement, and Integrated intensity information for each reflection was obtained by reduction of the data frames with the program APEX2.[81] The integration method employed a three-dimensional profiling algorithm and all data were corrected for Lorentz and polarization factors, as well as for crystal decay effects. Finally, the data was merged and scaled to produce a suitable data set. The absorption correction program SADABS[84] was employed to correct the data for absorption effects. Systematic reflection conditions and statistical tests of the data suggested the space group Pnma. A solution was obtained readily (Z=4; Z'=0.5) using XT/XS in APEX2.[81,83] Hydrogen atoms were placed in idealized positions and were set riding on the respective parent atoms. All non-hydrogen atoms were refined with anisotropic thermal parameters. Absence of additional symmetry and voids were confirmed using PLATON (ADDSYM).[86] The structure was refined (weighted least squares refinement on F^2) to convergence.[81,83] Olex2 was employed for the final data presentation and structure plots.[87]

3.2.4 Computational Details

X-ray crystal structures of **3-1** and **3-2** were imported into Gaussian 09, Revision D.01[101] without further optimization (i.e. single point calculations). The BP86[102-103] functional was used, in combination with the 6-311G(d)[104] basis set for the C, H, O, N atoms, and the all-electron correlation consistent basis sets for Dy (cc-pVTZ-DK3),[104] Ru (cc-pVTZ-DK),[105] Fe (cc-pVTZ-DK).[106] The integration grid was set to ultrafine. The Douglas-Kroll-Hess (DKH)[107-108] 2nd order scalar relativistic scheme was applied. Topological analysis (Quantum Theory of Atoms in Molecules, QTAIM)[108] was performed based on the generated Kohn-Sham orbitals by employing AIMAll.[109] In addition, both single point calculations and geometry optimizations have been performed for **3-1** and **3-2** with Amsterdam Density Functional modeling suite (ADF 2017)[110-112] utilizing BP86 functional, TZ2P[113] basis sets and ZORA[114-116] method for scalar relativistic effect. QTAIM analyses were successively performed by adf2aim utility, which is part of the ADF package.

3.3 Results & Discussion

3.3.1 Synthesis & Structure of Dy-TM Heterobimetallics

In selecting the lanthanide and transition metal for the synthesis of the target molecules, lanthanide oxophilicity and sterics were considered. Firstly, the anionic charge must be localized on the transition metal fragment as to favor a Ln-TM bond. Additionally, the lanthanide ion must be sterically accessible. In the absence of these design principles, bridging isocarbonyl structures, Ln-OC-TM, are more likely.[117-118] With this in mind, we identified the rigid, yet still sterically accessible $[PyCp_2]^{2-}$ ligand to carry out the synthesis (**Figure 3.2**).[79-80] Reacting anhydrous $Dy(OTf)_3$ with the disodium salt Na_2PyCp_2 afforded the bridging triflate dimer $[(PyCp_2)Dy(\mu\text{-}OTf)]_2$.[119] This dimer readily dissociates in thf to the monomeric form $[(PyCp_2)Dy(thf)(OTf)]$ and reacts with stoichiometric amounts of KFp or KRp to furnish $PyCp_2Dy\text{-}FeCp(CO)_2$ (**3-1**) and $PyCp_2Dy\text{-}RuCp(CO)_2$ (**3-2**).

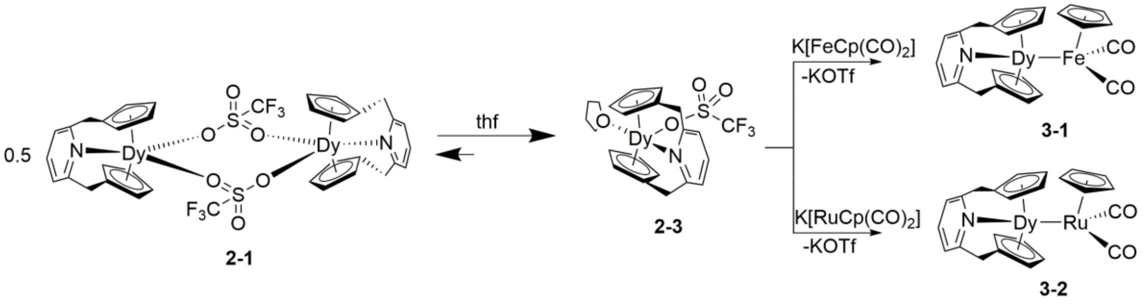

Fig. 3.2: Synthetic schemes for Dy-TM heterobimetallic compounds.

The molecular structures of **3-1** and **3-2** (**Figure 3.3**; see also **Tables B.1, B.2**) feature Dy-Fe and Dy-Ru distances of 2.884(2) Å and 2.951(1) Å. To the best of our knowledge, these are the first direct, unsupported Dy-TM bonds reported thus far. It is interesting to note that the Dy-Ru bond in **3-2** is approximately 0.03 Å longer than the Dy-Ru distances in a reported hydride-bridged species.[120] All other Dy-ligand distances in **3-1** and **3-2** are statistically the same (*d*(Dy-N) = 2.452(9) Å and 2.470(3) Å ; *d*(Dy-C) = 2.628(7) Å and 2.631(3) Å).

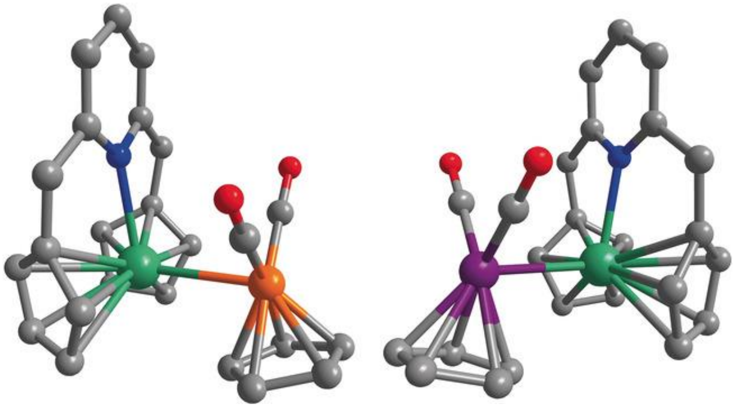

Figure 3.3: Molecular structure of **3-1** (left) and **3-2** (right).[121] Hydrogen atoms have been omitted for clarity. Dy green, Ru purple, Fe orange, N blue, O red, C gray.

3.3.2 Spectroscopic Data for Dy-TM Heterobimetallic Complexes

The nature of the Ln-TM bond was probed using infrared and ^{57}Fe Mössbauer spectroscopy (**Figure 3.4**). The energies of the CO stretching modes were assessed to evaluate the electron density of the transition metal center. Given the similarity of these energies (ν_{CO} 1910/1840 cm^{-1} for **3-1** and ν_{CO} 1930/1851 cm^{-1} for **3-2**) with other compounds such as Cu-Fp (1914/1849 cm^{-1}) and Zn-Fp (1944/1888 cm^{-1}), it can be concluded compounds **3-1** and **3-2** contain a formally Ln^{3+} ion bonded to a TM^0.[122]

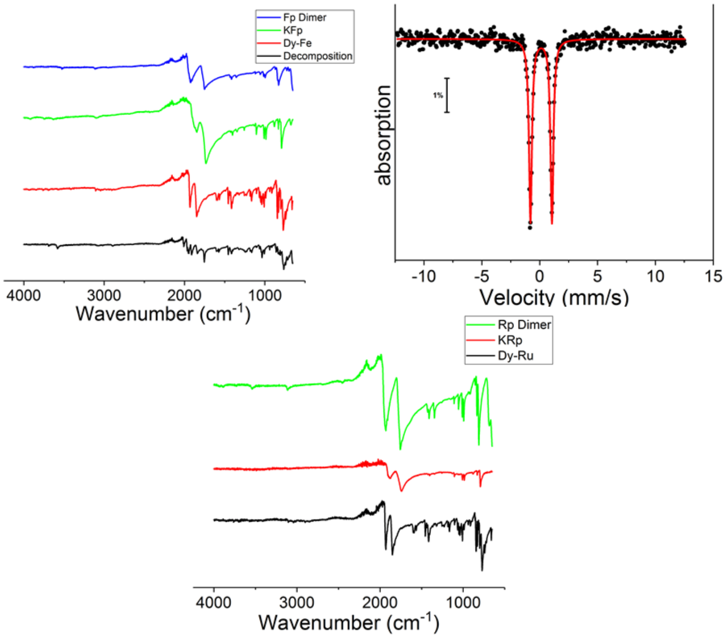

Figure 3.4.: Infrared and ^{57}Fe Mössbauer spectrum of **3-1** (top) and infrared spectrum of **3-2** (bottom). IR spectra include spectra of starting materials.

This is further supported with ^{57}Fe Mössbauer spectroscopy. The isomer shift (δ) is a good indicator of the s electron density at the iron nucleus (δ decreases with increasing s electron density). Complex **3-1** exhibited a single doublet at 5 K. This value is slightly larger than other Fp species ligated to non-π donors such as $Cp(CO)_2Fe\text{-}CH_3$ ($\delta = 0.069$ mm/s, $\Delta E_Q = 1.746$ mm/s at 78 K) and $Cp(CO)_2Fe\text{-}R_2Ge^{4+}$ ($R_2 = \kappa^2\text{-}[C_6H_3\text{-}2\text{-}(C(CF_3)_2O)\text{-}4(CH_3)]^{2-}$) ($\delta = 0.084$ mm/s, ΔE_Q, 1.74 mm/s at 78 K).[123-124] A possible explanation to these differences in δ is stronger Fe→Dy σ donation compared to the other species.

3.3.3 Computational Analysis of Dysprosium Heterobimetallics

There is precedence for utilizing the QTAIM model[125] to describe aspects of heterometallic interactions in Ln-TM bonded complexes computationally.[126] Accordingly, we used DFT calculations to obtain relevant parameters. Our analysis was carried out using the Gaussian09[127] (BP86;[102-103] Dy: cc-pVTZ-DK3 (all electron);[104] Ru[105] or Fe:[106] cc-pVTZ-DK (all electron); 6–311G(d))[128-129] and ADF[110-112] (BP86; TZ2P; ZORA) software packages. Both packages were used for calculations on the experimentally observed molecular geometries of **3-1** and **3-2** from single-crystal X-ray diffraction, and the geometries were optimized with the ADF package (**Table B.4**). In all cases, we observed critical points along the lines between Dy and Fe or Dy and Ru (**Figure 3.5**). For **3-1**, these LCPs are found at the very center of the Dy-Fe bond (*d* (Dy–LCP) = *d*(Fe–LCP) = 1.44 Å) while for **3-2**, the LCPs are closer to the Dy than to the Ru ion (*d*(Dy–LCP): 1.41 Å; *d*(Ru–LCP) = 1.54 Å).

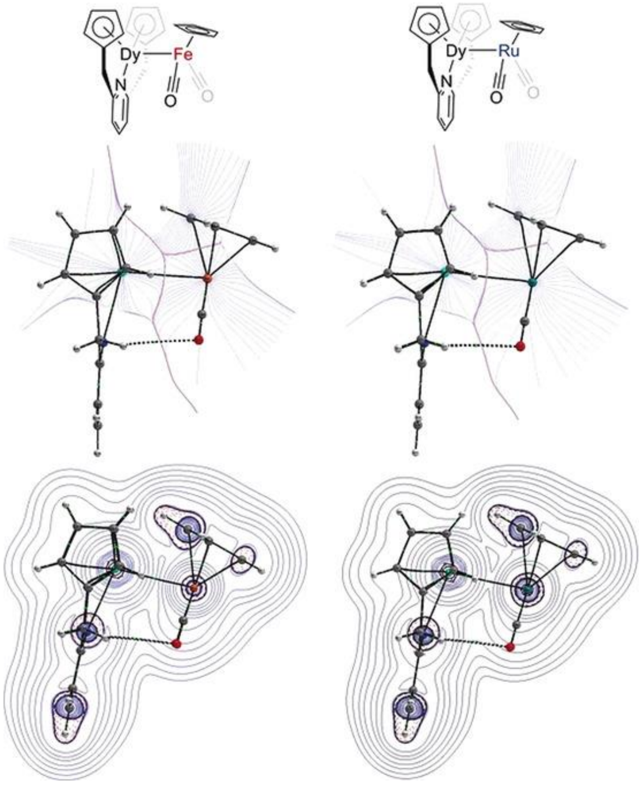

Figure 3.5: Basin paths with interatomic surface paths (center) and contour plots of $\nabla^2\rho$ (bottom) for **3-1** (left) and **3-2** (right)

Interestingly, when the experimental crystal structure was used, the delocalization index (DI-G09 or DI-ADF) was slightly larger for Dy-Fe (0.45 or 0.44) than for Dy-Ru (0.43 or 0.42) while the reverse was true for geometry-optimized structures (DI(Dy,Fe) = 0.47; DI(Dy,Ru) = 0.48). Although the differences in the calculated DIs are admittedly small, larger DIs for the Dy-Fe as compared to the Dy-Ru bonded system would indicate increased electron sharing between Dy and the first-row transition metal Fe as compared to its heavier congener Ru. This surprising finding appears to be further supported by consistently larger positive Laplacians of the electron density at the LCPs($\nabla^2\rho$(LCP)) for Dy-Ru than for Dy-Fe. As has been pointed out,[129-130] care must be taken in interpreting these QTAIM results, and no direct translation of them into a chemist's interpretation of bond, bonding, or bond strength is obvious. However, these results do support a model in which more direct interactions occur between Dy and Fe than between Dy and Ru. Qualitatively, these findings are in line with the significantly greater nucleophilicity of $[FeCp(CO)_2]^-$ as compared to that of $[RuCp(CO)_2]^-$,[131] and may be interpreted as a result of the stronger ruthenium–ligand interactions (as compared to iron–ligand interactions), which attenuate the contribution of the Ru-centered anionic charge to the electrostatic stabilizing interaction of the polar, yet not purely ionic, Dy-Ru bond.

3.3.4 Magnetization Dynamics of Dysprosium Heterobimetallics

Static and dynamic magnetic measurements were carried out for complexes **3-1** and **3-2**. In the variable temperature studies under a constant direct current (dc) field of 1000 Oe (**Figure 3.6**), the room temperature $\chi_M T$ values were determined to be 13.75, and 13.56, emu K mol^{-1} for **3-1** and **3-2** respectively. This is relatively close to the expected value of

14.17 emu K mol^{-1} for one Dy^{3+} ($^{6}H_{15/2}$, $S = 5/2$ $L = 5$, $g = 4/3$) ion. Also, both have a decrease in $\chi_M T$ values with decreasing temperature with a slight increase at 2 K. This decrease is likely a thermal depopulation of Stark sublevels with possible ferromagnetic interactions at 2 K.[132]

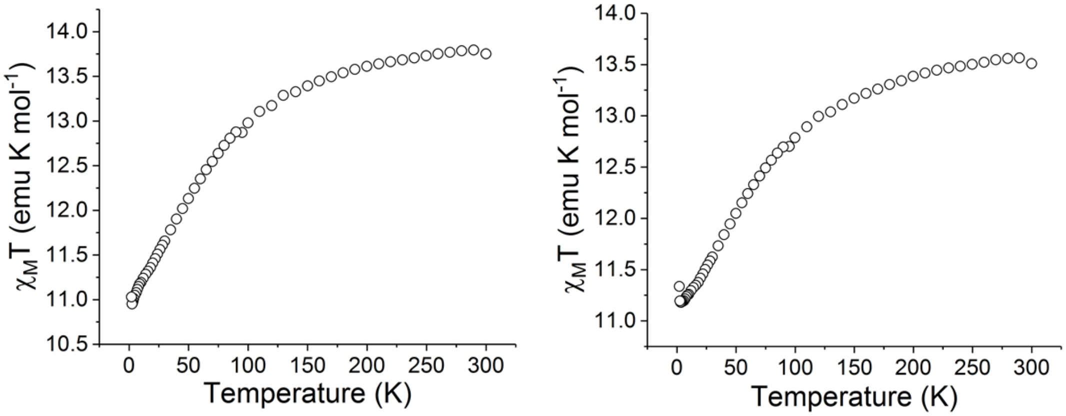

Figure 3.6: dc magnetic susceptibility of complexes **3-1** (left) and **3-2** (right).

According to the *M vs. H* plots (**Figures B.2**, **B.4**), both complexes do not reach magnetic saturation even at fields of 7 T with values much lower (4.73 μ_B for **3-1**, 4.87 μ_B for **3-2**) than the expected free ion value for Dy^{3+} (10 μ_B). In addition, the *M vs. H/T* plots of these two complexes are not superimposable (**Figures B.3**, **B.5**). This can be attributed to breaking the degeneracy of the $^{6}H_{15/2}$ ground state by crystal field effects and the high magnetic anisotropy of the Dy^{3+} ion.

To study the magnetization dynamics of complexes, alternating current (ac) magnetic measurements were carried out (**Figure 3.7**). This is the earliest example of magnetization dynamics being evaluated in Ln-TM bonded compounds. Under no applied dc field, neither complex exhibits a signal in the out of phase component of the ac susceptibility (χ''). Therefore, the compounds do not exhibit slow magnetic relaxation. Both compounds, however, exhibit field induced slow relaxation in the presence of a dc field. A study to determine the optimal dc field for each complex concluded the ideal field to be 1500 Oe for **3-1** and 1600 Oe for **3-2**.[11] Complexes **3-1** and **3-2** exhibit signals in χ'' at temperatures 10-2 K.

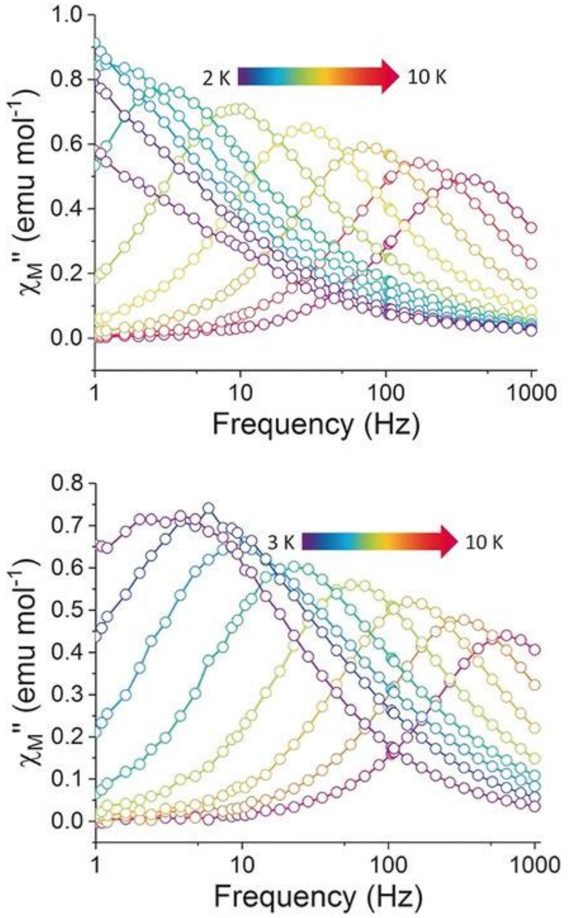

Figure 3.7: Frequency dependence of χ_M'' for **3-1** and **3-2**. A dc field of 1500 and 1600 Oe was applied for **3-1**and **3-2**, respectively.

Generating Cole-Cole plots (χ' *vs.* χ'') based on the generalized Debeye model, relaxation times (τ) were extracted for the two compounds. These relaxation times were used to construct Arrhenius plots (*ln*(τ) *vs. 1/T*) in order to obtain an energy barrier to reverse spin (U_{eff}). There are two common methods to calculate U_{eff}. The first is fitting the linear portion of the Arrhenius plot based on **Equation 1**.

$$\tau^{-1} = \tau_0^{-1} \exp\left(-{}^{U_{eff}}\!/_{k_b T}\right) \text{ Equation 1}$$

This portion of the Arrhenius plot corresponds to the temperature region in which the predominant relaxation mechanism is Orbach. After fitting the data, the U_{eff} for the complexes were calculated to be 40 and 36 cm^{-1} for **3-1** and **3-2** respectively. Another method to fit the data considers other modes of relaxation, such as Raman and quantum tunneling of relaxation (QTM) using **Equation 2**.[44]

$$\tau^{-1} = AH^4T + \tau_{QTM}^{-1} + CT^{n2} + \tau_0^{-1}\exp({}^{-U_{eff}}\!/_{k_B T}) \text{ Equation 2}$$

U_{eff} values were reported to be 43 and 46 cm^{-1} for complexes **3-1**, and **3-2** respectively (**Figure 3.8).** The barriers to magnetization reversal are effectively identical for **3-1** and **3-2** whereas the optimal dc fields are different, and, importantly, magnetic relaxation is slower for **3-1** than for **3-2** at a given temperature, and **3-2** displays larger coefficients for direct and Raman processes. These observations are likely to be consequences of subtle changes in the nature of the Ln-TM bonding as well as changes of the effect of spin–phonon coupling on magnetic relaxation,[44,133] as the energies of all TM–ligand vibrational modes, and especially those of the Dy-TM one, will be strongly altered upon going from **3-1** to **3-2**.

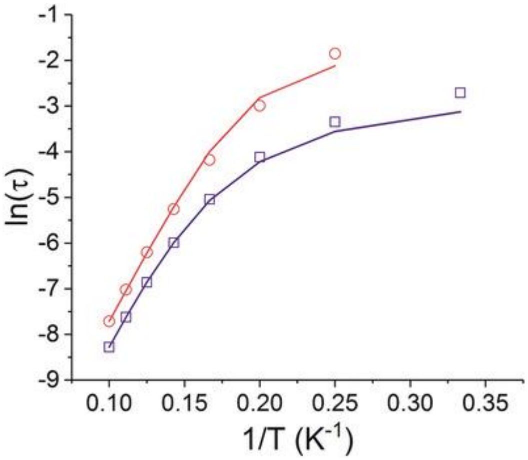

Figure 3.8: Arrhenius plots for **3-1** (orange circles) and **3-2** (purple squares). The solid lines represent fits to the experimental data based on **Equation 2**.

3.4 Conclusion & Outlook

The first reported discrete molecules containing a Dy-Fe and Dy-Ru bond were structurally characterized. These complexes were stable enough to perform magnetization and spectroscopic studies. The data obtained for these molecules suggest strong TM→Dy σ donation with evidence supporting stronger Fe donation to Dy^{3+} than other Fp-X interactions. Despite faster relaxation times for **3-2** as compared to **3-1**, similar U_{eff} values were calculated (46 cm^{-1} for **3-2** and 43 cm^{-1} for **3-2**) under an applied dc field.

The method developed and evaluated in this chapter has the potential to be a versatile approach to prepare isostructural compounds of different Ln-TM combinations for systematic studies. Work to prepare the entire lanthanide series with this system will be discussed in later chapters.

4. TOWARDS UNDERSTANDING OF LANTHANIDE–TRANSITION METAL BONDING: INVESTIGATIONS OF THE FIRST CE–FE BONDED COMPLEX*

4.1 Introduction

Cerium takes a very special role in the chemistry of the lanthanide (Ln) ions.[134] It is the most abundant member of the Ln series in the earth's crust and the Ln-atypical +4 oxidation state is stabilized due to the favorable [Xe]4f^0 noble gas configuration of Ce^{4+} such that molecular Ce^{4+} complexes are well known. The Ce$^{3+/4+}$ redox-couple displays unusually high sensitivity to ligand field effects and can span several volts.[135] Recently, Ce^{3+} complexes have been investigated for their photophysical properties and this has led to exciting new discoveries of Ce^{3+} species as UVA photosensitizers[136] and potent photoreductants for catalytic organic transformations.[137-138] Another intriguing aspect of Ce^{3+} chemistry is the presence of magnetic anisotropy as a consequence of strong spin–orbit coupling. As such, even though the Ce^{3+} ion is an $S = 1/2$ species, several examples of Ce^{3+} complexes that exhibit field induced slow magnetic relaxation have been reported.[139]

Our group is particularly interested in studying magnetization dynamics of lanthanide–transition metal (Ln–TM) bonded complexes[26-27,68,140-141] and we have recently reported a new synthetic approach that allowed us to isolate complexes containing unsupported Dy–Fe and Dy–Ru bonds (**See Chapter 3**).

---

*The results in this chapter were published in *Chem. Commun.* **2018**, *54*, Reproduced by permission of The Royal Society of Chemistry Copyright, 2018 Royal Society of Chemistry.

In the present work, we show that our synthetic methodology can be applied to the much larger Ce^{3+} ion[142] ($r_{ion}(Dy^{3+})$ = 1.075 Å; $r_{ion}(Ce^{3+})$ = 1.220 Å) and report the preparation and magnetic characterization of the first complex with an unsupported Ce^{3+}–TM bond, (thf)$PyCp_2Ce$–$FeCp(CO)_2$ (**4-1**).

The nature of the Ce–Fe bond is discussed as having highly ionic contributions as judged by ^{57}Fe Mössbauer and IR spectroscopy as well as QTAIM DFT computational analysis. The structural and magnetic properties of **4-1** are further compared to those of the new mononuclear complex $(PyCp_2)Ce(OSO_2CF_3)(thf)$ (**4-3**) and new dinuclear $[(PyCp_2)Ce(\mu\text{-}O_2SOCF_3)]_2$ (**4-2**) (**Figure 4.1).**

4.2 Materials & Methods

4.2.1 General Considerations

Synthesis of 2,6-bis(methylenecyclopentadienyl)pyridine disodium salt (Na_2PyCp_2) and KFp were prepared as previously described[79-80,100,119] and carried out under strict anaerobic and anhydrous conditions using an Ar filled glovebox (Vigor) and solvents dried and flushed with Ar using a solvent purification system (JC Meyer Solvent System). All glassware used was oven dried and cycled into the glovebox overnight. Sodium cyclopentadienide (0.1 mol in THF), and anhydrous $Ce(OTf)_3$ were purchased from STREM. The $Ce(OTf)_3$ was dried for two days at 180 °C under vacuum prior to use. Samples used for magnetic characterization were either single crystalline material or microcrystalline powders. Magnetic samples of **4-1**, **4-2**, and **4-3** were prepared with an eicosane matrix in a high purity NMR tube which was flame sealed under vacuum. The eicosane (Acros Organics) was melted in a hot water bath (42 °C) and was dispersed homogeneously throughout the sample. Magnetic characterization of **4-1**, **4-2**, and **4-3** were obtained using a Quantum Design MPMS 3 SQUID magnetometer. Direct current (dc) measurements were acquired under an applied 1000 Oe field at a temperature range of 2-300 K. Alternating current (ac) measurements for **4-1**, **4-2**, and **4-3** under applied dc fields ranging from 500 Oe to 4000 Oe at temperature ranges of 4 to 1.8 K. Elemental analyses were carried out by Midwest Microlab. Cyclic voltammograms (CVs) were recorded in an Ar-filled glovebox using a GAMRY Ref600 potentiostat with a three-electrode setup: glassy carbon disk (BasInc) working electrode, silver pseudo reference electrode, and platinum wire counter electrode (Alfa Aesar). All CVs were recorded in a 1.0 mM [(PyCp$_2$)Ce(thf)(OTf)] THF solution with 0.1 M tetrabutylammonium hexafluorophosphate as the supporting electrolyte. All potentials were referenced to the ferrocene/ferrocenium redox couple measured for internally added ferrocene. IR spectra were obtained in the solid state in an argon filled glove box (Vigor) equipped with an Agilent CARY 630 FT-IR spectrometer (32 background scans, 32 scans @ 650-4000 cm^{-1}, Apodization: Happ-Genzel). ^{57}Fe Mössbauer spectra were collected on a model MS4 WRC low-field, variable temperature spectrometer (See Co., Edina, MN). Temperatures were varied using a temperature controller on the heating coil on the sample holder. The instrument was calibrated using an α-Fe foil at room temperature. Obtained spectra were fitted using WMOSS software (See Co.)

4.2.2 Synthesis

Synthesis of (thf)PyCp$_2$Ce-FeCp(CO)$_2$ (4-1): The material was prepared as previously described for (PyCp$_2$Dy-FeCp(CO)$_2$.[143] A solution of KFp (18.1 mg, 84 μmol) in THF (2 ml) and a solution of [(PyCp$_2$)Ce(μ-OTf)]$_2$ (50 mg, 84 μmol) in THF (2 ml) were placed in a freezer for 1 hour at -30 °C. The solution of KFp was added dropwise to the solution of [(PyCp$_2$)Dy(μ-OTf)]$_2$ and placed in the freezer. Yellow-orange block crystals suitable for X-Ray diffraction formed over one week and the solution was decanted off and crystals were dried in a 74.0 % (52.3 mg) yield. IR (solid, cm^{-1}) 1890 (ν_{CO}), 1814 (ν_{CO}), 1599, 1570, 1418, 1427, 1231, 1170, 1021, 885, 812, 759, 670 Anal. Calcd. For $C_{28}H_{28}CeFeNO_3$ C, 54.03; H, 4.53; N, 2.25. Found: C, 53.82; H, 4.54; N, 2.22.

Synthesis of [(PyCp$_2$)Ce(μ-OTf)]$_2$ (4-2). The material was prepared as previously described for [(PyCp$_2$)Dy(μ-OTf)]$_2$.[79-80,119] A 25 mL THF solution of Na$_2$PyCp$_2$ (0.5614, 2.01 mmol) was added dropwise to a 25 mL THF suspension of Ce(OTf)$_3$ (2.00 mmol, 1.175 g). The reaction was occasionally stirred manually for 2 h in a cold well at -30 °C and warmed to room temperature. After 2 d of stirring, the THF was removed and replaced with DCM (30 mL) and left to stir overnight. The solution was filtered and hexanes (50 mL) was slowly added to the filtrate and left overnight. The product was collected as golden yellow plate crystals in a 40.3 % (0.421 g) yield. Anal. Calcd. For $C_{36}H_{30}Ce_2F_6N_2O_6S_2$ C, 41.38; H, 2.89; N 2.68. Found: C, 41.11; H, 2.94; N, 2.58.

Synthesis of [(PyCp$_2$)Ce(thf)(OTf)] (4-3). The material was prepared as previously described for [(PyCp$_2$)Dy(thf)(OTf)].[119] Approximately 50 mg of **4-2** was dissolved in 2 mL of THF and layered with 5 mL of hexanes and placed in a freezer (-30 °C) overnight. The resulting bright yellow block crystals were collected for further characterization. Close to quantitative yields were obtained. Anal. Calcd. For $C_{22}H_{23}CeF_3NO_4S$ C, 44.44; H, 3.90; N, 2.36. Found: C, 44.32; H, 3.94; N, 2.29

4.2.3 X-ray Crystallography

Compound 4-1. A Leica MZ 75 microscope was used to identify a suitable yellow block with very well-defined faces with dimensions (max, intermediate, and min) 0.272 x 0.195 x 0.143 mm^3 from a representative sample of crystals of the same habit. The crystal mounted on a nylon loop was then placed in a cold nitrogen stream (Oxford) maintained at 110 K.

A BRUKER APEX 2 Duo X-ray (three-circle) diffractometer was employed for crystal screening, unit cell determination, and data collection. The goniometer was controlled using the APEX2 software suite, v2008-6.0.[81,144] The sample was optically centered with the aid of a video camera such that no translations were observed as the crystal was rotated through all positions. The detector was set at 6.0 cm from the crystal sample (APEX2, 512x512 pixel). The X-ray radiation employed was generated from a Mo X-ray tube (K_α = 0.71073 Å with a potential of 40 kV and a current of 40 mA). 45 data frames were taken at widths of 1.0°. These reflections were used in the auto-indexing procedure to determine the unit cell. A suitable cell was found and refined by nonlinear least squares and Bravais lattice procedures. The unit cell was verified by examination of the h k l overlays on several frames of data. No super-cell or erroneous reflections were observed. After careful examination of the unit cell, an extended data collection procedure (5 sets) was initiated using omega scans.

Integrated intensity information for each reflection was obtained by reduction of the data frames with the program APEX2.[81] The integration method employed a three-dimensional profiling algorithm and all data were corrected for Lorentz and polarization factors, as well as for crystal decay effects. Finally, the data was merged and scaled to produce a suitable data set. The absorption correction program SADABS[84] was employed to correct the data for absorption effects.

Systematic reflection conditions and statistical tests of the data suggested the space group Pnma. A solution was obtained readily (Z=4; Z'=0.5) using XT/XS in APEX2.[81,83] Hydrogen atoms were placed in idealized positions and were set riding on the respective parent atoms. All non-hydrogen atoms were refined with anisotropic thermal parameters. Absence of additional symmetry and voids were confirmed using PLATON (ADDSYM).[86] The structure was refined (weighted least squares refinement on F^2) to convergence.[81,86-87]

Compound 4-2. A Leica MZ 75 microscope was used to identify a suitable colorless plate with very well-defined faces with dimensions (max, intermediate, and min) 0.221 x 0.218 x 0.083 mm^3 from a representative sample of crystals of the same habit. The crystal mounted on a nylon loop was then placed in a cold nitrogen stream (Oxford) maintained at 110 K.

A BRUKER APEX 2 Duo X-ray (three-circle) diffractometer was employed for crystal screening, unit cell determination, and data collection. The goniometer was controlled using the APEX2 software suite, v2008-6.0.[81,84] The sample was optically centered with the aid of a video camera such that no translations were observed as the crystal was rotated through all positions. The detector was set at 6.0 cm from the crystal sample (APEX2, 512x512 pixel). The X-ray radiation employed was generated from a Mo X-ray tube (K_α = 0.71073 Å with a potential of 40 kV and a current of 40 mA).

45 data frames were taken at widths of 1.0°. These reflections were used in the auto-indexing procedure to determine the unit cell. A suitable cell was found and refined by nonlinear least squares and Bravais lattice procedures. The unit cell was verified by examination of the h k l overlays on several frames of data. No super-cell or erroneous reflections were observed.

After careful examination of the unit cell, an extended data collection procedure (10 sets) was initiated using omega and phi scans.

Integrated intensity information for each reflection was obtained by reduction of the data frames with the program APEX2.[81] The integration method employed a three-dimensional profiling algorithm and all data were corrected for Lorentz and polarization factors, as well as for crystal decay effects. Finally, the data was merged and scaled to produce a suitable data set. The absorption correction program SADABS[84] was employed to correct the data for absorption effects.

Systematic reflection conditions and statistical tests of the data suggested the space group P21/n. A solution was obtained readily (Z=2; Z'=0.5) using XT/XS in APEX2.[81,83] Hydrogen atoms were placed in idealized positions and were set riding on the respective parent atoms. All non-hydrogen atoms were refined with anisotropic thermal parameters. Absence of additional symmetry and voids were confirmed using PLATON (ADDSYM).[86] The structure was refined (weighted least squares refinement on F^2) to convergence.[81,86-87]

Compound 4-3. A Leica MZ 75 microscope was used to identify a suitable yellow block with very well-defined faces with dimensions (max, intermediate, and min) 0.228 x

0.213 x 0.162 mm^3 from a representative sample of crystals of the same habit. The crystal mounted on a nylon loop was then placed in a cold nitrogen stream (Oxford) maintained at 110 K. A BRUKER APEX 2 Duo X-ray (three-circle) diffractometer was employed for crystal screening, unit cell determination, and data collection. The goniometer was controlled using the APEX2 software suite, v2008-6.0.[81,84] The sample was optically centered with the aid of a video camera such that no translations were observed as the crystal was rotated through all positions. The detector was set at 6.0 cm from the crystal sample (APEX2, 512x512 pixel). The X-ray radiation employed was generated from a Mo sealed X-ray tube (K_α = 0.70173Å with a potential of 40 kV and a current of 40 mA).

45 data frames were taken at widths of 1.0°. These reflections were used in the auto-indexing procedure to determine the unit cell. A suitable cell was found and refined by nonlinear least squares and Bravais lattice procedures. The unit cell was verified by examination of the h k l overlays on several frames of data. No super-cell or erroneous reflections were observed.

After careful examination of the unit cell, an extended data collection procedure (6 sets) was initiated using omega scans.

Integrated intensity information for each reflection was obtained by reduction of the data frames with the program APEX2.[81] The integration method employed a three-dimensional profiling algorithm and all data were corrected for Lorentz and polarization factors, as well as for crystal decay effects. Finally, the data was merged and scaled to produce a suitable data set. The absorption correction program SADABS[84] was employed to correct the data for absorption effects.

Systematic reflection conditions and statistical tests of the data suggested the space group Pna21. A solution was obtained readily using XT/XS in APEX2.[81,83] Hydrogen atoms were placed in idealized positions and were set riding on the respective parent atoms. All non-hydrogen atoms were refined with anisotropic thermal parameters. Thermal ellipsoid on O18 suggested a disorder and was modeled successfully between two positions with an occupancy ratio of 0.52:0.48. Appropriate restraints / constraints were added to keep the bond distances, angles, and thermal ellipsoids meaningful. Absence of additional symmetry and voids were confirmed using PLATON (ADDSYM).[86] The structure was refined (weighted least squares refinement on F^2) to convergence.[81,87]

4.2.4 Computational Details

The X-ray crystal structure of **4-1** was imported into Gaussian 09, Revision D.01[127] without further optimization (i.e. single point calculations). The BP86[102-103] functional was used, in combination with the 6- 311G*[128] basis set for the C, H, O, N atoms, and the all-electron correlation consistent basis sets for Ce (cc-pVTZ-DK3)[104], and Fe (cc-pVTZ-DK)[106]. The integration grid was set to ultrafine. The Douglas-Kroll-Hess (DKH)[107,145] 2nd order scalar relativistic scheme was applied. Furthermore, both single point calculations and geometry optimizations were performed for **4-1** with Orca 4.0.0[146] utilizing the BP86 functional, with the ZORA[112] Hamiltonian, in combination with the ZORA recontracted basis set[147] for Ce (SARC-ZORA-TZVP), Fe, C, N, O, and H (ZORA-def2-TZVP). Topological analysis (Quantum Theory of Atoms in Molecules, QTAIM)[108] was performed on the Kohn-Sham orbitals generated from both Gaussian and Orca by employing AIMAll.[148] In addition, both single point calculations and geometry optimizations were performed for **4-1** with the Amsterdam Density Functional modeling suite (ADF 2017)[110-112] utilizing the BP86 functional, TZ2P[113] basis sets and the ZORA method for scalar relativistic effects. QTAIM analyses were performed with the adf2aim utility, which is part of the ADF package.

4.3 Results and Discussion

4.3.1 Synthesis & Structure of Cerium Complexes

The $[PyCp_2]^{2-}$ ligand is a rare example of a strongly chelating and structurally rigid binding platform that stabilizes organometallic Ln complexes without introducing significant steric encumbrance around labile coordination sites of the Ln ion and was therefore utilized in the present study. The reaction of anhydrous $Ce(OSO_2CF_3)_3$ and the disodium salt Na_2PyCp_2 yielded the dimeric complex $[(PyCp_2)Ce\text{-}(\mu\text{-}O_2SOCF_3)]_2$ (**4-2**) after crystallization from CH_2Cl_2-hexanes mixtures. Complex **4-2** readily dissociates in thf solvent into the monomeric complex $(PyCp_2)Ce(O_2SOCF_3)(thf)$ (**4-3**) which can be crystallized from thf–hexanes solvent mixtures.

The weakly binding triflate anion of **4-3** is a good leaving group and allows for its facile substitution by $[FeCp(CO)_2]^-$ in the reaction of **4-3** with stoichiometric amounts of $K[FeCp(CO)_2]$ in thf at low temperatures to yield crystalline material of the Ce–Fe bonded complex $(thf)PyCp_2Ce–FeCp(CO)_2$ (**Figure 4.1**).

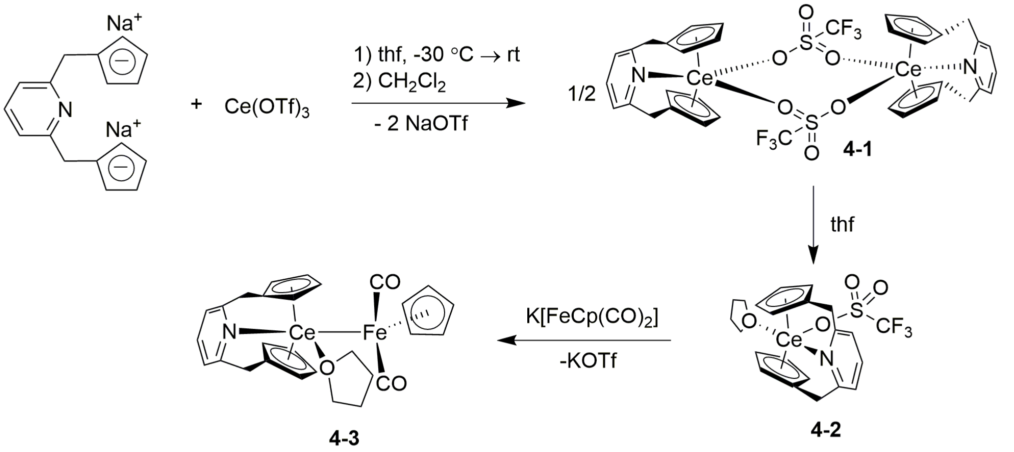

Figure 4.1: Synthetic overview of complexes **4-1**, **4-2**, and **4-3**.

The molecular structures of compounds **4-1**, **4-2**, and **4-3** were investigated by means of single crystal X-ray diffraction studies (**Figure 4.1** and **Tables C.1** and **C.2**). While the Ce–C distances are similar in **4-1** (2.759[2]–2.827[2] Å), 2 (2.730[2]–2.794[2] Å), and **4-3** (2.712[4]–2.825[4] Å) the Ce–N distance in **4-1** (2.779[2] Å) is significantly longer than that in **4-2** (2.621[2] Å) and 3 (2.618[3] Å). There are several structural differences observed between the mononuclear Ce^{3+} complexes **4-1** and **4-3** as compared to their previously reported Dy^{3+} analogues **2-1** and **2-3**.[119,143] The binding of the triflate anion in **4-3** involves close interactions with two of the triflate O-atoms (d(Ce–$O_{triflate}$) = 2.697[3], 2.749[3] Å) while only one Dy–$O_{triflate}$ interaction (2.335[1] Å) was observed in **2-3**. In comparing the Ln–Fe bonded complexes **4-1** and **3-1**, we notice that the increase in ionic radius[142] (1.075 Å for Dy^{3+} to 1.220 Å for $Ce^{3+)}$ allows for the additional binding of a thf molecule to Ce. The Ce–Fe distance in **4-1** (3.1546[5] Å) is longer than the Dy–Fe distance in **3-1** (2.884[2] Å) and is to the best of our knowledge the first structurally characterized unsupported direct bond between an iron ion and a formally Ce^{3+} ion.

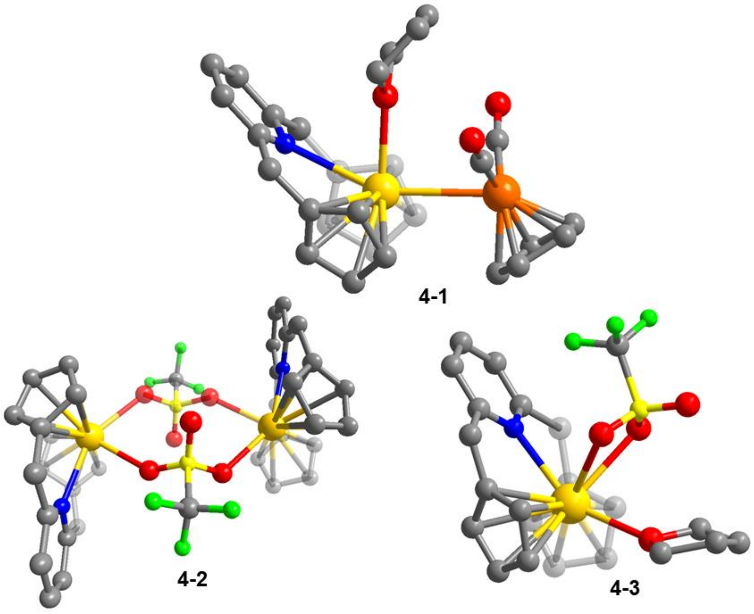

Figure 4.2: Molecular structure of **4-1** (top), **4-2** (bottom left), and **4-3** (bottom right). Hydrogen atoms have been omitted for clarity. Ce yellow, Fe orange, N blue, O red, C gray.

The binding of an additional thf solvent molecule to Ce in **4-1** also affects the coordination environment of the Fe ion. While the Fe–C_{Cp} and Fe–C_{CO} distances in **4-1** (2.109[2] Å and 1.733[2] Å) and **3-1** (2.10[1] Å and 1.716[9] Å) are comparable, the ∠(Ln–Fe–$Cp_{centroid}$) (121.8° in **4-1**; 105.9° in **3-1**) and ∠ (C_{CO}–Fe–C_{CO}) (95.4° for **4-1**; 89.4° for **3-1**) angles differ significantly.

4.3.2 Electrochemistry of 4-3

The $Ce^{3+/4+}$ redox potentials are known to be strongly dependent on the stabilizing ligand and have been shown to span an unusually large electrochemical potential window.[135] Cyclic voltammograms of **4-3** in thf solution (**Figure C.1**) display a single oxidation event at +200 mV (vs. $Fc^{0/+}$) which is not reversible at low scan rates (100 mV s^{-1}). Increasing the scan rates to values above 1 V s^{-1} results in partial recovery of the cathodic current at this potential. These observations suggest that the electrochemically generated oxidized +3 species is not stable and undergoes fast chemical change (EC mechanism). This irreversibility differs from other organometallic cerium systems such as $[Ce(COT'')_2]^-$ (COT'' = $C_8H_6(SiMe_3)_2$) and $[Li(thf)_2Ce(MPB)_2(thf)_2]$ (MPB = 6-tert-butyl-4-methylphenolate) which display reversible $Ce^{3+/4+}$ redox couples at 1.43 and 0.93 V.[149-150] It is therefore possible that the oxidation event observed for **4-3** involves delocalized or ligand based orbitals.

4.3.3 Spectroscopic Properties of 4-1

These structural differences around the Fe site have direct consequences for the spectroscopic parameters of **4-1** (**Figure 4.3**). The ^{57}Fe Mössbauer spectrum of **4-1** at 4.6 K indicates a single component with an isomer shift (δ) of 0.133 mm s^{-1} and a quadrupole splitting (ΔE_Q) of 2.075 mm s^{-1}, while we previously found $\delta = 0.129$ mm s^{-1} and $\Delta E_Q = 1.859$ mm s^{-1} for **3-1** at 5 K. The significant difference in ΔE_Q (between **4-1** and **3-1**) is in agreement with the high sensitivity of ΔE_Q to changes in the geometry of the electric field gradient around the Fe nucleus. However, given the above discussed structural variations, we cannot include a direct comparison of the values of δ of **4-1** and **3-1** into the comparative discussion of the strength of electron donation from Fe→Ce or Fe→Dy.

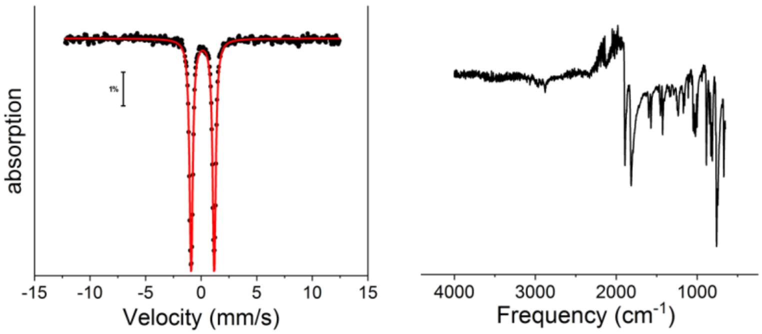

Figure 4.3: ^{57}Fe Mössbauer (left) and infrared spectrum (right) of **4-1**. Black dots are experimental points whereas the red line corresponds to fit discussed in **4.2**.

The solid-state IR spectra of Ce–Fe bonded **4-1** feature CO stretching modes at 1890 and 1814 cm^{-1} which are at lower energies than the CO stretching frequencies in the Dy–Fe analogue **3-1** (1910, 1840 cm^{-1}). This observation suggests stronger Fe–CO π-backbonding interactions in **4-1** as compared to **3-1** and would therefore also imply higher electron density on the Fe site in **4-1**, which in turn could be a result of smaller Fe→Ce donor interactions in **4-1** as compared to Fe→Dy interactions in **3-1**. Indeed, this interpretation is further supported by our computational analysis (**Figure 4.4**).

4.3.4 Computational Analysis of 4-1

To gain computational insight into the nature of the Ce–Fe bond in **4-1**, we followed the frequently employed QTAIM[108] approach utilizing Gaussian G09-D01,[103-104,127] BP86/Ce, cc-pVTZ-DK3 (all electron) Fe, cc-pVTZ-DK (all electron) C, N, O, H, 6-311G*, Orca 4.0.0,[104,128-146] (single point and geometry optimizations with the ZORA Hamiltonian; BP86/Ce, SARC-ZORA-TZVP; Fe, C, N, O, H, ZORA-def2-TZVP), and ADF[110-112] (single point and geometry optimizations with the ZORA Hamiltonian, BP86/TZ2P). The computational results following either single point calculations based on the experimental crystal structure or after full geometry optimization are summarized in (**Tables C.3, C.4, and C.5**) and are almost identical to each other, independent of the approach. We readily identify a line critical point (lcp) between Ce and Fe which is slightly more proximal to Fe than to Ce (d(Ce-lcp) = 1.60 Å; d(Fe-lcp) = 1.55 Å), which is in contrast to the perfectly central position of the lcp between Dy and Fe in **3-1** (**Figure 4.4**).

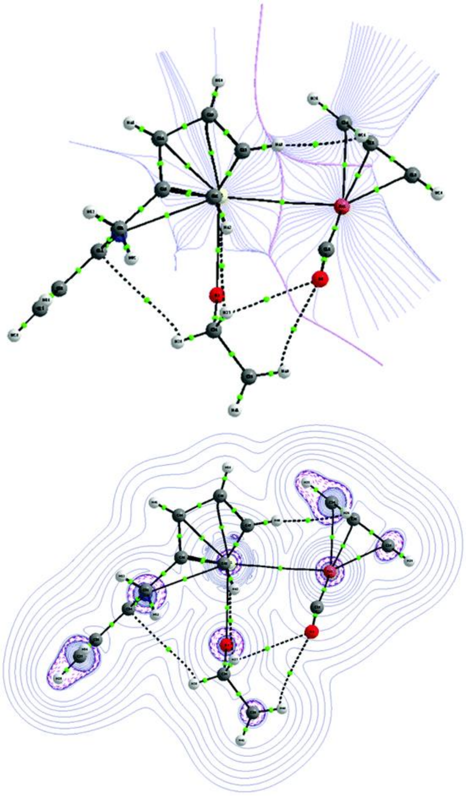

Figure 4.4: Top: Basin paths with interatomic surface (IAS) paths. Bottom: Contour plots of $\nabla^2\rho$.

Another striking difference between **4-1** and **3-1** is the much lower calculated delocalization index (DI) of 0.35 for the Ce–Fe bond in **4-1** (DI(Dy–Fe in **3-1**) = 0.45). This result supports the formulation of weaker Fe→Ce donation in **4-1** as compared to

Fe→Dy donation in **3-1** and is therefore in agreement with lower energy CO stretching frequencies in **4-1** as compared to **3-1**.

4.3.5 Magnetic Properties of Cerium Complexes

Although Ce^{3+} is an S = 1/2 species, strong spin–orbit coupling results in significant magnetic anisotropy and can lead to slow magnetic relaxation for Ce^{3+} complexes. Previously reported mononuclear Ce^{3+} complexes displayed solely field-induced slow magnetic relaxation[151-152] and only one example of a linear, trinuclear Zn(II)–Ce(III)–Zn(II) complex[153] has exhibited slow magnetic relaxation in the absence of static fields. We therefore investigated the static and dynamic magnetic properties of complexes **4-1**, **4-2**, and **4-3**. The temperature dependence of the molar magnetic susceptibility temperature product ($\chi_M T$) using a 1000 Oe direct current (dc) field are shown in **Figures C.2-4**. The experimental room temperature $\chi_M T$ values of 0.71 (for **4-1**), 1.63 (for **4-2**), and 0.75 (for **4-3**) emu mol^{-1} K are close to the expected values of 0.80 and 1.60 emu mol^{-1} K for one (**4-1** and **4-3**) or two (**4-2**) non-interacting Ce^{3+} ions ($^2F_{5/2}$, S = 1/2, L = 3, J = 5/2, and g = 6/7). All three complexes exhibit decreases in $\chi_M T$ with decreasing temperature, typically observed and attributed to thermal depopulation of Stark sublevels[132] in Ce^{3+}. All three complexes also exhibit a slight increase in $\chi_M T$ at 2 K, which could possibly be indicative of weak intermolecular ferromagnetic interactions.

Variable temperature *magnetization* (*M*) *versus Field* (*H*) measurements (**Figures C.5-C.7** for *M vs. H*; **Figures C.8-C.11**) indicate that compounds **4-1**, **4-2**, and **4-3** do not reach magnetic saturation even up to fields of 7 T (M at 1.8 K: 0.75 (for **4-1**), 1.48 (for **4-2**), and 0.62 μ_B (for **4-3**)). Although the *M vs. H/T* plots appear to be fairly superimposable, the lack of magnetic saturation would be in agreement with some amount of magnetic anisotropy which is consistent with the dynamic magnetic measurements discussed below.

In the absence of applied dc fields, none of the three investigated complexes exhibited signals in the out-of-phase component of the alternating current (ac) magnetic susceptibility (χ'') at temperatures of 3 or 2 K. However, application of dc fields resulted in signals with well-defined maxima in χ'' at temperatures below 4 K for all three complexes (**Figure 4.5 for 4-1**, **Figures C.11-C.16**).

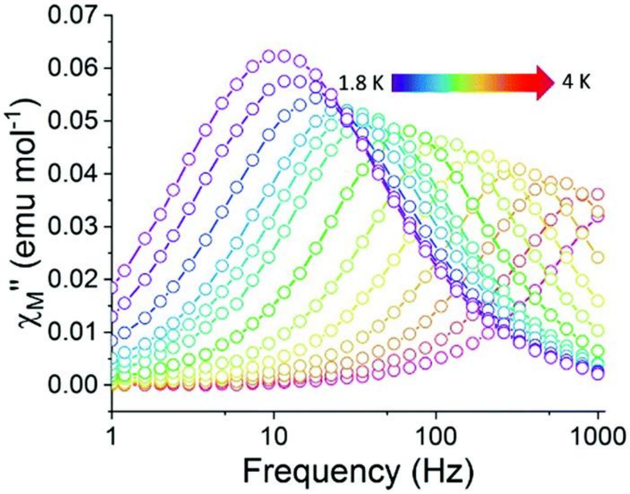

Figure 4.5: Out-of-phase component of the ac susceptibility (χ_m'') of **4-1** between 1.8-4 K (H_{dc} = 500 Oe)

Fits of the resulting Cole–Cole plots (**Figures C.17-C.19**) to the generalized Debye equation resulted in the dc field-dependence of the magnetic relaxation times τ for **4-1**, **4-2**, and **4-3** (**Figures C.20-C.22**). All three complexes exhibit a typical initial increase of magnetic relaxation times with increasing field up to an optimal dc field, followed by decrease in τ values at higher fields. This behavior can be interpreted by an initial decrease of contributions from quantum tunneling of the magnetization (QTM) to relaxation, followed by introduction of field-induced direct processes at higher fields. The optimal dc fields differ strongly for the three complexes (500 Oe for **4-1**, 1500 Oe for **4-2**, 4000 Oe for **4-3**), and interestingly is the smallest for Ce–Fe bonded complex **4-1**. The optimal field for Dy–Fe bonded **3-1** was previously reported as 1500 Oe. The field dependence of τ was fitted to **Equation 4.1**

$$\tau^{-1} = AH^{n_1}T + \frac{B_1}{1 + B_2H^2} + D \text{ Equation 4.1}$$

Here, A represents the direct relaxation parameter, B_1 and B_2 are QTM parameters, and D accounts for Orbach and Raman contributions which are field independent.[73]

Constraining n_1 to a value of 4, the value expected for a Kramers ion in the absence of hyperfine interactions[44] (I = 0 for all Ce isotopes), we observe the fitting values for each parameter as shown in (**Table C.5**) These optimal fields were applied to obtain the temperature dependence of χ_M'' (**Figure 4.5** for **4-1**, **Figures C.26 C.27** for **4-2** and **4-3**) of each complex (**Figures C.23-C.25** for χ_M'). Extraction of the relaxation times from the corresponding Cole–Cole plots (**Figures C.28-C.30**) allowed for generation of Arrhenius plots shown in **Figure 4.6**. It should be mentioned that for compound **4-3** the appearance of a second, slower relaxation process was observed at temperatures below 2.4 K. Although both processes could be fitted using the CC fit software,[154] we only show the τ values associated with the faster process for **4-3** in **Figure 4.6**.

There are multiple approaches to estimating an effective energy barrier (U_{eff}) to magnetization reversal from Arrhenius plots. The linear regime of the temperature dependent part of the Arrhenius plot can be fitted to estimate U_{eff}, by assuming that magnetic relaxation occurs solely via the Orbach mechanism, using **Equation 4.2.**

$$\tau^{-1} = \tau_0^{-1} e^{\frac{-U_{eff}}{k_B T}} \text{ Equation 4.2}$$

The calculated barriers according to **Equation 4.2** are 33 cm^{-1}, 24 cm^{-1}, and 21 cm^{-1} with τ_0 values of 2.71 x 10^{-8} s, 1.51 x 10^{-7} s, and 5.85 x 10^{-7} s for compounds **4-1**, **4-2**, and **4-3**, respectively. Alternatively, the data can be fit over the whole experimental temperature range according to **Equation 4.3**.

$$\tau^{-1} = AH^4T + \tau_{QTM}^{-1} + CT^{n_2} + \tau_0^{-1} e^{\frac{-U}{k_B T}} \text{ Equation 4.3}$$

In the fitting routine, we restricted n_2 to a value of 5, which is the expected value for a Kramers ion with low lying excited states,[44] and the values for A, B_1, and B_2 were restrained to the above determined values from the dc field dependence of τ to avoid over parameterization. According to this model, we obtained U values of 29 cm^{-1}, 28 cm^{-1}, and 38 cm^{-1} with associated τ_0 values of 3.50 x 10^{-9} s, 3.02 x 10^{-9} s, and 1.66 x 10^{-10} s for compounds **4-1**, **4-2**, and **4-3**, respectively.

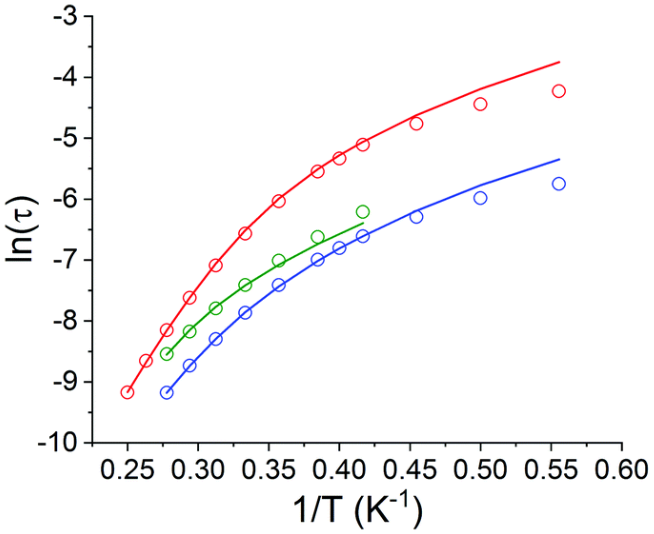

Figure 4.6: Arrhenius plot of magnetization relaxation times **4-1** (red), **4-2** (blue), and **4-3** (green) under optimal dc fields. Open circles correspond to experimental data, whereas the lines correspond to the fit according to **Equation 4.3**.

Although the reported U values are similar to other cerium compounds that exhibit field induced slow magnetic relaxation, we are hesitant to make direct comparisons as the reported examples did not account for direct relaxation processes in the fit equation. Independent of the exact U values, we can summarize the dynamic magnetization properties and note that the dc field dependence of the three complexes varies significantly (with **4-1** showing the lowest optimal dc fields) and that under optimal dc fields, Ce–Fe bonded complex **4-1** displays longer relaxation times at a given temperature. These findings may suggest that the incorporation of Ln–TM bonding could contribute to future SMM design guidelines.

4.4 Conclusion & Outlook

A series of organometallic cerium complexes were prepared and assessed for their magnetic properties. Of particular note, complex **4-1** contained a direct, unsupported lanthanide-transition metal bond between a cerium and iron ion. Structural, spectroscopic, and computational comparisons with the Dy analogue **3-1** suggested that there was stronger Fe→Dy σ donation as compared to Fe→Ce. While no cerium complex displayed slow magnetic relaxation under zero field, complex **3-1** exhibited field-induced slow magnetic relaxation at the lowest applied field with longer relaxation times as compared to **4-2** and **4-3**. Most importantly, this study demonstrated the $PyCp_2^{2-}$ ligand system can be utilized to isolate Ln-TM bonds outside of Dy-TM, leading to the possibility of using this system for a systematic study of Ln-TM bonding. Efforts towards this series will be discussed in later chapters.

5. ASSESSING THE NATURE OF LANTHANIDE-TRANSITION METAL BONDING IN DISCRETE MOLECULES: A PERSPECTIVE

5.1 Introduction

As mentioned in previous chapters, the goal of the project was not only to prepare a complex containing a lanthanide-transition metal bond, but also to design a system in which the lanthanide and transition metal could be readily substituted to fully assess the nature of the bond across the lanthanide series. This endeavor is certainly challenging, as it requires rational ligand design in addition to time to fully characterize these new compounds. We have previously reported the synthesis and characterization of complexes containing Dy-TM (**Chapter 3**) and Ce-Fe bonds (**Chapter 4**) which were successfully isolated utilizing the rigid, sterically accessible $[PyCp_2]^{2-}$ ligand system. Spectroscopic studies implied strong TM→Ln σ donation which was further supported via computational analysis. Dynamic magnetization studies performed concluded all Ln-TM bonded complexes exhibited field induced slow magnetic relaxation.

In this chapter, I will discuss the ongoing work to synthesize Ln-TM combinations across the lanthanide series. Spectroscopic and magnetic analysis will be presented with the goal to establish trends as how the substitution of the lanthanide changes the nature of the metal-metal bond. Additionally, future work will be proposed in relation to the synthesis of more Ln-TM bonded complexes, increased complex solubility, and new spectroscopic methods sensitive enough to distinguish different Ln-TM bonds. Also, proposed work will aim to improve SMM behavior in complexes bearing Ln-TM bonds.

5.2 Materials & Methods

5.2.1 General Considerations

Synthesis of 2,6-bis(methylenecyclopentadienyl)pyridine disodium salt, $[(PyCp_2)Ln(\mu\text{-}OTf)]_2$ $[(PyCp_2)Ln(OTf)(thf)]$, KFp, and KRp were carried out under strict anaerobic and anhydrous conditions using an Ar filled glovebox (Vigor) utilizing previous procedures[79-80,100] and solvents dried and flushed with Ar using an SPS system (JC Meyer Solvent System). All glassware used was oven dried and cycled into the glovebox overnight. 2,6-bis(hydroxymethyl)pyridine and thionyl chloride to synthesize 2,6-bis(chloromethyl)pyridine were purchased from Acros Organics and EMD Millipore respectively. Anhydrous, $Ln(OTf)_3$, bis(cyclopentadienyliron dicarbonyl), and NaCp (0.1 mol in THF) were purchased from STREM. Anhydrous $Yb(OTf)_3$ was purchased from Millipore Sigma. All lanthanide triflate salts were dried under vacuum at 200 °C for 2 days prior to use. The complex bis(cyclopentadienylruthenium dicarbonyl) dimer was purchased from Sigma Aldrich. Samples used for magnetic characterization was crystalline material prepared by dissolving materials in minimal amounts of THF and placing in a freezer (-30 °C) overnight. All magnetic samples were prepared with an eicosane matrix in a high purity NMR tube which was flame sealed under vacuum. The eicosane (Acros Organics) was melted in a hot water bath (42 °C) and was dispersed homogeneously throughout the sample. Magnetic characterization of all compounds was obtained using a Quantum Design MPMS 3 SQUID magnetometer. Direct current (dc) measurements were acquired under an applied 1000 Oe field at a temperature range of 2-300 K. Alternating current (ac) measurements for the compounds were taken under various dc fields at temperature ranges of 10-2 K. Elemental analyses were carried out by Midwest Microlab. All IR spectra were obtained in the solid state in an argon filled glove box (Vigor) equipped with an Agilent CARY 630 FT-IR spectrometer (32 background scans, 32 scans @ 650-4000 cm^{-1}, Apodization: Happ-Genzel). Mössbauer spectra were collected on a model MS4 WRC low-field, variable temperature spectrometer (See Co., Edina, MN). Zero magnetic field spectra were obtained by removing the 500 G magnets from the exterior of the instrument. Temperatures were varied using a temperature controller on the heating coil on the sample holder. The instrument was calibrated using an α-Fe foil at room temperature. Obtained spectra were fitted using WMOSS software (See Co.).

5.2.2 Synthesis

Synthesis of $[(PyCp_2)Pr(\mu\text{-}OTf)]_2$ (5-1). Method of synthesis as previously reported by Paolucci et al. (2002).[79-80]

Synthesis of $[(PyCp_2)Nd(\mu\text{-}OTf)]_2$ (5-2). Method of synthesis as previously reported by to Paolucci et al. (2002).[79-80]

Synthesis of $[(PyCp_2)Sm(\mu\text{-}OTf)]_2$ (5-3). Method of synthesis as previously reported by Paolucci et al. (2002).[79-80]

Synthesis of $[(PyCp_2)Eu(\mu\text{-}OTf)]_2$ (5-4). To a solution of $Eu(OTf)_3$ (1.1983 g, 2.00 mmol) in 30 mL of THF, a solution of $(PyCp_2)Na_2$ (0.5460 g, 2.00 mmol) in 60 mL of THF was added dropwise and kept in a cold well at -30 °C. The reaction was occasionally stirred manually over 2 h and warmed to room temperature. After 2 d of stirring, the THF was removed and replaced with CH_2Cl_2 (30 mL) and left to stir overnight. The reaction was filtered and hexanes (50 mL) was slowly added to the filtrate and left overnight. Dark red crystals were collected and the remaining mother liquor was collected and solvent removed. This was redissolved in CH_2Cl_2, layered with hexanes, and placed in a freezer (-30 °C) overnight to collect more crystals. The total yield was 0.2482 g (23 %). Anal. Calcd. for $C_{36}H_{30}Eu_2F_6N_2O_6S_2 \cdot CH_2Cl_2$ (5-4): C, 38.52; H, 2.80; N, 2.43. Found. C, 39.32; H, 2.79; N, 2.34.

Synthesis of [(PyCp$_2$)Gd(μ-OTf)]$_2$ (5-5). The synthesis was carried out in a similar fashion as **5-4** using 1.2089 g (2.00 mmol) of $Gd(OTf)_3$ and 0.5640 g (2.00 mmol) of $(PyCp_2)Na_2$. The total yield was 0.3850 g (36 %). Anal. Calcd. for $C_{36}H_{30}Gd_2F_6N_2O_6S_2$ (5-5): C, 40.06; H, 2.80; N, 2.60. Found: C, 39.73; H, 2.78; N, 2.39.

Synthesis of [(PyCp$_2$)Tb(μ-OTf)]$_2$ (5-6). The synthesis was carried out in a similar fashion as **5-4** using 1.2122 g (2.00 mmol) of $Tb(OTf)_3$ and 0.5640 g (2.00 mmol) of $(PyCp_2)Na_2$. The desired product was isolated as pale yellow crystals in a 24% (0.2578 g) yield. Anal. Calcd. for $C_{36}H_{30}Tb_2F_6N_2O_6S_2$ (5-6): C, 39.94; H, 2.79; N, 2.59. Found: C, 39.57; H, 2.68; N, 2.32.

Synthesis of [(PyCp$_2$)Ho(μ-OTf)]$_2$ (5-7). The synthesis was carried out in a similar fashion as **5-4** using 1.2243 g (2.00 mmol) of $Ho(OTf)_3$ and 0.5640 g (2.00 mmol) of $(PyCp_2)Na_2$. The desired product was isolated as pale orange crystals in a 27% (0.3000 g) yield. Anal. Calcd. for $C_{36}H_{30}Ho_2F_6N_2O_6S_2 \cdot 2CH_2Cl_2$ (5-7): C, 36.15; H, 2.56; N, 2.22. Found: C, 36.18; H, 2.68; N, 2.09

Synthesis of [(PyCp$_2$)Er(μ-OTf)]$_2$ (5-8). The synthesis was carried out in a similar fashion as **5-4** using 1.2289 g (2.00 mmol) of $Er(OTf)_3$ and 0.5640 g (2.00 mmol) of

(PyCp$_2$)Na$_2$. The desired product was isolated as light pink crystals in a 16.2% (0.1780 g) yield. Anal. Calcd. for $C_{36}H_{30}Er_2F_6N_2O_6S_2{\bullet}CH_2Cl_2$ (5-8): C, 37.53; H, 2.72; N, 2.37. Found: C, 37.37; H, 2.59; N, 2.10.

Synthesis of [(PyCp$_2$)Tm(μ-OTf)]$_2$ (5-9). The synthesis was carried out in a similar fashion as **5-4** using 1.2323 g (2.00 mmol) of Tm(OTf)$_3$ and 0.5640 g (2.00 mmol) of (PyCp$_2$)Na$_2$. The desired product was isolated as pale yellow crystals in a 13% (0.1440 g) yield. Anal. Calcd. for $C_{36}H_{30}Tm_2F_6N_2O_6S_2{\cdot}CH_2Cl_2$ (5-9): C, 37.42; H, 2.72; N, 2.36. Found: C, 37.23; H, 2.72; N, 2.26.

Synthesis of [(PyCp$_2$)Yb(μ-OTf)]$_2$ (5-10). Method of synthesis as previously reported by Paolucci et al. (2002).[79-80]

Synthesis of [(PyCp$_2$)Lu(μ-OTf)]$_2$ (5-11). The synthesis was carried out in a similar fashion as **5-4** using 1.2443 g (2.00 mmol) of Lu(OTf)$_3$ and 0.5640 g (2.00 mmol) of (PyCp$_2$)Na$_2$. The desired product was isolated as pale yellow crystals in a 11% (0.1230 g) yield. Anal. Calcd. for $C_{36}H_{30}Lu_2F_6N_2O_6S_2{\bullet}CH_2Cl_2$ (5-9): C, 37.05; H, 2.69; N, 2.34. Found: C, 36.97; H, 2.70; N, 2.75.

Synthesis of (thf)PyCp$_2$Pr-FeCp(CO)$_2$ (5-12). A solution of KFp (18.1 mg, 84.0 μmol) in THF (2 mL) and a solution of [(PyCp$_2$)Pr(thf)(OTf)] (50.0 mg, 84.0 μmol) in THF (2 mL) were placed in a freezer for 1 hour at -30 °C. The solution of KFp was added dropwise to the solution of [(PyCp$_2$)Pr(thf)(OTf)] and placed in the freezer at -30 °C. Brownish yellow crystals suitable for X-Ray diffraction formed overnight and the solution was decanted off and crystals were dried. No yield was obtained. IR (solid, cm^{-1}) 1890

(ν_{CO}), 1814 (ν_{CO}), 1598, 1570, 1427, 1424, 1231, 1170, 886, 757 Anal. Calcd. for $C_{28}H_{28}PrFeNO_3$ (5-10) C, 53.95; H, 4.54; N, 2.24.

Synthesis of PyCp$_2$Nd-FeCp(CO)$_2$ (5-13). A solution (2 mL) of KFp (21.8 mg, 83 μmol) in THF was added dropwise to a 2 mL solution of [(PyCp$_2$)Nd(OTf)(thf)] (50.0 mg, 83 μmol) and the mixture was stirred for 5 min. An aliquot of solution was placed in a vial and this vial was added to a larger vial filled with toluene. Slow evaporation afforded yellow crystals of the desired complex. No yield was obtained due to the small amount of material produced.

Synthesis of (thf)PyCp$_2$Nd-FeCp(CO)$_2$ (5-14). The heterobimetallic complex was synthesized similarly to **5-10** using 68.2 mg (114 μmol) of [(PyCp$_2$)Pr(thf)(OTf)] and 24.6 mg (114 μmol) of KFp. The greenish yellow crystals were isolated in a 38.5 % (27.5 mg) yield. IR (solid, cm^{-1}) 1908 (ν_{CO}), 1838 (ν_{CO}), 1565, 1560, 1417, 1415, 1228, 1165, 833, 771 Anal. Calcd. for $C_{28}H_{28}NdFeNO_3$ (5-12) C, 53.67; H, 4.50; N, 2.24. Found: C, 52.75; H, 3.80; N, 2.17.

Synthesis of PyCp$_2$Sm-FeCp(CO)$_2$ (5-15). The heterobimetallic complex was synthesized similarly to **5-10** using 35.6 mg (58.9 μmol) of [(PyCp$_2$)Sm(thf)(OTf)] and 12.7 mg (58.9 μmol) of KFp. The red crystals were isolated in a 44.2 % (14.6 mg) yield. IR (solid, cm^{-1}) 1907 (ν_{CO}), 1836 (ν_{CO}), 1588, 1563, 1411, 1409, 1008, 833, 768 Anal. Calcd. For (5-15) $C_{24}H_{24}SmFeNO_2$ C, 51.42; H, 3.60; N, 2.50. Found: C, 50.63; H, 3.62; N, 2.57.

Synthesis of PyCp$_2$Gd-FeCp(CO)$_2$ (5-16). The heterobimetallic complex was synthesized similarly to **5-10** using 44.1 mg (57 μmol) of [(PyCp$_2$)Gd(thf)(OTf)] and 12.3

mg (57 μmol) of KFp. The yellow crystals were isolated in a 52.7 % (23.9 mg) yield. IR (solid, cm^{-1}) 1909 (ν_{CO}), 1840 (ν_{CO}), 1589, 1566, 1417, 1411, 1166, 1008, 786, 772 Anal. Calcd. for $C_{24}H_{24}GdFeNO_2$ (5-16) C, 50.79; H, 3.55; N, 2.47. Found: C, 50.55; H, 3.68; N, 2.50.

Synthesis of PyCp$_2$Tb-FeCp(CO)$_2$ (5-17). The heterobimetallic complex was synthesized similarly to **5-10** using 48.9 mg (80 μmol) of [(PyCp$_2$)Tb(thf)(OTf)] and 17.2 mg (80 μmol) of KFp. The yellow crystals were isolated in a 43.5 % (17.8 mg) yield. IR (solid, cm^{-1}) 1910 (ν_{CO}), 1836 (ν_{CO}), 1589, 1566, 1414, 1411, 1166, 1034, 1007, 841, 768 Anal. Calcd. for $C_{24}H_{24}TbFeNO_2$ (5-17) C, 50.64; H, 3.54; N, 2.46. Found: C, 49.90; H, 3.47; N, 2.68.

Synthesis of PyCp$_2$Ho-FeCp(CO)$_2$ (5-18). The heterobimetallic complex was synthesized similarly to **5-10** using 45.2 mg (73 μmol) of [(PyCp$_2$)Ho(thf)(OTf)] and 15.7 mg (73 μmol) of KFp. The yellow crystals were isolated in a 52.4 % (22.0 mg) yield. IR (solid, cm^{-1}) 1912 (ν_{CO}), 1831 (ν_{CO}), 1590, 1566, 1455, 1417, 1166, 1008, 844, 772 Anal. Calcd. for $C_{24}H_{24}HoFeNO_2$ (5-18) C, 50.12; H, 3.50; N, 2.44. Found: C, 49.68; H, 3.57; N, 2.39.

Synthesis of PyCp$_2$Er-FeCp(CO)$_2$ (5-19). The heterobimetallic complex was synthesized similarly to **5-10** using 30.0 mg (48 μmol) of [(PyCp$_2$)Er(thf)(OTf)] and 10.4 mg (73 μmol) of KFp. The yellow crystals were isolated in a 49.9 % (13.9 mg) yield. IR (solid, cm^{-1}) 1913 (ν_{CO}), 1833 (ν_{CO}), 1566, 1563, 1455, 1419, 1415, 1166, 1009, 774 Anal. Calcd. for $C_{24}H_{24}ErFeNO_2$ (5-19) C, 49.91; H, 3.49; N, 2.43. Found: C, 49.84; H, 3.43; N, 2.47.

Synthesis of PyCp$_2$Tm-FeCp(CO)$_2$ (5-20). The heterobimetallic complex was synthesized similarly to **5-10** using 31.1 mg (50 μmol) of [(PyCp$_2$)Tm(thf)(OTf)] and 10.8 mg (50 μmol) of KFp. The product was isolated as yellow crystals. No yield was obtained. Anal. Calcd. for $C_{24}H_{24}TmFeNO_2$ (5-20) C, 49.77; H, 3.48; N, 2.42. Found: C, 49.53; H, 3.53; N, 2.43.

Synthesis of PyCp$_2$Yb-FeCp(CO)$_2$ (5-21). The heterobimetallic complex was synthesized similarly to **5-10** using 63.8 mg (102 μmol) of [(PyCp$_2$)Yb(thf)(OTf)] and 22.0 mg (102 μmol) of KFp. The brown crystals were isolated in a 22.6 % (13.5 mg) yield. IR (solid, cm^{-1}) 1913 (ν_{CO}), 1841 (ν_{CO}), 1590, 1567, 1457, 1440, 1051, 1008, 860, 777 Anal. Calcd. for $C_{24}H_{24}YbFeNO_2$ (5-21) C, 49.42; H, 3.46; N, 2.40. Found: C, 48.42; H, 3.64; N, 2.47.

Synthesis of PyCp$_2$Lu-FeCp(CO)$_2$ (5-22). The heterobimetallic complex was synthesized similarly to **5-10** using 39.2 mg (62 μmol) of [(PyCp$_2$)Lu(thf)(OTf)] and 13.5 mg (62 μmol) of KFp. The yellow crystals were isolated in a 65.9 % (22.0 mg) yield. IR (solid, cm^{-1}) 1915 (ν_{CO}), 1833 (ν_{CO}), 1592, 1567, 1454, 1419, 1166, 1041, 1009, 860, 778 Anal. Calcd. for $C_{24}H_{24}LuFeNO_2$ (5-20) C, 49.26; H, 3.44; N, 2.39. Found: C, 49.32; H, 3.61; N, 2.20.

Synthesis of PyCp$_2$Nd-RuCp(CO)$_2$ (5-23). A solution (2 mL) of KRp (26.8 mg, 107 μmol) in THF was added dropwise to a 2 mL solution of [(PyCp$_2$)Nd(OTf)(thf)] (61.3 mg, 107 μmol) and the mixture was stirred for 5 min. An aliquot of solution was placed in a vial and this vial was added to a larger vial filled with toluene. Slow evaporation afforded light blue crystals of the desired complex. No yield was obtained due to the small amount of material produced.

Synthesis of PyCp$_2$Sm-RuCp(CO)$_2$ (5-24). The heterobimetallic complex was synthesized similarly to **5-10** using 40.7 mg (67.2 μmol) of [(PyCp$_2$)Sm(thf)(OTf)] and 17.6 mg (67.2 μmol) of KRp. The yellow crystals were isolated in a 74.8 % (30.5 mg) yield. IR (solid, cm^{-1}) 1930 (ν_{CO}), 1851 (ν_{CO}), 1590, 1566, 1477, 1411, 1165, 1007, 768 Anal. Calcd. for $C_{24}H_{24}SmRuNO_2$ (5-24) C, 47.58; H, 3.33; N, 2.31. Found: C, 47.49; H, 3.38; N, 2.30.

Synthesis of PyCp$_2$Gd-RuCp(CO)$_2$ (5-25). The heterobimetallic complex was synthesized similarly to **5-10** using 39.5 mg (64.6 μmol) of [(PyCp$_2$)Gd(thf)(OTf)] and 16.9 mg (64.6 μmol) of KRp. The colorless crystals were isolated in a 75.8 % (30.0 mg) yield. IR (solid, cm^{-1}) 1912 (ν_{CO}), 1831 (ν_{CO}), 1590, 1566, 1455, 1417, 1166, 1008, 844, 772 Anal. Calcd. for $C_{24}H_{24}GdRuNO_2$ (5-25) C, 47.04; H, 3.29; N, 2.29. Found: C, 46.95; H, 3.39; N, 2.36.

Synthesis of PyCp$_2$Tb-RuCp(CO)$_2$ (5-26). The heterobimetallic complex was synthesized similarly to **5-10** using 35.0 mg (57 μmol) of [(PyCp$_2$)Tb(thf)(OTf)] and 14.9 mg (57 μmol) of KRp. The colorless crystals were isolated in a 68.5 % (24.0 mg) yield. IR (solid, cm^{-1}) 1928 (ν_{CO}), 1847 (ν_{CO}), 1589, 1417, 1414, 1417, 1164, 1034 1007, 841, 769 Anal. Calcd. for $C_{24}H_{24}TbRuNO_2$ (5-26) C, 46.92; H, 3.28; N, 2.28. Found: C, 46.76; H, 3.26; N, 2.01.

Synthesis of PyCp$_2$Ho-RuCp(CO)$_2$ (5-27). The heterobimetallic complex was synthesized similarly to **5-10** using 38.9 mg (62 μmol) of [(PyCp$_2$)Ho(thf)(OTf)] and 16.3

mg (62 μmol) of KRp. The light pink crystals were isolated in an 81.9 % (31.9 mg) yield. IR (solid, cm^{-1}) 1933 (ν_{CO}), 1832 (ν_{CO}), 1590, 1566, 1455, 1417, 1412, 1008, 844, 772 Anal. Calcd. for $C_{24}H_{24}HoRuNO_2$ (5-27) C, 46.46; H, 3.25; N, 2.26. Found: C, 46.11; H, 3.25; N, 2.26.

Synthesis of PyCp$_2$Er-RuCp(CO)$_2$ (5-28). The heterobimetallic complex was synthesized similarly to **5-10** using 30.0 mg (48 μmol) of [(PyCp$_2$)Er(thf)(OTf)] and 12.6 mg (48 μmol) of KRp. The light pink crystals were isolated in a 77.7 % (23.4 mg) yield. IR (solid, cm^{-1}) 1912 (ν_{CO}), 1831 (ν_{CO}), 1590, 1566, 1455, 1417, 1166, 1008, 844, 772 Anal. Calcd. for $C_{24}H_{24}ErRuNO_2$ (5-28) C, 46.29; H, 3.24; N, 2.25. Found: C, 46.21; H, 3.58; N, 2.19.

Synthesis of PyCp$_2$Tm-RuCp(CO)$_2$ (5-29). The heterobimetallic complex was synthesized similarly to **5-10** using 31.0 mg (46 μmol) of [(PyCp$_2$)Tm(thf)(OTf)] and 12.0 mg (46 μmol) of KRp. The product was isolated as colorless crystals. No yield was obtained due to the small amount of material produced. Anal. Calcd. for $C_{24}H_{24}TmRuNO_2$ (5-29) C, 46.16; H, 3.23; N, 2.24. Found: C, 45.94; H, 3.33; N, 2.21.

Synthesis of PyCp$_2$Yb-RuCp(CO)$_2$ (5-30). The heterobimetallic complex was synthesized similarly to **5-10** using 66.3 mg (106 μmol) of [(PyCp$_2$)Yb(thf)(OTf)] and 27.6 mg (106 μmol) of KRp. The product was isolated as brown crystals in a 51.5% (34.2 mg) yield. IR (solid, cm^{-1}) 1912 (ν_{CO}), 1831 (ν_{CO}), 1590, 1566, 1455, 1417, 1166, 1008, 844, 772 Anal. Calcd. for $C_{24}H_{24}HoFeNO_2$ (5-30) C, 45.86; H, 3.21; N, 2.23. Found: C, 45.71; H, 3.50; N, 2.23.

Synthesis of $PyCp_2Lu$-$RuCp(CO)_2$ (5-31). The heterobimetallic complex was synthesized similarly to **5-10** using 37.1 mg (59 μmol) of [$(PyCp_2)Lu(thf)(OTf)$] and 15.4 mg (59 μmol) of KRp. The colorless crystals were isolated in a 73.2 % (27.2 mg) yield. IR (solid, cm^{-1}) 1934 (ν_{CO}), 1855 (ν_{CO}), 1567, 1417, 1414, 1166, 1009, 860, 776 Anal. Calcd. for $C_{24}H_{24}LuRuNO_2$ (5-31) C, 45.72; H, 3.20; N, 2.22. Found: C, 45.72; H, 3.30; N, 2.14.

5.2.3 X-Ray Crystallography

Compound 5-12. A Leica MZ 75 microscope was used to identify a suitable yellow block with very well-defined faces with dimensions (max, intermediate, and min) 0.158 x 0.152 x 0.143 mm^3 from a representative sample of crystals of the same habit. The crystal mounted on a nylon loop was then placed in a cold nitrogen stream (Oxford) maintained at 110 K.

A BRUKER Apex 2 Duo X-ray (three circle) diffractometer was employed for crystal screening, unit cell determination, and data collection. The goniometer was controlled using the APEX3 software suite.[81] The sample was optically centered with the aid of a video camera such that no translations were observed as the crystal was rotated through all positions. The X-ray radiation employed was generated from a Mo Sealed X-ray tube (K_α = 0.71073Å) with a potential of 40 kV and a current of 40 mA.

45 data frames were taken at widths of 1°. These reflections were used to determine the unit cell. The unit cell was verified by examination of the *h k l* overlays on several frames of data. No super-cell or erroneous reflections were observed.

After careful examination of the unit cell, an extended data collection procedure (3 sets) was initiated using omega and phi scans.

Integrated intensity information for each reflection was obtained by reduction of the data frames with the program APEX3.[81] The integration method employed a three-dimensional profiling algorithm and all data were corrected for Lorentz and polarization factors, as well as for crystal decay effects. Finally, the data was merged and scaled to produce a suitable data set. The absorption correction program SADABS[84] was employed to correct the data for absorption effects.

Systematic reflection conditions and statistical tests of the data suggested the space group *Pnma*. A solution was obtained readily (Z=4; Z'=0.5) using XT/XS in APEX3.[81,83] Hydrogen atoms were placed in idealized positions and were set riding on the respective parent atoms. All non-hydrogen atoms were refined with anisotropic thermal parameters. Absence of additional symmetry and voids were confirmed using PLATON (ADDSYM).[86] The structure was refined (weighted least squares refinement on F^2) to convergence.[83,87] Olex 2 was employed for the final data presentation and structure plots.[87]

Compound 5-13. A Leica MZ 75 microscope was used to identify a suitable yellow plate with very well-defined faces with dimensions (max, intermediate, and min) 0.142 x 0.134 x 0.054 mm^3 from a representative sample of crystals of the same habit. The crystal mounted on a nylon loop was then placed in a cold nitrogen stream (Oxford) maintained at 110 K.

A BRUKER Quest X-ray (fixed-Chi geometry) diffractometer with a PHOTON II detector was employed for crystal screening, unit cell determination, and data collection.

The goniometer was controlled using the APEX3 software suite.[81] The sample was optically centered with the aid of a video camera such that no translations were observed as the crystal was rotated through all positions. The X-ray radiation employed was generated from a Mo-Iμs X-ray tube (K_{α} = 0.71073Å).

45 data frames were taken at widths of 1°. These reflections were used to determine the unit cell. The unit cell was verified by examination of the *h k l* overlays on several frames of data. No super-cell or erroneous reflections were observed.

After careful examination of the unit cell, an extended data collection procedure (3 sets) was initiated using omega and phi scans.

Integrated intensity information for each reflection was obtained by reduction of the data frames with the program APEX3.[81] The integration method employed a three-dimensional profiling algorithm and all data were corrected for Lorentz and polarization factors, as well as for crystal decay effects. Finally, the data was merged and scaled to produce a suitable data set. The absorption correction program SADABS[84] was employed to correct the data for absorption effects.

Systematic reflection conditions and statistical tests of the data suggested the space group *Pnma*. A solution was obtained readily (Z=4; Z'=0.5) using XT/XS in APEX3.[81,83] Hydrogen atoms were placed in idealized positions and were set riding on the respective parent atoms. All non-hydrogen atoms were refined with anisotropic thermal parameters. Absence of additional symmetry and voids were confirmed using PLATON (ADDSYM).[86] The structure was refined (weighted least squares refinement on F^2) to convergence.[83,87] Olex 2 was employed for the final data presentation and structure plots.[87]

Compound 5-14. A Leica MZ 75 microscope was used to identify a suitable yellow plate with very well-defined faces with dimensions (max, intermediate, and min) 0.172 x 0.142 x 0.031 mm^3 from a representative sample of crystals of the same habit. The crystal mounted on a nylon loop was then placed in a cold nitrogen stream (Oxford) maintained at 110 K.

A BRUKER Quest X-ray (fixed-Chi geometry) diffractometer with a PHOTON II detector was employed for crystal screening, unit cell determination, and data collection. The goniometer was controlled using the APEX3 software suite.[81] The sample was optically centered with the aid of a video camera such that no translations were observed as the crystal was rotated through all positions. The X-ray radiation employed was generated from a Mo-Iμs X-ray tube (K_α = 0.71073Å).

45 data frames were taken at widths of 1°. These reflections were used to determine the unit cell. The unit cell was verified by examination of the *h k l* overlays on several frames of data. No super-cell or erroneous reflections were observed.

After careful examination of the unit cell, an extended data collection procedure (3 sets) was initiated using omega and phi scans.

Integrated intensity information for each reflection was obtained by reduction of the data frames with the program APEX3.[81] The integration method employed a three-dimensional profiling algorithm and all data were corrected for Lorentz and polarization factors, as well as for crystal decay effects. Finally, the data was merged and scaled to produce a suitable data set. The absorption correction program SADABS[84] was employed to correct the data for absorption effects.

Systematic reflection conditions and statistical tests of the data suggested the space group *Pnma*. A solution was obtained readily (Z=4; Z'=0.5) using XT/XS in APEX3.[81,83] Hydrogen atoms were placed in idealized positions and were set riding on the respective parent atoms. All non-hydrogen atoms were refined with anisotropic thermal parameters. Absence of additional symmetry and voids were confirmed using PLATON (ADDSYM).[86] The structure was refined (weighted least squares refinement on F^2) to convergence.[83,87] Olex 2 was employed for the final data presentation and structure plots.[87]

Compound 5-15. A Leica MZ 75 microscope was used to identify a reddish orange block with very well-defined faces with dimensions (max, intermediate, and min) 0.105 x 0.092 x 0.071 mm3 from a representative sample of crystals of the same habit. The crystal mounted on a nylon loop was then placed in a cold nitrogen stream (Oxford) maintained at 110 K.

A BRUKER APEX 2 Duo X-ray (three-circle) diffractometer was employed for crystal screening, unit cell determination, and data collection. The goniometer was controlled using the APEX3 software suite, v2017.3-0.[81] The sample was optically centered with the aid of a video camera such that no translations were observed as the crystal was rotated through all positions. The detector (Bruker - PHOTON) was set at 6.0 cm from the crystal sample. The X-ray radiation employed was generated from a Mo sealed X-ray tube (K_α = 0.71073Å with a potential of 40 kV and a current of 40 mA).

45 data frames were taken at widths of 1.0°. These reflections were used in the auto-indexing procedure to determine the unit cell. A suitable cell was found and refined by nonlinear least squares and Bravais lattice procedures. The unit cell was verified by

examination of the *h k l* overlays on several frames of data. No super-cell or erroneous reflections were observed.

After careful examination of the unit cell, an extended data collection procedure (4 sets) was initiated using omega and phi scans.

Integrated intensity information for each reflection was obtained by reduction of the data frames with the program APEX3.[81] The integration method employed a three-dimensional profiling algorithm and all data were corrected for Lorentz and polarization factors, as well as for crystal decay effects. Finally, the data was merged and scaled to produce a suitable data set. The absorption correction program SADABS[84] was employed to correct the data for absorption effects.

Systematic reflection conditions and statistical tests of the data suggested the space group *Pnma*. A solution was obtained readily (Z=4; Z'=0.5) using XT/XS in APEX2.[81,83] Hydrogen atoms were placed in idealized positions and were set riding on the respective parent atoms. All non-hydrogen atoms were refined with anisotropic thermal parameters. Absence of additional symmetry and voids were confirmed using PLATON (ADDSYM).[86] The structure was refined (weighted least squares refinement on F^2) to convergence.[83,87] Olex 2 was employed for the final data presentation and structure plots.[87]

Compound 5-16. A Leica MZ 75 microscope was used to identify a suitable yellow block with very well-defined faces with dimensions (max, intermediate, and min) 0.162 x 0.152 x 0.021 mm^3 from a representative sample of crystals of the same habit. The crystal mounted on a nylon loop was then placed in a cold nitrogen stream (Oxford) maintained at 110 K.

A BRUKER Quest X-ray (fixed-Chi geometry) diffractometer with a PHOTON II detector was employed for crystal screening, unit cell determination, and data collection. The goniometer was controlled using the APEX3 software suite.[81] The sample was optically centered with the aid of a video camera such that no translations were observed as the crystal was rotated through all positions. The X-ray radiation employed was generated from a Mo-Iμs X-ray tube (K_{α} = 0.71073Å).

45 data frames were taken at widths of 1°. These reflections were used to determine the unit cell. The unit cell was verified by examination of the *h k l* overlays on several frames of data. No super-cell or erroneous reflections were observed.

After careful examination of the unit cell, an extended data collection procedure (3 sets) was initiated using omega and phi scans.

Integrated intensity information for each reflection was obtained by reduction of the data frames with the program APEX3.[81] The integration method employed a three-dimensional profiling algorithm and all data were corrected for Lorentz and polarization factors, as well as for crystal decay effects. Finally, the data was merged and scaled to produce a suitable data set. The absorption correction program SADABS[84] was employed to correct the data for absorption effects.

Systematic reflection conditions and statistical tests of the data suggested the space group *Pnma*. A solution was obtained readily (Z=4; Z'=0.5) using XT/XS in APEX3.[81,83] Hydrogen atoms were placed in idealized positions and were set riding on the respective parent atoms. All non-hydrogen atoms were refined with anisotropic thermal parameters. Absence of additional symmetry and voids were confirmed using PLATON

(ADDSYM).[86] The structure was refined (weighted least squares refinement on F^2) to convergence.[83,87] Olex 2 was employed for the final data presentation and structure plots.[87]

Compound 5-17. A Leica MZ 75 microscope was used to identify a suitable yellow block with very well-defined faces with dimensions (max, intermediate, and min) 0.118 x 0.093 x 0.084 mm3 from a representative sample of crystals of the same habit. The crystal mounted on a nylon loop was then placed in a cold nitrogen stream (Oxford) maintained at 110 K.

A BRUKER APEX 2 Duo X-ray (three-circle) diffractometer was employed for crystal screening, unit cell determination, and data collection. The goniometer was controlled using the APEX2 software suite, v2008-6.0.[81] The sample was optically centered with the aid of a video camera such that no translations were observed as the crystal was rotated through all positions. The detector was set at 6.0 cm from the crystal sample (APEX2, 512x512 pixel). The X-ray radiation employed was generated from a Mo sealed X-ray tube (K_α = 0.70173Å with a potential of 40 kV and a current of 40 mA).

45 data frames were taken at widths of 1.0°. These reflections were used in the auto-indexing procedure to determine the unit cell. A suitable cell was found and refined by nonlinear least squares and Bravais lattice procedures. The unit cell was verified by examination of the *h k l* overlays on several frames of data. No super-cell or erroneous reflections were observed.

After careful examination of the unit cell, an extended data collection procedure (3 sets) was initiated using omega and phi scans.

Integrated intensity information for each reflection was obtained by reduction of the data frames with the program APEX2.[81] The integration method employed a three-dimensional profiling algorithm and all data were corrected for Lorentz and polarization factors, as well as for crystal decay effects. Finally, the data was merged and scaled to produce a suitable data set. The absorption correction program SADABS[84] was employed to correct the data for absorption effects.

Systematic reflection conditions and statistical tests of the data suggested the space group *Pnma*. A solution was obtained readily (Z=4, Z'=0.5) using XT/XS in APEX2.[81,83] Hydrogen atoms were placed in idealized positions and were set riding on the respective parent atoms. All non-hydrogen atoms were refined with anisotropic thermal parameters. Absence of additional symmetry and voids were confirmed using PLATON (ADDSYM).[86] The structure was refined (weighted least squares refinement on F^2) to convergence.[83,87] Olex 2 was employed for the final data presentation and structure plots.[87]

Compound 5-18. A Leica MZ 75 microscope was used to identify a yellow block with very well-defined faces with dimensions (max, intermediate, and min) 0.183 x 0.107 x 0.062 mm3 from a representative sample of crystals of the same habit. The crystal mounted on a nylon loop was then placed in a cold nitrogen stream (Oxford) maintained at 110 K.

A BRUKER APEX 2 Duo X-ray (three-circle) diffractometer was employed for crystal screening, unit cell determination, and data collection. The goniometer was controlled using the APEX3 software suite, v2017.3-0.[81] The sample was optically centered with the aid of a video camera such that no translations were observed as the crystal was rotated through all positions. The detector (Bruker - PHOTON) was set at 6.0 cm from the crystal sample. The X-ray radiation employed was generated from a Mo sealed X-ray tube (K_α = 0.71073Å with a potential of 40 kV and a current of 40 mA).

45 data frames were taken at widths of 1.0°. These reflections were used in the auto-indexing procedure to determine the unit cell. A suitable cell was found and refined by nonlinear least squares and Bravais lattice procedures. The unit cell was verified by examination of the *h k l* overlays on several frames of data. No super-cell or erroneous reflections were observed.

After careful examination of the unit cell, an extended data collection procedure (4 sets) was initiated using omega and phi scans.

Integrated intensity information for each reflection was obtained by reduction of the data frames with the program APEX3.[81] The integration method employed a three-dimensional profiling algorithm and all data were corrected for Lorentz and polarization factors, as well as for crystal decay effects. Finally, the data was merged and scaled to produce a suitable data set. The absorption correction program SADABS[84] was employed to correct the data for absorption effects.

Systematic reflection conditions and statistical tests of the data suggested the space group *Pnma*. A solution was obtained readily (Z=4; Z'=0.5) using XT/XS in APEX2.[81,83] Hydrogen atoms were placed in idealized positions and were set riding on the respective parent atoms. All non-hydrogen atoms were refined with anisotropic thermal parameters. Absence of additional symmetry and voids were confirmed using PLATON

(ADDSYM).[86] The structure was refined (weighted least squares refinement on F^2) to convergence.[83,87] Olex 2 was employed for the final data presentation and structure plots.[87]

Compound 5-19. A Leica MZ 75 microscope was used to identify a yellow block with very well-defined faces with dimensions (max, intermediate, and min) 0.085 x 0.043 x 0.038 mm3 from a representative sample of crystals of the same habit. The crystal mounted on a nylon loop was then placed in a cold nitrogen stream (Oxford) maintained at 110 K.

A BRUKER APEX 2 Duo X-ray (three-circle) diffractometer was employed for crystal screening, unit cell determination, and data collection. The goniometer was controlled using the APEX3 software suite, v2017.3-0.[81] The sample was optically centered with the aid of a video camera such that no translations were observed as the crystal was rotated through all positions. The detector (Bruker - PHOTON) was set at 6.0 cm from the crystal sample. The X-ray radiation employed was generated from a Mo sealed X-ray tube (K_α = 0.71073Å with a potential of 40 kV and a current of 40 mA).

45 data frames were taken at widths of 1.0°. These reflections were used in the auto-indexing procedure to determine the unit cell. A suitable cell was found and refined by nonlinear least squares and Bravais lattice procedures. The unit cell was verified by examination of the *h k l* overlays on several frames of data. No super-cell or erroneous reflections were observed.

After careful examination of the unit cell, an extended data collection procedure (3 sets) was initiated using omega and phi scans.

Integrated intensity information for each reflection was obtained by reduction of the data frames with the program APEX3.[81] The integration method employed a three-dimensional profiling algorithm and all data were corrected for Lorentz and polarization factors, as well as for crystal decay effects. Finally, the data was merged and scaled to produce a suitable data set. The absorption correction program SADABS[84] was employed to correct the data for absorption effects.

Systematic reflection conditions and statistical tests of the data suggested the space group *Pnma*. A solution was obtained readily (Z=4; Z'=0.5) using XT/XS in APEX2.[81,83] Hydrogen atoms were placed in idealized positions and were set riding on the respective parent atoms. All non-hydrogen atoms were refined with anisotropic thermal parameters. Absence of additional symmetry and voids were confirmed using PLATON (ADDSYM).[86] The structure was refined (weighted least squares refinement on F^2) to convergence.[83,87] Olex 2 was employed for the final data presentation and structure plots.[87]

Compound 5-20. A Leica MZ 75 microscope was used to identify a suitable colorless block with very well-defined faces with dimensions (max, intermediate, and min) 0.182 x 0.164 x 0.16 mm3 from a representative sample of crystals of the same habit. The crystal mounted on a nylon loop was then placed in a cold nitrogen stream (Oxford) maintained at 110 K.

A BRUKER APEX 2 Duo X-ray (three-circle) diffractometer was employed for crystal screening, unit cell determination, and data collection. The goniometer was controlled using the APEX3 software suite, v2017.3-0.[81] The sample was optically centered with the aid of a video camera such that no translations were observed as the crystal was rotated through all positions. The detector (Bruker - PHOTON) was set at 6.0 cm from the crystal sample. The X-ray radiation employed was generated from a Mo sealed X-ray tube (K_α = 0.71073Å with a potential of 40 kV and a current of 40 mA).

45 data frames were taken at widths of 1.0°. These reflections were used in the auto-indexing procedure to determine the unit cell. A suitable cell was found and refined by nonlinear least squares and Bravais lattice procedures. The unit cell was verified by examination of the *h k l* overlays on several frames of data. No super-cell or erroneous reflections were observed.

After careful examination of the unit cell, an extended data collection procedure (4 sets) was initiated using omega and phi scans.

Integrated intensity information for each reflection was obtained by reduction of the data frames with the program APEX3.[81] The integration method employed a three-dimensional profiling algorithm and all data were corrected for Lorentz and polarization factors, as well as for crystal decay effects. Finally, the data was merged and scaled to produce a suitable data set. The absorption correction program SADABS[84] was employed to correct the data for absorption effects. Systematic reflection conditions and statistical tests of the data suggested the space goup $P2_1/n$. A solution was obtained readily (Z=4; Z'=0.5) using XT/XS in APEX3.[81,83] Hydrogen atoms were placed in idealized positions and were set riding on the respective parent atoms. All non-hydrogen atoms were refined with anisotropic thermal parameters. Absence of additional symmetry and voids were confirmed using PLATON (ADDSYM).[86] The structure was refined (weighted least squares refinement on F^2) to convergence.[83,87] Olex 2 was employed for the final data presentation and structure plots.[87]

Compound 5-21. A Leica MZ 75 microscope was used to identify a suitable brown block with very well-defined faces with dimensions (max, intermediate, and min) 0.072 x 0.064 x 0.038 mm3 from a representative sample of crystals of the same habit. The crystal mounted on a nylon loop was then placed in a cold nitrogen stream (Oxford) maintained at 110 K.

A BRUKER Quest X-ray (fixed-Chi geometry) diffractometer with a PHOTON II detector was employed for crystal screening, unit cell determination, and data collection. The goniometer was controlled using the APEX3 software suite.[81] The sample was optically centered with the aid of a video camera such that no translations were observed as the crystal was rotated through all positions. The X-ray radiation employed was generated from a Mo-Iμs X-ray tube (K_α = 0.71073Å).

45 data frames were taken at widths of 1°. These reflections were used to determine the unit cell. The unit cell was verified by examination of the *h k l* overlays on several frames of data. No super-cell or erroneous reflections were observed.

After careful examination of the unit cell, an extended data collection procedure (3 sets) was initiated using omega and phi scans.

Integrated intensity information for each reflection was obtained by reduction of the data frames with the program APEX3.[81] The integration method employed a three-dimensional profiling algorithm and all data were corrected for Lorentz and polarization factors, as well as for crystal decay effects. Finally, the data was merged and scaled to produce a suitable data set. The absorption correction program SADABS[84] was employed to correct the data for absorption effects.

Systematic reflection conditions and statistical tests of the data suggested the space group *Pnma*. A solution was obtained readily (Z=4; Z'=0.5) using XT/XS in APEX3.[81,83] Hydrogen atoms were placed in idealized positions and were set riding on the respective parent atoms. All non-hydrogen atoms were refined with anisotropic thermal parameters. Absence of additional symmetry and voids were confirmed using PLATON (ADDSYM).[86] The structure was refined (weighted least squares refinement on F^2) to convergence.[83,87] Olex 2 was employed for the final data presentation and structure plots.[87]

Compound 5-22. A Leica MZ 75 microscope was used to identify a suitable yellow block with very well-defined faces with dimensions (max, intermediate, and min) 0.172 x 0.144 x 0.072 mm3 from a representative sample of crystals of the same habit. The crystal mounted on a nylon loop was then placed in a cold nitrogen stream (Oxford) maintained at 110 K.

A BRUKER APEX 2 Duo X-ray (three-circle) diffractometer was employed for crystal screening, unit cell determination, and data collection. The goniometer was controlled using the APEX2 software suite, v2008-6.0.[81] The sample was optically centered with the aid of a video camera such that no translations were observed as the crystal was rotated through all positions. The detector was set at 6.0 cm from the crystal sample (APEX2, 512x512 pixel). The X-ray radiation employed was generated from a Mo sealed X-ray tube (K_α = 0.70173Å with a potential of 40 kV and a current of 40 mA).

45 data frames were taken at widths of 1.0°. These reflections were used in the auto-indexing procedure to determine the unit cell. A suitable cell was found and refined by nonlinear least squares and Bravais lattice procedures. The unit cell was verified by examination of the *h k l* overlays on several frames of data. No super-cell or erroneous reflections were observed.

After careful examination of the unit cell, an extended data collection procedure (4 sets) was initiated using omega and phi scans.

Integrated intensity information for each reflection was obtained by reduction of the data frames with the program APEX2.[81] The integration method employed a three-dimensional profiling algorithm and all data were corrected for Lorentz and polarization factors, as well as for crystal decay effects. Finally, the data was merged and scaled to produce a suitable data set. The absorption correction program SADABS[84] was employed to correct the data for absorption effects.

Systematic reflection conditions and statistical tests of the data suggested the space group *Pnma*. A solution was obtained readily (Z=4, Z'=0.5) using XT/XS in APEX2.[81,83] Hydrogen atoms were placed in idealized positions and were set riding on the respective parent atoms. All non-hydrogen atoms were refined with anisotropic thermal parameters. Absence of additional symmetry and voids were confirmed using PLATON (ADDSYM).[86] The structure was refined (weighted least squares refinement on F^2) to convergence.[83,87] Olex 2 was employed for the final data presentation and structure plots.[87]

Compound 5-23. A Leica MZ 75 microscope was used to identify a suitable colorless plate with very well-defined faces with dimensions (max, intermediate, and min) 0.212 x

0.146 x 0.065 mm^3 from a representative sample of crystals of the same habit. The crystal mounted on a nylon loop was then placed in a cold nitrogen stream (Oxford) maintained at 110 K.

A BRUKER APEX 2 Duo X-ray (three-circle) diffractometer was employed for crystal screening, unit cell determination, and data collection. The goniometer was controlled using the APEX2 software suite, v2008-6.0.[81] The sample was optically centered with the aid of a video camera such that no translations were observed as the crystal was rotated through all positions. The detector was set at 6.0 cm from the crystal sample (APEX2, 512x512 pixel). The X-ray radiation employed was generated from a Mo sealed X-ray tube (K_α = 0.70173Å with a potential of 40 kV and a current of 40 mA).

45 data frames were taken at widths of 1.0°. These reflections were used in the auto-indexing procedure to determine the unit cell. A suitable cell was found and refined by nonlinear least squares and Bravais lattice procedures. The unit cell was verified by examination of the *h k l* overlays on several frames of data. No super-cell or erroneous reflections were observed.

After careful examination of the unit cell, an extended data collection procedure (4 sets) was initiated using omega and phi scans.

Integrated intensity information for each reflection was obtained by reduction of the data frames with the program APEX2.[81] The integration method employed a three-dimensional profiling algorithm and all data were corrected for Lorentz and polarization factors, as well as for crystal decay effects. Finally, the data was merged and scaled to produce a suitable data set. The absorption correction program SADABS[84] was employed to correct the data for absorption effects.

Systematic reflection conditions and statistical tests of the data suggested the space group *Pnma*. A solution was obtained readily (Z=4, Z'=0.5) using XT/XS in APEX2.[81,83] Hydrogen atoms were placed in idealized positions and were set riding on the respective parent atoms. All non-hydrogen atoms were refined with anisotropic thermal parameters. Absence of additional symmetry and voids were confirmed using PLATON (ADDSYM).[86] The structure was refined (weighted least squares refinement on F^2) to convergence.[83,87] Olex 2 was employed for the final data presentation and structure plots.[87]

Compound 5-24. A Leica MZ 75 microscope was used to identify a yellow block with very well-defined faces with dimensions (max, intermediate, and min) 0.247 x 0.104 x 0.082 mm^3 from a representative sample of crystals of the same habit. The crystal mounted on a nylon loop was then placed in a cold nitrogen stream (Oxford) maintained at 110 K.

A BRUKER APEX 2 Duo X-ray (three-circle) diffractometer was employed for crystal screening, unit cell determination, and data collection. The goniometer was controlled using the APEX3 software suite, v2017.3-0.[81] The sample was optically centered with the aid of a video camera such that no translations were observed as the crystal was rotated through all positions. The detector (Bruker - PHOTON) was set at 6.0 cm from the crystal sample. The X-ray radiation employed was generated from a Mo sealed X-ray tube (K_α = 0.71073Å with a potential of 40 kV and a current of 40 mA).

45 data frames were taken at widths of 1.0°. These reflections were used in the auto-indexing procedure to determine the unit cell. A suitable cell was found and refined by

nonlinear least squares and Bravais lattice procedures. The unit cell was verified by examination of the *h k l* overlays on several frames of data. No super-cell or erroneous reflections were observed.

After careful examination of the unit cell, an extended data collection procedure (5 sets) was initiated using omega and phi scans.

Integrated intensity information for each reflection was obtained by reduction of the data frames with the program APEX3.[81] The integration method employed a three-dimensional profiling algorithm and all data were corrected for Lorentz and polarization factors, as well as for crystal decay effects. Finally, the data was merged and scaled to produce a suitable data set. The absorption correction program SADABS[84] was employed to correct the data for absorption effects.

Systematic reflection conditions and statistical tests of the data suggested the space group *Pnma*. A solution was obtained readily (Z=4; Z'=0.5) using XT/XS in APEX2.[81,83] Hydrogen atoms were placed in idealized positions and were set riding on the respective parent atoms. All non-hydrogen atoms were refined with anisotropic thermal parameters. Absence of additional symmetry and voids were confirmed using PLATON (ADDSYM).[86] The structure was refined (weighted least squares refinement on F^2) to convergence.[83,87] Olex 2 was employed for the final data presentation and structure plots.[87]

Compound 5.25 A Leica MZ 75 microscope was used to identify a suitable colorless block with very well-defined faces with dimensions (max, intermediate, and min) 0.118 x 0.093 x 0.084 mm^3 from a representative sample of crystals of the same habit. The crystal mounted on a nylon loop was then placed in a cold nitrogen stream (Oxford) maintained at 110 K.

A BRUKER APEX 2 Duo X-ray (three-circle) diffractometer was employed for crystal screening, unit cell determination, and data collection. The goniometer was controlled using the APEX2 software suite, v2008-6.0.[81] The sample was optically centered with the aid of a video camera such that no translations were observed as the crystal was rotated through all positions. The detector was set at 6.0 cm from the crystal sample (APEX2, 512x512 pixel). The X-ray radiation employed was generated from a Mo sealed X-ray tube (K_α = 0.70173Å with a potential of 40 kV and a current of 40 mA).

45 data frames were taken at widths of 1.0°. These reflections were used in the auto-indexing procedure to determine the unit cell. A suitable cell was found and refined by nonlinear least squares and Bravais lattice procedures. The unit cell was verified by examination of the *h k l* overlays on several frames of data. No super-cell or erroneous reflections were observed.

After careful examination of the unit cell, an extended data collection procedure (4 sets) was initiated using omega and phi scans.

Integrated intensity information for each reflection was obtained by reduction of the data frames with the program APEX2.[81] The integration method employed a three-dimensional profiling algorithm and all data were corrected for Lorentz and polarization factors, as well as for crystal decay effects. Finally, the data was merged and scaled to produce a suitable data set. The absorption correction program SADABS[84] was employed to correct the data for absorption effects.

Systematic reflection conditions and statistical tests of the data suggested the space group *Pnma*. A solution was obtained readily (Z=4, Z'=0.5) using XT/XS in APEX2.[81,83] Hydrogen atoms were placed in idealized positions and were set riding on the respective parent atoms. All non-hydrogen atoms were refined with anisotropic thermal parameters. Absence of additional symmetry and voids were confirmed using PLATON (ADDSYM).[86] The structure was refined (weighted least squares refinement on F^2) to convergence.[83,87] Olex 2 was employed for the final data presentation and structure plots.[87]

Compound 5.26. A Leica MZ 75 microscope was used to identify a suitable pink block with very well-defined faces with dimensions (max, intermediate, and min) 0.372 x 0.246 x 0.087 mm^3 from a representative sample of crystals of the same habit. The crystal mounted on a nylon loop was then placed in a cold nitrogen stream (Oxford) maintained at 110 K.

A BRUKER APEX 2 Duo X-ray (three-circle) diffractometer was employed for crystal screening, unit cell determination, and data collection. The goniometer was controlled using the APEX2 software suite, v2008-6.0.[81] The sample was optically centered with the aid of a video camera such that no translations were observed as the crystal was rotated through all positions. The detector was set at 6.0 cm from the crystal sample (APEX2, 512x512 pixel). The X-ray radiation employed was generated from a Mo sealed X-ray tube (K_α = 0.70173Å with a potential of 40 kV and a current of 40 mA).

45 data frames were taken at widths of 1.0°. These reflections were used in the auto-indexing procedure to determine the unit cell. A suitable cell was found and refined by nonlinear least squares and Bravais lattice procedures. The unit cell was verified by

examination of the *h k l* overlays on several frames of data. No super-cell or erroneous reflections were observed.

After careful examination of the unit cell, an extended data collection procedure (4 sets) was initiated using omega and phi scans.

Integrated intensity information for each reflection was obtained by reduction of the data frames with the program APEX2.[81] The integration method employed a three-dimensional profiling algorithm and all data were corrected for Lorentz and polarization factors, as well as for crystal decay effects. Finally, the data was merged and scaled to produce a suitable data set. The absorption correction program SADABS[84] was employed to correct the data for absorption effects.

Systematic reflection conditions and statistical tests of the data suggested the space group *Pnma*. A solution was obtained readily (Z=4, Z'=0.5) using XT/XS in APEX2.[81,83] Hydrogen atoms were placed in idealized positions and were set riding on the respective parent atoms. All non-hydrogen atoms were refined with anisotropic thermal parameters. Absence of additional symmetry and voids were confirmed using PLATON (ADDSYM).[86] The structure was refined (weighted least squares refinement on F^2) to convergence.[83,87] Olex 2 was employed for the final data presentation and structure plots.[87]

Compound 5-27. A Leica MZ 75 microscope was used to identify a suitable colorless plate with very well-defined faces with dimensions (max, intermediate, and min) 0.212 x 0.146 x 0.065 mm^3 from a representative sample of crystals of the same habit. The crystal mounted on a nylon loop was then placed in a cold nitrogen stream (Oxford) maintained at 110 K.

A BRUKER APEX 2 Duo X-ray (three-circle) diffractometer was employed for crystal screening, unit cell determination, and data collection. The goniometer was controlled using the APEX2 software suite, v2008-6.0.[81] The sample was optically centered with the aid of a video camera such that no translations were observed as the crystal was rotated through all positions. The detector was set at 6.0 cm from the crystal sample (APEX2, 512x512 pixel). The X-ray radiation employed was generated from a Mo sealed X-ray tube (K_α = 0.70173Å with a potential of 40 kV and a current of 40 mA).

45 data frames were taken at widths of 1.0°. These reflections were used in the auto-indexing procedure to determine the unit cell. A suitable cell was found and refined by nonlinear least squares and Bravais lattice procedures. The unit cell was verified by examination of the *h k l* overlays on several frames of data. No super-cell or erroneous reflections were observed.

After careful examination of the unit cell, an extended data collection procedure (4 sets) was initiated using omega and phi scans.

Integrated intensity information for each reflection was obtained by reduction of the data frames with the program APEX2.[81] The integration method employed a three-dimensional profiling algorithm and all data were corrected for Lorentz and polarization factors, as well as for crystal decay effects. Finally, the data was merged and scaled to produce a suitable data set. The absorption correction program SADABS[84] was employed to correct the data for absorption effects.

Systematic reflection conditions and statistical tests of the data suggested the space group *Pnma*. A solution was obtained readily (Z=4, Z'=0.5) using XT/XS in APEX2.[81,83]

Hydrogen atoms were placed in idealized positions and were set riding on the respective parent atoms. All non-hydrogen atoms were refined with anisotropic thermal parameters. Absence of additional symmetry and voids were confirmed using PLATON (ADDSYM).[86] The structure was refined (weighted least squares refinement on F^2) to convergence.[83,87] Olex 2 was employed for the final data presentation and structure plots.[87]

Compound 5-28. A Leica MZ 75 microscope was used to identify a suitable pink block with very well-defined faces with dimensions (max, intermediate, and min) 0.342 x 0.286 x 0.064 mm^3 from a representative sample of crystals of the same habit. The crystal mounted on a nylon loop was then placed in a cold nitrogen stream (Oxford) maintained at 110 K.

A BRUKER APEX 2 Duo X-ray (three-circle) diffractometer was employed for crystal screening, unit cell determination, and data collection. The goniometer was controlled using the APEX2 software suite, v2008-6.0.[81] The sample was optically centered with the aid of a video camera such that no translations were observed as the crystal was rotated through all positions. The detector was set at 6.0 cm from the crystal sample (APEX2, 512x512 pixel). The X-ray radiation employed was generated from a Mo sealed X-ray tube (K_α = 0.70173Å with a potential of 40 kV and a current of 40 mA).

45 data frames were taken at widths of 1.0°. These reflections were used in the auto-indexing procedure to determine the unit cell. A suitable cell was found and refined by nonlinear least squares and Bravais lattice procedures. The unit cell was verified by examination of the *h k l* overlays on several frames of data. No super-cell or erroneous reflections were observed.

After careful examination of the unit cell, an extended data collection procedure (4 sets) was initiated using omega and phi scans.

Integrated intensity information for each reflection was obtained by reduction of the data frames with the program APEX2.[81] The integration method employed a three-dimensional profiling algorithm and all data were corrected for Lorentz and polarization factors, as well as for crystal decay effects. Finally, the data was merged and scaled to produce a suitable data set. The absorption correction program SADABS[84] was employed to correct the data for absorption effects.

Systematic reflection conditions and statistical tests of the data suggested the space group *Pnma*. A solution was obtained readily (Z=4, Z'=0.5) using XT/XS in APEX2.[81,83] Hydrogen atoms were placed in idealized positions and were set riding on the respective parent atoms. All non-hydrogen atoms were refined with anisotropic thermal parameters. Absence of additional symmetry and voids were confirmed using PLATON (ADDSYM).[86] The structure was refined (weighted least squares refinement on F^2) to convergence.[83,87] Olex 2 was employed for the final data presentation and structure plots.[87]

Compound 5-29. A Leica MZ 75 microscope was used to identify a suitable reddish, colorless block with very well-defined faces with dimensions (max, intermediate, and min) 0.249 x 0.218 x 0.153 mm^3 from a representative sample of crystals of the same habit. The crystal mounted on a nylon loop was then placed in a cold nitrogen stream (Oxford) maintained at 110 K.

A BRUKER APEX 2 Duo X-ray (three-circle) diffractometer was employed for crystal screening, unit cell determination, and data collection. The goniometer was controlled using the APEX2 software suite, v2008-6.0.[81] The sample was optically centered with the aid of a video camera such that no translations were observed as the crystal was rotated through all positions. The detector was set at 6.0 cm from the crystal sample (APEX2, 512x512 pixel). The X-ray radiation employed was generated from a Mo sealed X-ray tube (K_α = 0.70173Å with a potential of 40 kV and a current of 40 mA).

45 data frames were taken at widths of 1.0°. These reflections were used in the auto-indexing procedure to determine the unit cell. A suitable cell was found and refined by nonlinear least squares and Bravais lattice procedures. The unit cell was verified by examination of the *h k l* overlays on several frames of data. No super-cell or erroneous reflections were observed.

After careful examination of the unit cell, an extended data collection procedure (4 sets) was initiated using omega and phi scans.

Integrated intensity information for each reflection was obtained by reduction of the data frames with the program APEX2.[81] The integration method employed a three-dimensional profiling algorithm and all data were corrected for Lorentz and polarization factors, as well as for crystal decay effects. Finally, the data was merged and scaled to produce a suitable data set. The absorption correction program SADABS[84] was employed to correct the data for absorption effects.

Systematic reflection conditions and statistical tests of the data suggested the space group *Pnma*. A solution was obtained readily (Z=4, Z'=0.5) using XT/XS in APEX2.[81,83] Hydrogen atoms were placed in idealized positions and were set riding on the respective parent atoms. All non-hydrogen atoms were refined with anisotropic thermal parameters.

Absence of additional symmetry and voids were confirmed using PLATON (ADDSYM).[86] The structure was refined (weighted least squares refinement on F^2) to convergence.[83,87] Olex 2 was employed for the final data presentation and structure plots.[87]

Compound 5-30. A Leica MZ 75 microscope was used to identify a suitable brown plate with very well-defined faces with dimensions (max, intermediate, and min) 0.281 x 0.217 x 0.105 mm^3 from a representative sample of crystals of the same habit. The crystal mounted on a nylon loop was then placed in a cold nitrogen stream (Oxford) maintained at 110 K.

A BRUKER APEX 2 Duo X-ray (three-circle) diffractometer was employed for crystal screening, unit cell determination, and data collection. The goniometer was controlled using the APEX2 software suite, v2008-6.0.[81] The sample was optically centered with the aid of a video camera such that no translations were observed as the crystal was rotated through all positions. The detector was set at 6.0 cm from the crystal sample (APEX2, 512x512 pixel). The X-ray radiation employed was generated from a Mo sealed X-ray tube (K_α = 0.70173Å with a potential of 40 kV and a current of 40 mA).

45 data frames were taken at widths of 1.0°. These reflections were used in the auto-indexing procedure to determine the unit cell. A suitable cell was found and refined by nonlinear least squares and Bravais lattice procedures. The unit cell was verified by examination of the *h k l* overlays on several frames of data. No super-cell or erroneous reflections were observed.

After careful examination of the unit cell, an extended data collection procedure (4 sets) was initiated using omega and phi scans.

Integrated intensity information for each reflection was obtained by reduction of the data frames with the program APEX2.[81] The integration method employed a three-dimensional profiling algorithm and all data were corrected for Lorentz and polarization factors, as well as for crystal decay effects. Finally, the data was merged and scaled to produce a suitable data set. The absorption correction program SADABS[84] was employed to correct the data for absorption effects.

Systematic reflection conditions and statistical tests of the data suggested the space group *Pnma*. A solution was obtained readily (Z=4, Z'=0.5) using XT/XS in APEX2.[81,83] Hydrogen atoms were placed in idealized positions and were set riding on the respective parent atoms. All non-hydrogen atoms were refined with anisotropic thermal parameters. Absence of additional symmetry and voids were confirmed using PLATON (ADDSYM).[86] The structure was refined (weighted least squares refinement on F^2) to convergence.[83,87] Olex 2 was employed for the final data presentation and structure plots.[87]

Compound 5-31. A Leica MZ 75 microscope was used to identify a suitable colorless block with very well-defined faces with dimensions (max, intermediate, and min) 0.212 x 0.205 x 0.072 mm3 from a representative sample of crystals of the same habit. The crystal mounted on a nylon loop was then placed in a cold nitrogen stream (Oxford) maintained at 110 K.

A BRUKER APEX 2 Duo X-ray (three-circle) diffractometer was employed for crystal screening, unit cell determination, and data collection. The goniometer was controlled using the APEX2 software suite, v2008-6.0.[81] The sample was optically centered with the aid of a video camera such that no translations were observed as the crystal was rotated through all positions. The detector was set at 6.0 cm from the crystal sample (APEX2, 512x512 pixel). The X-ray radiation employed was generated from a Mo sealed X-ray tube (K_α = 0.70173Å with a potential of 40 kV and a current of 40 mA).

45 data frames were taken at widths of 1.0°. These reflections were used in the auto-indexing procedure to determine the unit cell. A suitable cell was found and refined by nonlinear least squares and Bravais lattice procedures. The unit cell was verified by examination of the *h k l* overlays on several frames of data. No super-cell or erroneous reflections were observed.

After careful examination of the unit cell, an extended data collection procedure (4 sets) was initiated using omega and phi scans.

Integrated intensity information for each reflection was obtained by reduction of the data frames with the program APEX2.[81] The integration method employed a three-dimensional profiling algorithm and all data were corrected for Lorentz and polarization factors, as well as for crystal decay effects. Finally, the data was merged and scaled to produce a suitable data set. The absorption correction program SADABS[84] was employed to correct the data for absorption effects.

Systematic reflection conditions and statistical tests of the data suggested the space group *Pnma*. A solution was obtained readily (Z=4, Z'=0.5) using XT/XS in APEX2.[81,83] Hydrogen atoms were placed in idealized positions and were set riding on the respective parent atoms. All non-hydrogen atoms were refined with anisotropic thermal parameters. Absence of additional symmetry and voids were confirmed using PLATON

(ADDSYM).[86] The structure was refined (weighted least squares refinement on F^2) to convergence.[83,87] Olex 2 was employed for the final data presentation and structure plots.[87]

5.3 Results & Discussion

5.3.1 Synthesis & Structure of Synthesized Lanthanide-Transition Metal Bonded Complexes

The synthetic approach introduced in Chapters 3 and 4 has proven itself as fruitful in terms of generality. Starting from [(PyCp$_2$)Ln(thf)(OTf)] synthons, various Ln-TM bonded complexes across the entire lanthanide series can be accessed. In fact, many of the prepared complexes are the very first examples of lanthanides bonded to a transition metal (Pr, Sm, Tb, Ho, Er, Tm). While most Ln-TM combinations immediately result in crystals upon addition of KFp (or KRp) to a solution of [(PyCp$_2$)Ln(thf)(OTf)], it takes approximately a week at -30 °C in a freezer until crystals are formed for some of the earlier lanthanides. One possibility for this observation is the decreased Lewis acidity of the earlier lanthanides. Given the decrease in ionic radii across the lanthanides, earlier lanthanides are less Lewis acidic, leading to longer reaction times.[142] In addition, the larger lanthanides can accommodate the binding of an additional thf ligand with Ln-Fe combinations Ce, Pr, and Nd having a thf molecule bound, as evidenced by the molecular structure obtained via X-ray diffraction studies.

It should be noted, attempts to isolate a Eu-TM bonded complex have been ultimately unsuccessful. Upon addition of a solution of KFp or KRp to [(PyCp$_2$)Eu(thf)(OTf)], no visible change occurs. Layering the reaction with hexanes results in dark red plate crystals of the starting material [(PyCp$_2$)Eu(thf)(OTf)]. As the Eu^{3+} is one of the most readily reduced lanthanides, it is possible the highly reducing Rp^- or Fp^- molecules act as reducing agents.[155] Attempts to isolate a Eu(II) complex from this synthesis have also been unsuccessful.

Utilizing single-crystal X-ray diffractometry, the molecular structures of every synthesized Ln-TM combination have been studied. Of particular significance, lanthanide ions contract across the series, resulting in a decrease in ionic radii. This trend parallels the trend in Ln-TM distances, which decrease going from Ce to Lu (**Table 5.1**). There is also a substantial decrease in the Ln-TM distance transitioning from (thf)$PyCp_2Nd$-$FeCp(CO)_2$ to $PyCp_2Sm$-$FeCp(CO)_2$ (~0.25 Å). In fact the three (thf)$PyCp_2Ln$-$FeCp(CO)_2$ (Ln = Ce, Pr, Nd) have Ln-TM distances above 3 Å, whereas all other combinations have a distance of less than 3 Å.

Table 5.1: Summary of Ln-TM distances in prepared complexes.

Ln-Fe	Ln-Fe Distance (Å)	Ln-Ru	Ln-Ru Distance (Å)
(thf)Ce-Fe	3.1546(5)	Nd-Ru	3.0088(4)
(thf)Pr-Fe	3.1491(5)	Sm-Ru	2.9872(3)
(thf)Nd-Fe	3.1516(8)	Gd-Ru	2.9653(5)
Nd-Fe	2.9290(4)	Tb-Ru	2.9648(5)
Sm-Fe	2.9051(10)	Dy-Ru	2.9508(5)
Gd-Fe	2.893(2)	Ho-Ru	2.9452(3)
Tb-Fe	2.891(2)	Er-Ru	2.9351(5)
Dy-Fe	2.884(2)	Tm-Ru	2.9286(5)
Ho-Fe	2.8766(8)	Yb-Ru	2.9233(5)
Er-Fe	2.8652(19)	Lu-Ru	2.9165(7)
Tm-Fe	2.8586(9)		
Yb-Fe	2.8523(19)		
Lu-Fe	2.838(1)		

One interesting observation has to do with the molecular structure of Nd-Fe bonded complexes (**Figure 5.1**).

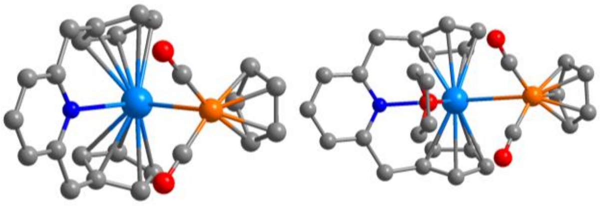

Figure 5.1: Molecular structures of **5-13** (left) and **5-14** (right). Hydrogens have been omitted for clarity. Carbon, gray; oxygen, red; nitrogen, blue; iron, orange; neodymium, light blue.

If the complex is crystallized in the freezer, the thf bound complex (thf)PyCp$_2$Nd-FeCp(CO)$_2$ is isolated (**Figure 5.1**). In contrast, obtaining crystals via slow evaporation of the solvent (thf) at room temperature results in the thf free complex PyCp$_2$Nd-FeCp(CO)$_2$. Additionally, attempts to prepare PyCp$_2$Nd-RuCp(CO)$_2$ in the freezer have been unsuccessful. It has only been successfully prepared via slow evaporation at room temperature. Efforts to isolate larger quantities of the thf free complexes have been challenging, as the crystals of both PyCp$_2$Nd-FeCp(CO)$_2$ and PyCp$_2$Nd-RuCp(CO)$_2$ immediately turn brown after decanting off mother liquor with some white powder mixed in with the solid (presumed to be KOTf). The decomposed mixture is insoluble in Et$_2$O, toluene, and thf.

As versatile as this synthesis has been with preparing molecules containing a Ln-TM bond, a major drawback is the lack of solubility of these complexes. The crystals isolated from the reactions are insoluble in thf, toluene, Et$_2$O, 1,4-dioxane, and 2-methyltetrahydrofuran, and decompose in CH$_2$Cl$_2$ and acetonitrile. In order to better characterize these complexes, it is imperative to increase the solubility of them. One possible route is to modify the Fp$^-$ anion by replacing hydrogens with methyl groups. Ideally, the reaction of KFp* (Fp* = [C$_5$Me$_5$Fe(CO)$_2$]$^-$) and the lanthanide synthons will generate complexes bearing a lanthanide-transition metal bond (**Figure 5.2**).[156]

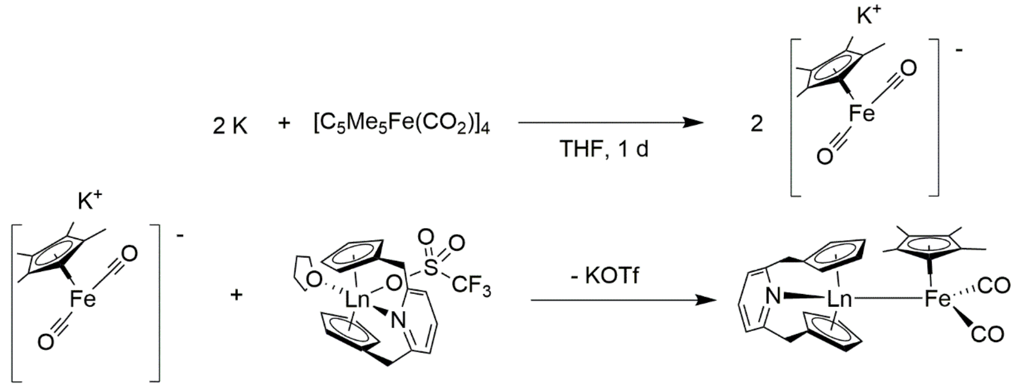

Figure 5.2: Synthesis of Fp* (top) and proposed synthesis of Ln-Fp* complexes (bottom).

Naturally, the next step to study Ln-TM bonded complexes would be to study the effect different transition metals have on the nature of this interaction. Ideally, other anionic transition metal carbonyl fragments could be employed and behave similarly to KFp and KRp. In other reports, anionic transition metal fragments such as Wp$^-$ ([CpW(CO)$_3$]$^-$), Mc$^-$ ([Mn(CO)$_5$]$^-$), Mp$^-$ ([CpMo(CO)$_3$]$^-$), or Crp$^-$ ([CpCr(CO)$_3$]$^-$) have been utilized to synthesize complexes bearing Cu-TM bonds (TM = W, Mn, Mo, Cr, Co) (**Figure 5.3**).[157]

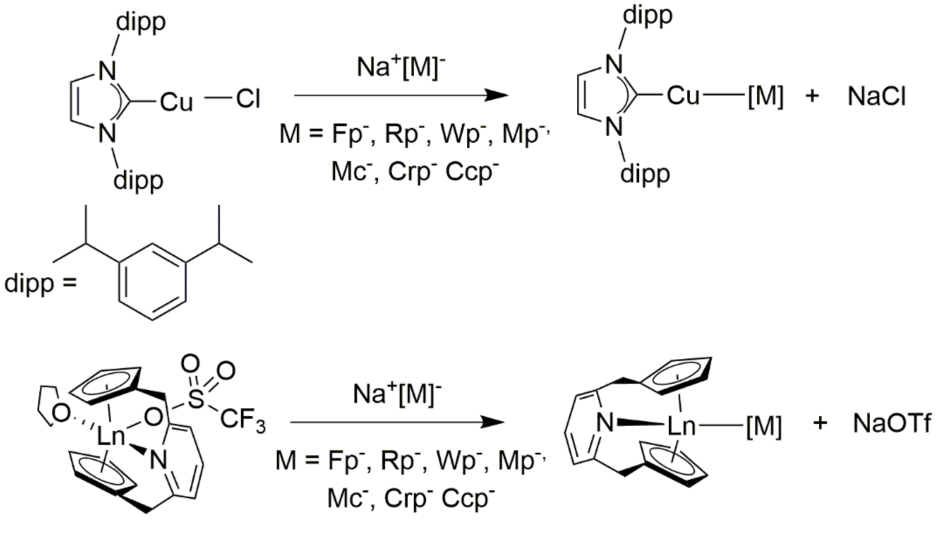

Figure 5.3: Synthesis of Cu-TM bonds via the synthesis of an *N*-heterocyclic carbene copper complex and anionic metal carbonyl fragments (top). Proposed synthesis of Ln-TM bonds with Ln-OTf complex (bottom). Adapted from Banerjee et al (2014).[157]

An analogous synthesis with these fragments along with lanthanide synthons we have prepared ([(PyCp$_2$)Ln(thf)(OTf)] Ln = Ce, Pr, Nd, Sm, Eu, Gd, Tb, Dy, Ho, Er, Tm, Yb, Lu) is certainly plausible. A potential drawback to this approach has to do with the relative nucleophilicities of these fragments (**Table 5.2**).

Table 5.2: Relative nucleophilicities of metal carbonyl anions.[158]

Anion	Relative Nucleophilicity
$[CpFe(CO)_2]^-$	70,000,000
$[CpRu(CO)_2]^-$	7,500,000
$[CpNi(CO)]^-$	5,500,000
$[Re(CO)_5]^-$	25,000
$[CpW(CO)_3]^-$	~500
$[Mn(CO)_5]^-$	77
$[CpMo(CO)_3]^-$	67
$[CpCr(CO)_3]^-$	4
$[Co(CO)_4]^-$	1

Previous work has demonstrated that Fp^- and Ru^- are significantly better nucleophiles than other anionic transition metal fragments.[158] Fenske-Hall computational studies performed suggested the anionic charge is localized on the metal center in the case of Fp^- and Rp^- as opposed to the charge delocalization over the entire fragment observed in Mp, Crp^-, and Wp^-. This lack of negative charge on the metal center of these fragments has resulted in isolation of lanthanide isocarbonyl complexes as opposed to the desired Ln-

TM bond.[26,159-160] It is possible that employing a triflate bearing synthon would lead to the desired complex, as it has not been utilized before to the best of our knowledge

An alternative approach proposed is through the use of an anionic rhenium fragment. An anionic Rhenium(I) β-diketiminate fragment has recently been used as a metalloligand to generate a heterometallic complex containing Re-Zn and Zn-Zn bonds (**Figure 5.4**).[161]

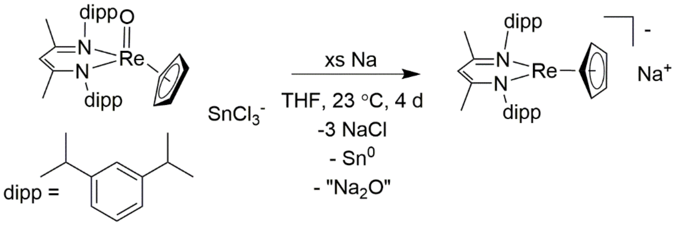

Figure 5.4: Synthesis of Na[CpRe(BDI)]. Adapted from Lohrey et al. (2019).[161]

This complex was successfully prepared via the reaction between $ZnCl_2$ and Na[CpRe(BDI)] (BDI = *N,N'*-bis(2,6-diisopropylphenyl)-3,5-dimethyl-β-diketiminate) (**Figure 5.5**).

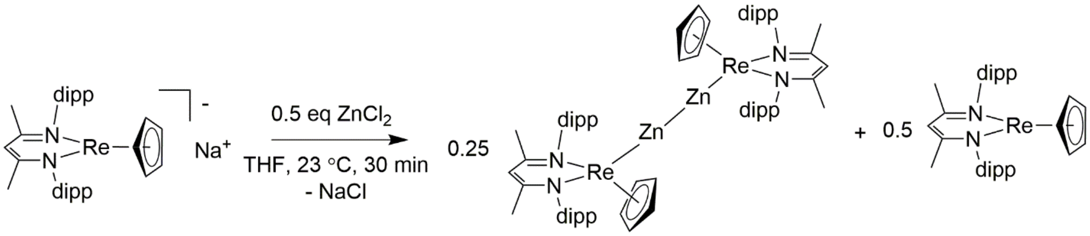

Figure 5.5: Synthesis of complex containing Re-Zn bonds. Adapted from Lohrey et al (2019).[161]

Density functional theory (DFT) calculations concluded the Re-Zn interaction formed via a dative interaction from a lone pair on Re located in a 5d orbital and an empty 4p Zn-based orbital. A similar approach using Na[CpRe(BDI)] and $[PyCp_2Ln(OTf)(thf)]$ could be employed to synthesize Ln-Re bonds (**Figure 5.6**). Considering the Ln-Fe and Ln-Ru has been characterized as a strong σ TM-Ln donation, this approach to form Ln-TM bonds seems more viable than less nucleophilic anionic transition metal carbonyl fragments.

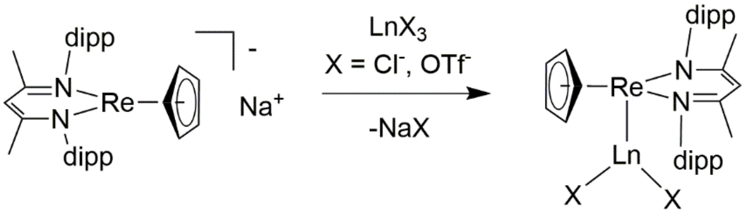

Figure 5.6: Proposed synthesis of Ln-Re bonded complex.

5.3.2 Spectroscopic Analysis of Lanthanide-Transition Metal Bonded Complexes

In evaluating the infrared and ^{57}Fe Mössbauer spectra of the Ln-TM bonded complexes isolated with this system, it was determined the nature of the bond can be described as showing strong TM→Ln σ donation. Infrared spectroscopy was used to assess the electron density around the iron center. Most of the complexes have similar υ_{CO} stretches to that of TM-Fp bonded complexes (**Table 5.3**).[122] It can be concluded that the bonding is best described as a formally iron(0) ion binding to a trivalent lanthanide ion. It should be noted that Ln-TM combinations containing a tetrahydrofuran molecule bound to the lanthanide differ slightly than the later lanthanides in the series with no solvent molecule bound. The CO stretching modes are complexes with a Pr-Fe and Ce-Fe bond are at slightly lower in energy as compared to other complexes.

Table 5.3: CO stretching frequencies of synthesized Ln-TM complexes.

Ln-Fe	υ_{CO} (cm^{-1})	Ln-Ru	υ_{CO} (cm^{-1})
(thf)Ce-Fe	1891/1814	Sm-Ru	1930/1851
(thf)Pr-Fe	1890/1814	Gd-Ru	1930/1852
(thf)Nd-Fe	1908/1836	Tb-Ru	1928/1847
Sm-Fe	1907/1836	Dy-Ru	1930/1851
Gd-Fe	1909/1840	Ho-Ru	1933/1852
Tb-Fe	1910/1836	Er-Ru	1933/1854
Dy-Fe	1910/1840	Yb-Ru	1934/1856
Ho-Fe	1912/1831	Lu-Ru	1934/1855
Er-Fe	1913/1843		
Yb-Fe	1914/1843		
Lu-Fe	1915/1833		

It can be concluded that there is more electron density on the iron in complexes with a bound thf molecule on the lanthanide ion. This is likely due to the weaker Ln-TM interaction given the electron donation of the thf molecule to the lanthanide.

Table 5.4: Summary of ^{57}Fe Mössbauer data for Ln-Fe complexes.

Ln-Fe	δ (mm/s)	ΔE_Q (mm/s)
(thf)Ce-Fe	0.133	2.075
Dy-Fe	0.129	1.859
Lu-Fe	0.122	1.846

The more positive isomer shift in **3-1** as compared to **5-21** suggests a stronger Fe→Ln in the latter compound (**Table 5.4**). In order to establish this trend with more certainty, more spectra are necessary.

Future studies would benefit from utilizing even more sensitive spectroscopic techniques to potentially quantify covalency in Ln-TM bonded complexes. A possible alternative avenue that has so far not been explored is resonance Raman experiments. In contrast to traditional Raman experiments, resonance Raman involves selecting an incident photon source close to that of the energy of the electronic transition of the molecule of interest.[162] The frequency resonance can lead to greatly enhanced intensity of Raman scattering as compared to a traditional Raman experiment. Resonance Raman has been utilized to study electronic communication in bimetallic complexes.[163-164]

In a recent literature example, the weak iron-ruthenium interaction in a ferrocene diamide complex was probed. (**Figure 5.7**)[165]

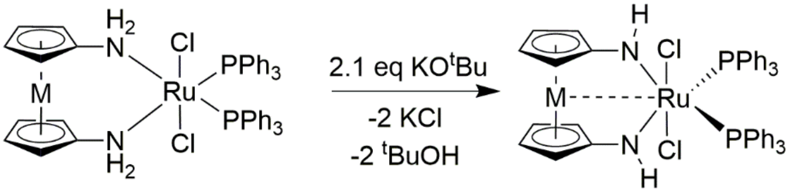

Figure 5.7: Synthesis of ferrocene amido complex with Fe-Ru interaction. Adapted from Green et al. (2013).[165]

Initially, ultraviolet-visible (UV-Vis) spectroscopy exhibited weakly absorbing signals attributed to an iron-ruthenium charge transfer band at 530 nm as well as other signals at 360 and 352 nm. When the intensity of the excitation laser wavelength was increased, the vibrational mode signal of the complex at 342 cm^{-1} significantly increased. Ultimately, this supported the existence of an iron-ruthenium interaction when compared to other literature examples.[166]

In a similar manner, resonance Raman spectroscopy could be utilized to assess the nature of Ln-TM bonds. Initially, UV-vis experiments will be carried out to identify any Ln-TM charge transfer bands. The energy of this transition would indicate regions in the Raman spectrum in which an enhanced signal could potentially be observed as a result of resonance with the electronic transition. If these transitions differ in energy when substituting a lanthanide, it can provide insight into the relative strength of different Ln-TM bonds.

5.3.3 Assessment of Magnetization Dynamics of Lanthanide-Transition Metal Complexes

Currently, no complex that has been discussed in this thesis containing a Ln-TM bond has demonstrated slow magnetic relaxation under zero applied dc field. The Dy-TM complexes discussed in Chapter 3 exhibited similar U_{eff} values under an applied dc field. Additionally, the Ce-Fe bonded complex exhibited field induced slow magnetic relaxation at a lower optimum applied field (500 Oe for **4-1** verus 1500 Oe for **3-1** and 1600 Oe for **3-2**), albeit at lower temperatures and a lower calculated U_{eff} than **3-1** and **3-2**. Other Ln-TM heterobimetallic complexes such as Tb-TM, Ho-TM, and Er-TM do not exhibit an out-of-phase component of the ac susceptibility under any condition (**Appendix D**). It is likely that for the case of non-Kramers oblate ions such as terbium the ligand symmetry surrounding the ion leads to the lack of a bistable ground state. In the case of erbium or holmium, the axial ligand field from the cyclopentadienide ligands is not ideal for prolate ions resulting in no barrier for magnetization reversal. Additionally, static magnetic measurements, such as dc susceptibility, support the conclusion that magnetic behavior arises from the paramagnetic lanthanide ion with no contributions from the transition metal center.

The magnetic behavior of these complexes falls in line with current theory of single-molecule magnets. Referring specifically to Dy-based SMMs, it is desirable for negatively charged ligands to coordinate axially to achieve a large separation of the ground m_J and first excited state. Ligands that coordinate equatorially in the Dy case can either result in the lowest m_J value being the magnetic ground state, quantum tunneling of magnetization, or both.[167]

Comparing the magnetic properties of **2-3** and **3-1**, only **2-3** demonstrates slow magnetic relaxation (albeit at frequencies too high to measure on our SQUID magnetometer) whereas **3-1** does not have a signal in the out-of-phase component of ac susceptibility under no applied dc field. While these complexes have cyclopentadienide ligands coordinated axially, their equatorial ligands differ. Triflate and thf in **2-3** are weaker ligands in comparison to the anionic Fp^- in **3-1**. The stronger equatorial ligand in **3-1** is the likely cause of the lack of barrier to magnetization reversal in the complex. This conclusion is further supported in literature, with similar systems exhibiting better performances as SMMs with weaker bound ligands in the equatorial field.[60.116] Conversely, the axially coordinated Cp^- ligands on the Er system are likely the cause for poor SMM behavior in the erbium analogue of **3-1**.

In order to improve SMM behavior of Ln-TM bonded complexes, reducing the strength of equatorial or axial ligands need to be considered. A possible approach could be implementing the anionic rhenium fragment [CpReBDI]$^-$ previously described. The negatively charged rhenium species readily reacts with $ZnCl_2$ to generate a heterometallic complex supported by both Re-Zn and Zn-Zn bonds. Under similar conditions, trivalent lanthanide salts such as $ErCl_3$ or $Er(OTf)_3$ could be reacted in a 1:2 fashion (**Figure 5.8**).

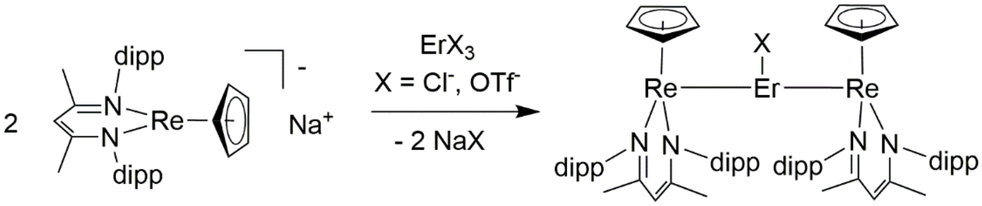

Figure 5.8: Proposed synthesis of Re-Er-Re sandwich complex.

The proposed molecule would contain two Re-Er bonds with the rhenium binding equatorially. To remove the axially bound chloride or triflate, a weakly binding anion such as tetrakis(pentafluorophenyl)borate could be utilized to generate a system similar to the metallocenium complexes that are the current benchmarks in the field of SMMs (**Figure 5.9**).

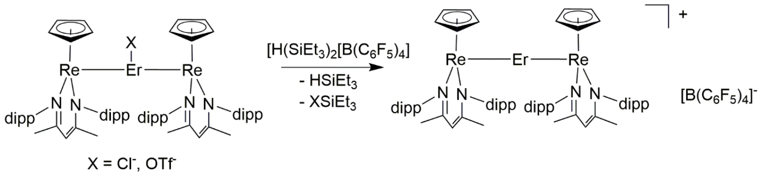

Figure 5.9: Proposed synthesis of cationic erbium complex.

5.4 Conclusion & Outlook

After the successful synthesis and isolation of complexes containing Dy-TM and Ce-TM bonds with the [PyCp$_2$]$^{2-}$ ligand system, analogous lanthanide synthons were prepared to assess the ability to make Ln-TM bonds across the series. With the exception of europium, promethium, and lanthanum, a Ln-Fe or Ln-Ru bonded complex could be successfully synthesized with this system. As predicted, the Ln-TM distance in these complexes decreases as the ionic radius of the lanthanide decreases.

Spectroscopic characterization of these complexes via IR suggests that the electron density of the transition metal center does slightly change as a function of the nature of the lanthanide ion. This is also consistent with Mössbauer spectroscopic measurements of Lu-Fe and Dy-Fe bonded complexes. Efforts to find a spectroscopic method that will be sensitive enough to unambiguously detect differences in Ln-TM bonding are currently being pursued.

While Ln-TM bonded complexes **3-1**, **3-2**, and **4-1** exhibit slow magnetic relaxation under applied dc fields, no compounds discussed in this chapter demonstrate any form of slow magnetic relaxation. Possible improvements to enhance magnetic behavior are suggested utilizing an anionic rhenium fragment. In addition, efforts to study different lanthanide-transition metal combinations for bonding have been proposed using other anionic transition metal carbonyl fragments.

6. CONCLUSION

6.1 Magnetization Dynamics of Lanthanide Organometallic Dysprosium Complexes

Utilizing the $[PyCp_2]^{2-}$ ligand, dinculear dysprosium complexes were successfully synthesized. These complexes were prepared via the reaction between anhydrous $Dy(OTf)_3$ or $DyCl_3$ and Na_2PyCp_2. It was determined that the bridging triflate interaction in **2-1** as compared to **2-2** was weaker, as evidenced by the triflate complex breaking down into a monomeric form **2-3** upon the addition of thf. Magnetization dynamic studies concluded that all three complexes exhibited slow magnetic relaxation under zero applied dc field, and U_{eff} was calculated for **2-1** and **2-2**. The barrier for magnetization reversal was identical (49 cm^{-1}) for **2-1** and **2-2** and demonstrated similar magnetic properties according to computational analysis.

These complexes were prepared with the intention of implementing them in synthesis. Specifically, these complexes were targeted to design a synthetic scheme to prepare lanthanide-transition metal bonds in discrete molecules. We hypothesized that incorporating triflate ligands in this system would allow the compounds to readily undergo substitution chemistry. We were encouraged that the bridging complex **2-1** readily dissociates in coordinating solvent, as it would seem to support that this interaction was indeed weak.

6.2 Assessing Lanthanide-Transition Metal Bonding in Discrete Molecules

Through the use of the triflate complex $[(PyCp_2)Ln(\mu\text{-}OTf)]_2$ (or $[(PyCp_2)Ln(OTf)(thf)]$), molecules containing a Ln-TM bond can be successfully isolated.

As the magnetization dynamics of these complexes was of interest to us, we initially studied complexes **3-1** and **3-2** containing a Dy-TM bond (TM = Fe, Ru). Initially, spectroscopic studies were performed after **3-1** and **3-2** were structurally characterized. Infrared spectroscopy suggested the bonding was σ donation from a transition metal center with a formal oxidation state of 0 to the Dy ion with a formal oxidation state of +3. This was further supported with ^{57}Fe Mössbauer spectroscopy. Computational studies supplemented experimental findings, concluding that there is some electron sharing between the two metals. Neither Dy-TM bonded complex displayed slow magnetic relaxation under zero field, but both exhibited a signal in χ'' under applied dc fields. These magnetization dynamics studies determined **3-1** and **3-2** had similar calculated barriers (43 cm^{-1} for **3-1**, 46 cm^{-1} for **3-2**) under similar applied dc fields (1500 Oe for **3-1**, 1600 Oe for **3-2**).

The versatility of this synthetic route to prepare Ln-TM complexes was further tested with the earlier lanthanide cerium. The complex containing a Ce-Fe bond, **4-1**, was successfully synthesized and characterized. Spectroscopic studies performed concluded a weaker Ln-TM interaction in **4-1** when compared to **3-1**. The lower energy CO stretches support this claim. It is likely the additionally bound THF molecule in **4-1** results in a weaker Ce-Fe interaction. Complex **4-1** exhibited field induced slow magnetic relaxation at a 500 Oe optimal field and had a calculated barrier of 29 cm^{-1}.

While this synthesis has proven to be a valuable approach to synthesize Ln-TM bonded compounds, it is not universal across the lanthanide series. Attempts to synthesize complexes containing a Eu-Fe, Pr-Ru, Ce-Ru, and Eu-Ru have been unsuccessful. Despite these shortcomings, this new approach has been utilized to great success and has resulted in first ever examples of many Ln-TM bonds. Spectroscopic studies that have currently been performed determined small changes in Ln-TM bonding upon substitution of the lanthanide. Additionally, magnetization dynamic measurements performed as of now have yet to determine a complex with a Ln-TM bond that exhibits slow magnetic relaxation under zero field.

The next step in studying Ln-TM bonds would be preparing different Ln-TM combinations. Other anionic transition metal carbonyl fragments are promising for this synthesis along with a recently reported anionic rhenium species. More importantly, the Re complex could be potentially utilized to improve SMM behavior in Ln-TM bonded compounds. Other modifications to this system to improve solubility and reactivity are currently underway.

Ultimately, this work has provided the most comprehensive look into lanthanide-transition bonding to date. Not only has this work resulted in new Ln-TM bonding combinations, but also it has resulted in extensive spectroscopic, magnetic, and computational insights that had not been previously done before. Additionally, the ability to compare Ln-TM bonding between 3d and 4d transition metal has been established with this synthetic approach. The initial findings studies on this system has determined a strong TM→Ln σ donation that is relatively independent of lanthanide identity. Ideally, the work discussed in this thesis will be able to open the doors to new Ln-TM bonding combinations and contribute to efforts towards a system that supports Ln-TM bonds across the entire lanthanide series.

REFERENCES

[1] Cotton, F. A.; Murillo, C. A.; Walton R. A. Multiple Bonds between Metal Atoms. 3rd Edition, Springer Science and Business Media Inc., 2005

[2] Cotton, F. A.; Curtis, N. F.; Harris, C. B.; Johnson, B. F. G.; Lippard S. J.; Mague, J. T.; Robinson, W. R.; Wood, J. S. Mononuclear and Polynuclear Chemistry of Rhenium(III): Its Pronounced Homophilicity. *Science* **1964**, 145, 1305-1307.

[3] Eisenhart, R. J.; Clouston, L. J.; Lu, C. C. Configuring Bonds between First-Row Transition Metals. *Acc. Chem. Res.* **2015**, *48*, 2885-2894.

[4] Ramirez, B. L.; Sharma, P.; Eisenhart, R. J.; Gagliardi, L.; Lu, C. C. Bimetallic Nickel-Lutetium Complexes: Tuning the Properties and Catalytic Hydrogenation Activity of the Ni Site by Varying the Lu Coordination Environment. *Chem. Sci.* **2019**, *10*, 3375-3384.

[5] Mazzacano, T. J.; Mankad, N. P. Base Metal Catalysts for Photochemical C-H Borylation that Utilize Metal-Metal Cooperativity. *J. Am. Chem. Soc.* **2013**, *135*, 17258-17261.

[6] Liddle, S. T.; Mills, D. P.; Metal-Metal Bonds in f-Element Chemistry. *Dalton Trans* **2009**, *0*, 5592-5605.

[7] Peligot, M. P. Sur un Nouvel Oxyde de Chrome. *C. R. Acad. Sci.* **1844**, *19*, 609-615

[8] Nguyen, T; Sutton, A. D.; Brynda, M.; Fettinger, J. C.; Long, G. J.; Power, P. P. Synthesis of a Stable Compound with Fivefold Bonding between Two Chromium(I) Centers. *Science* **2005**, *310*, 844-847.

[9] Falvello, L. R.; Foxman, B. M; Murillo, C. A. Fitting the Pieces of the Puzzle: The δ Bond. *Inorg. Chem.* **2014**, *53*, 9441-9456.

[10] Wang, X. B.; Wang, L. S. Probing the Electronic Structure and Metal-Metal Bonding of $Re_2Cl_8^{2-}$ in the Gas Phase. *J. Am. Chem. Soc.* **2000**, *122*, 2096-2100.

[11] Campbell, F. L. III; Cotton, F. A.; Powell, G. L. Correlation of Molybdenum-Molybdenum Quadruple Bond Length with Angle of Internal Rotation, using Data for 10 Compounds. *Inorg. Chem.* **1984**, *23*, 4222-4226.

[12] Cotton, F. A.; Gruhn, N. E.; Gu, J.; Huang, P.; Lichtenberger, D. L.; Murillo, C. A.; Van Dorn, L. O.; Wilkinson, C. C. Closed-Shell Molecules that Ionize more Readily than Cesium. *Science* **2002**, *298*, 1971-1974.

[13] Chiarella, G. M.; Cotton, F. A.; Durivage, J. C.; Lichtenberger, D. L; Murillo, C. A. Solubilizing the most Easily Ionized Molecules and Generating Powerful Reducing Agents. *J. Am. Chem. Soc.* **2013,** *135*, 17889-17896.

[14] Brown-Xu, S. E.; Chisholm, M. H.; Durr, C. B.; Spilker, T. F.; Young, P. J. MM Quadruply Bonded Complexes Supported by Vinylbenzene Ligands: Synthesis, Characterization, Photophysical Properties, and Applications as Synthons. *Chem. Sci.* **2015**, *6*, 1780-1791.

[15] Qin, J.-S.; Yuan, S.; Wang, Q.; Alsalme, A.; Zhou, Z.-C. Mixed-Linker Strategy for the Construction of Multifunctional Metal-Organic Frameworks. *J. Mater. Chem. A*, **2017**, *5*, 4280-4291.

[16] Shtemenko, A. V.; Chifotides, H. T.; Yegorova, D. E.; Shtemenko, N. I.; Dunbar, K. R. Synthesis and X-Ray Crystal Structure of the Dirhenium Complex $Re_2(i\text{-}C_3H_7COO)_4Cl_2$ and its interaction with DNA Purine Nucleobases. *J. Inorg. Biochem.* **2015**, *153*, 114-120.

[17] Morse, M. D. Clusters of Transition-Metal Atoms. *Chem. Rev.* **1986**, *86*, 1049-1109.

[18] Collman, J. P., Boulatov, R. Heterodinuclear Transition-Metal Complexes with Multiple Metal-Metal Bonds. *Angew. Chem. Int. Ed.* **2002**, *41*, 3948-3961.

[19] Collman, J. P.; Arnold, H. J.; Weissman. K. J.; Burton, J. M. Heterometallic Mixed Triad Multiple Bonds Metal-Porphyrin Dimers. *J. Am. Chem. Soc.* **1994**, *116*, 9761-9762.

[20] Krogman, J. P.; Thomas, C. M. Metal-Metal Multiple Bonding in C_3-Symmetric Bimetallic Complexes of the First Row Transition Metals. *Chem. Commun.* **2014**, *50*, 5115-5127.

[21] Cotton, F. A.; Chen, H.; Daniels, L. M.; Feng, X. Partial Paramagnetism of the Chromium-Chromium Quadruple Bond. *J. Am. Chem. Soc.* **1992**, *114*, 8980-8983.

[22] Brogden, D. W.; Turov, Y.; Nippe, M.; Li Manni, G.; Hillard, E. A.; Clérac, R.; Gagliardi, L.; Berry, J. F. Oxidative Stretching of Metal-Metal Bonds to their Limits. *Inorg. Chem.* **2014**, *53*, 4777-4790.

[23] Waltz, K. M.; He, X.; Muhoro, C.; Hartwig, J. F. Hydrocarbon Functionalization by Transition Metal Boryls. *J. Am. Chem. Soc.* **1995**, *117*, 11357-11358.

[24] Clouston, L. J.; Bernales, V.; Carlson, R. K. Gagliardi, L.; Lu, C. C. Bimetallic Cobalt-Dinitrogen Complexes: The Impact of the Supporting Metal on N_2 Activation. *Inorg. Chem.* **2015**, *54*, 9263-9270.

[25] Krogman, J. P.; Foxman, B. M.; Thomas, C. M. Activation of CO_2 by a Heterobimetallic Zr/CO Complex. *J. Am. Chem. Soc.* **2011**, *133*, 14582-14585.

[26] Beletskaya, I. P.; Voskoboynikov, A. Z.; Chuklanova, E. B.; Kirillova, N. I.; Shestakova, A. K.; Parshina, I. N.; Gusev, A. I.; Magomedov, G. K. I. Bimetallic Lanthanide Complexes with Lanthanide-Transition Metal Bonds. Molecular

Structure of $(C_4H_8O)(C_5H_5)_2LuRu(CO)_2(C_5H_5)$. The use of ^{139}La NMR spectroscopy. *J. Am. Chem. Soc.* **1993**, *115*, 3156-3166.

[27] Arnold, P. L.; McMaster, J.; Liddle, S. T. An unsupported Lanthanide-Transition Metal Bond; Synthesis and Crystal Structure of an Nd-Fe Amido N-Heterocyclic Carbene Complex. *Chem. Commun.* **2009**, 818-820.

[28] Butovskii, M. V.; Döring, C.; Bezulgy, V.; Wagner, F. R.; Grin, Y.; Kempe, R. Molecules containing Rare-Earth Atoms Solely Bonded to Transition Metals. *Nature Chemistry* **2010**, *2*, 741-744.

[29] Butovskii, M. V.; Oelkers, B.; Bauer, T.; Bakker, J. M.; Bezulgy, V.; Wagner, F. R.; Kempe R. Lanthanoid-Transition Metal Bonding in Bismetallocenes. *Chem. Eur. J.* **2014**, *20*, 2804-2811.

[30] Sternal, R. S.; Marks, T. J. Actinide-to Transition Metal Bonds. Synthesis, Characterization, and Properties of Metal-Metal Bonded Systems having the tris(cyclopentadienyl)Actinide Fragment. *Organometallics,* **1987**, *6*, 2621-2623.

[31] Organo-f-Element Thermochemistry. Actinide-Group 14 Element and Actinide-Transition-Element Bond Disruption Enthalpies and Stoichiometric/Catalytic Chemical Implication thereof in Heterobimetallic tris(cyclopentadienyl)Uranium(IV) Compounds. *Organometallics* **1991**, *10,* 1450-1457.

[32] Larson, P.; Mazin, I. I.; Papaconstantopoulos, D. A. Calculation of Magnetic Anisotropy in $SmCo_5$. *Phys. Rev. B.* **2003**, *67*, 214405-214413.

[33] Troiani, F.; Affronte, M. Molecular Spins for Quantum Information Technologies. *Chem. Soc. Rev.* **2011**, *40*, 3119–3129.

[34] Bogani, L.; Wernsdorfer, W. Molecular Spintronics using Single-Molecule Magnets. *Nat. Mater.* **2008**, *7,* 179–186

[35] Affronte, M. Molecular Nanomagnets for Information Technologies. *J. Mater. Chem.* **2009**, *19*, 1731–1737.

[36] Layfield, R. A.; Murugesu, M. *Lanthanides and Actinides in Molecular Magnetism*, 1st Ed.; Wiley, 2005.

[37] Sessoli, R. Gatteschi, D.; Caneschi, A.; Novak, M. A. Magnetic Bistability in a Metal-Ion Cluster. *Nature,* **1993**, *365*, 141-143.

[38] Guo, F.-S.; Day, B. M.; Chen, Y.-C.; Tong, M.-L.; Mansikkamäki, A; Layfield, R. A. Magnetic Hysteresis up to 80 Kelvin in a Dysprosium Metallocene Single-Molecule Magnet. *Science* **2018**, *21*, 1400-1403.

[39] Drung, D.; Assmann, C.; Beyer, J.; Kirsten, A.; Peters, M.; Ruede, F.; Schurig, Th. Highly Sensitive and Easy to Use SQUID Sensors. *Transactions on Applied Superconductivity.* **2007**, *17*, 699-704.

[40)] Jaklevic, R. C.; Lambe, J.; Silver, A. H.; Mercereau J. E. Quantum Interference effects in Josephson Tunneling. *Physical Review Letters* **1964**, *12*, 159-164.

[41] Bain, G. A.; Berry, J. F. Diamagnetic Corrections and Pascal's Constants. *J. Chem. Educ.* **2008**, *85*, 532-536.

[42] Gatteschi, D.; Sessoli, R.; Villain, J. *Molecular Nanomagnets*; Oxford University Press, 2006.

[43] Debye, P. Zur Theorie der Spezifischen Waerme. *Annalen der Physik* **1912**, *39,* 789-839.

[44] Liddle, S. T.; van Slageren, J. Improving f-Element Single-Molecule Magnets. *Chem. Soc. Rev.* **2015**, *44,* 6655-6669.

[45] Gatteschi, D.; Sessoli, R. Quantum Tunneling of Magnetization and Related Phenomena in Molecular Materials. *Angew. Chem. Int. Ed*. **2003**, *42*, 268–297.

[46] Glaser, T. Rational Design of Single- Molecule Magnets: A Supramolecular Approach. *Chem. Commun.* **2011**, *47,* 116-130.

[47] Feltham, H. L. C.; Brooker, S. Review of Purely 4f and Mixed-Metal nd-4f Single-Molecule Magnets Containing only one Lanthanide Ion. *Coord. Chem. Rev.* **2014**, *276,* 1-33.

[48] Novikov, V. V.; Pavlov, A. A.; Nelyubina, Y. V.; Boulob, M. E.; Varzatskii, O. A.; Voloshin, Y. Z.; Winpenny, R. E. P. A Trigonal Prismatic Mononuclear Cobalt(II) Complex Showing Single-Molecule Magnet Behavior. *J. Am. Chem. Soc.* **2015**, *137*, 9792-9795.

[49] https://www.quora.com/What-is-a-magnetic-hysteresis-loop (Accessed April 30th, 2019)

[50] Latendresse, T. P.; Bhuvanesh, N. S.; Nippe, M. Slow Magnetic Relaxation in a Lanthanide-[1]Metallocenophane Complex. *J. Am. Chem. Soc.* **2017**, *139*, 8058-8061.

[51] Ungur, L.; Chibotaru, L. F. Magnetic Anisotropy in the Excited States of Low Symmetry Lanthanide Complexes. *Phys. Chem. Phys. Rev.* **2011**, *13*, 20086-20090.

[52] Woodruff, D. N.; Winpenny, R. E. P.; Layfield, R. A. Lanthanide Single-Molecule Magnets. *Chem. Rev.* **2013**, *113* (7), 5110–5148.

[53] Waldmann, O. A Criterion for the Anisotropy Barrier in Single-Molecule Magnets. *Inorg. Chem.* **2007**, *46* (24), 10035–10037.

[54] Ako, A. M.; Hewitt, I. J.; Mereacre, V.; Clérac, R.; Wernsdorfer, W.; Anson, C. E.; Powell, A. K. A Ferromagnetically Coupled Mn_{19} Aggregate with a Record S=83/2 Ground Spin State. *Angew. Chem. Int. Ed.* **2006**, *45* (30), 4926–4929.

[55] Neese, F.; Pantazis, D. A. What is not Required to make a Single-Molecule Magnet. *Faraday Discuss*. **2010,** *148*, 229–238.

[56] Yao, X.-N.; Du, J.-Z.; Zhang, Y.-Q.; Leng, X.-B.; Yang, M.-W.; Jiang, S.-D.; Wang, Z.-X.; Ouyang, Z.-W.; Deng, L.; Wang, B.-W.; Gao, S. Two-Coordinate Co(II) Imido Complexes as Outstanding Single-Molecule Magnets. *J. Am. Chem. Soc.* **2017**, *139*, 373–380.

[57] Zadrozny, J. M.; Atanasov, M.; Bryan, A. M.; Lin, C.-Y.; Rekken, B. D.; Power, P. P.; Neese, F.; Long, J. R. Slow Magnetization Dynamics in a Series of Two-Coordinate Iron(II) Complexes. *Chem. Sci.* **2013**, *4*, 125-138.

[58] Benelli, C.; Gatteschi, D. Introduction to Molecular Magnetism: From Transition Metals to Lanthanides, 1st ed.; John Wiley & Sons, Inc., 2015.

[59] Smith, C. A. The Synthesis and Magnetochemistry of Transition and Lanthanide Metal Compounds. University of Manchester, Manchester, U. K., 2013.

[60] Day, B. M.; Guo, F.-S.; Layfield, R. A. Cyclopentadienyl Ligands in Lanthanide Single-Molecule Magnets: One Ring to Rule them All? *Acc. Chem. Res.* **2018**, *51*, 1880-1889.

[61] Ishikawa, N.; Sugita, M.; Ishikawa, T.; Koshihara, S.-y.; Kaizu, Y. Lanthanide Double-Decker Complexes Functioning as Magnets at the Single-Molecular Level. *J. Am. Chem. Soc.* **2003**, *125*, 8694–8695.

[62] Ishikawa, N.; Sugita, M.; Tanaka, N.; Ishikawa, T.; Koshihara, S.-y.; Kaizu, Y. Upward Temperature Shift of the Intrinsic Phase Lag of the Magnetization of Bis(phthalocyaninato)terbium by Ligand Oxidation Creating an S = 1/2 Spin. *Inorg. Chem.* **2004**, *43*, 5498–5500.

[63] Chen, Y.-C.; Liu, J.-L.; Ungur, L.; Liu, J.; Li, Q.-W.;Wang, L.-F.; Ni, Z.-P.; Chibotaru, L. F.; Chen, X.-M.; Tong, M.-L. Symmetry-Supported Magnetic Blocking at 20 K in Pentagonal Bipyramidal Dy(III) Single-Ion Magnets. *J. Am. Chem. Soc.* **2016**, *138*, 2829–2837.

[64] Ding, Y.-S.; Chilton, N. F.; Winpenny, R. E. P.; Zheng, Y.-Z. On Approaching the Limit of Molecular Magnetic Anisotropy: A Near-Perfect Pentagonal Bipyramidal Dysprosium(III) Single-Molecule Magnet. *Angew. Chem. Int. Ed.* **2016**, *55*, 16071–16074.

[65] Chilton, N. F. Design Criteria for High-Temperature Single-Molecule Magnets. *Inorg. Chem.* **2015**, *54*, 2097–2099.

[66] Goodwin, C. A. P.; Ortu, F.; Reta, D.; Chilton, N. F.; Mills, D. P. Molecular Magnetic Hysteresis at 60 Kelvin in Dysprosocenium. *Nature* **2017**, *548*, 439–442.

[67] Day, B. M.; Chen, Y.-C.; Tong, M.-L.; Mansikkamäki, A.; Layfield, R. A. A Dysprosium Metallocene Single-Molecule Magnet Functioning at the Axial Limit. *Angew. Chem. Int. Ed.* **2017**, *56*, 11445–11449.

[68] Butovskii, M. V.; Kempe, R. Rare Earth-Metal Bonding in Molecular Compounds: Recent Advances, Challenges, and Perspectives. *New J. Chem.* **2015**, *39*, 7544-7548.

[69] Papatriantafyllopoulou C.; Wernsdorfer, W.; Abboud, K. A.; Christou, G.; Mn_{21}Dy Cluster with a Record Magnetization Reversal Barrier for a Mixed 3d/4f Single-Molecule Magnet. *Inorg. Chem.* **2011**, *50*, 421-423.

[70] Waldmann, O.; A Criterion for the Anisotropy Barrier in Single-Molecule Magnets. *Inorg. Chem.* **2007**, *46*, 10035-10037.

[71] Ruiz, E.; Cirera, J.; Cano, J.; Alvarez, S.; Loose, C.; Kortus, J. Can Large Magnetic Anisotropy and High Spin really Coexist? *Chem. Commun.* **2008**, *0*, 52-54.

[72] Alexandropoulos, D. I.; Schulte, K. A.; Vignesh, K. R.; Dunbar, K. R. Slow Magnetic Dynamics in a Family of Mononuclear Lanthanide Complexes Exhibiting the Rare Cubic Coordination Geometry. *Chem. Commun.* **2018**, *54*, 10136-10139.

[73] Dickie, C. M.; Laughlin, A. L.; Wofford, J. D.; Bhuvanesh, N. S.; Nippe, M. Transition Metal Redox Switches for Reversible “On/Off” and “Slow/Fast” Single-Molecule Magnetic Behavior in Dysprosium and Erbium bis-Diamido Ferrocene Complexes. *Chem. Sci.* **2017**, *8*, 8039-8049.

[74] Dong, W.-K.; Zheng, S.-S.; Zhang, J.-T.; Zhang, Y.; Sun, Y.-X. Luminescent Properties of Heterotrinuclear 3d-4f Complexes Constructed from a Naphthalenediol-based Acyclic bis(Salamo)-Type Ligand. *Spectrochimica Acta Part A: Molecular and Biomolecular Spectroscopy* **2017**, *184*, 141-150.

[75] Rinehart, J. D.; Long, J. R. Exploiting Single-Ion Anisotropy in the Design of f-element Single-Molecule Magnets. *Chem. Sci.* **2011**, *2*, 2078-2085.

[76] Layfield, R. A. Organometallic Single Molecule-Magnets. *Organometallics* **2014**, *33*, 1084-1089.

[77] Demir, S.; Zadronzny, J. M.; Nippe, M.; Long, J Exchange Coupling and Magnetic Blocking in Bipyrimidyl Radical-Bridged Dilanthanide Complexes. J. *Chem. Am. Soc.* **2012**, *134*, 18546-18549.

[78] Sulway, S. A.; Layfield, R. A.; Tuna, F.; Wernsdorfer, W.; Winpenny, R. E. P. Single-Molecule Magnetism in Cyclopentadienyl-Dysprosium Chlorides. *Chem. Commun.* **2012**, *48*, 1508-1510.

[79] Paolucci, G.; Zanon, J.; Lucchini, V.; Damrau, W. E.; Siebel, E.; Fischer, D. R. New Dinuclear 5-*ansa*-Lanthocene Derivatives. Crystal Structures of $[Ln\{2,6\text{-}(CH_2C_5H_4)_2C_5H_3N\}\mu\text{-}O_2SOCF_3]_2$ (Ln = Nd, Y, Yb) and a VT Solution NMR (^{1}H, ^{19}F) Study of the Fluxional Yttrium Homologue. *Organometallics* **2002**, *21*, 1088-1094.

[80] Paolucci. G.; D'Ippolito, R.; Ye, C.; Qian, C.; Gräper, J, Fischer, D. R. New Dinuclear bis(cyclopentadienyl)Lanthanoid Chlorides Containing η^5-C_5H_4 Ligands Linked by a Metal-Coordinated 2,6-Dimethylenepyridyl Unit. *Journal of Organometallic Chemistry* **1994**, *471*, 97-104.

[81] APEX2 "Program for Data Collection on Area Detectors" BRUKER AXS Inc., 5465 East Cheryl Parkway, Madison, WI 53711-5373 USA

[82] Sheldrick, G. M. "Cell_Now (version 2008/1): Program for Obtaining Unit Cell Constants from Single Crystal Data": University of Göttingen, Germany

[83] Sheldrick, G.M. (2008). Acta Cryst. A64, 112-122. Sheldrick, G. M. (2015), Acta Cryst. A71, 3-8. Sheldrick, G. M. (2015). Acta Cryst. C71, 3-8. XT, XS, BRUKER AXS Inc., 5465 East Cheryl Parkway, Madison, WI 53711-5373 USA.

[84] G. M. Sheldrick, *SADABS*, "Program for Absorption Correction of Area Detector Frames", BRUKER AXS Inc., 5465 East Cheryl Parkway, Madison, WI 53711-5373 USA.

[85] TWINABS, Sheldrick, G.M. "Program for Absorption Correction of Area Detector Frames", BRUKER AXS Inc., 5465 East Cheryl Parkway, Madison, WI 53711-5373 USA.

[86] Spek, A. L., "PLATON - A Multipurpose Crystallographic Tool" J. Appl. Cryst. 2003, 36, 7-13.; Spek, A. L., Utrecht University, Utrecht, The Netherlands 2008.

[87] Dolomanov, O. V.; Bourhis, L. J.; Gildea, R. J.; Howard, J. A. K.; Puschmann, H. OLEX2: A Complete Structure Solution, Refinement, and Analysis Program. *J. Appl. Cryst.* **2009**, *42*, 339-341.

[88] Aquilante, F.; Autschbach, J.; Carlson, R. K.; Chibotaru, L. F.; Delcey, M. G.; De Vico, L.; Galván, I. F.; Ferré, N.; Frutos, L. M.; Gagliardi, L.; Garavelli, M.; Giussani, A.; Hoyer, C. E.; Li Manni, G.; Lischka, H.; Ma, D.; Malmqvist, P. Å.; Müeller, T.; Nenov, A.; Olivucci, M.; Pedersen, T. B.; Peng, D.; Plasser, F.; Pritchard, B.; Reiher, M; Rivalta, I.; Schapiro, I.; Segarra-Martí, J.; Stenrup, M.; Truhlar, D. G.; Ungur, L.; Valentini, A.; Vanciollie, S.; Veryazov, V.; Vysotskiy, V. P.; Weingart, O.; Zapata, F.; Lindh, R. MOLCAS 8: New Capabilities for Multiconfigurational Quantum Chemical Calculations across the Periodic Table. *Journal of Computational Chemistry* **2016**, *37*, 506-541.

[89] Hess, B. A.; Marian, C. M.; Wahlgren, U.; Gropen, O. A Mean-Field Spin-Orbit Method Applicable to Correlated Wavefunctions. *Chem. Phys. Lett.* **1996**, *251*, 365−371.

[90] Roos, B. O.; Lindh, R.; Malmqvist, P.-Å.; Veryazov, V.; Widmark, P.-O. New Relativistic Atomic Natural Orbital Basis Sets for Lanthanide Atoms with Applications to the Ce Diatom and LuF_3. *J. Phys. Chem. A* **2008**, *112*, 11431-11435

[91] Roos, B. O.; Malmqvist, P.-Å. Relativistic Quantum Chemistry: The Multiconfigurational Approach. *Phys. Chem. Chem. Phys.* **2004**, *6*, 2919-2927.

[92] Malmqvist, P.-Å.; Roos, B. O.; Schimmelpfennig, B. The Restricted Active Space (RAS) State Interaction Approach with Spin-Orbit Coupling. *Chem. Phys. Let.* **2002**, *357*, 230-240.

[93] Chibotaru, L. F.; Ungur, L. *Ab initio* Calculation of Anisotropic Magnetic Complexes of. I. Unique Definition of Pseudospin Hamiltonians and their Derivation. *J. Chem. Phys.* **2012**, *137*, 064112-22.

[94] Chibotaru, L. F.; Ungur, L.; Soncini, A. The Origin of Nonmagnetic Kramers Doublets in the Ground State of Dysprosium Triangles: Evidence for a Toroidal Magnetic Moment. *Angew. Chem. Int. Ed.* **2008**, *47*, 4126-4129.

[95] Ungur, L.; Van den Heuvel, W.; Chibotaru, L. F. *Ab initio* Investigation of the Non-Colinear Magnetic Excitations in Dysprosium Triangles. *New J. Chem.* **2009,** *33*, 1224-1230.

[96] Chibotaru, L. F.; Ungur, L.; Aronica, C.; Elmoll, H.; Pilet, G.; Luneau, D. Structure, Magnetism, and Theoretical Study of a Mixed-Valence $Co_3^{II}Co_4^{III}$ Heptanuclear Wheel: Lack of SMM Behavior despite Negative Magnetic Anisotropy. *J. Chem. Am. Soc.* **2008**, *130*, 12445-12455.

[97] Löble, M. W.; Keith, J. M.; Altman, A. B.; Stieber, S. C. E.; Batista, E. R.; Boland, K. S.; Conradson, S. D.; Clark, D. L.; Lezama Pacheo, J.; Kozimor, S. A.; Martin, R. L.; Minasian, S. G.; Olson, A. C.; Scott, B. L.; Shuh, D. K.; Tyliszczak, T.; Wilkerson, M. P.; Zehnder, R. A. Covalency in Lanthanides. An X-ray Absorption Spectroscotpy and Density Functional Theory Study of $LnCl_6^{x-}$ (X = 3, 2). *J. Am. Chem. Soc.* **2015**, *137*, 2506-2523.

[98] Cross, J. N.; Su, J.; Batista, E. R.; Cary, S. K.; Evans, W. J.; Kozimor, S. A.; Mocko, V.; Scott, B. L.; Stein, B. W.; Windorff, C. J.; Yang, P. Covalency in Americium(III) Hexachloride. *J. Am. Chem. Soc.* **2017**, *139*, 8667-8677.

[99] Minasian, S. G.; Batista, E. R.; Booth, C. H.; Clark. D. L.; Keith, J. M.; Kozimor, S. A.; Lukens, W. W.; Martin, R. L.; Shuh, D. K.; Stieber, S. C. E.; Tyliszczak, T.; Wen, X.-D. Quantitative Evidence for Lanthanide-Oxygen Orbital Mixing in CeO_2, PrO_2, and TbO_2. *J. Am. Chem. Soc.* **2017**, *139*, 18052-18064.

[100] Plotkin, J. S.; Shore, S. G. Convenient Preparation and Isolation of Pure Potassium Cyclopentadienyldicarbonylferrate, $K[(\eta^5\text{-}C_5H_5)Fe(CO)_2]$. *Inorg. Chem.* **1981**, *20*, 285-287.

[101] *Gaussian 09, Revision D.01*; M. J. Frisch, G. W. Trucks, H. B. Schlegel, G. E. Scuseria, M. A. Robb, J. R. Cheeseman, G. Scalmani, V. Barone, G. A. Petersson, H. Nakatsuji, X. Li, M. Caricato, A. Marenich, J. Bloino, B. G. Janesko, R. Gomperts, B. Mennucci, H. P. Hratchian, J. V. Ortiz, A. F. Izmaylov,

J. L. Sonnenberg, D. Williams-Young, F. Ding, F. Lipparini, F. Egidi, J. Goings, B. Peng, A. Petrone, T. Henderson, D. Ranasinghe, V. G. Zakrzewski, J. Gao, N. Rega, G. Zheng, W. Liang, M. Hada, M. Ehara, K. Toyota, R. Fukuda, J. Hasegawa, M. Ishida, T. Nakajima, Y. Honda, O. Kitao, H. Nakai, T. Vreven, K. Throssell, J. A. Montgomery, Jr., J. E. Peralta, F. Ogliaro, M. Bearpark, J. J. Heyd, E. Brothers, K. N. Kudin, V. N. Staroverov, T. Keith, R. Kobayashi, J. Normand, K. Raghavachari, A. Rendell, J. C. Burant, S. S. Iyengar, J. Tomasi, M. Cossi, J. M. Millam, M. Klene, C. Adamo, R. Cammi, J. W. Ochterski, R. L. Martin, K. Morokuma, O. Farkas, J. B. Foresman, and D. J. Fox, Gaussian, Inc.: Wallingford CT, 2009.

[102] Becke, A. D. Density Functional Exchange-Energy Approximation with Correct Asymptotic Behavior. *Phys. Rev.* **1988**, *38*, 3098-3100.

[103] Perdew, J. P.; Density-Functional Approximation for the Correlation Energy of the Inhomogenous Electron Gas. *Phys. Rev.* **1986**, *33*, 8822-8824.

[104] Peterson, K. A.; Lu, Q.; Correlation Consistent Basis Sets for Lanthanides: The Atoms La-Lu. *J. Chem. Phys.* **2016**, *145*, 054111-054124.

[105] Peterson, K. A. Energy-Consistent Relativistic Pesudopotentials and Correlation Consistent Basis Sets for the 4d Elements Y-Pd. *J. Chem. Phys.* **2007**, *126*, 124101-124114.

[106] Balabanov, N. B.; Peterson, K. A. Systematically Convergent Basis sets for Transition Metals. I. All-Electron Correlation Consistent Basis sets for 3d Elements Sc-Zn. *J. Chem. Phys.* **2005**, *123*, 064107-064122.

[107] Douglas, M.; Kroll, N. M. Quantum Electrodynamical Corrections to the fine Structure of Helium. *Ann. Phys.* **1974**, *82*, 89-155.

[108] Bader, R. F. W. Atoms in Molecules. *Acc. Chem. Res.* **1985**, *18*, 9-15.

[109] *AIMAll*, Version 17.01.25; Keith, T. A. TK Gristmill Software: Overland Park KS, 2017.

[110] Fonseca Guerra, C.; Snijders, J. G.; te Velde, G.; Baerends, E. J. Towards an order-N DFT Method. *Theor. Chem. Acc.* **1998**, *99*, 391-403.

[111] te Velde, G.; Bickelhaupt, F. M.; Baerends, E. J.; Fonseca Guerra, C.; van Gisbergen, S. J. A.; Snijders, J. G.; Ziegler, T. Chemistry with ADF. *J. Comput. Chem.* **2001**, *22*, 931-967.

[112] ADF2017, SCM, Theoretical Chemistry, Vrije Universiteit, Amsterdam, The Netherlands, http://www.scm.com. List of authors and contributors: E.J. Baerends, T. Ziegler, A.J. Atkins, J. Autschbach, O. Baseggio, D. Bashford, A. Bérces, F.M. Bickelhaupt, C. Bo, P.M. Boerrigter, L. Cavallo, C. Daul, D.P. Chong, D.V. Chulhai, L. Deng, R.M. Dickson, J.M. Dieterich, D.E. Ellis, M. van Faassen, L. Fan, T.H. Fischer, C. Fonseca Guerra, M. Franchini, A. Ghysels, A.

Giammona, S.J.A. van Gisbergen, A. Goez, A.W. Götz, J.A. Groeneveld, O.V. Gritsenko, M. Grüning, S. Gusarov, F.E. Harris, P. van den Hoek, Z. Hu, C.R. Jacob, H. Jacobsen, L. Jensen, L. Joubert, J.W. Kaminski, G. van Kessel, C. König, F. Kootstra, A. Kovalenko, M.V. Krykunov, E. van Lenthe, D.A. McCormack, A. Michalak, M. Mitoraj, S.M. Morton, J. Neugebauer, V.P. Nicu, L. Noodleman, V.P. Osinga, S. Patchkovskii, M.Pavanello, C.A. Peeples, P.H.T. Philipsen, D. Post, C.C. Pye, H. Ramanantoanina, P. Ramos, W. Ravenek, J.I. Rodríguez, P. Ros, R. Rüger, P.R.T. Schipper, D. Schlüns, H. van Schoot, G. Schreckenbach, J.S. Seldenthuis, M. Seth, J.G. Snijders, M. Solà, M. Stener, M. Swart, D. Swerhone, V. Tognetti, G. te Velde, P. Vernooijs, L. Versluis, L. Visscher, O. Visser, F. Wang, T.A. Wesolowski, E.M. van Wezenbeek, G. Wiesenekker, S.K. Wolff, T.K. Woo, A.L. Yakovlev.

[113] Van Lenthe, E; Baerends, E. J. Optimized Slater-type Basis Sets for the Elements 1-118. *J. Comput. Chem.* **2003**, *24*, 1142-1156.

[114] Van Lenthe, E; Baerends, E. J.; Snijders, J. G. Relativistic Regular Two-component Hamiltonians. *J. Chem. Phys* **1993**, *99*, 1156-1170.

[115] Van Lenthe, E; Baerends, E. J.; Snijders, J. G. Relativistic Total Energy using Approximations. *J. Chem. Phys* **1994**, *101*, 9783-9784.

[116] Van Lenthe, E; Ehlers, A.; Baerends, E. J. Geometry Optimizations in the Zero Order Regular Approximation for Relativistic Effects. *J. Chem. Phys* **1999**, *110*, 8943-8954.

[117] Dickie, C. M.; Nippe, M. Magnetization Dynamics of a Heterometallic Dy-isocarbonyl Complex. *Inorg. Chem. Front.* **2016**, *3*, 97-103.

[118] Pugh, T.; Chilton, N. F.; Layfield R. A. A Low-Symmetry Dysprosium Metallocene Single-Molecule Magnet with a High Anisotropy Barrier. *Angew. Chem. Int. Ed.* **2016**, *55*, 1-5.

[119] Burns, C. P.; Wilkins, B. O.; Dickie, C. M.; Latendresse, T. P.; Vernier, L.; Vignesh, K. R.; Bhuvanesh, N. S.; Nippe, M. A Comparative Study of Magnetization Dynamics in Dinuclear Dysprosium Complexes featuring Bridging Chloride or Trifluoromethanesulfonate Ligands. *Chem. Commun.* **2017**, *53*, 8419-8422.

[120] Wylie, W. N. O.; Kang, X.; Luo, Y.; Hou, Z. PNP-Ligated Heterometallic Rare Earth/Ruthenium Hydride Complexes Bearing Phosphinophenyl and Phosphinomethyl Bridging Ligands. *Organometallics* **2014**, *33*, 1030-1043.

[121] CCDC 1833341 (**3-1**) and 1833341 (**3-2**) contain the supplementary crystallographic data for this paper. These data can be obtained free of charge from the Cambridge Crystallographic Data Centre

[122] Karunananda, M. K.; Vázquez, F. X.; Alp, E. E.; Bi, W.; Chattopadhyay, S.; Shibata, T.; Mankad, N. P. Experimental Determination of Redox Cooperativity and Electronic Structures in Catalytically Active Cu-Fe and Zn-Fe Heterobimetallic Complexes. *Dalton Trans.* **2014**, *43*, 13661-13671.

[123] Nakazawa, H.; Ichimura, S.; Nishihara, Y.; Miyoshi, K.; Nakashima, S.; Sakai, H. Bond Character between Iron and Phosphorus in Fe-P(E)YZ (E = O, S: Y, Z = Alkoxy, Amino, Phenyl) as Inferred from ^{57}Fe Mössbauer Measurements. *Organometallics*, **1998**, *17*, 5061-5067.

[124] Kano, N.; Yoshinari, N.; Shibata, Y.; Miyachi, M.; Kawashima, T.; Enomoto, M.; Okazawa, A.; Kojima, N.; Guo, J.-D.; Nagase, S. Anionic Iron Complexes with a Bond between Ate-Type Pentacoordinated Germanium and an Iron Atom. *Organometallics* **2012**, *31*, 8059-8062.

[125] Bader, R. F. W. *Atoms in Molecules: A Quantum Theory*, Clarendon Press, Oxford, 1990, p.xviii, p. 438.

[126] Vlaisavljevich, B.; Miró, P.; Cramer, C. J.; Gagliardi, L.; Infante, I. Liddle, S. T. On the Nature of Actinide- and Lanthanide-Metal Bonds in Heterobimetallic Compounds. *Chem. Eur. J.* **2011**, *17*, 8424-8433.

[127] Gaussian09, Revision D.01, M. J. Frisch et al.,Gaussian, Inc.: Wallingford CT, **2009**.

[128] Krishnan, R.; Binkley, J. S.; Seeger, R.; Pople, J. A. Self-Consistent Molecular Orbital Methods: XX. A Basis Set for Correlated Wave Functions. *J. Chem. Phys.* **1980**, *72*, 650-655.

[129] Foroutan-Nejad, C.; Shahbazian, S.; Marek, R. Toward a Consistent Interpretation of QTAIM: Tortuous Link between Chemical Bonds, Interactions, and Bond/Line Paths. *Chem. Eur. J.* **2014**, *20*, 10140-10152.

[130] Shahbazian, S. Why Bond Critical Points are not “Bond” Critical Points. *Chem. Eur. J.* **2018**, *24*, 5401-5405.

[131] King, R. B. Applications of Metal Carbonyl Anions in the Synthesis of Unusual Organometallic Compounds. *Acc. Chem. Res.* **1970**, *3*, 417-427.

[132] Jiang, S. D.; Wang, B. W.; Wang, Z. M.; Gao, S. A Mononuclear Dysprosium Complex Featuring Single-Molecule Magnet Behavior. *Angew. Chem. Int. Ed.* **2010**, *49*, 7448-7451.

[133] Lunghi, A.; Totti, F.; Sessoli, R.; Sanvito, S. The Role of Anharmonic Phonons in Under-barrier Spin Relaxation of Single-Molecule Magnets. *Nature Communications* **2017**, *8*, 14620-14626.

[134] Anwander, R.; Dolg, M.; Edelmann, F. T. The Difficult Search for Organocerium(IV) Compounds. *Chem. Soc. Rev.* **2017**, *46*, 6697-6709.

[135] Piro, N. A.; Robinson, J. R.; Walsh, P. J.; Schelter, E. J. The Electrochemical Behavior of Cerium(III/IV) Complexes: Thermodynamics, Kinetics, and Applications in Synthesis. *Coord. Chem. Rev.* **2014**, *260*, 21-36.

[136] Yin, H.; Jin, Y.; Hertzog, J. E.; Mullane, K. C.; Carroll, P. J.; Manor, B. C.; Anna, J. M.; Schelter, E. J. The Hexachlorocerate(III) Anion: A Potent, Benchtop Stable, and Readily Available Ultraviolet A Photosensitizer for Aryl Chlorides. *J. Am. Chem. Soc.* **2016**, *138*, 16266-16273.

[137] Qiao, Y.; Yang, Q.; Schelter, E. J. Photoinduced Miyaura Borylation by a Rare-Earth-Metal Reductant: The Hexachlorocerate(III) Anion. *Angew. Chem. Int. Ed.* **2018**, *57*, 10999-11003.

[138] Yin, H.; Carroll, P. J.; Manor, B. C.; Anna, J. M.; Schelter, E. J. Cerium Photosensitizers: Structure-Function Relationships and Applications in Photocatalytic Aryl Coupling Reactions. *J. Am. Chem. Soc.* **2016**, *138,* 5984-5993.

[139] Pointillart, F.; Cador, O.; Le Guennic, B.; Ouahab, L. Uncommon Lanthanide Ions in Purely 4f Single-Molecule Magnets. *Coord. Chem. Rev.* **2017**, *346*, 150-175.

[140] Butovskii, M. V.; Tok, O. L.; Wagner, F. R.; Kempe, R. Bismetallocenes: Lathanoid-Transition Metal Bonds through Alkane Elimination. *Angew. Chem. Int. Ed.* **2008**, *47*, 6469-6472.

[141] Blake, M. P.; Kaltsoyannis, N.; Mountford, P. Heterobimetallic Complexes Containing Ca-Fe or Yb-Fe Bonds: Synthesis and Molecular and Electronic Structures of $[M\{CpFe(CO)_2\}_2(THF)_3]_2$ (M = Ca or Yb). *J. Am. Chem. Soc.* **2011**, *133*, 15358-15361.

[142] D'Angelo, P.; Zitolo, A.; Migliorati, V.; Chillemi, G.; Duvail, M.; Vitorge, P.; Abadie, S.; Spezia, R. Revised Ionic Radii of Lanthanoid(III) Ions in Aqueous Solution. *Inorg. Chem.* **2011**, *50*, 4572-4579.

[143] Burns, C. P.; Yang, X.; Wofford, J. D.; Bhuvanesh, N. S.; Hall, M. B.; Nippe, M. *Angew. Chem. Int. Ed.* **2018**, *57*, 1-6.

[144] XT, XS, BRUKER AXS Inc., 5465 East Cheryl Parkway, Madison, WI, USA, pp. 53711– 5373

[145] Hess, B. A. Relativistic Electronic-Structure Calculations Employing a Two-Component No-Pair Formalism with External-Field Projection Operators. *Phys. Rev. A.* **1986**, *33*, 3742-3748.

[146] ORCA 4.0.0, WIREs Comput Mol Sci 2018, 8:e1327

[147] Pantazis, D. A.; Chen, X.-Y.; Landis, C. R.; Neese, F. All-Electron Scalar Relativistic Basis Sets for Third-Row Transition Metal Atoms. *J. Chem. Theory Comput.* **2008**, *4*, 908-919.

[148] AIMAll, Version 17.01.25; Keith, T. A. TK Gristmill Software: Overland Park KS, 2017

[149] Mahoney, B. D.; Piro, N. A.; Carroll, P. J; Schelter, E. J. Synthesis, Electrochemistry, and Reactivity of Cerium(III/IV) Methylene-Bis-Phenolate Complexes. *Inorg. Chem.* **2013** *52*, 5970-5977.

[150] Le Roy, J. J.; Korobkov, I.; Kim, J. E.; Schelter, E. J.; Murugesu, M. Structural and Magnetic Conformation of a Cerocene $[Ce(COT'')_2]^-$ Exhibiting a Uniconfigurational f^1 Ground State and Slow-Magnetic Relaxation. *Dalton Trans.* **2014**, *43*, 2737-2740.

[151] Upadhyay, A.; Vignesh, K. R.; Das, C.; Kumar Singh, S.; Rajaraman, G.; Shanmugam, M. *Inorg. Chem.* **2017**, *56*, 14260-14276.

[152] Wada, H.; Ooka, S.; Yamamura, T.; Kajiwara, T. Light Lanthanide Complexes with Crown Ether in its Aza Derivative which Show Slow Magnetic Relaxation Behaviors. *Inorg. Chem.* **2017**, *56*, 147-155

[153] Hino, S.; Maeda, M.; Yamashita, K.; Kataoka, Y.; Nakano, M.; Yamamura, T.; Nojiri, H.; Kofu, M.; Yamamuro, O.; Kajiwara, T. Linear Trinuclear Zn(II)-Ce(III)-Zn(II) Complex which Behaves as a Single-Molecule Magnet. *Dalton Trans.* **2013**, *42*, 2683-2686.

[154] N. F. Chilton, *CC Fit*, The University of Manchester, UK, 2014

[155] David, F.; Ionova, G.; Guillaumont, R. E° (3/2) Redox Potentials of Lanthanides and Actinides with f^qd Electron Configuration. *Journal of Radioanalytical and Nuclear Chemistry* **1992**, *1*, 35-40.

[156] Catheline, D.; Astruc, D. Synthesis and Characterization of $C_5(CH_3)_5Fe(CO)_3{}^+PF_6{}^-$ and $C_5(CH_3)_5Fe(CO)_2{}^-K^+$ *Journal of Organometallic Chemistry* **1982**, *226*, C52-C54.

[157] Banerjee, S.; Karunananda, M. K.; Bagherzadeh, S.; Jayarathne, U.; Parmlee, S. R.; Waldhart, G. W.; Mankad, N. P. Synthesis and Characterization of Heterobimetallic Complexes with Direct Cu-M Bonds (M = Cr, Mn, Co, Mo, Ru, W) Supported by *N*-Heterocyclic Carbenes: A Toolkit for Catalytic Reaction Discovery. *Inorg. Chem.* **2014**, *53*, 11307-11315.

[158] Dessy, R. E.; King, R. B.; Waldrop, M. Organometallic Electrochemistry. V. The Transition Series. *J. Am. Chem. Soc.* **1966**, *88*, 5112-5117.

[159] Bursten, B. E.; Gatter, M. G. Molecular Orbital Studies of Organometallic Hydride Complexes. 1. Acidic vs. Hydridic Behavior of some $(\eta^5\text{-}C_5H_5)MLnH$ Systems. *J. Am. Chem. Soc.* **1984**, *106*, 2554-2558.

[160] Beletskaya, I. P.; Suleimanov, G. Z.; Shifrina, R. R.; Mekhdiev, R. Yu. Synthesis and Structure of Metal Carbonyl Derivatives of Lanthanum, Samarium, and Ytterbium. *Journal of Organometallic Chemistry* **1986**, 239-244.

[161] Lohrey, T. D.; Maron, L.; Bergman, R. G.; Arnold, J. Heterotetrametallic Re-Zn-Zn_Re Complex Generated by an Anionic Rhenium(I) β-Diketiminate. *J. Chem. Am. Soc.* **2019**, *141*, 800-804.

[162] Long, Derek A (2002). *The Raman Effect: A Unified Treatment of the Theory of Raman Scattering by Molecules*. Wiley.

[163] Curley, J. J.; Bergman, R. G.; Tilley, T. D. Preparation and Physical Properties of Early-Late Heterobimetallic Compounds Featuring Ir-M Bonds (M = Ti, Zr, Hf). *Dalton Trans.* **2012**, *41*, 192-200.

[164] Shin, K. S. K.; Zink, J. I. Quantitative Evaluation of the Relationships between Excited-State Geometry and the Intensities of Fundamentals, Overtones, and Combination Bands in Resonance Raman Spectra. *Inorg. Chem.* **1989**, *28*, 4358-4366.

[165] Green, A. G.; Kiesz, M. D.; Oria, J. V.; Elliot, A. G.; Buechler, A. K.; Hohenberger, J.; Meyer, K.; Zink, J. I.; Diaconescu, P. L. Characterization of an Iron-Ruthenium Interaction in a Ferrocene Diamide Complex. *J. Am. Chem. Soc.* **2013**, *52*, 5603-5610.

[166] Sato, M.; Sekino, M; Akabori, S. Pd(BF)$_2$ Complexes of 1,1'-bis(alkyl- of aryl-)thio]- and 1,1'-bis(diphenylphosphino)-ferrocenes. Bond Formation between Fe and Pd Atoms. *Journal of Organometallic Chemistry* **1988**, *344,* C31-C34.

[167] Liu, J.-L.; Chen, Y.-C.; Tong, M.-L. Symmetry Strategies for High Performance Lanthanide-Based-Single-Molecule Magnets. *Chem Soc. Rev.* **2018**, *47,* 2431-2453.

APPENDIX A

APPENDIX TO CHAPTER 2: A COMPARATIVE STUDY OF MAGNETIZATION DYNAMICS IN DINUCLEAR DYSPROSIUM COMPLEXES FEATURING BRIDGING CHLORIDE OR TRIFLUOROMETHANESULFONATE LIGANDS

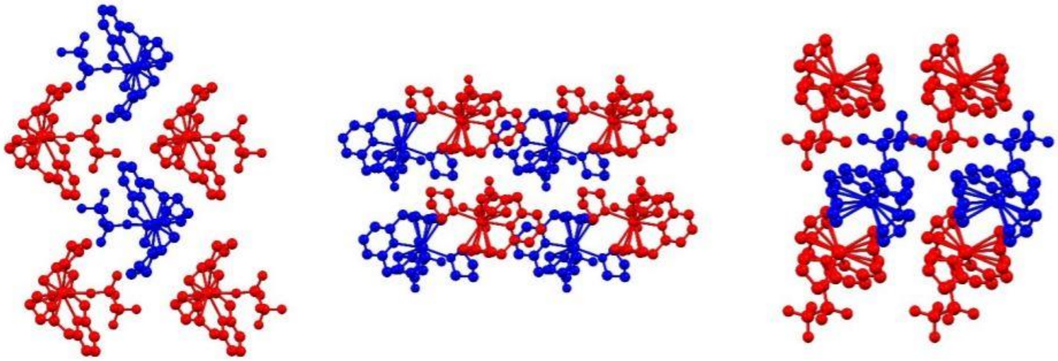

Figure A.1: Packing diagram for **2-3** viewing along a-(left), b-(center), and c-axis (right).

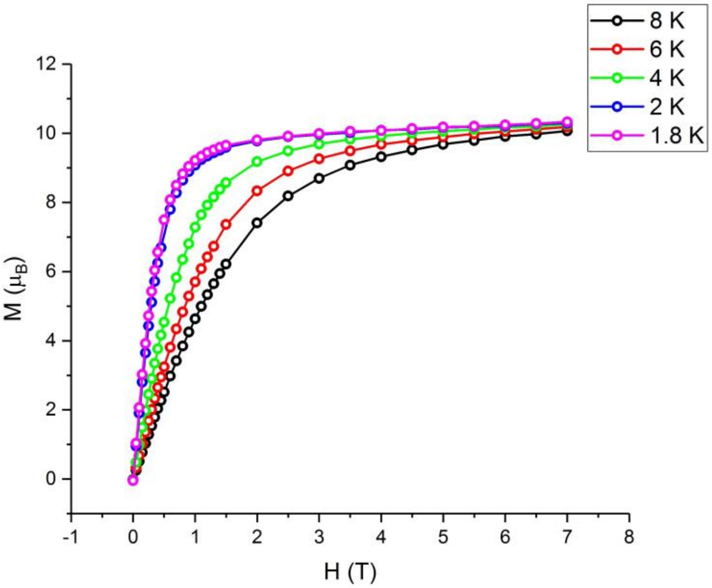

Figure A.2: Plot of Magnetization vs. Field at 8-1.8 K for **2-1**.

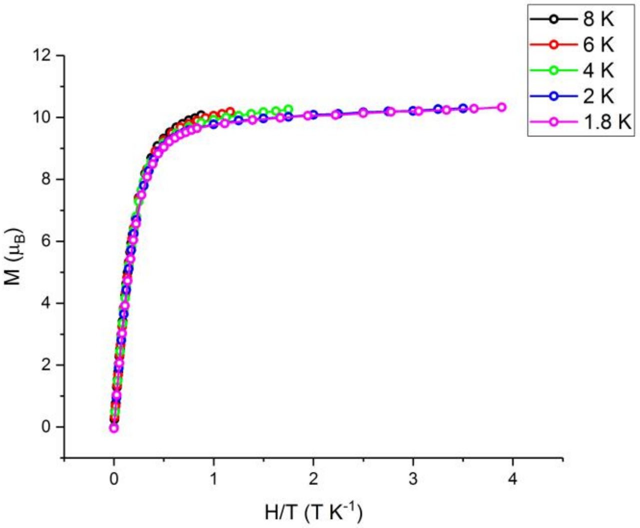

Figure A.3: Plot of Magnetization vs. H/T at 8-1.8 K for **2-1**.

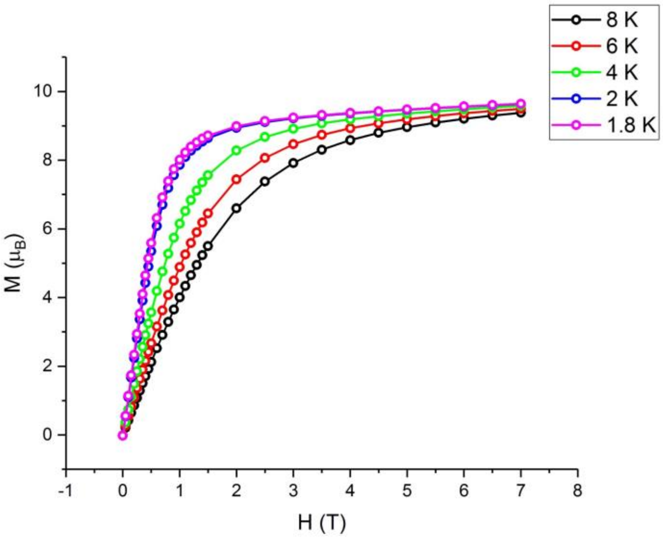

Figure A.4: Plot of Magnetization vs. Field at 8-1.8 K for **2-2**.

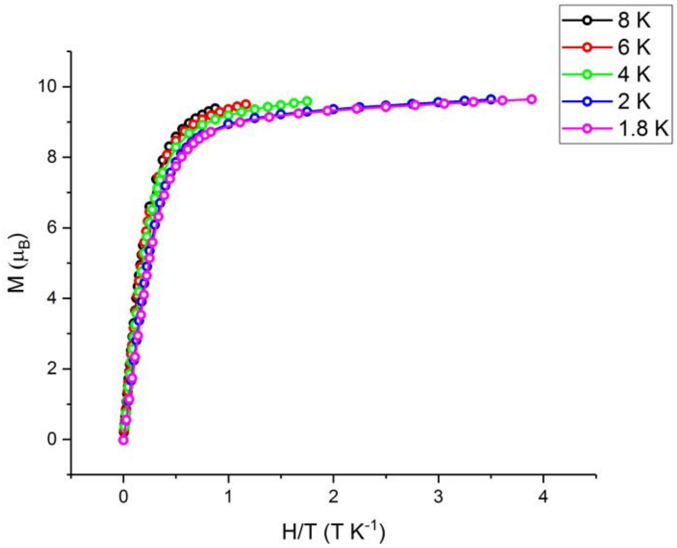

Figure A.5: Plot of Magnetization vs. H/T at 8-1.8 K for **2-2**.

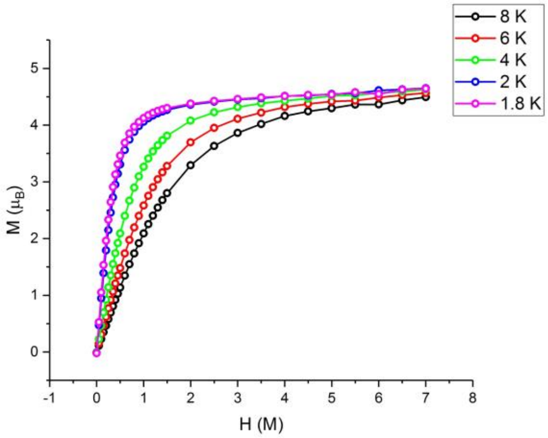

Figure A.6: Plot of Magnetization vs. Field at 8-1.8 K for **2-3**

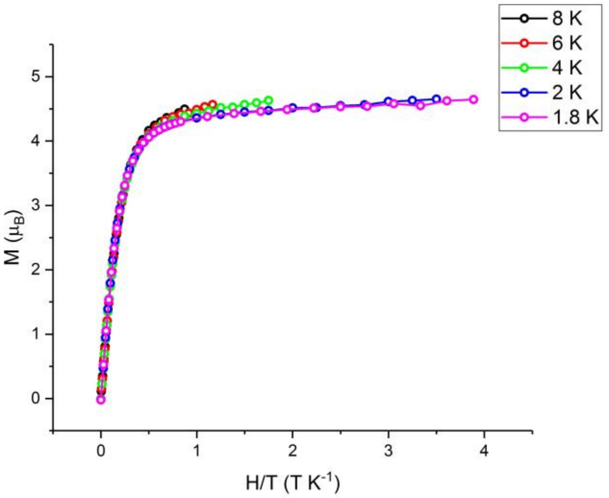

Figure A.7: Plot of Magnetization vs. H/T at 8-1.8 K for **2-3**.

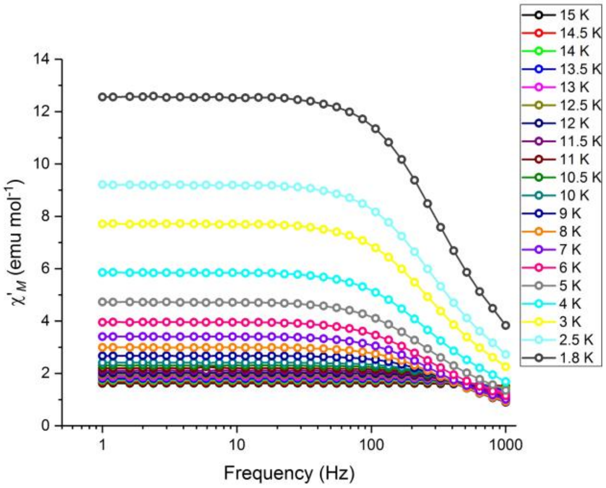

Figure A.8: Frequency dependence of the in-phase component (χ_M') of **2-1**.

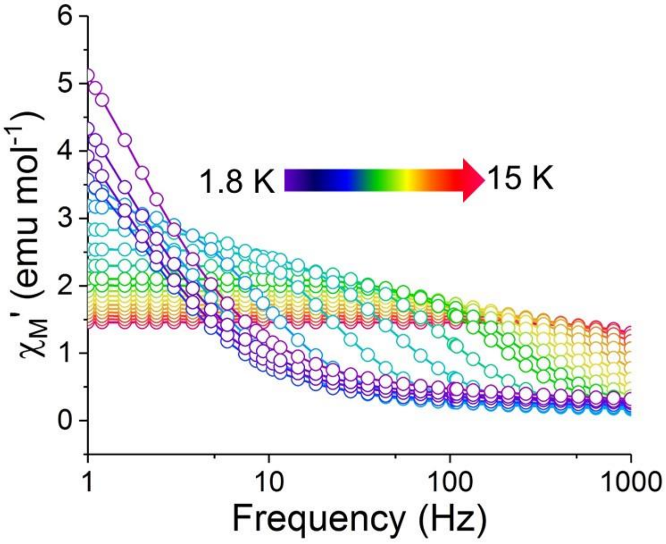

Figure A.9: Frequency dependence of the in-phase component (χ_M') of **2-2**.

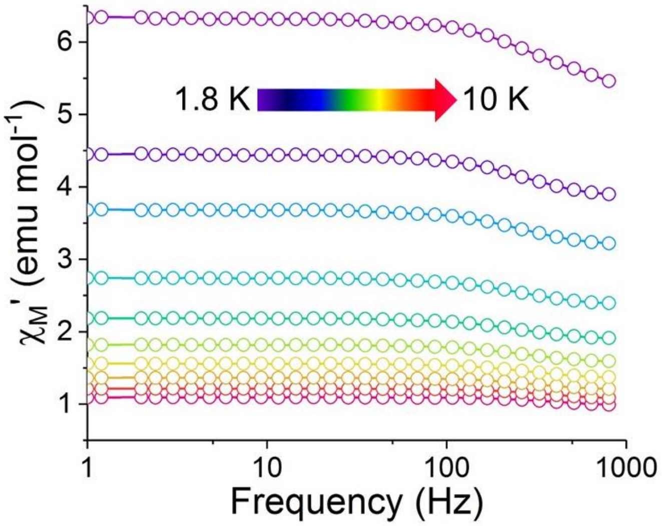

Figure A.10: Frequency dependence of the in-phase component (χ_M') of **2-3**.

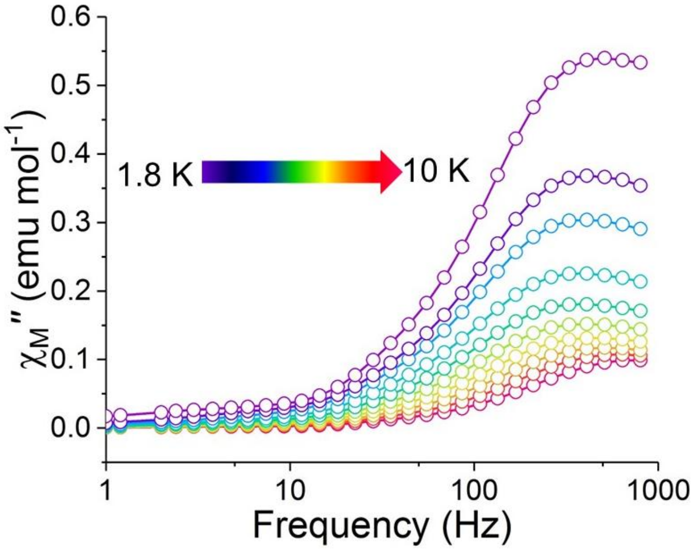

Figure A.11: Frequency dependence of the out-of-phase component (χ_M'') of **2-3**.

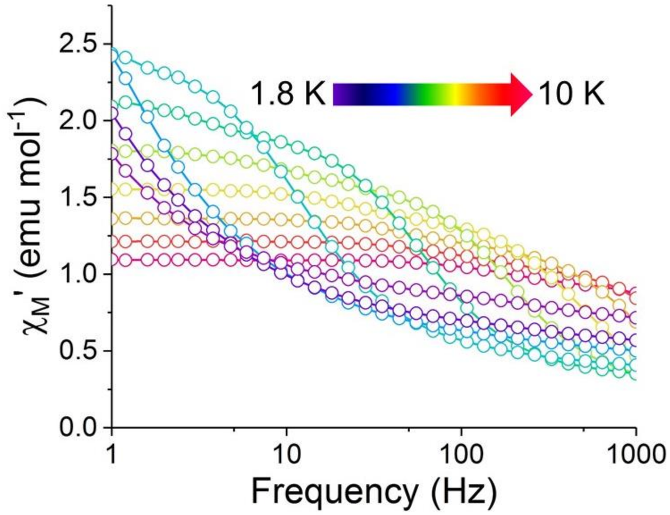

Figure A.12: Frequency dependence of the in-phase component (χ_M') of **2-3**, 1000 Oe.

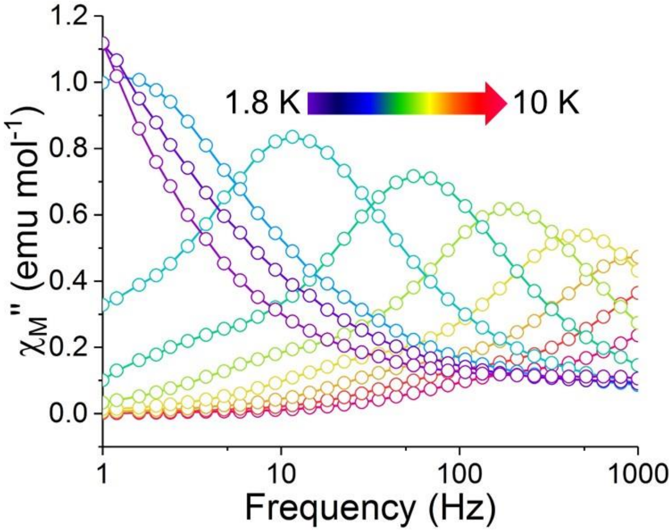

Figure A.13: Frequency dependence of the out-of-phase (χ_M'') of **2-3,** 1000 Oe.

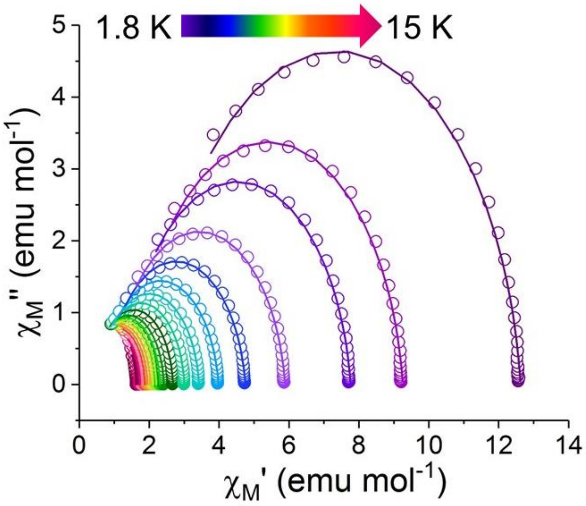

Figure A.14: Cole-Cole plots under zero dc field for **2-1**.

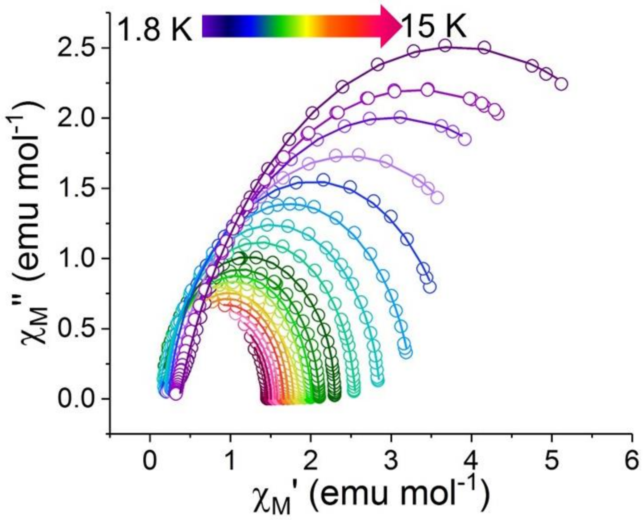

Figure A.15: Cole-Cole plots under zero dc field for **2-2**.

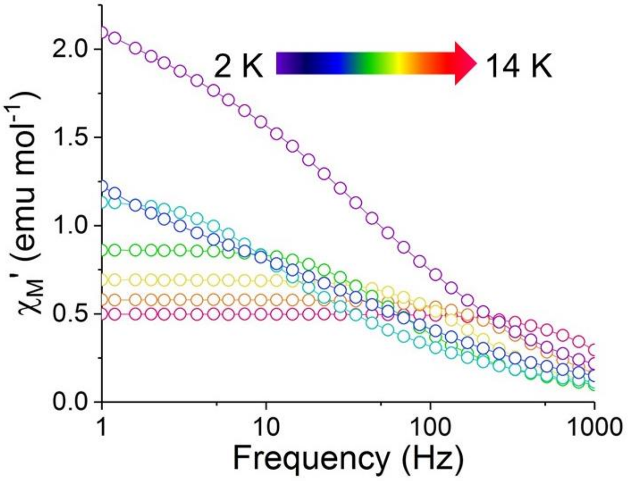

Figure A.16: Frequency dependence of the in-phase component (χ_M’) of dilute **2-1**.

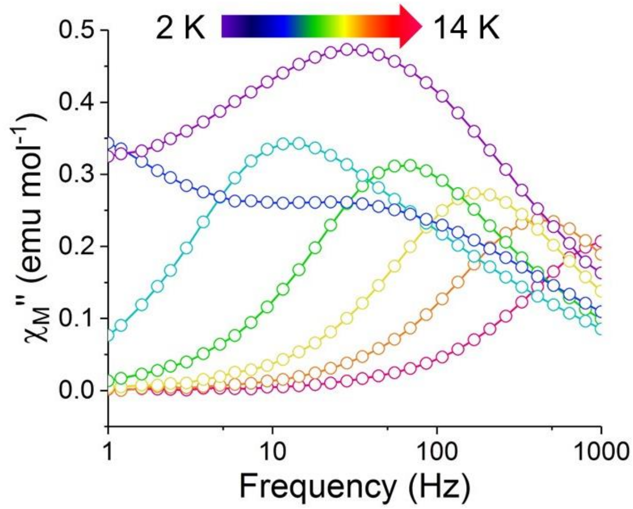

Figure A.17: Frequency dependence of out-of-phase (χ_M'') of dilute **2-1**.

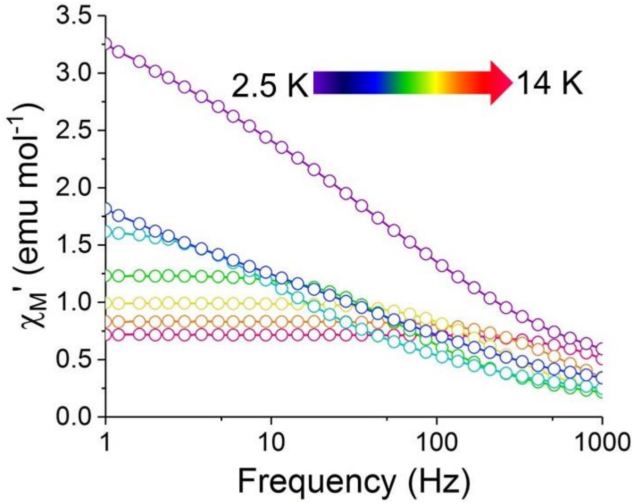

Figure A.18: Frequency dependence of the in-phase component (χ_M') of dilute **2-2**.

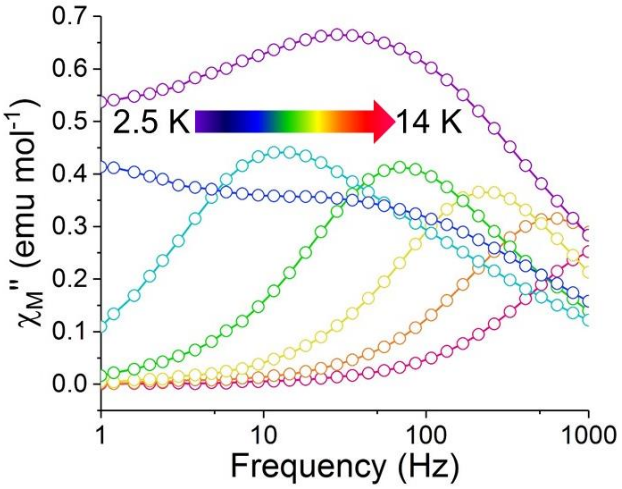

Figure A.19: Frequency dependence of (χ_M'') of dilute **2-2**.

Table A.1: Crystallographic Data for **2-1**, **2-2**, and **2-3**.

Compound	**2-1·CH_2Cl_2**	**2-2·CH_2Cl_2**	**2-2(thf)**
Formula	$C_{36}H_{34}Cl_4Dy_2F_6N_2O_6S_2$	$C_{35.76}H_{33.53}Dy_2N_2$	$C_{22}H_{23}DyF_3NO_4S$
Crystal system	Triclinic	Monoclinic	Triclinic
Space group	P-1	$P2_1/n$	P-1
a, Å	12.259(1)	14.876(1)	8.2141(3)
b, Å	13.208(1)	7.1590(7)	11.0008(4)
c, Å	13.751(1)	16.663(2)	12.1504(5)
α,°	92.254(4)	90	82.426(2)
β,°	90.145(4)	92.235(4)	78.374(2)
γ, °	107.140(4)	90	88.147(2)
Volume, $Å^3$	2096.9(3)	1773.3(3)	9937.9(14)
Z	2	2	2
T, K	110	110	110
ρ_{calcd} (mg/m^3)	1.995	1.896	1.922
F(000)	1220	976	606
Θ_{min}, Θ_{max}, °	1.482, 25	3.908, 62.443	1.725, 27.664
$R_1{}^a$, $wR_2{}^b$ ($I > 2\sigma(I)$)	0.0617, 0.1560	0.0678, 0.1748	0.0149, 0.0361
$R_1{}^a$, $wR_2{}^b$ (all data)	0.0773, 0.1690	0.0831, 0.1845	0.0169. 0.0373

$^{a}R_1 = 3||F_o|-|F_c||/3|F_o|$. $^{b}wR_2 = [3[w(F_o^2 - F_c^2)^2]/3[w(F_o^2)^2]]^{1/2}$, $w = 1/\sigma^2(F_o^2) + (aP)^2 + bP$, where $P = [\max(0 \text{ or } F_o^2) + 2(F_c^2)]/3$.

Table A.2: Selected Bond Lengths and angles in molecular structures **2-1**, **2-2**, and **2-3**.

	2-1	**2-2**	**2-3**
Dy-C, Å (range)	2.5911-2.657(13)	2.61(1)-2.68(1)	2.587(2)-2.669(2)
	2.603(12)-2.670(13)	-	-
Dy-N, Å	2.562(9)	2.581(9)	25375(16)
	2.546(9)	-	-
Dy-O, Å (triflate)	2.322(9), 2.354(8)	-	2.3352(14)
	2.315(8), 2.376(8)	-	-
Dy-O, Å (thf)	-	-	2.4560(13)
O-Dy-O, °	75.4(3)	-	72.99(5)
	75.6(3)	-	-
Dy-Cl, Å	-	2.683(3), 2.785(3)	-
Cl-Dy-Cl, °	-	77.94(9)	-

Table A.3: Calculated g-tensor for Kramer's doublets of individual Dy sites.

Kramers doublet	g-tensor components	**1**		**2-3**	**2-2**	
1		Dy 1	Dy 2	Dy	Dy 1	Dy 2
	g_x	0.0083	0.0083	0.0995	0.0081	0.0082
	g_y	0.0250	0.0249	0.2004	0.0226	0.0227
	g_z	19.3038	19.2283	18.7695	19.0501	19.1629
2	g_x	1.2368	1.2365	0.2639	0.2529	0.2543
	g_y	6.7989	6.7729	0.9190	0.9696	0.9741
	g_z	12.5748	12.5515	17.9002	15.9790	16.0269
3	g_x	0.6673	0.6575	7.5583	2.8529	2.8664
	g_y	3.8125	3.8120	7.1917	3.3862	3.4131
	g_z	7.3693	7.3392	4.0711	14.1677	14.2213
4	g_x	2.8646	2.8650	3.8984	2.1680	2.1828
	g_y	4.4304	4.4306	4.9813	3.8553	3.8731
	g_z	10.8902	10.8632	8.5726	12.2455	12.2824
5	g_x	1.5013	1.4897	0.8492	0.6206	0.6193
	g_y	1.6700	1.6659	4.0447	1.0619	1.0724
	g_z	15.0689	15.0696	9.5789	15.5567	15.5648
6	g_x	8.6380	8.6308	4.8145	8.2151	8.2826
	g_y	6.9324	6.9118	5.9396	7.9019	7.9017
	g_z	3.3646	3.3529	7.8326	3.6546	3.6824
7	g_x	0.2139	0.2097	1.0721	0.1068	0.1122
	g_y	0.9202	0.9192	1.8331	2.1232	2.1333
	g_z	15.7195	15.6790	13.7933	13.1789	13.2285
8	g_x	0.4479	0.4472	0.0298	1.0347	1.0348

Table A.4: Lowest exchange doublets arising from magnetic coupling.

#	Energy (cm^{-1})	Tunneling splitting (cm^{-1})	g_z
1	0.000000000000 0.000001275082	1.28×10^{-6}	38.532
2	0.239069593853 0.239071092639	1.50×10^{-6}	0.081
3	**138.005807071743** **138.006292097241**	$\mathbf{4.85 \times 10^{-4}}$	**31.648**
4	138.127649799422 138.133378788417	5.73×10^{-3}	28.514
5	138.154082220392 138.159893316113	5.81×10^{-3}	0.368
6	138.274405289145 138.275070635627	6.65×10^{-4}	0.232

Table A.5: Lowest exchange doublets arising from magnetic coupling.

#	Energy (cm^{-1})	Tunneling splitting (cm^{-1})	g_z
1	0.000000000000 0.000001593754	1.59×10^{-6}	0.130
2	1.582867138374 1.582869352357	2.21×10^{-6}	38.211
3	133.742118771048 133.742136639318	1.79×10^{-5}	0.102
4	133.953725623240 133.953815131459	8.95×10^{-5}	0.082
5	135.098096546347 135.098169984440	7.34×10^{-5}	35.068
6	**135.247962328973** **135.248102733045**	$\mathbf{1.40 \times 10^{-4}}$	**35.070**

APPENDIX B

APPENDIX FOR CHAPTER 3: STRUCTURE AND MAGNETIZATION DYNAMICS OF DY−FE AND DY−RU BONDED COMPLEXES

Table B.1: Crystallographic Data for **3-1** and **3-2**.

Compound	**$(PyCp_2)DyFe(Cp)(CO)_2$ (1)**	**$(PyCp_2)DyRu(Cp)(CO)_2$ (2)**
Formula	$C_{24}H_{20}DyFeNO_2$	$C_{24}H_{20}DyNO_2Ru$
Crystal system	Orthorhombic	Orthorhombic
Space group	Pnma	Pnma
a, Å	16.055(6)	16.209(2)
b, Å	13.092(5)	13.082(2)
c, Å	9.136(4)	9.134(1)
α,°	90	90
β,°	90	90
γ, °	90	90
Volume, Å^3	1920.3(13)	1936.9(4)
Z	4	4
T, K	110	110
ρ_{calcd} (mg/m$_3$)	1.981	2.119
F(000)	1116	1188
Θ_{min}, Θ_{max}, °	2.537, 24.983	2.513, 25.242
R_1^a, wR_2^b ($I > 2\sigma(I)$)	0.0407, 0.0892	0.0215, 0.0525
R_1^a, wR_2^b (all data)	0.0620, 0.1000	0.0525, 0.0540

$^aR_1 = 3||F_o|-|F_c||/3|F_o|$. $^bwR_2 = [3[w(F_o^2 - F_c^2)^2]/3[w(F_o^2)^2]]^{½}$, $w = 1/\sigma^2(F_o^2) + (aP)^2 + bP$, where $P = [\max(0 \text{ or } F_o^2) + 2(F_c^2)]/3$.

Table B.2: Selected interatomic distances observed for **3-1** and **3-2**.

distances, Å	**3-1** (TM = Fe)	**3-2** (TM = Ru)
Dy-TM	2.883(2)	2.9508(5)
Dy-N	2.452(9)	2.470(3)
Dy-C	2.644(7)	2.640(3)
	2.671(7)	2.594(3)
	2.646(7)	2.593(3)
	2.584(7)	2.650(3)
	2.597(7)	2.680(3)
TM-C(CO)	1.716(9)	1.834(3)
TM-C(Cp)	2.09(1)	2.286(4)
	2.101(7)	2.270(3)
	2.106(8)	2.295(3)

Table B.3: Results from QTAIM Analyses (G09).

Compound	**$(PyCp_2)DyFe(Cp)(CO)_2$ (3-1)**	**$(PyCp_2)DyRu(Cp)(CO)_2$ (3-2)**
d(Dy-TM), Å	2.88305	2.95182
d(Dy-LCP), Å	1.44	1.41
d(LCP-TM), Å	1.44	1.54
DI (Dy, TM)	0.45	0.43
ρ(lcp)[a]	0.036	0.04
$\nabla^2\rho$ (lcp)[b]	0.047	0.061
G (lcp)[d]	0.019	0.023
V(lcp)[d]	-0.026	-0.031
H(lcp)[e]	-0.007	-0.008

[a] ρ (lcp): Electron density at line critical point (e/bohr^3)

[b] $\nabla^2\rho$ (lcp): Laplacian of electron density (e/bohr^5)

[c] G (lcp): Lagrangian form of kinetic energy density (hartree/bohr^3)

[d] V (lcp): Virial Field = Potential energy density (hartree/bohr^3)

[e] H (lcp): Electronic energy density (hartree/bohr^3)

Table B.4: Results from QTAIM Analyses (ADF, Crystal Structure).

Compound	**(PyCp$_2$)DyFe(Cp)(CO)$_2$ (3-1)**	**(PyCp$_2$)DyRu(Cp)(CO)$_2$ (3-2)**
d(Dy-TM), Å	2.88305	2.95182
d(Dy-LCP), Å	1.44	1.41
d(LCP-TM), Å	1.44	1.54
DI (Dy, TM)	0.4374	0.422
ρ(lcp)[a]	0.036	0.04
$\nabla^2\rho$ (lcp)[b]	0.045	0.058
G (lcp)[d]	0.019	0.023
V(lcp)[d]	-0.026	-0.032
H(lcp)[e]	-0.007	-0.008

[a] ρ (lcp): Electron density at line critical point (e/bohr^3)
[b] $\nabla^2\rho$ (lcp): Laplacian of electron density (e/bohr^5)
[c] G (lcp): Lagrangian form of kinetic energy density (hartree/bohr^3)
[d] V (lcp): Virial Field = Potential energy density (hartree/bohr^3)
[e] H (lcp): Electronic energy density (hartree/bohr^3)

Table B.5: Results from QTAIM Analyses (ADF, Geometry Optimized Structure).

Compound	**(PyCp$_2$)DyFe(Cp)(CO)$_2$ (3-1)**	**(PyCp$_2$)DyRu(Cp)(CO)$_2$ (3-2)**
d(Dy-TM), Å	2.86	2.95
d(Dy-LCP), Å	1.44	1.41
d(LCP-TM), Å	1.42	1.54
DI (Dy, TM)	0.4748	0.4826
ρ(lcp)[a]	0.037	0.04
$\nabla^2\rho$ (lcp)[b]	0.046	0.054
G (lcp)[d]	0.02	0.022
V(lcp)[d]	-0.028	-0.032
H(lcp)[e]	-0.009	-0.009

[a] ρ (lcp): Electron density at line critical point (e/bohr^3)
[b] $\nabla^2\rho$ (lcp): Laplacian of electron density (e/bohr^5)
[c] G (lcp): Lagrangian form of kinetic energy density (hartree/bohr^3)
[d] V (lcp): Virial Field = Potential energy density (hartree/bohr^3)
[e] H (lcp): Electronic energy density (hartree/bohr^3)

Table B.6: Results obtained from fitting the field dependence of **3-1** and **3-2**.

	3-1	**3-2**
A, $s^{-1}K^{-1}T^{-4}$	1550	3124
B_1, s^{-1}	750	267
B_2, T^{-2}	9920	778
D, s^{-1}	0	10.07

Table B.7: Parameters obtained from fitting of the Arrhenius Plots of **3-1** and **3-2**.

Compound	**3-1**	**3-2**
A, $s^{-1}K^{-1}T^{-4}$	1550	3124
C, $s^{-1}K^{-5}$	0.0017	0.012
τ_{QTM}, s	0.300	0.0746
τ^{-1}_{QTM}, s^{-1}	3.32	13.4
n_2,	5	5
U_{eff}, cm^{-1}	43.0	45.5
τ_0, s	$1.00*10^{-6}$	$5.36*10^{-7}$

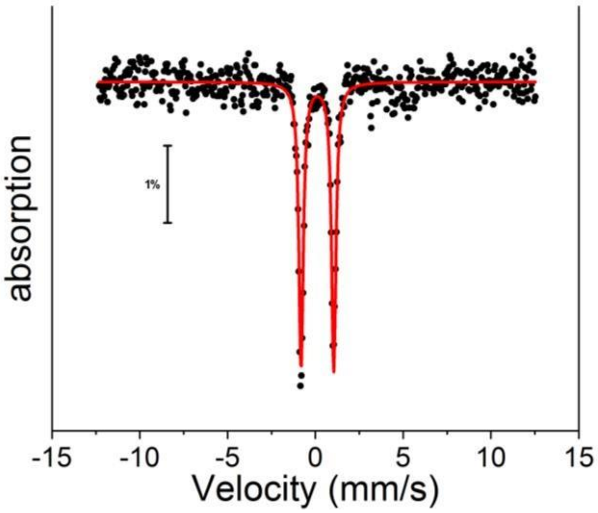

Figure B.1: ^{57}Fe Mössbauer of **3-1** at 120 K.

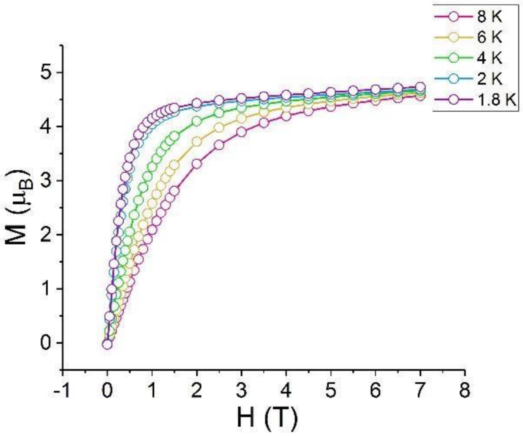

Figure B.2: Magnetization versus field of **3-1** at indicated temperatures.

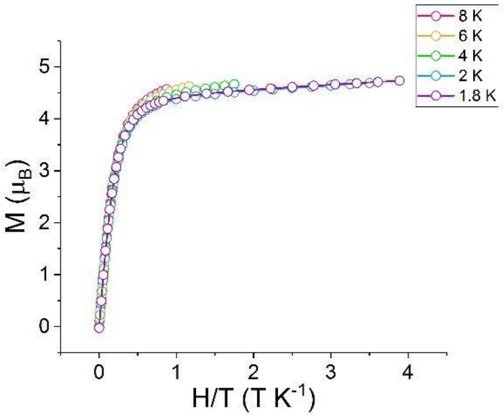

Figure B.3: Magnetization versus H/T of **3-1** at indicated temperatures.

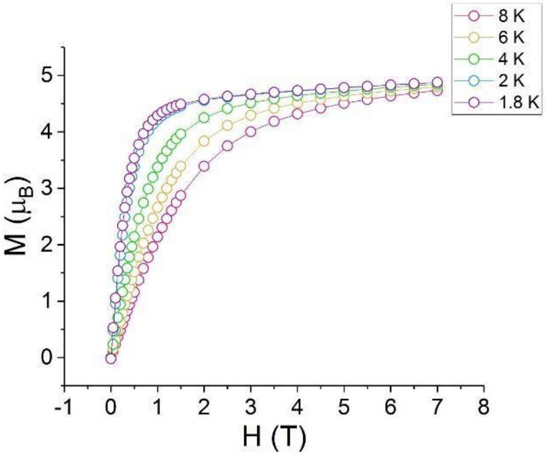

Figure B.4: Magnetization versus field of **3-2** at indicated temperatures.

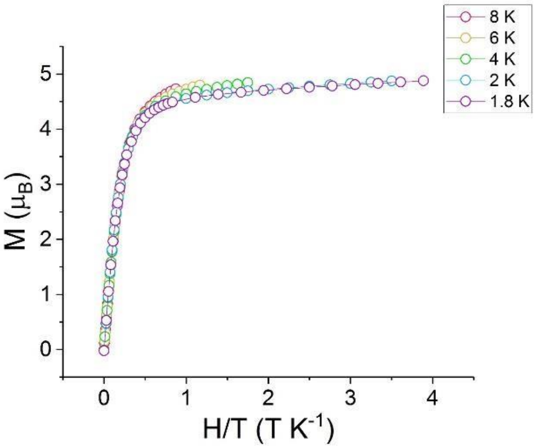

Figure B.5: Magnetization versus H/T for 3-2 at indicated temperatures.

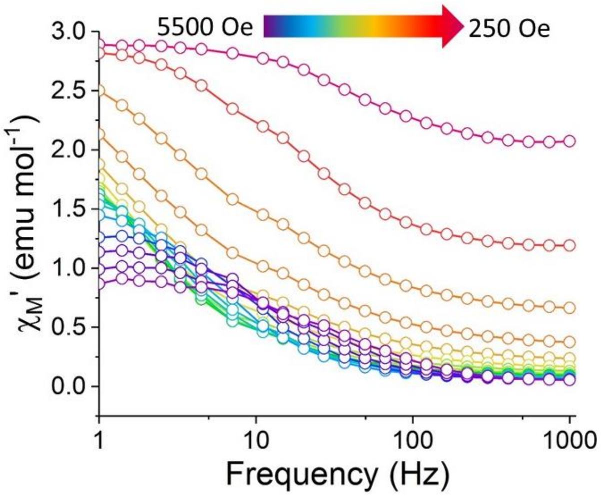

Figure B.6: Frequency dependence of the in-phase component (χ_M') of **3-1**.

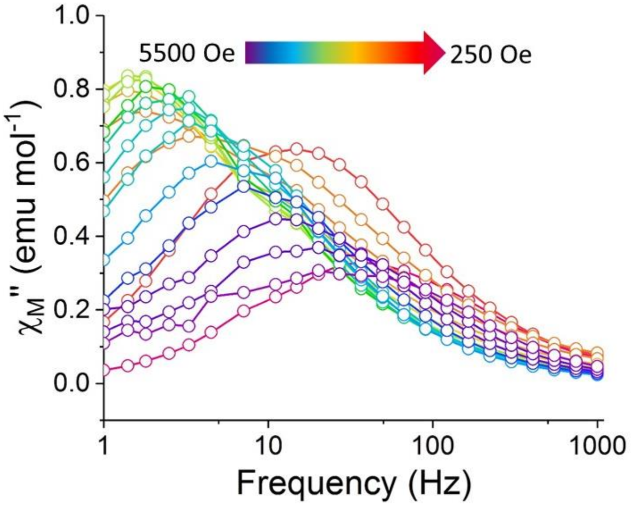

Figure B.7: Frequency dependence of the out-of-phase component (χ_M'') **3-1**.

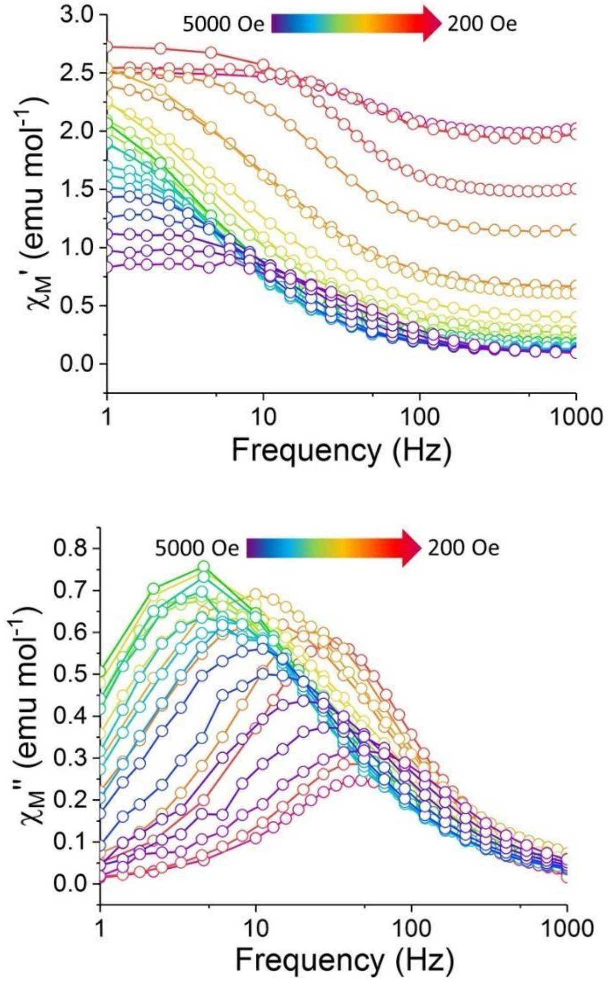

Figure B.8: In-phase (χ'_M) and out-of-phase (χ''_M) components of **3-2**.

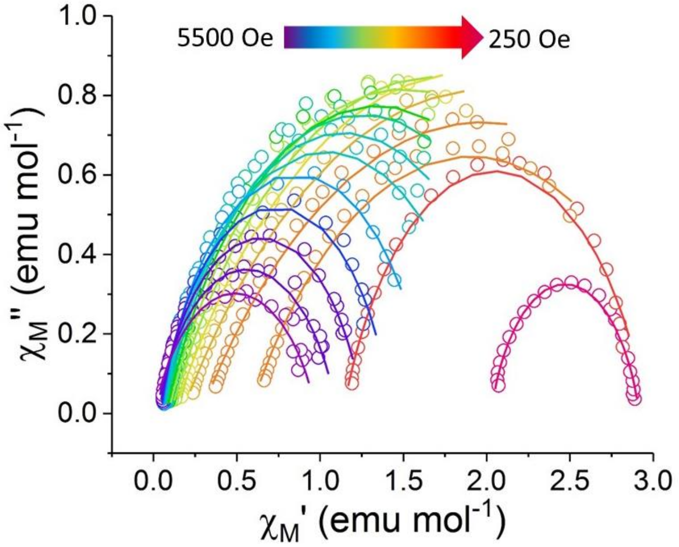

Figure B.9: Cole-Cole plots for **3-1** with varying dc fields at 4 K.

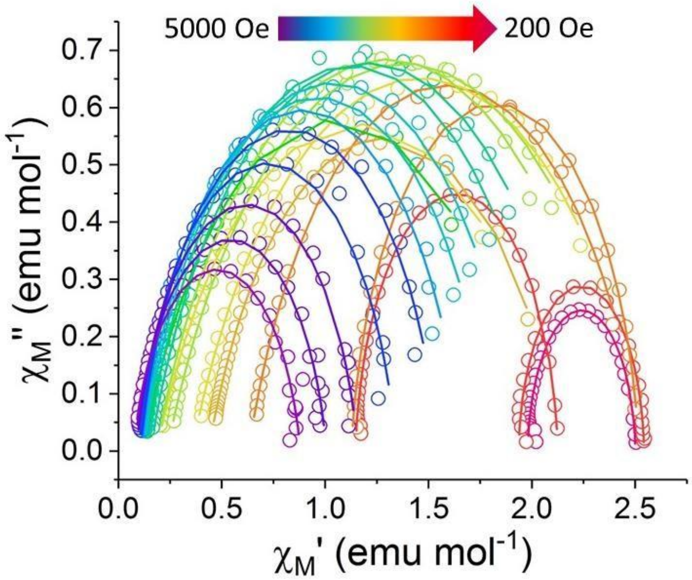

Figure B.10: Cole-Cole plots for **3-2** with varying dc fields at 4 K.

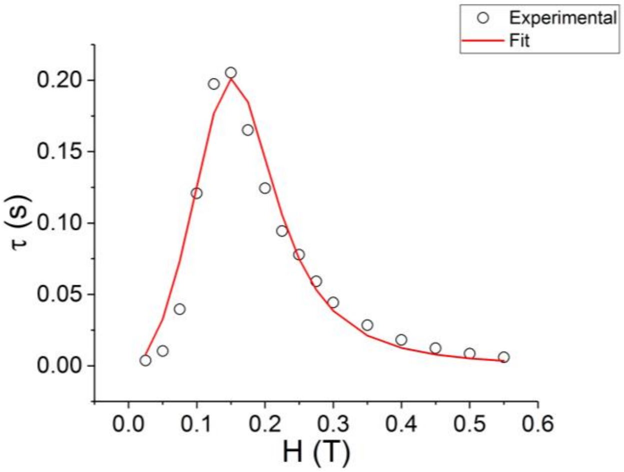

Figure B.11: Field dependence of τ for **3-1** at 4 K.

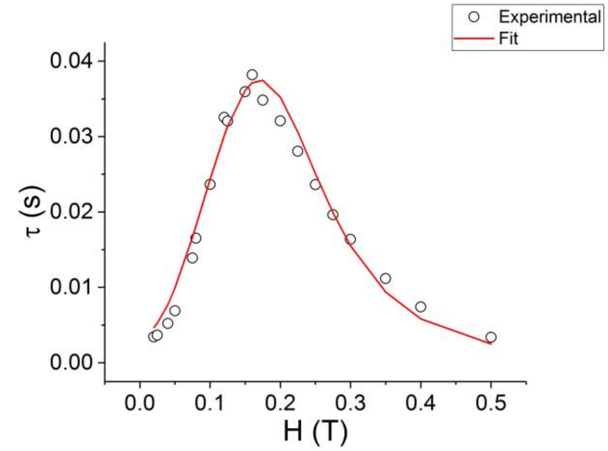

Figure B.12: Field dependence of τ for **3-2** at 4 K.

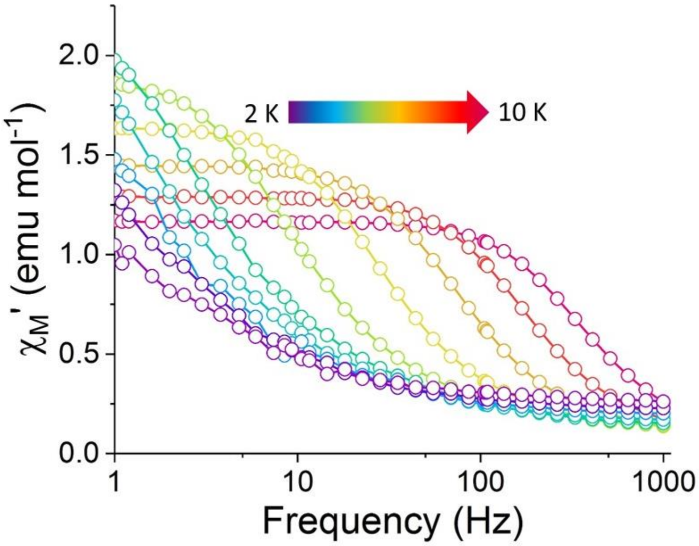

Figure B.13: Frequency of the in-phase (χ_m’) component of **3-1**.

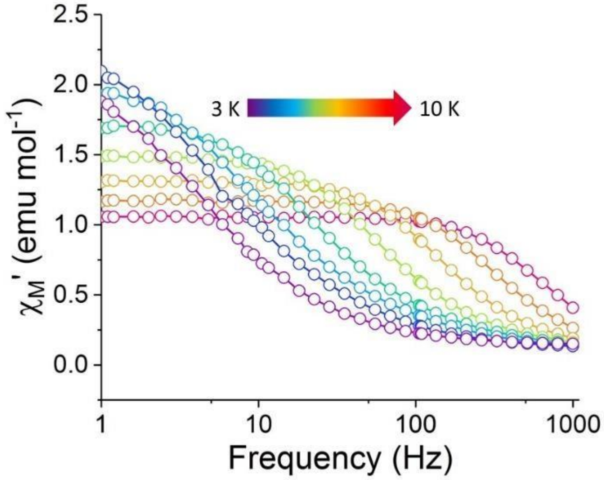

Figure B.14: Frequency of the in-phase (χ_m’) component of **3-2**.

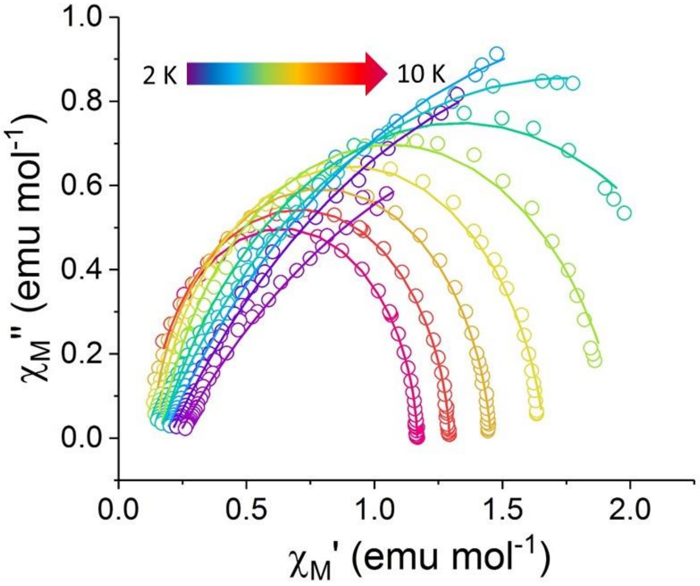

Figure B.15: Cole-Cole plots for **3-1** under 1500 Oe dc field.

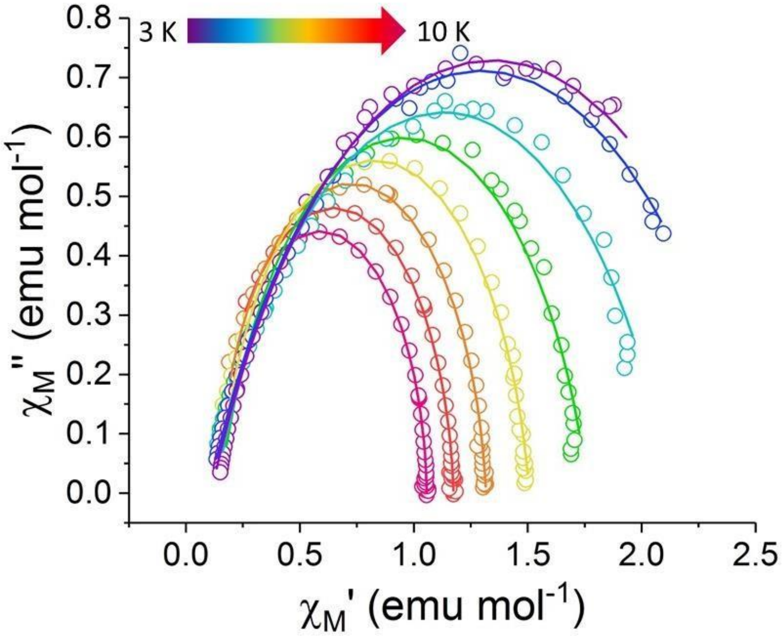

Figure B.16: Cole-Cole plots for **3-2** under 1600 Oe dc field.

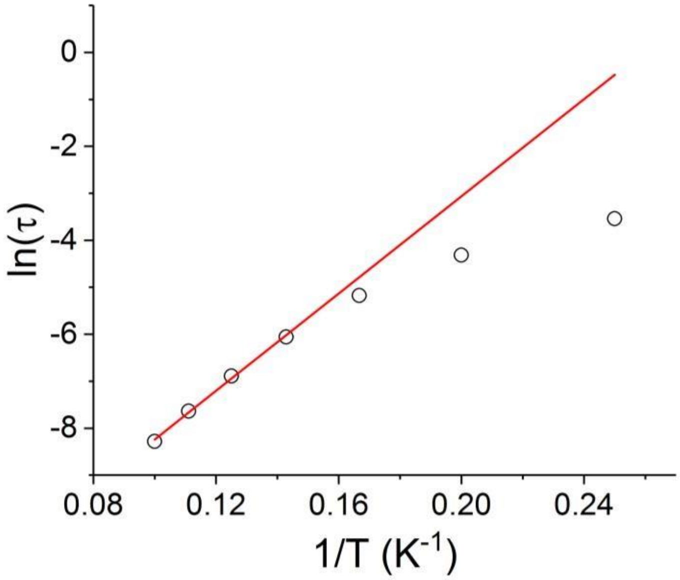

Figure B.17: Arrhenius plot for **3-1** (linear fit).

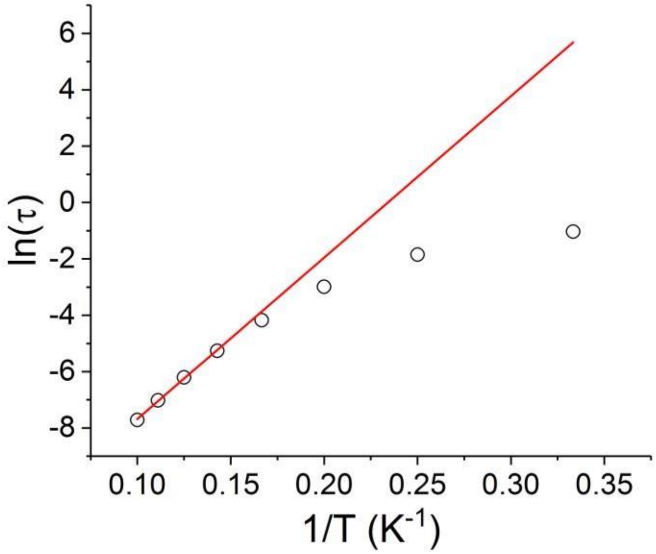

Figure B.18: Arrhenius plot for **3-2** (linear fit).

APPENDIX C

APPENDIX FOR CHAPTER 4: TOWARDS UNDERSTANDING OF LANTHANIDE–TRANSITION METAL BONDING: INVESTIGATIONS OF THE FIRST CE–FE BONDED COMPLEX

Table C.1: Crystallographic Data for **4-1**, **4-2**, and **4-3**.

Compound	**4-1**	**4-2**	**4-3**
Formula	$C_{28}H_{28}CeFeNO_3$	$C_{36}H_{30}Ce_2F_6N_2O_6S_2$	$C_{22}H_{23}CeF_3NO_4S$
Crystal system	Orthorhombic	Monoclinic	Orthorhombic
Space group	Pnma	$P2_1/n$	$Pna2_1$
a, Å	17.612(2)	9.9043(3)	14.8353(4)
b, Å	13.421(2)	9.2078(2)	9.9906(3)
c, Å	10.146(1)	30.3459(6)	15.3663(4)
α,°	90	90	90
β,°	90	102.970(1)	90
γ, °	90	90	90
Volume, $Å^3$	2398(1)	1808.2(1)	2277.5(1)
Z	4	2	4
T, K	110	110	110
ρ_{calcd} (mg/m^3)	1.724	1.919	1.734
F(000)	1244	1020	1180
Θ_{min}, Θ_{max}, °	4.637, 27.498	2.054, 27.499	2.432, 32.990
R_1[a], wR_2[b] ($I > 2\sigma(I)$)	0.0195, 0.0444	0.0165, 0.0380	0.0242, 0.0453
R_1[a], wR_2[b] (all data)	0.0226, 0.0464	0.0174, 0.0384	0.0425. 0.0520

[a] $R_1 = 3||F_o|-|F_c||/3|F_o|$. [b] $wR_2 = [3[w(F_o^2 - F_c^2)^2]/3[w(F_o^2)^2]]^{½}$, $w = 1/\sigma^2(F_o^2) + (aP)^2 + bP$, where $P = [\max(0 \text{ or } F_o^2) + 2(F_c^2)]/3$.

Table C.2: Selected bond lengths and angles in molecular structures of **4-1**, **4-2**, and **4-3**.

	4-1	**4-2**	**4-3**
Ce-C, Å (min-max range)	2.759(2) – 2.827(2)	2.730(2) – 2.794(2)	2.712(4) – 2.825(4)
Ce-N, Å	2.779(2)	2.621(2)	2.618(3)
Ce-Fe, Å	3.1546(5)	-	-
Ce-O, Å (triflate)	-	2.561(1)	2.749(3)
	-	2.546(1)	2.697(3)
Ce-O, Å (thf)	2.533(2)	-	2.556(3)
O-Ce-O, °	-	77.22(4)	76.5(1)
	-		75.4(1)
Fe-Ce-O, °	86.67(5)	-	-

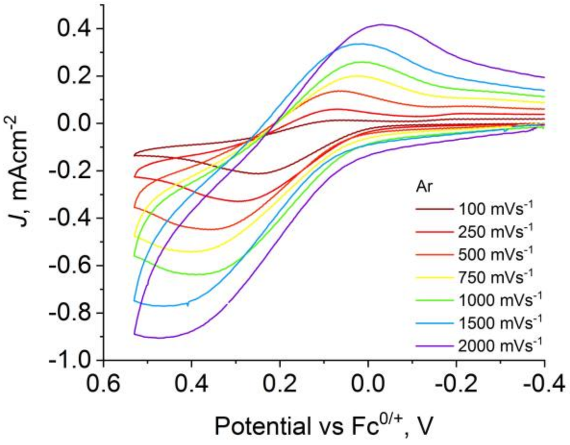

Figure C.1: Cyclic voltammograms of **4-3**.

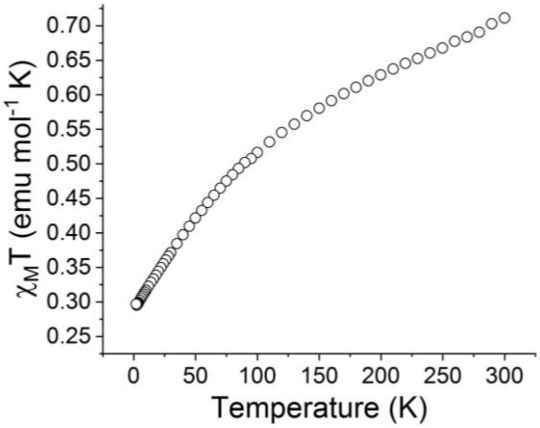

Figure C.2: Temperature dependence of χ_MT at 1000 Oe field for **4-1**.

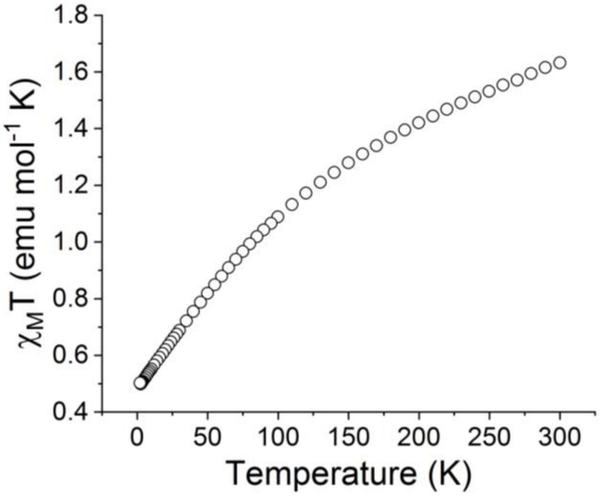

Figure C.3: Temperature dependence of χ_MT at 1000 Oe field for **4-2**.

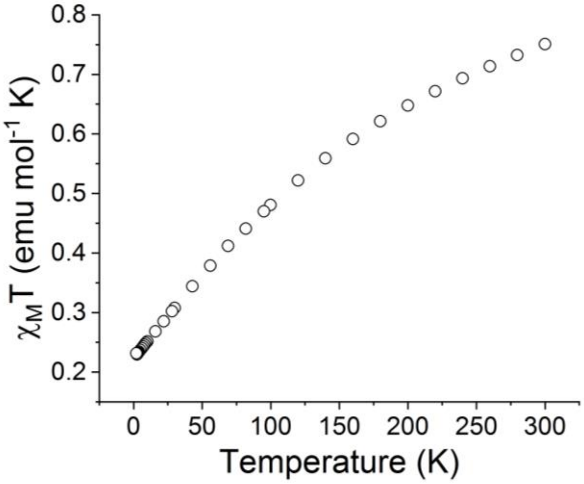

Figure C.4: Temperature dependence of $\chi_M T$ at 1000 Oe field for **4-3**.

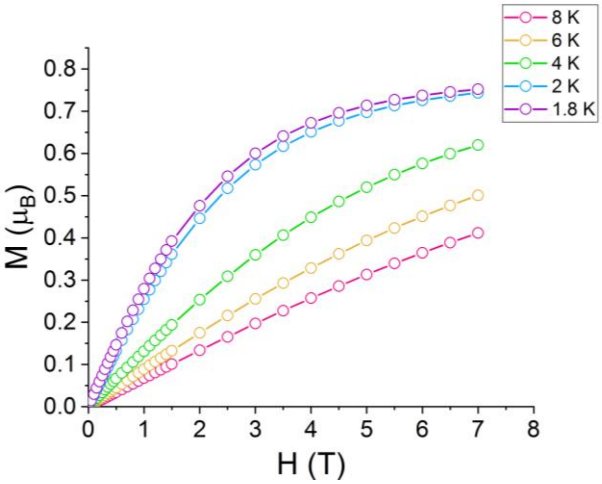

Figure C.5: Plot of Magnetization Vs. Field at 8-1.8 K for **4-1**.

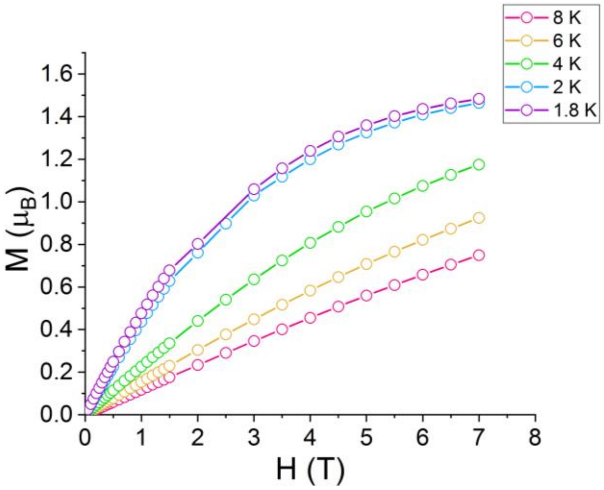

Figure C.6: Plot of Magnetization Vs. Field at 8-1.8 K for **4-2**.

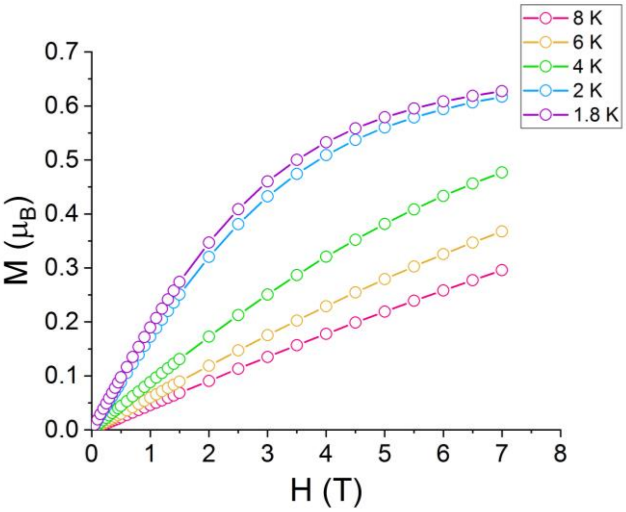

Figure C.7: Plot of Magnetization Vs. Field at 8-1.8 K for **4-3**.

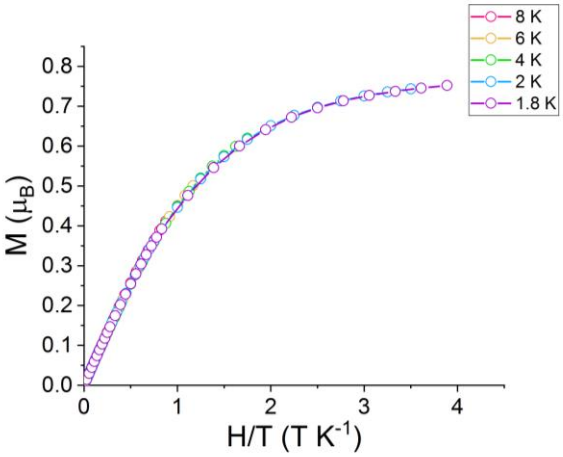

Figure C.8: Plot of Magnetization Vs. H/T at 8-1.8 K for **4-1**.

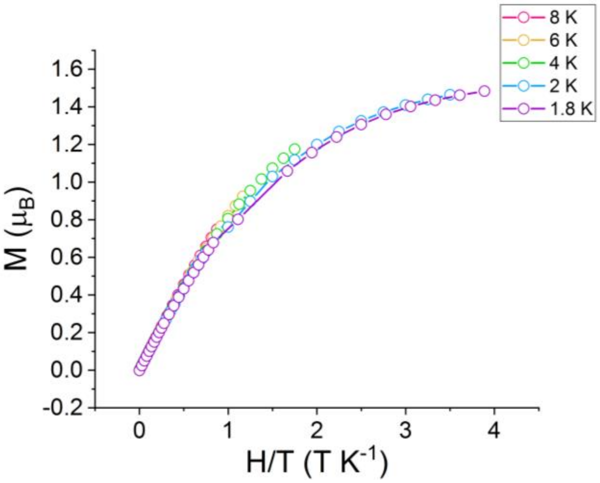

Figure C.9: Plot of Magnetization Vs. H/T at 8-1.8 K for **4-2**.

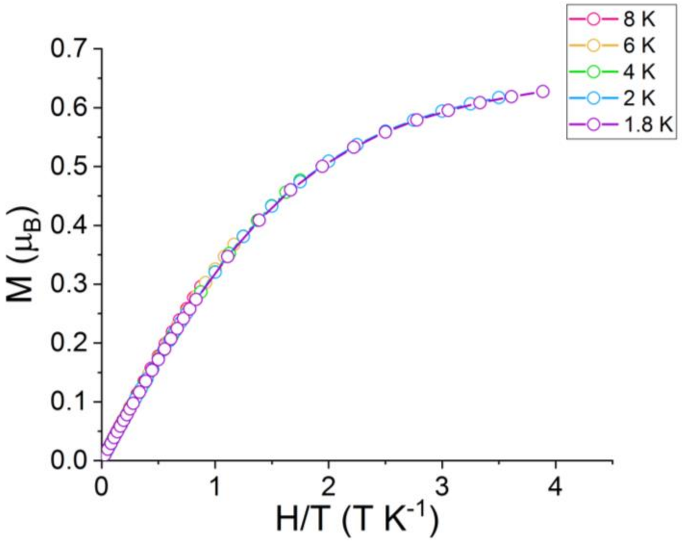

Figure C.10: Plot of Magnetization Vs. H/T at 8-1.8 K for **4-3**.

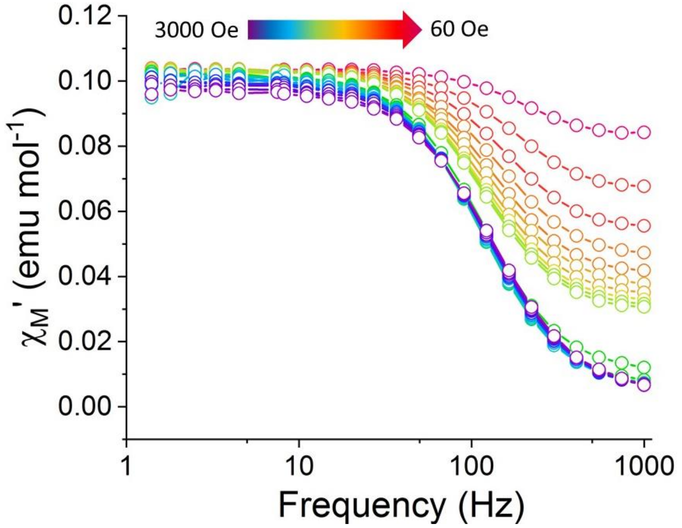

Figure C.11: In phase (χ_m') component of the ac susceptibility of **4-1**.

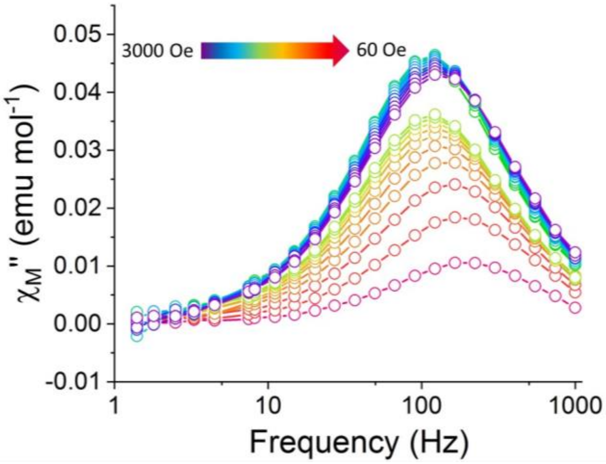

Figure C.12: Out of phase (χ_m'') component of the ac susceptibility of **4-1**.

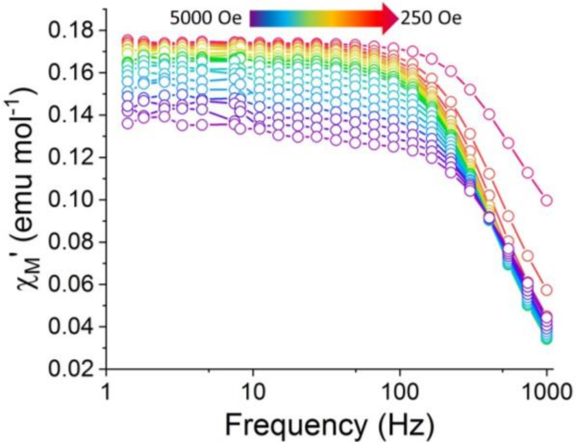

Figure C.13: In phase (χ_m') component of the ac susceptibility of **4-2**.

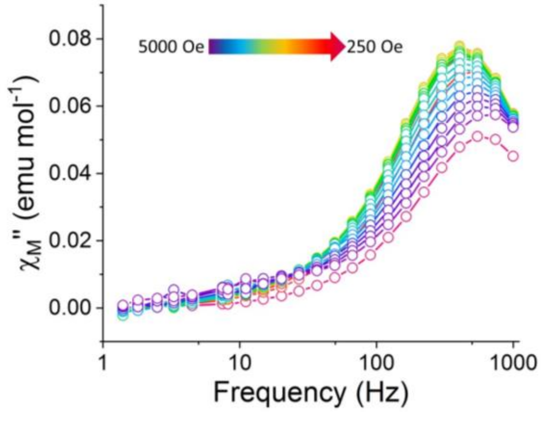

Figure C.14: Out of phase (χ_m'') component of the ac susceptibility of **4-2**.

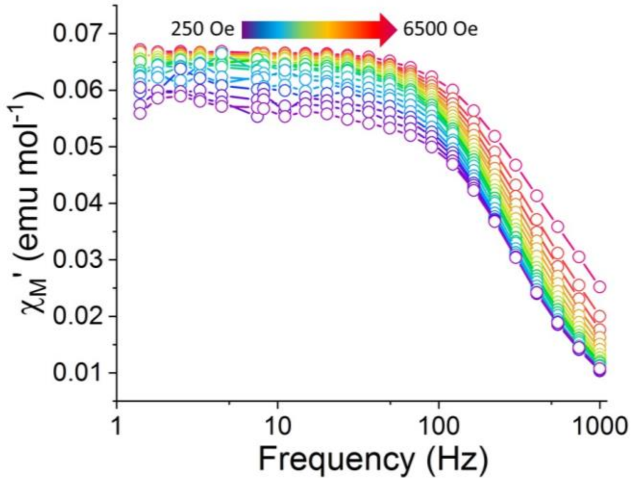

Figure C.15: In phase (χ_m’) component of the ac susceptibility of **4-3**.

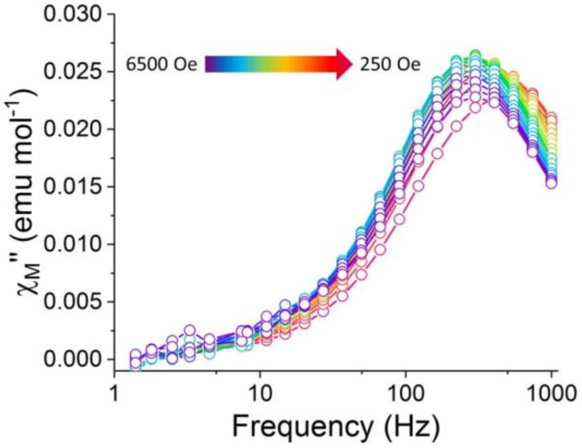

Figure C.16: Out of phase (χ_m’’) component of the ac susceptibility of **4-3**.

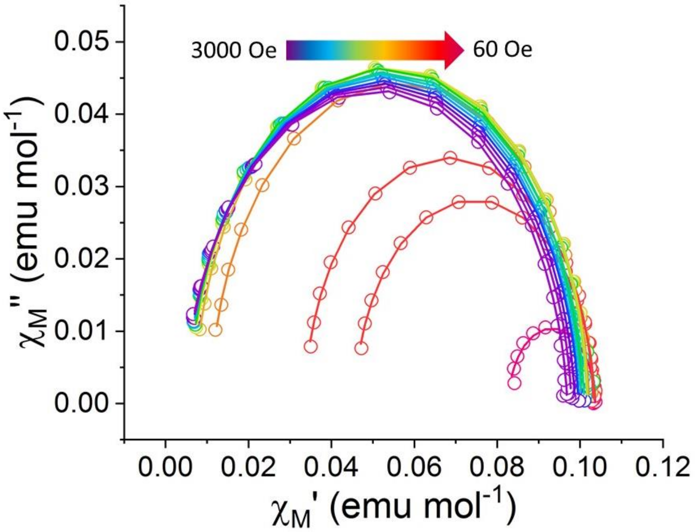

Figure C.17: Variable field Cole-Cole plot at 3 K for **4-1**.

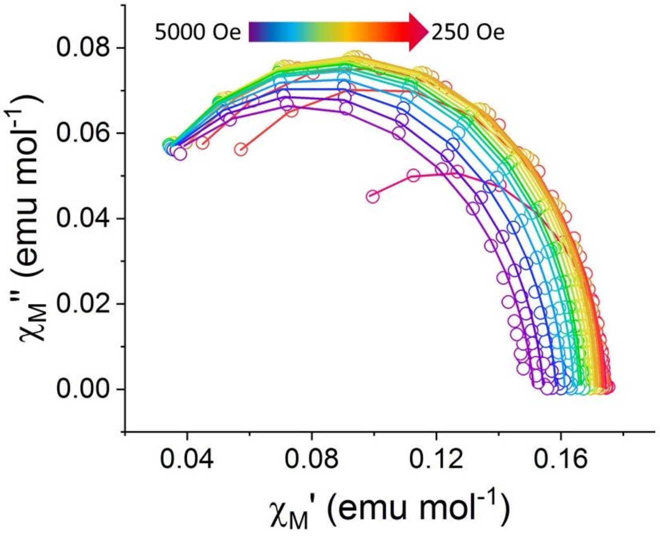

Figure C.18: Variable field Cole-Cole plot at 3 K for **4-2**.

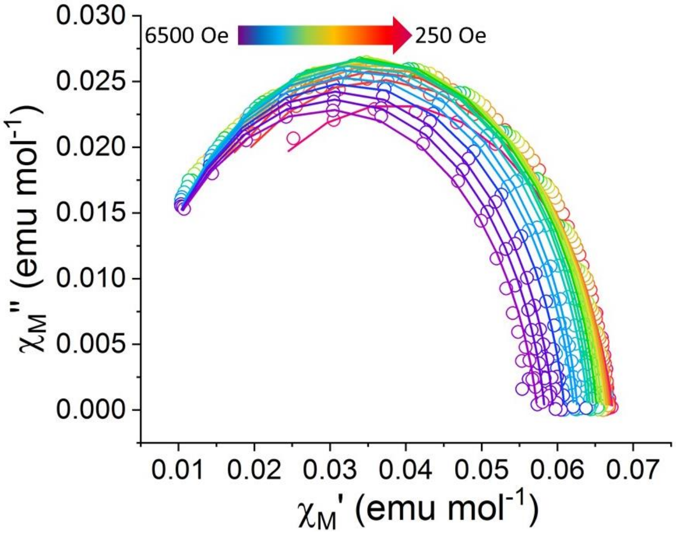

Figure C.19: Variable field Cole-Cole plot at 3 K for **4-3**.

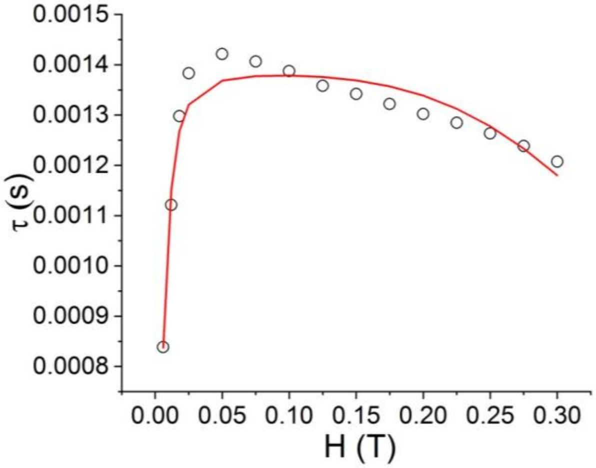

Figure C.20: Field dependence of τ for **4-1** at 3 K.

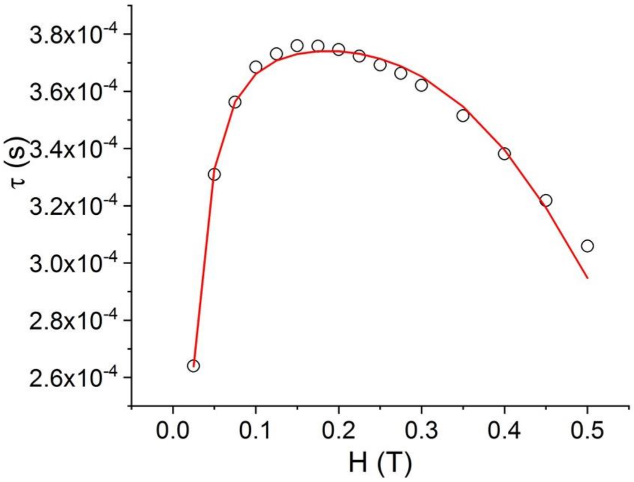

Figure C.21: Field dependence of τ for **4-2** at 3 K.

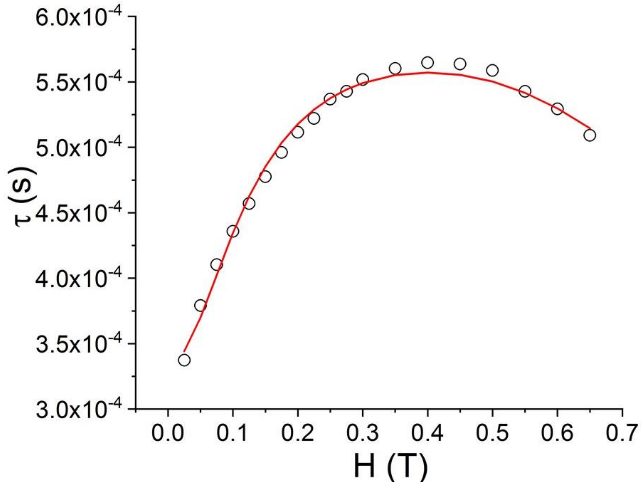

Figure C.22: Field dependence of τ for **4-3** at 3 K.

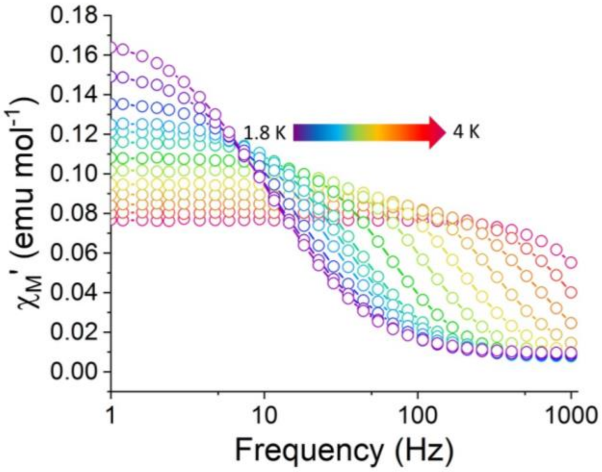

Figure C.23: In phase (χ_m') component of the ac susceptibility of **4-1** at 500 Oe.

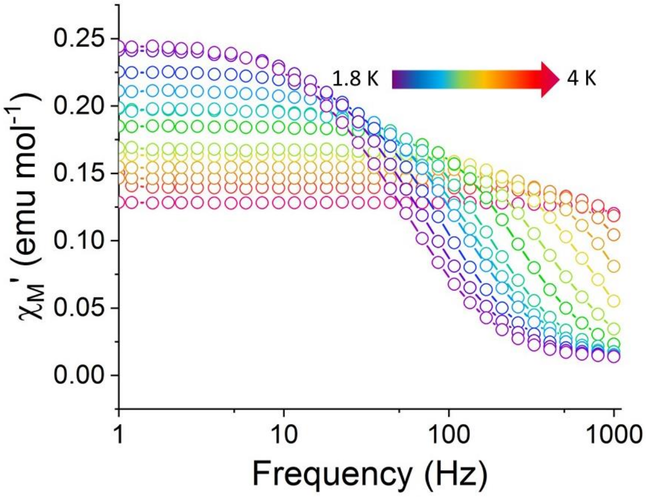

Figure C.24: In phase (χ_m') component of the ac susceptibility of **4-2** at 1500 Oe.

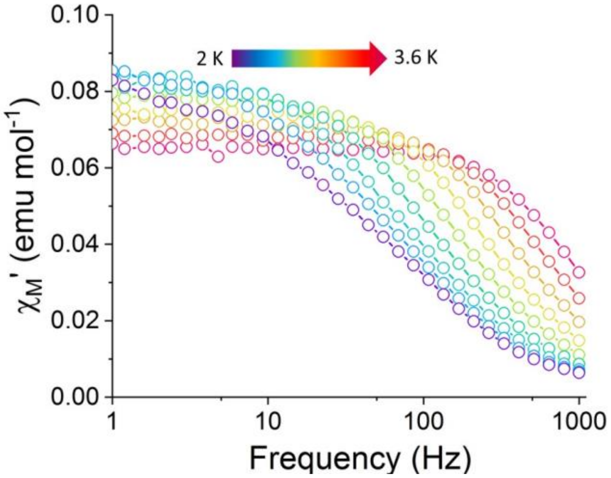

Figure C.25: In phase (χ_m') component of the ac susceptibility of **4-3** at 4000 Oe.

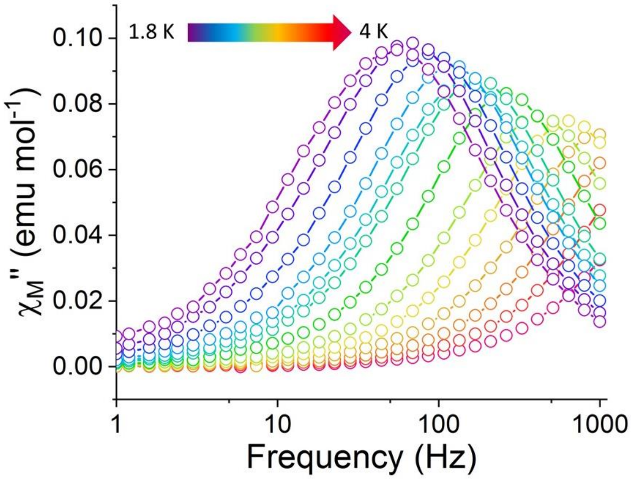

Figure C.26: Out of phase (χ_m'') component of the ac susceptibility of **4-2**, 1500 Oe.

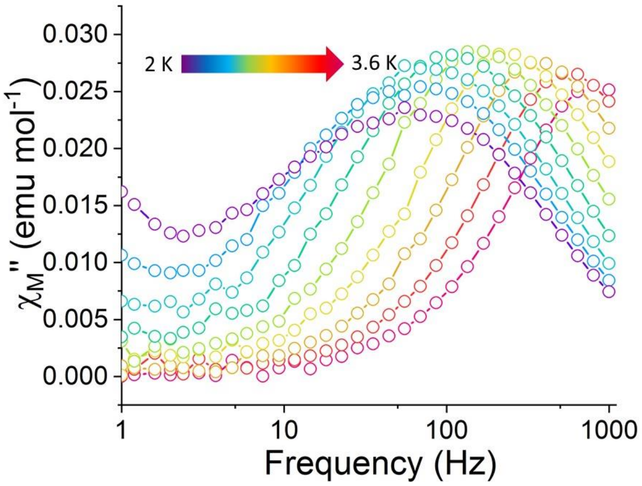

Figure C.27: Out of phase (χ_m'') component of the ac susceptibility of 4-3, 4000 Oe.

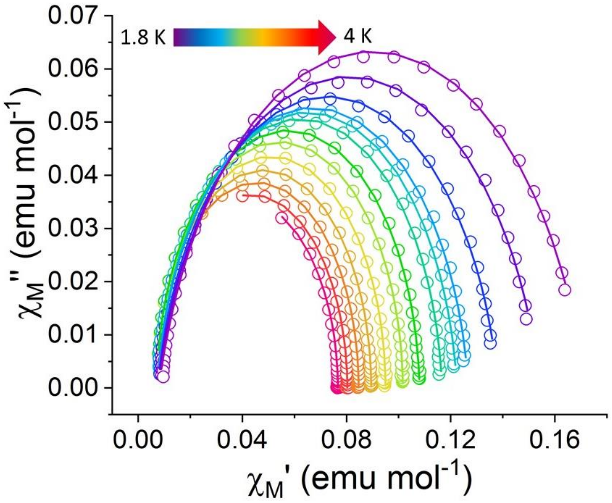

Figure C.28: Variable temperature Cole-Cole plot for **4-1** under 500 Oe field.

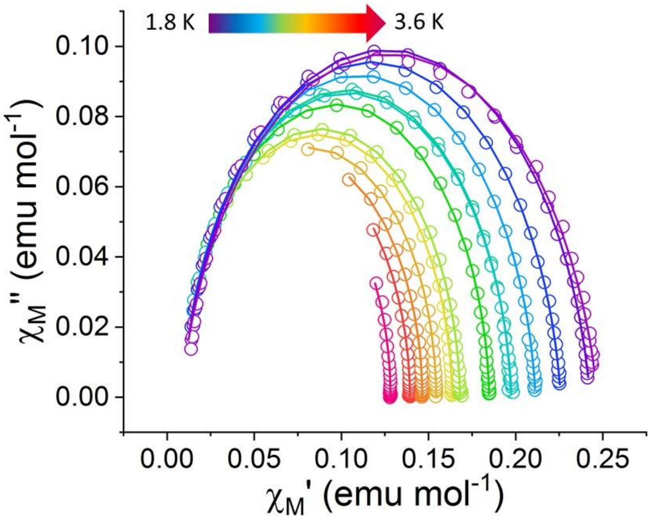

Figure C.29: Variable temperature Cole-Cole plot for **4-2** under 1500 Oe field.

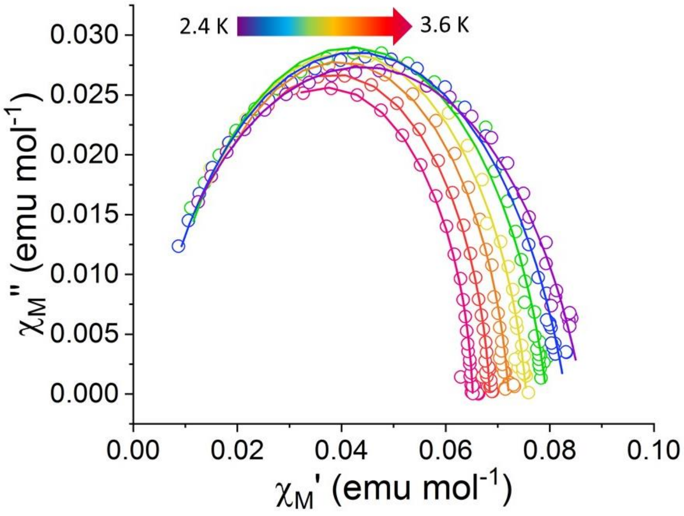

Fig. C.30: Variable temperature Cole-Cole plot for **4-3** under 4000 Oe field.

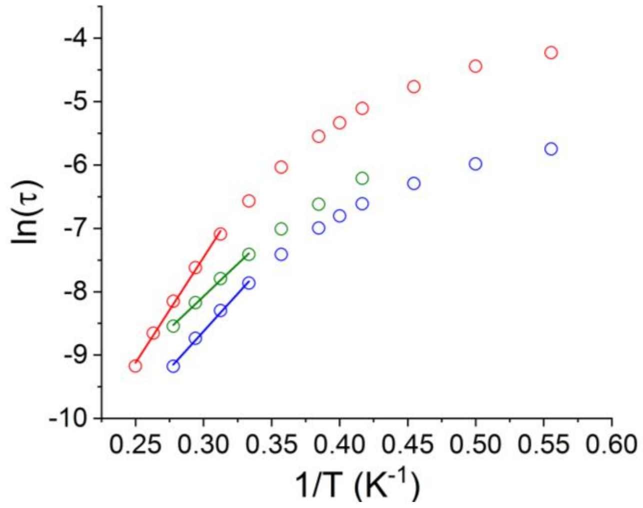

Figure C.31: Arrhenius plot for **4-1** (red), **4-2** (blue), and **4-3** (green) (linear fit).

Table C.3: Computational analysis of **4-1** (Gaussian & Orca).

	Gaussian Single Point	**Orca Single Point**	**Orca Full Optimization**
d(Ce-lcp), Å	1.60	1.60	1.60
d(Fe-lcp), Å	1.55	1.55	1.55
DI	0.3541	0.3424	0.3424
ρ(lcp)[a]	0.028	0.028	0.028
$\nabla^2\rho$ (lcp)[b]	0.030	0.026	0.027
G (lcp)[d]	0.012	0.011	0.012
V(lcp)[d]	-0.016	-0.016	-0.016
H(lcp)[e]	-0.004	-0.005	-0.004

[a] ρ (lcp): Electron density at line critical point (e/bohr^3)
[b] $\nabla^2\rho$ (lcp): Laplacian of electron density (e/bohr^5)
[c] G (lcp): Lagrangian form of kinetic energy density (hartree/bohr^3)
[d] V (lcp): Virial Field = Potential energy density (hartree/bohr^3)
[e] H (lcp): Electronic energy density (hartree/bohr^3)

Table C.4: Computational analysis of **4-1** (ADF).

	ADF Single Point	ADF Full Optimization
d(Ce-lcp), Å	1.60	1.60
d(Fe-lcp), Å	1.55	1.54
DI	0.3549	0.3626
ρ(lcp)[a]	0.028	0.029
$\nabla^2\rho$ (lcp)[b]	0.029	0.031
G (lcp)[d]	0.012	0.013
V(lcp)[d]	-0.017	-0.018
H(lcp)[e]	-0.005	-0.005

[a] ρ (lcp): Electron density at line critical point (e/bohr^3)

[b] $\nabla^2\rho$ (lcp): Laplacian of electron density (e/bohr^5)

[c] G (lcp): Lagrangian form of kinetic energy density (hartree/bohr^3)

[d] V (lcp): Virial Field = Potential energy density (hartree/bohr^3)

[e] H (lcp): Electronic energy density (hartree/bohr^3)

Table C.5: Parameters obtained from fitting the field dependence of **4-1**, **4-2**, and **4-3**.

Compound	4-1	4-2	4-3
A, $s^{-1}K^{-1}T^{-4}$	14553	6076	621
B_1 s^{-1}	1224	3791	1296
B_2, T^{-2}	39975	3624	114
D, s^{-1}	700	2628	1696

Table C.6: Parameters obtained from fitting of the Arrhenius plots **4-1**, **4-2**, and **4-3**.

Compound	4-1	4-2	4-3
A, $s^{-1}K^{-1}T^{-4}$	14553	6076	621
C, $s^{-1}K^{-5}$	1.86	8.41	6.41
τ_{QTM}, s	0.083	0.022	0.015
τ^{-1}_{QTM}, s^{-1}	12.1	46	68
n_2,	5	5	5
U_{eff}, cm^{-1}	29	28	38
τ_0, s	$3.50\cdot10^{-9}$	$3.02\cdot10^{-9}$	$1.66\cdot10^{-10}$

APPENDIX D

APPENDIX FOR CHAPTER 5: ASSESSING THE NATURE OF LANTHANIDE-TRANSITION METAL BONDING IN DISCRETE MOLECULES: A PERSPECTIVE

Table D.1: Crystallographic Data for **5-12**

Compound	**(thf)(PyCp$_2$)PrFe(Cp)(CO)$_2$**
Formula	$C_{28}H_{28}PrFeNO_2$
Crystal system	Orthorhombic
Space group	Pnma
a, Å	17.580(6)
b, Å	13.375(6)
c, Å	10.120(8)
α,°	90
β,°	90
γ, °	90
Volume, Å^3	2378(3)
Z	4
T, K	110
ρ_{calcd} (mg/m$_3$)	1.740
F(000)	1248
Θ_{min}, Θ_{max}, °	5.127, 30.718
R$_1$^{a}, wR$_2$^{b} (I > 2σ(I))	0.0204, 0.0455
R$_1$^{a}, wR$_2$^{b} (all data)	0.0257, 0.0481

[a] $R_1 = 3||F_o|-|F_c||/3|F_o|$. [b] $wR_2 = [3[w(F_o^2 - F_c^2)^2]/3[w(F_o^2)^2]]^{½}$, $w = 1/\sigma^2(F_o^2) + (aP)^2 + bP$, where $P = [\max(0 \text{ or } F_o^2) + 2(F_c^2)]/3$.

Table D.2: Crystallographic Data for **5-13**, **5-14**, and **5-23**.

Compound	**5-13**	**5-14**	**5-23**
Formula	$C_{28}H_{28}NdFeNO_3$	$C_{24}H_{20}NdFeNO_2$	$C_{24}H_{20}NdRuNO_2$
Crystal system	Orthorhombic	Orthrombic	Orthorhombic
Space group	Pnma	Pnma	Pnma
a, Å	17.567(4)	16.209(8)	16.350(8)
b, Å	13.235(3)	13.236(4)	13.239(8)
c, Å	13.092(8)	9.153(2)	9.199(7)
α,°	90	90	90
β,°	90	90	90
γ, °	90	90	90
Volume, $Å^3$	2362(1)	1964(1)	1992(1)
Z	4	4	4
T, K	110	110	110
ρ_{calcd} (mg/m^3)	1.762	1.875	2.000
F(000)	1252	1092	1164
Θ_{min}, Θ_{max}, °	2.327, 27.535	2.983, 27.495	5.220, 27.497
$R_1{}^a$, $wR_2{}^b$ ($I > 2\sigma(I)$)	0.0321, 0.0687	0.0133, 0.308	0.0129, 0.0305
$R_1{}^a$, $wR_2{}^b$ (all data)	0.0388, 0.0746	0.0138, 0.0313	0.0137. 0.0308

[a] $R_1 = 3||F_o|-|F_c||/3|F_o|$. [b] $wR_2 = [3[w(F_o{}^2 – F_c{}^2)^2]/3[w(F_o{}^2)^2]]^{½}$, $w = 1/\sigma^2(F_o{}^2) + (aP)^2 + bP$, where $P = [\max(0 \text{ or } F_o{}^2) + 2(F_c{}^2)]/3$.

Table D.3: Crystallographic Data for **5-15** and **5-24**.

Compound	**(PyCp$_2$)SmFe(Cp)(CO)$_2$**	**(PyCp$_2$)SmRu(Cp)(CO)$_2$**
Formula	$C_{24}H_{20}SmFeNO_2$	$C_{24}H_{20}SmNO_2Ru$
Crystal system	Orthorhombic	Orthorhombic
Space group	Pnma	Pnma
a, Å	16.151(4)	13.322(2)
b, Å	13.176(3)	13.197(2)
c, Å	9.138(3)	9.183(6)
α,°	90	90
β,°	90	90
γ, °	90	90
Volume, Å^3	1944(1)	1978(4)
Z	4	4
T, K	110	110
ρ_{calcd} (mg/m$_3$)	1.915	2.034
F(000)	1110	1172
Θ_{min}, Θ_{max}, °	2.522, 26.298	2.496, 30.236
$R_1{}^a$, $wR_2{}^b$ ($I > 2\sigma(I)$)	0.0286, 0.0560	0.0170, 0.0422
$R_1{}^a$, $wR_2{}^b$ (all data)	0.0412, 0.0612	0.0199, 0.0438

$^a R_1 = 3||F_o|-|F_c||/3|F_o|$. $^b wR_2 = [3[w(F_o{}^2 - F_c{}^2)^2]/3[w(F_o{}^2)^2]]^{½}$, $w = 1/\sigma^2(F_o{}^2) + (aP)^2 + bP$, where $P = [\max(0 \text{ or } F_o{}^2) + 2(F_c{}^2)]/3$.

Table D.4: Crystallographic Data for **5-16** and **5-25**.

Compound	**$(PyCp_2)GdFe(Cp)(CO)_2$**	**$(PyCp_2)GdRu(Cp)(CO)_2$**
Formula	$C_{24}H_{20}GdFeNO_2$	$C_{24}H_{20}GdNO_2Ru$
Crystal system	Orthorhombic	Orthorhombic
Space group	Pnma	Pnma
a, Å	16.068(3)	13.260(6)
b, Å	13.138(3)	13.144(5)
c, Å	9.133(2)	9.144(1)
α,°	90	90
β,°	90	90
γ, °	90	90
Volume, $Å^3$	1972(1)	1954(4)
Z	4	4
T, K	110	110
ρ_{calcd} (mg/m_3)	1.938	2.082
F(000)	1118	1180
Θ_{min}, Θ_{max}, °	2.522, 26.298	2.946, 28.576
R_1[a], wR_2[b] ($I > 2\sigma(I)$)	0.0318, 0.0560	0.0223, 0.0559
R_1[a], wR_2[b] (all data)	0.0364, 0.0612	0.0258, 0.0573

[a] $R_1 = 3||F_o|-|F_c||/3|F_o|$. [b] $wR_2 = [3[w(F_o^2 - F_c^2)^2]/3[w(F_o^2)^2]]^{½}$, $w = 1/\sigma^2(F_o^2) + (aP)^2 + bP$, where $P = [\max(0 \text{ or } F_o^2) + 2(F_c^2)]/3$.

Table D.5: Crystallographic Data for **5-17** and **5-26**.

Compound	**$(PyCp_2)TbFe(Cp)(CO)_2$**	**$(PyCp_2)TbRu(Cp)(CO)_2$**
Formula	$C_{24}H_{20}TbFeNO_2$	$C_{24}H_{20}TbNO_2Ru$
Crystal system	Orthorhombic	Orthorhombic
Space group	Pnma	Pnma
a, Å	15.954(8)	16.259(2)
b, Å	13.016(6)	13.114(8)
c, Å	9.070(5)	9.162(1)
α,°	90	90
β,°	90	90
γ, °	90	90
Volume, Å^3	1884(1)	1954(4)
Z	4	4
T, K	110	110
ρ_{calcd} (mg/m$_3$)	2.007	2.089
F(000)	1112	1184
Θ_{min}, Θ_{max}, °	2.553, 25.824	2.505, 28.761
R_1[a], wR_2[b] (I > 2σ(I))	0.0382, 0.0789	0.0209, 0.0501
R_1[a], wR_2[b] (all data)	0.0513 0.0831	0.0234, 0.0511

[a] $R_1 = 3||F_o|-|F_c||/3|F_o|$. [b] $wR_2 = [3[w(F_o^2 - F_c^2)^2]/3[w(F_o^2)^2]]^{½}$, $w = 1/\sigma^2(F_o^2) + (aP)^2 + bP$, where $P = [\max(0 \text{ or } F_o^2) + 2(F_c^2)]/3$.

Table D.6: Crystallographic Data for **5-18** and **5-27**.

Compound	**$(PyCp_2)HoFe(Cp)(CO)_2$**	**$(PyCp_2)HoRu(Cp)(CO)_2$**
Formula	$C_{24}H_{20}HoFeNO_2$	$C_{24}H_{20}HoNO_2Ru$
Crystal system	Orthorhombic	Orthorhombic
Space group	Pnma	Pnma
a, Å	16.087(2)	13.624(5)
b, Å	13.114(2)	13.096(1)
c, Å	9.143(5)	9.143(7)
α,°	90	90
β,°	90	90
γ, °	90	90
Volume, $Å^3$	1929(1)	1945(3)
Z	4	4
T, K	110	110
ρ_{calcd} (mg/m_3)	1.981	2.118
F(000)	1120	1192
Θ_{min}, Θ_{max}, °	2.522, 26.298	2.507, 30.119
R_1[a], wR_2[b] ($I > 2\sigma(I)$)	0.0268, 0.0523	0.0170, 0.0422
R_1[a], wR_2[b] (all data)	0.0390, 0.0568	0.0187, 0.0497

[a] $R_1 = 3||F_o|-|F_c||/3|F_o|$. [b] $wR_2 = [3[w(F_o^2 - F_c^2)^2]/3[w(F_o^2)^2]]^{½}$, $w = 1/\sigma^2(F_o^2) + (aP)^2 + bP$, where $P = [\max(0 \text{ or } F_o^2) + 2(F_c^2)]/3$.

Table D.7: Crystallographic Data for **5-19** and **5-28**.

Compound	**(PyCp$_2$)ErFe(Cp)(CO)$_2$**	**(PyCp$_2$)ErRu(Cp)(CO)$_2$**
Formula	$C_{24}H_{20}ErFeNO_2$	$C_{24}H_{20}ErNO_2Ru$
Crystal system	Orthorhombic	Orthorhombic
Space group	Pnma	Pnma
a, Å	16.049(9)	16.223(9)
b, Å	13.101(7)	13.105(7)
c, Å	9.127(5)	9.134(3)
α,°	90	90
β,°	90	90
γ, °	90	90
Volume, Å^3	1919(1)	1942(3)
Z	4	4
T, K	110	110
ρ_{calcd} (mg/m$_3$)	1.999	2.130
F(000)	1124	1196
Θ_{min}, Θ_{max}, °	2.538, 24.998	4.380, 30.117
$R_1{}^a$, $wR_2{}^b$ ($I > 2\sigma(I)$)	0.0286, 0.0777	0.0241, 0.0588
$R_1{}^a$, $wR_2{}^b$ (all data)	0.0602, 0.0847	0.0330, 0.0650

$^a R_1 = 3||F_o|-|F_c||/3|F_o|$. $^b wR_2 = [3[w(F_o{}^2 - F_c{}^2)^2]/3[w(F_o{}^2)^2]]^{½}$, $w = 1/\sigma^2(F_o{}^2) + (aP)^2 + bP$, where $P = [\max(0 \text{ or } F_o{}^2) + 2(F_c{}^2)]/3$.

Table D.8: Crystallographic Data for **5-20** and **5-29**.

Compound	**$(PyCp_2)TmFe(Cp)(CO)_2$**	**$(PyCp_2)TmRu(Cp)(CO)_2$**
Formula	$C_{24}H_{20}TmFeNO_2$	$C_{24}H_{20}TmNO_2Ru$
Crystal system	Orthorhombic	Orthorhombic
Space group	Pnma	Pnma
a, Å	16.040(6)	16.239(2)
b, Å	13.088(4)	13.090(4)
c, Å	9.121(3)	9.182(9)
α,°	90	90
β,°	90	90
γ, °	90	90
Volume, Å^3	1915(1)	1940(6)
Z	4	4
T, K	110	110
ρ_{calcd} (mg/m$_3$)	2.009	2.137
F(000)	1128	1200
Θ_{min}, Θ_{max}, °	2.569, 28.810	5.124, 27.495
R_1[a], wR_2[b] ($I > 2\sigma(I)$)	0.0285, 0.0578	0.0210, 0.0545
R_1[a], wR_2[b] (all data)	0.0409, 0.0650	0.0245, 0.0571

[a] $R_1 = 3||F_o|-|F_c||/3|F_o|$. [b] $wR_2 = [3[w(F_o^2 - F_c^2)^2]/3[w(F_o^2)^2]]^{½}$, $w = 1/\sigma^2(F_o^2) + (aP)^2 + bP$, where $P = [\max(0 \text{ or } F_o^2) + 2(F_c^2)]/3$.

Table D.9: Crystallographic Data for **5-21** and **5-30**.

Compound	**(PyCp$_2$)YbFe(Cp)(CO)$_2$**	**(PyCp$_2$)YbRu(Cp)(CO)$_2$**
Formula	$C_{24}H_{20}YbFeNO_2$	$C_{24}H_{20}YbNO_2Ru$
Crystal system	Orthorhombic	Orthorhombic
Space group	Pnma	Pnma
a, Å	16.035(1)	16.242(8)
b, Å	13.035(3)	13.072(5)
c, Å	9.125(1)	9.136(2)
α,°	90	90
β,°	90	90
γ, °	90	90
Volume, Å^3	1907(1)	1940(3)
Z	4	4
T, K	110	110
ρ_{calcd} (mg/m$_3$)	2.031	2.152
F(000)	1132	1204
Θ_{min}, Θ_{max}, °	2.725, 27.491	5.258, 27.500
$R_1{}^a$, $wR_2{}^b$ ($I > 2\sigma(I)$)	0.0481, 0.0874	0.0206, 0.0536
$R_1{}^a$, $wR_2{}^b$ (all data)	0.0862, 0.1052	0.0234, 0.0560

$^a R_1 = 3||F_o|-|F_c||/3|F_o|$. $^b wR_2 = [3[w(F_o{}^2 – F_c{}^2)^2]/3[w(F_o{}^2)^2]]^{½}$, $w = 1/\sigma^2(F_o{}^2) + (aP)^2 + bP$, where $P = [\max(0 \text{ or } F_o{}^2) + 2(F_c{}^2)]/3$.

Table D.10: Crystallographic Data for **5-23** and **5-31**.

Compound	**(PyCp$_2$)LuFe(Cp)(CO)$_2$**	**(PyCp$_2$)LuRu(Cp)(CO)$_2$**
Formula	$C_{24}H_{20}LuFeNO_2$	$C_{24}H_{20}LuNO_2Ru$
Crystal system	Orthorhombic	Orthorhombic
Space group	Pnma	Pnma
a, Å	15.970(4)	13.178(3)
b, Å	13.041(3)	13.026(2)
c, Å	9.088(2)	9.103(2)
α,°	90	90
β,°	90	90
γ, °	90	90
Volume, Å^3	1893(1)	1919(1)
Z	4	4
T, K	110	110
ρ_{calcd} (mg/m$_3$)	2.054	2.183
F(000)	1136	1208
Θ_{min}, Θ_{max}, °	3.396, 24.986	2.518, 24.997
$R_1{}^a$, $wR_2{}^b$ (I > 2σ(I))	0.0252, 0.0518	0.0192, 0.0415
$R_1{}^a$, $wR_2{}^b$ (all data)	0.0355, 0.0575	0.0258, 0.0452

$^{a}R_1 = 3||F_o|-|F_c||/3|F_o|$. $^{b}wR_2 = [3[w(F_o^2 - F_c^2)^2]/3[w(F_o^2)^2]]^{½}$, $w = 1/\sigma^2(F_o^2) + (aP)^2 + bP$, where $P = [\max(0 \text{ or } F_o^2) + 2(F_c^2)]/3$.

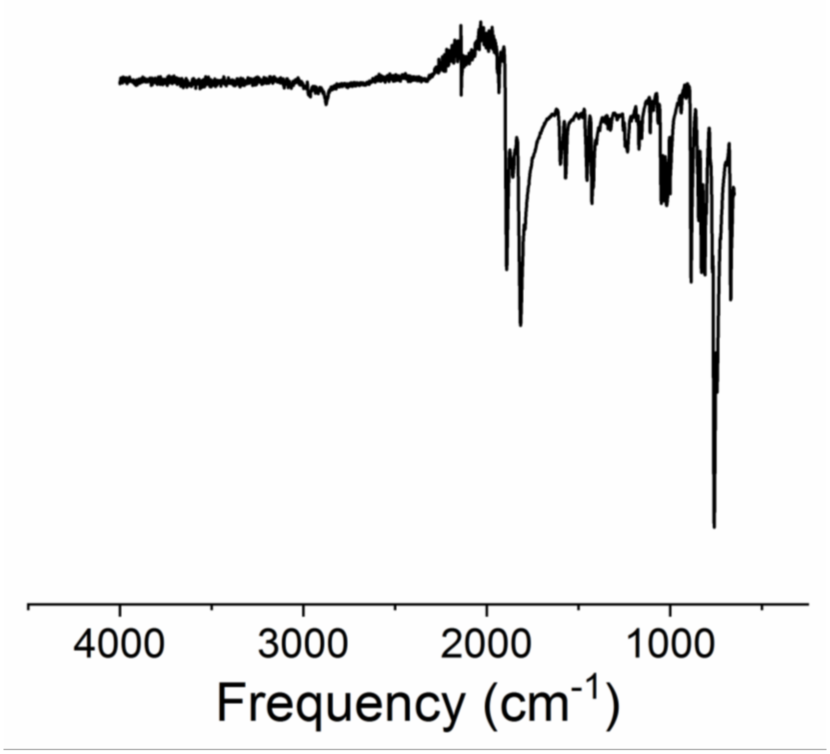

Figure D.1: IR spectrum of **5-12**.

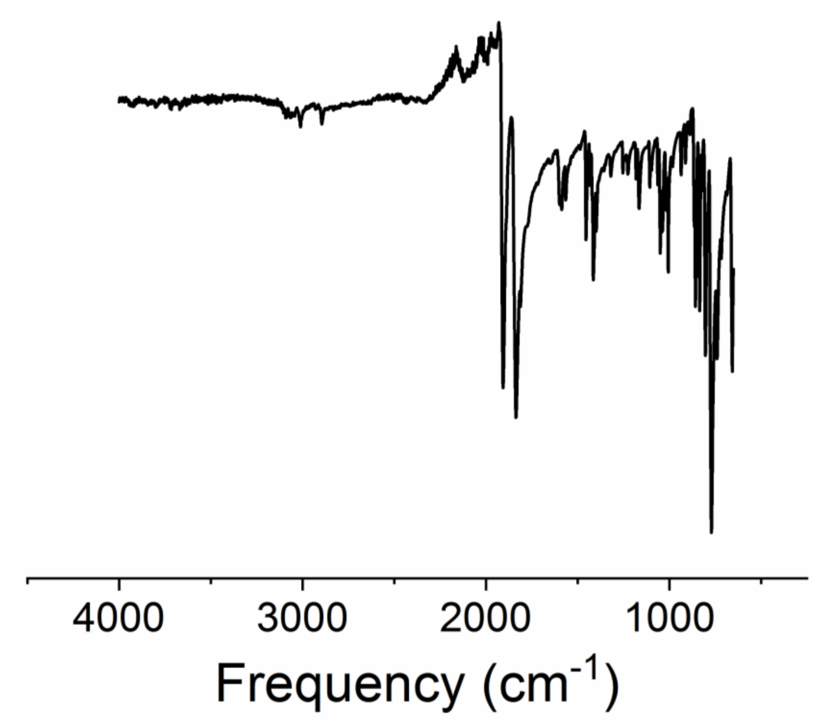

Figure D.2: IR spectrum of **5-14**.

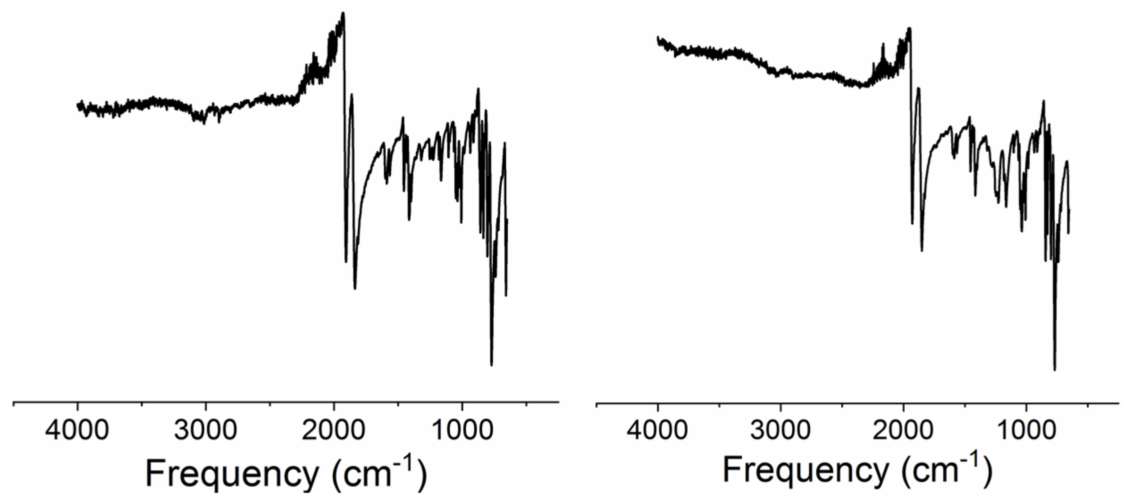

Figure D.3: IR spectra of **5-15** (left) and **5-24** (right).

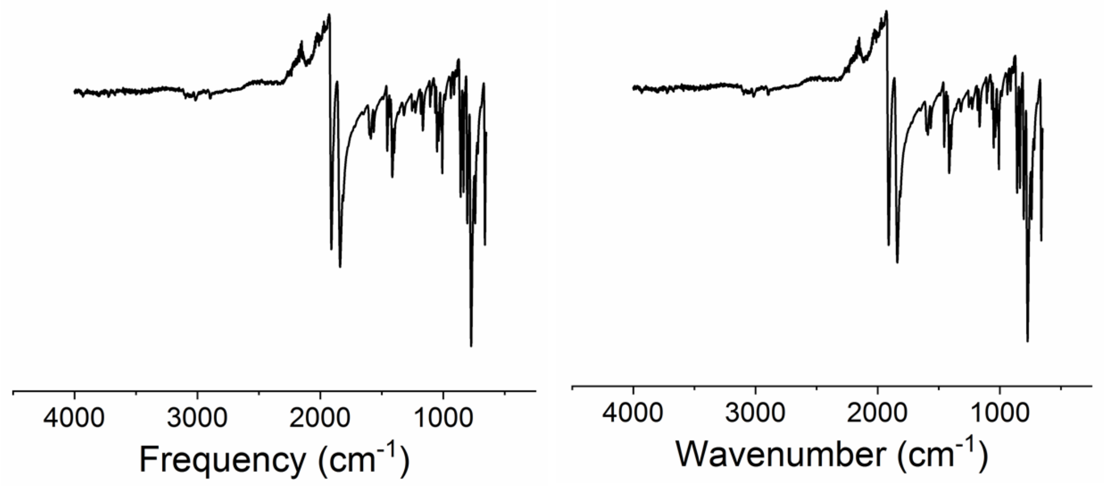

Figure D.4: IR spectra of **5-16** (left) and **5-25** (right).

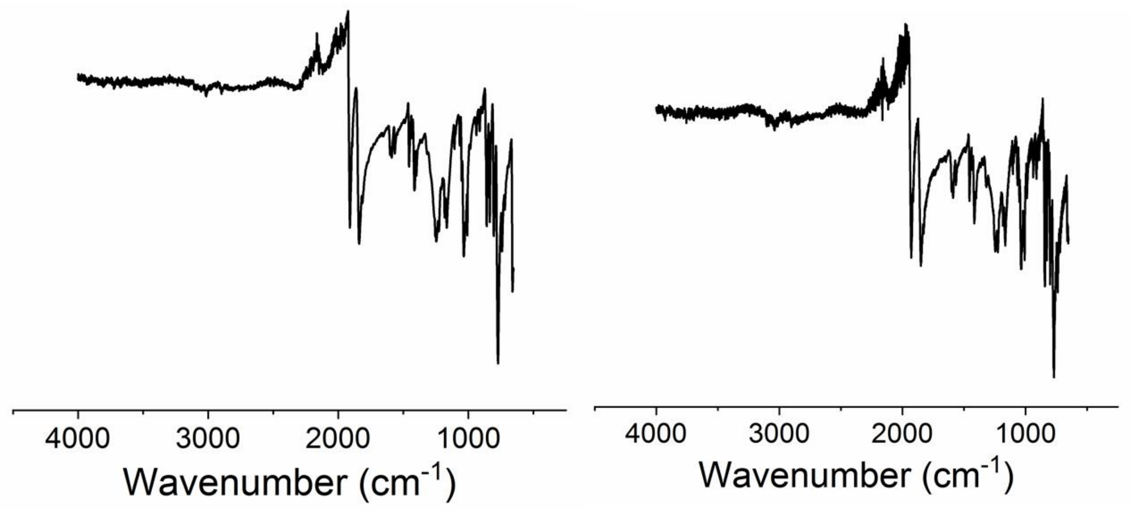

Figure D.5: IR spectra of **5-17** (left) and **5-26** (right).

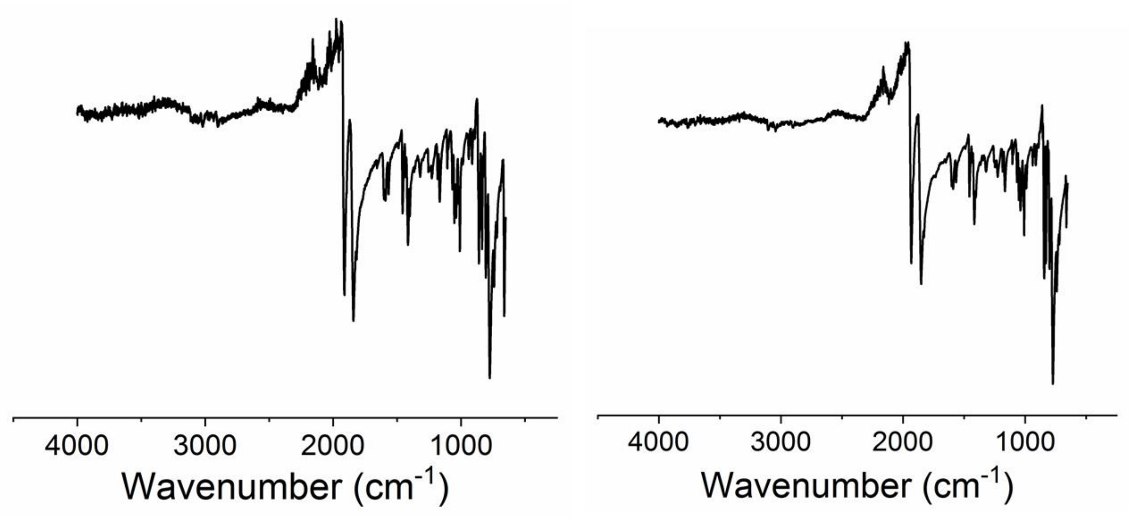

Figure D.6: IR spectra of **5-18** (left) and **5-27** (right).

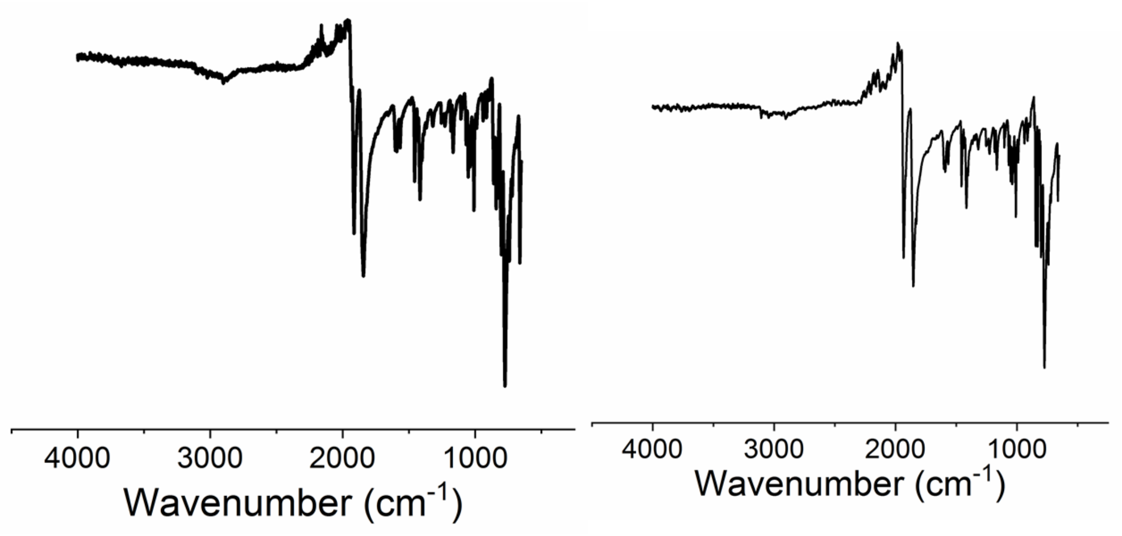

Figure D.7: IR spectra of **5-19** (left) and **5-28** (right).

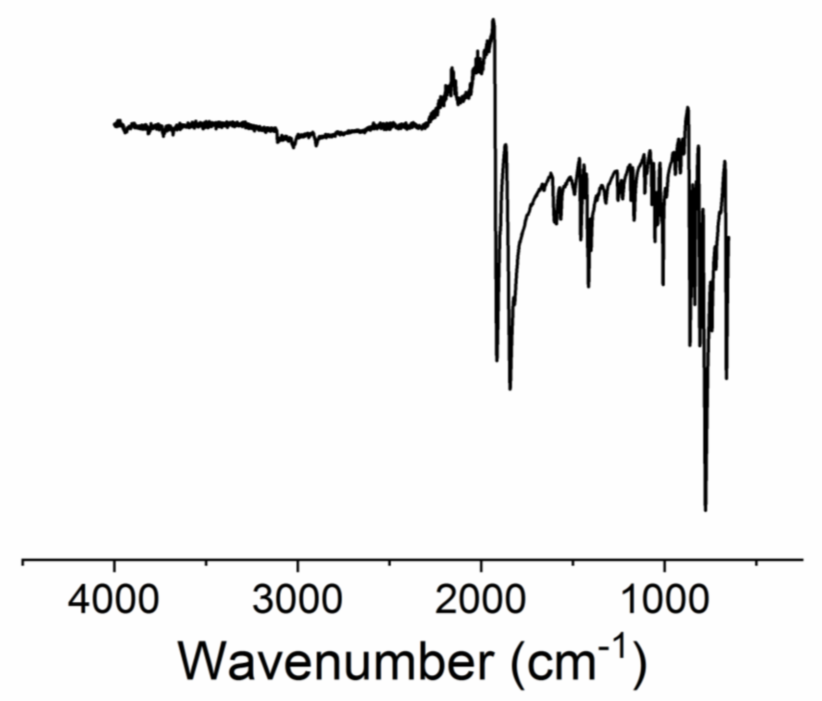

Figure D.8: IR spectrum of **5-21**.

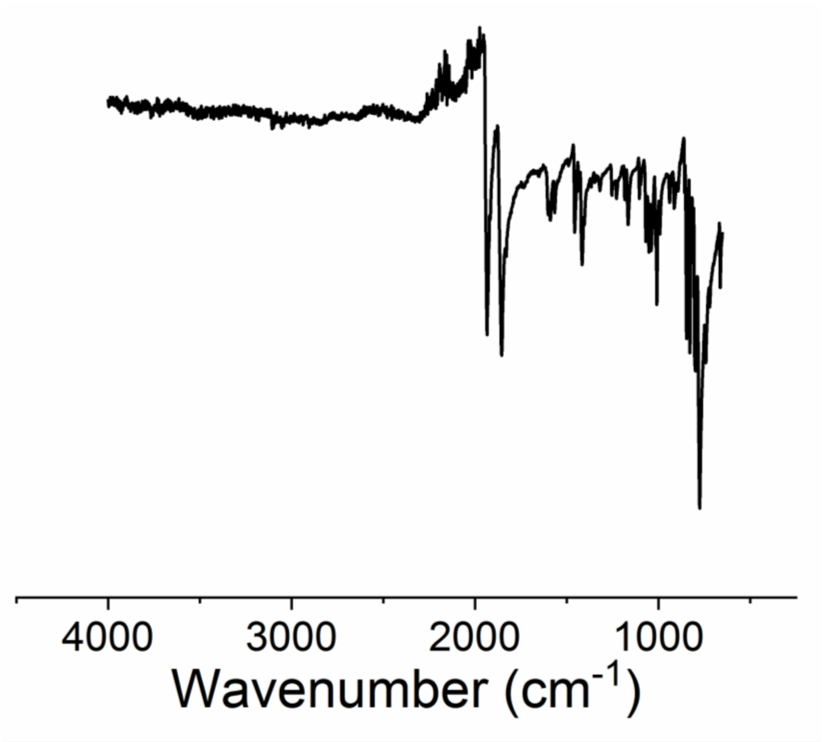

Figure D.9: IR spectrum of **5-30**.

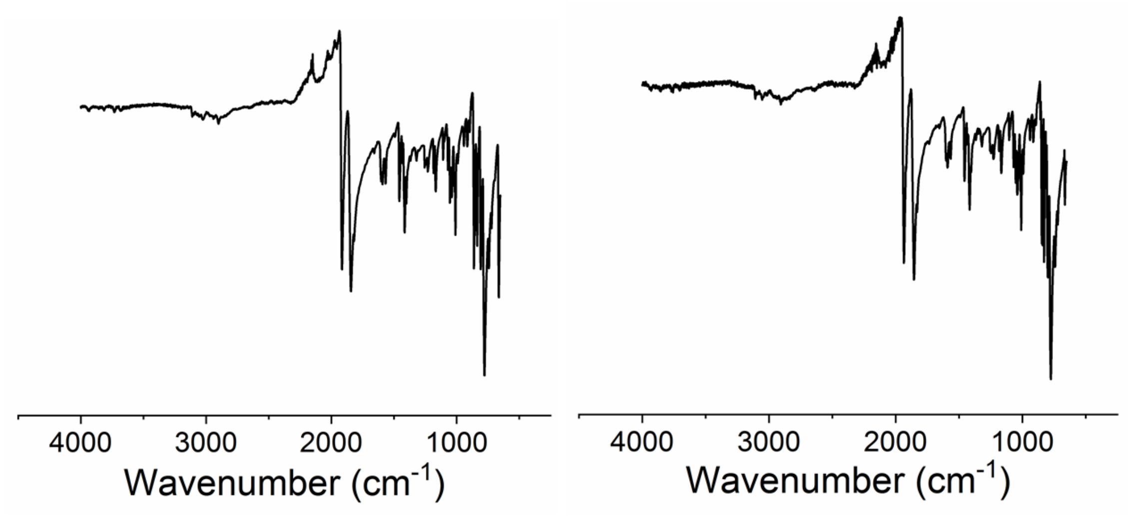

Figure D.10: IR spectra of **5-22** (left) and **5-31** (right).

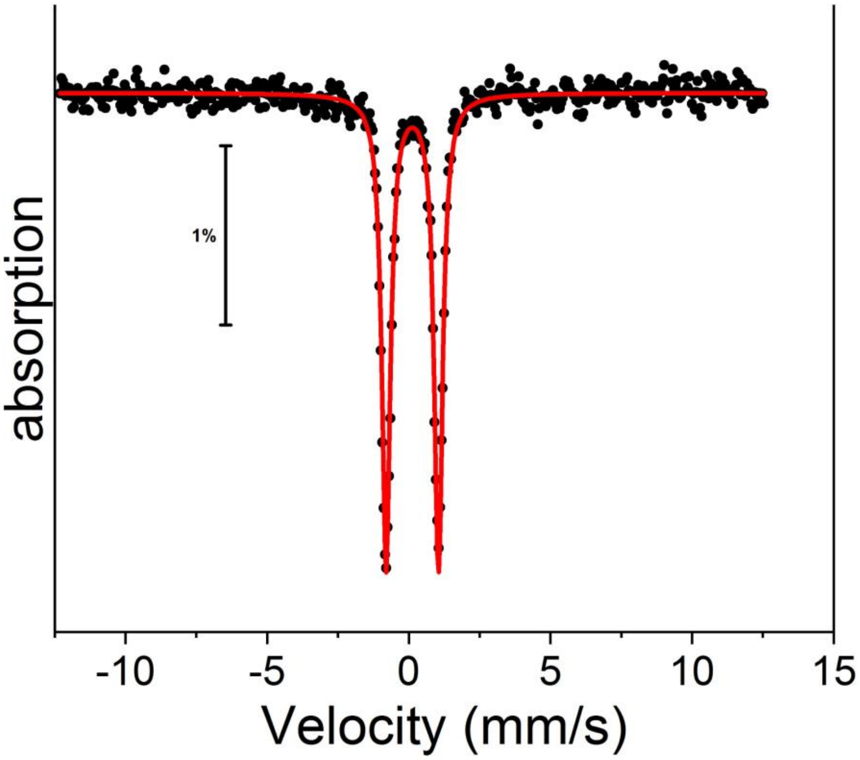

Figure D.11: ^{57}Fe Mössbauer spectrum of **5-22** at 5 K.

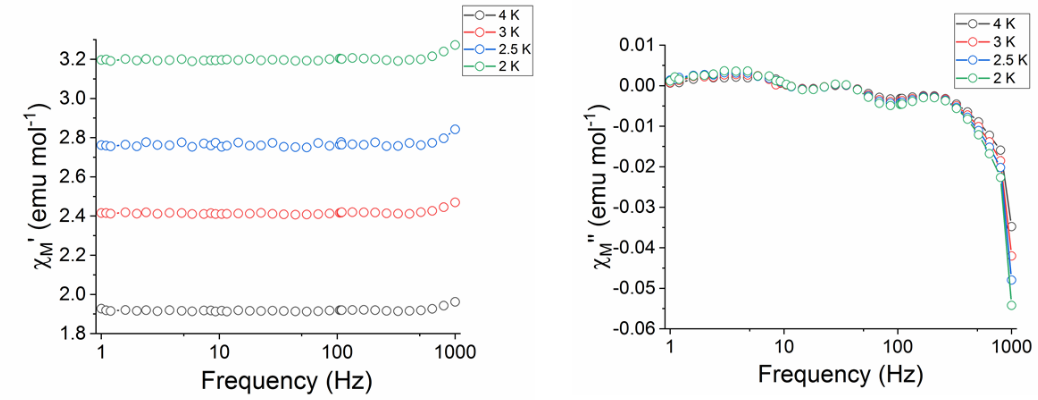

Figure D.12: In phase (χ_m') component and out of phase component (χ_m'') **5-17**.

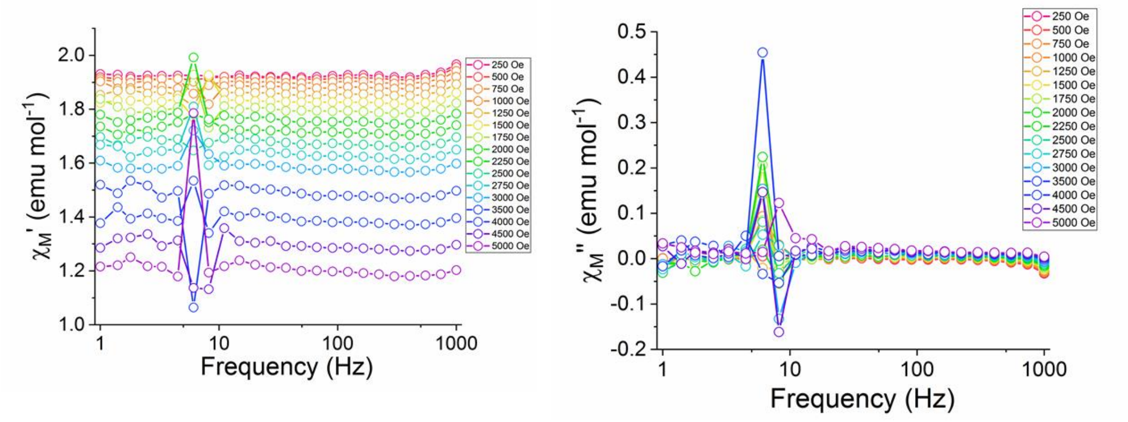

Figure D.13: In phase (χ_m') and out of phase component (χ_m'') of **5-26**, no field.

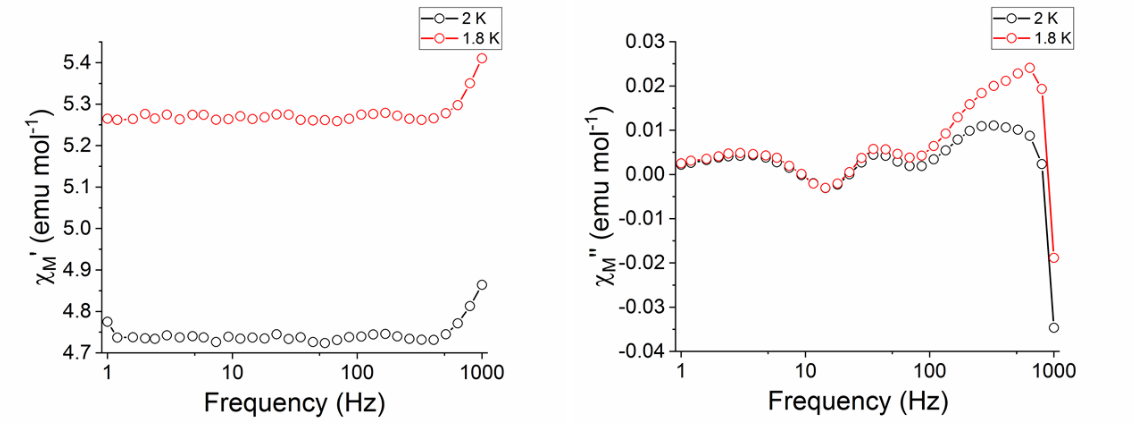

Figure D.14: In phase (χ_m') and out of phase component (χ_m'') of **5-26**, under field.

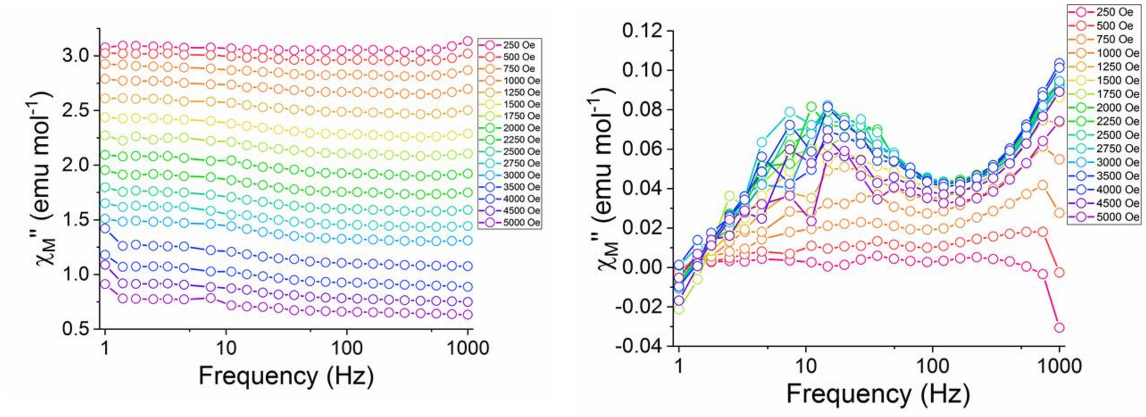

Figure D.15: In phase (χ_m') and out of phase component (χ_m'') of **5-18**, no field.

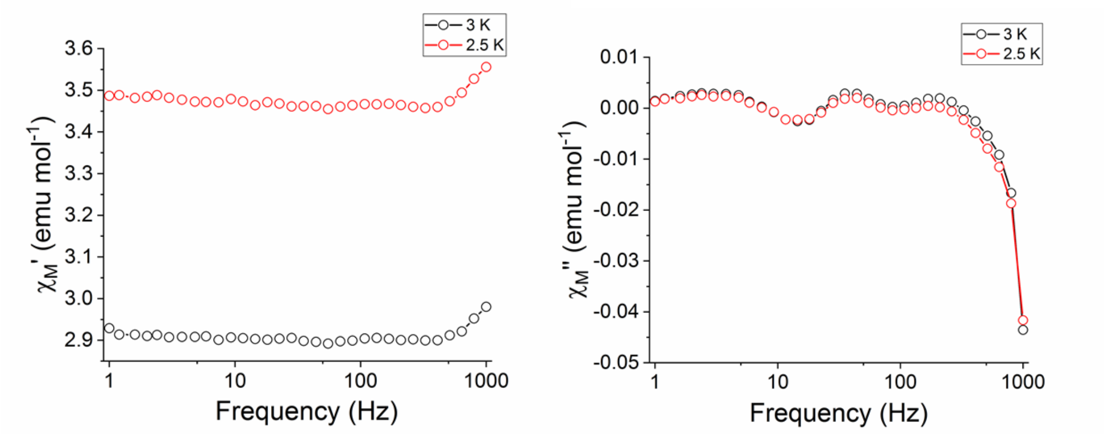

Figure D.16: In phase (χ_m') and out of phase component (χ_m'') of **5-27**, no field.

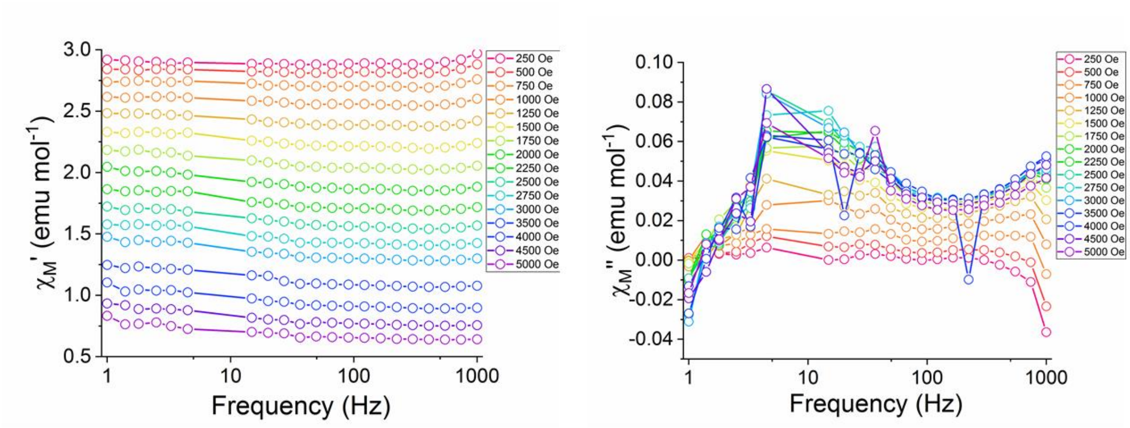

Figure D.17: In phase (χ_m') and out of phase component (χ_m'') of **5-27**, under field.

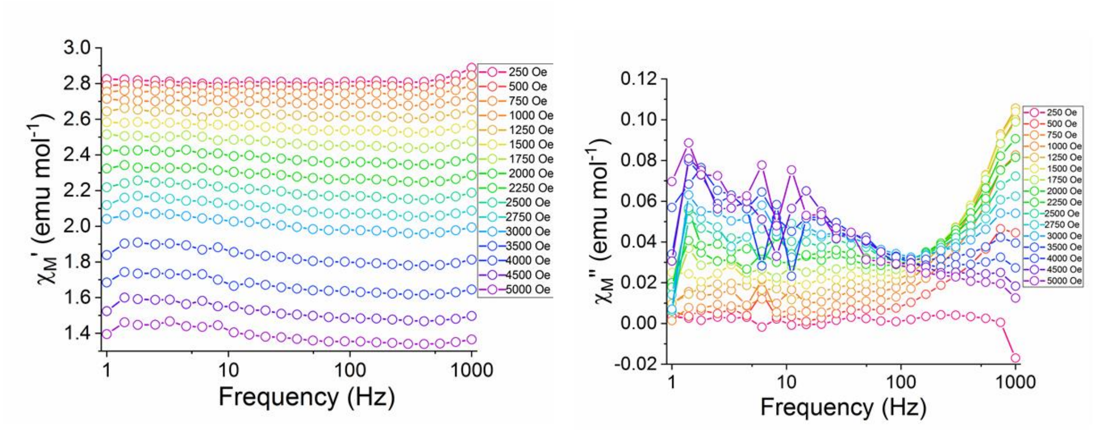

Figure D.18: In phase (χ_m') and out of phase component (χ_m'') of **5-19**, under field.